The Electronic Transport Properties of Undoped and Doped Arsenic Triselenide

A thesis presented by

Raymond Patrick Barclay

(Sponsoring establishment

Dundee College of Technology)

to the CNAA

in partial fulfilment of the

requirements for the degree of

Doctor of Philosophy

March 1985

DECLARATION

I declare that while registered as a candidate for the degree for which this thesis is presented I have not been a candidate for any other award. I further declare that except where stated the work contained in this thesis is original and was performed by the author. The author is grateful to Dr J T Edmond of Dundee University who helped with the preparation of the bulk glass, Dr. A. Long of Glasgow University who helped with the structural and chemical analysis of the arsenic triselenide films, and Mark Munro of Dundee College of Technology who assisted with the preparation of the computer programs.

Signed 

Raymond Patrick Barclay.

ADVANCED STUDIES

In addition to the original research reported in this thesis the author followed a programme of postgraduate study. This program included attendance at the lectures and tutorials of the joint Scottish M. Sc course in the Physics and Technology of Amorphous Materials held at Dundee University during 1981-82. Also the author attended the Chelsea Meeting on Liquid and Amorphous Semiconductors in 1982, 1983 and 1984, presenting a paper at the 1984 meeting.

ACKNOWLEDGMENTS

The author is greatly indebted to and wishes to thank the following without whose help this work would not have been possible.

Dr. Joseph M. Marshall and Dr. Charles Main for their supervision and encouragement throughout this investigation.

Henry Fortuna, Charles Bullock and Anthony Hepburn for many enlightening and critical discussions during both the theoretical and experimental aspects of this project.

Dr. R.R. Gardner for extending to the author the use of the facilities of the Physics Department at Dundee College of Technology.

Mr. J. Anderson and the technical staff of the Department of Physics for their help and advice during the course of this study.

The Science and Engineering Research council and Dundee College of Technology for providing the financial assistance which made this work possible.

THE ELECTRONIC TRANSPORT PROPERTIES OF UNDOPED AND DOPED ARSENIC TRISELENIDE

RAYMOND P BARCLAY

The electronic and transport properties of doped and undoped arsenic triselenide have been characterised in an extensive study. Measurement of optical absorption, d.c. conductivity, thermoelectric power and fast charge transient photoconductivity were made. In addition, an improved time of flight technique and a modulated steady state photocurrent experiment were developed.

Results obtained from undoped, vitreous, evaporated and sputtered samples were explained on the basis of a multiple trapping transport model with trap levels E_2 (0.62eV) and E_3 (0.42eV) above the valence band edge.

Variation of the dispersion parameter with temperature in vitreous material supports the presence of structure at E_2 in the distribution of localised states N(E). Deviations from power law behaviour in the transient photodecay also suggest a structured N(E) and a computer simulation of the thermalisation process was developed in order to obtain N(E) from the data. For sputtered material a feature incorporated at E_3 in a continuous tail of states gave the the best fit to the data. Determination of N(E) using two other recently developed spectroscopic techniques also gave excellent agreement in the energy position E_3.

The spectroscopic analysis offered a new technique for obtaining values of the capture coefficient C and offers the possibility of obtaining the energy dependence of C (if any).

In nickel doped specimens the Fermi-level was shifted by as much as 0.6eV, the conductivity increased by 11 orders of magnitude and n-type conduction, rarely seen in chalcogenides, observed. These unique findings were explained by inclusion of an acceptor level (E_4 0.22eV), introduced by nickel, into the intrinsic model density of states.

Results obtained when incorporating indium infer a shift in the valence band edge by 0.03 eV rather than a shift of the Fermi-level. A decrease in the trap density at E_3 with increasing indium content is also inferred.

Table of Contents

Chapter 1

INTRODUCTION TO AMORPHOUS SEMICONDUCTORS

1.1 General Review

The study of the physical properties of amorphous semiconductors has become a very active and important field in solid state physics. The pioneering work was begun, by the Leningrad school [1, 2] nearly three decades ago, but only in the last fifteen years or so has the interest been widespread.

The interest arose from two sides. The realization in 1968, by Ovshinsky [3], that films of chalcogenide alloys show fast and reversible switching from a high to a low resistance state was one reason for the rapid growth of interest. This initiated long discussions about the physical interpretation of switching, the fundamental question being whether the switching is either of thermal nature or of electronic nature. Also, the successful use of amorphous selenium and amorphous arsenic triselenide in the development of the Xerox reprographic process prompted further research through fundamental scientific interest[4, 5]. The experimenters were surprised to discover that the above mentioned materials had "anomalous transport properties" i.e. the measurement of the transient photodecay did not obey conventionally-expected statistics. To explain this behaviour different transport mechanisms were investigated which offered a more detailed insight into the microscopic transport mechanism.

A further wave of interest occurred in 1975 when Spear and

his group[6] reported the successful doping by substitution of impurity atoms into a tetrahedrally bonded material, amorphous silicon. The breakthrough meant that it was possible not only to control carrier concentration but also conductivity type in the amorphous semiconductor. This discovery opened up a wide variety of potential applications, in both electronics and optoelectronics. The excellent photoconductivity combined with the ability of this material to absorb a significant fraction of the energy in sunlight as well as its thin film large area mass producability, matches a strong need in low cost solar photovoltaic systems. Applications in thin film integrated electronic devices, transistors, optoelectronic imaging sensors, and electrophotography are also expected to arise from this material.

In addition to the appreciable effort dedicated to a-Si as a new electronic material, a considerable amount of effort for conductivity type control in chalcogenide glasses has been attempted in various ways[7, 8]. However there has been no clear experimental evidence on the controllability reported so far for the chalcogenide glasses

1.2 Amorphous Solids and Glasses

Condensed matter can be categorized into liquids, crystalline solids and non-crystalline or amorphous solids. The structure and properties of crystalline solids have been studied intensively with the aid of quantum mechanics for nearly half a century, and a fairly complete understanding has been gained of some crystalline materials.

In the idealized description of a crystal each pattern unit is associated with a lattice point and a unit cell. A given lattice point is in exactly the same environment as any other lattice point, and the contents of every other unit cell. A lattice can be completely characterized by the possible symmetry operations that leave it unaltered. The cells extend infinitely in all directions and the crystal is said to possess long range order(LRO).

The electronic structure of the constituent atoms determines the kinds of chemical bonds that form between them. The nature of these bonds, i.e. their strength, number and directionality, together with the prevailing thermodynamic correlation, governs the resulting crystal structure(if any), and the properties of the crystal. The immediate surroundings of a given atom, such as the number of the nearest and next nearest neighbours and their distance, are identical to those of any corresponding atom in any other unit cell. This is called the short range order(SRO).

In practice, ideal crystals do not exist, mainly due to the fact that no real material can satisfy the condition specified by infinite long range order. REAL crystals, therefore, are materials of finite dimensions. Under normal circumstances (i.e. when the crystal extends in all directions by many interatomic spacings), this dimensional limitation is of minor importance and only leads to small perturbations from the ideal crystalline theory.

A material which has ordered regions which are more than 20Å across can be readily identified by X-ray or electron diffraction. The

diffraction pattern of a single crystal consists of isolated points, that of a polycrystalline material is a series of concentric but sharp rings. As the crystallites become smaller the rings broaden into diffuse haloes with no distinguishing changes below about 20Å. An amorphous material may conveniently be defined as one without LRO, meaning order beyond approximately 20Å. Figure 1.1 shows a typical example of the radial distribution function for amorphous Ge. The figure shows clearly that the short range order extends to about 10 Å, (that being about three nearest-neighbour distances), and then merges into the statistical background. Most amorphous materials produce radial distribution functions with features similar to figure 1.1.

The liquid state is amorphous insofar as it possesses SRO and not LRO. A liquid, however, is in dynamic thermal equilibrium, its free energy is minimized and its molecules are in constant Brownian movement. When a liquid is cooled the molecular movements become sluggish and below the melting point crystallization will occur under the right conditions, i.e., if there is sufficient time for nucleation and crystal growth to take place. If crystallization cannot proceed, however, the material forms a supercooled liquid state in which molecular motion takes place but not crystallization. Upon further cooling a point will be reached when the molecules cannot rearrange themselves in response to the decreasing temperature and the structure freezes in. The temperature at which this occurs, i.e., when the cooling rate equals the relaxation rate, is called the glass transition temperature or simply glass temperature (Tg). Amorphous solids formed in this way are called "glasses","glassy solids" or

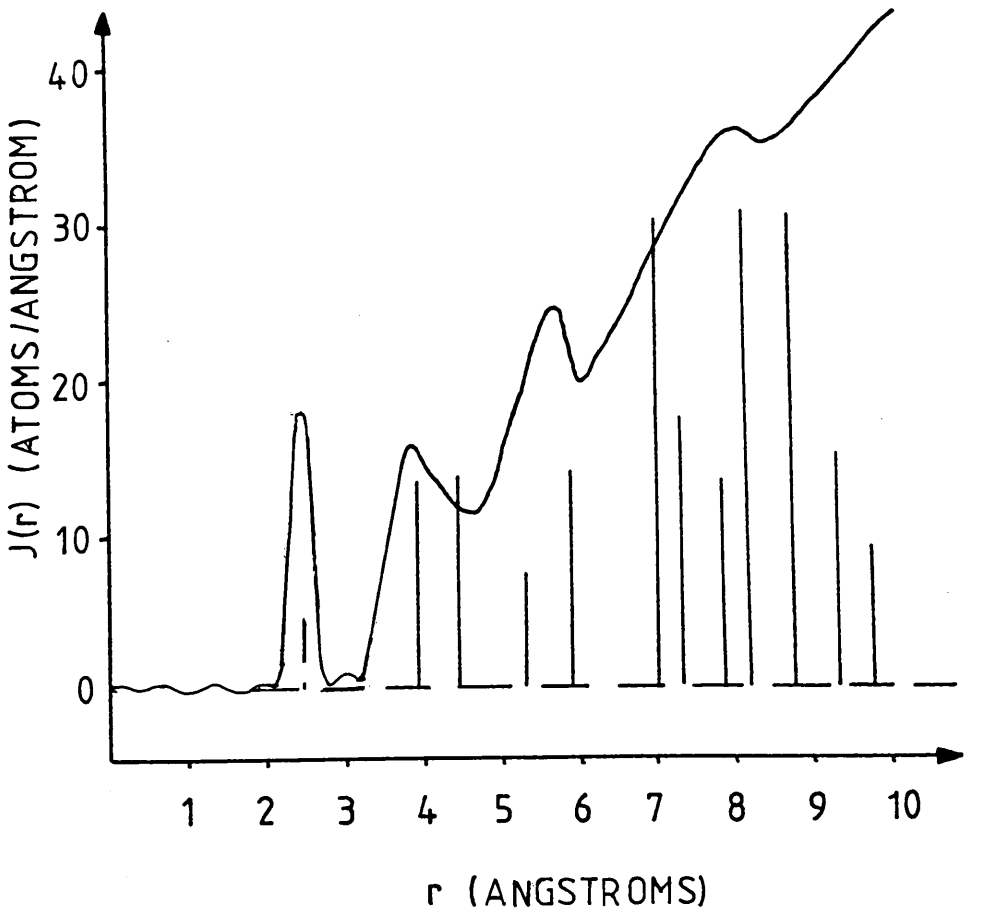

Figure 1.1 The radial distribution function (RDF) of amorphous germanium. The vertical lines indicate the sharp peaks expected in crystalline germanium.

"vitreous solids". There are, however, many other methods of preparing amorphous solids, two of which, r.f. sputtering and thermal evaporation are described in chapter 5.

In an attempt to determine the properties that lead to the breakdown of LRO in non-crystalline materials, model amorphous structures have been generated, relaxed and optimized by computer, then analyzed. One important concept arising out of such structural work is that of a Continuous Random Network (CRN). This ideal amorphous structure represents a fundamental concept on which most theoretical considerations are based. The major reason, however, why theory and experimental measurements do not agree in many cases is because it has now been realized that materials prepared experimentally have structures deviating appreciable from the ideal continuous random network.

1.3 Electronic Structure of Amorphous Solids

It has been known since the work of Bloch[9] that there are universal features in the electronic structures of crystals. The most important of these are the presence of energy bands separated by forbidden gaps, the fact that the crystal momentum is a good quantum number, and the result that the electron wavefunction has the form of a plane wave modulated by a function which has the same periodicity as the lattice.

The first steps towards an understanding of the theory of the electronic structure of disordered solids were not taken until almost 20 years after the work of Bloch, when Frohlich [10] pondered the

nature of the eigenstates in the tails of the bands. It was not until much later that Mott[11] combined these ideas with the work of Anderson[12] on the absence of diffusion in a three dimensional random potential to give a simple model containing the essential features common to all disordered systems.

This model can be considered as a natural extrapolation of the results for a crystalline semiconductor with the disorder treated as a small perturbation which causes the scattering of the electrons after they have traveled a mean distance L known as the mean free path. The electron has a wavefunction of the Bloch type which extends through the whole lattice. If we were to introduce disorder progressively into the lattice, we would eventually reach a point where L becomes equal to the lattice spacing a. Obviously L cannot become less than a, so this is the limiting case. From the Heisenburg uncertainty principle,

$$\Delta k \Delta x \sim 1 \tag{1.1}$$

so if k = 1/a (a typical value) this criterion becomes

$$\frac{\Delta k}{k} = \frac{a}{\Delta x} \tag{1.2}$$

so that k is no longer a useful quantum number, and the phase of the bloch function will change in a random way over a distance of the order of the lattice spacing. The wavefunction will still however extend throughout the lattice (see figure 1.2).

Although the mean free path of the electrons cannot be less than a, it is still possible to increase the disorder by introducing a

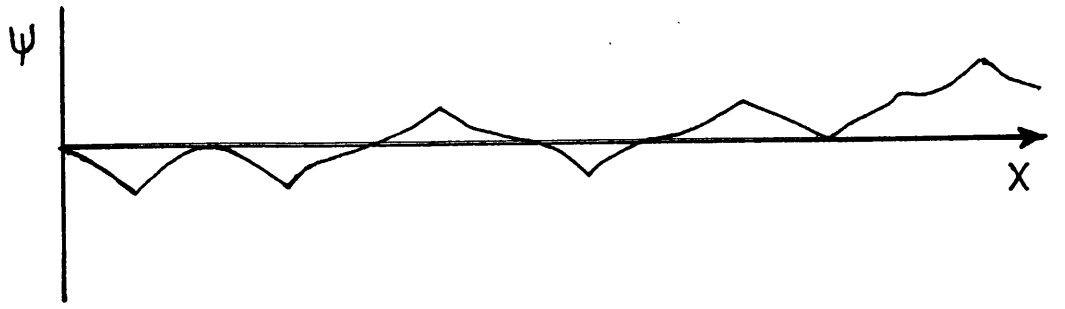

Figure 1.2 Forms of wavefunction in the Anderson model when L≫a.

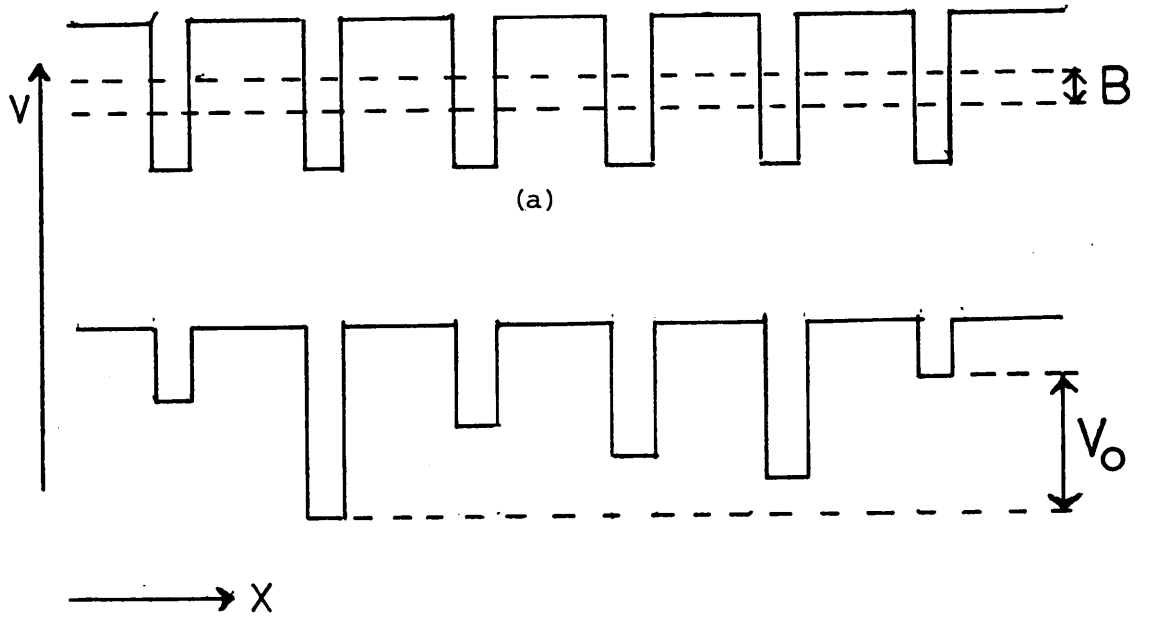

Figure 1.3 (a) Potential wells for a crystalline lattice
(b) Potential wells for the Anderson lattice.

random fluctuation of potential, Vo, on each lattice site (as shown in figure 1.3). This is the model used by Anderson in 1958 - note that the randomness is confined to the depth of the potential wells, and does not involve their spatial separation. Anderson showed that for a tight binding (narrow) band, a fundamental change occurs to the electron wavefunction when the disorder becomes so great that

$$\frac{V_o}{B} > \left[\frac{V_o}{B}\right]_{CRIT} \sim 5 \qquad (1.3)$$

where

$$B = 2zJ \qquad (1.4)$$

is the bandwidth of the tight binding band, J is the overlap integral, and z is the coordination of the lattice. This fundamental change is called Anderson localisation - all the electronic states in the band suddenly become localised (with wavefunctions similar to that sketched in figure 1.4) - even although there may be significant wavefunction overlap! Figure 1.5 illustrates the way in which the conductivity is expected to change with increasing disorder.

More recent work[13, 14] has shown that Anderson's critical value of the disorder potential Vo=5B was too restrictive, and indicated that a value of Vo nearer 2B is all that is required.

It was stated in the above section that in order to obtain Anderson localisation of a complete band, the bandwidth, B, must be small. In an amorphous semiconductor, however, wide conduction bands are generally found. How then can Anderson localisation be applied to these wide band materials?

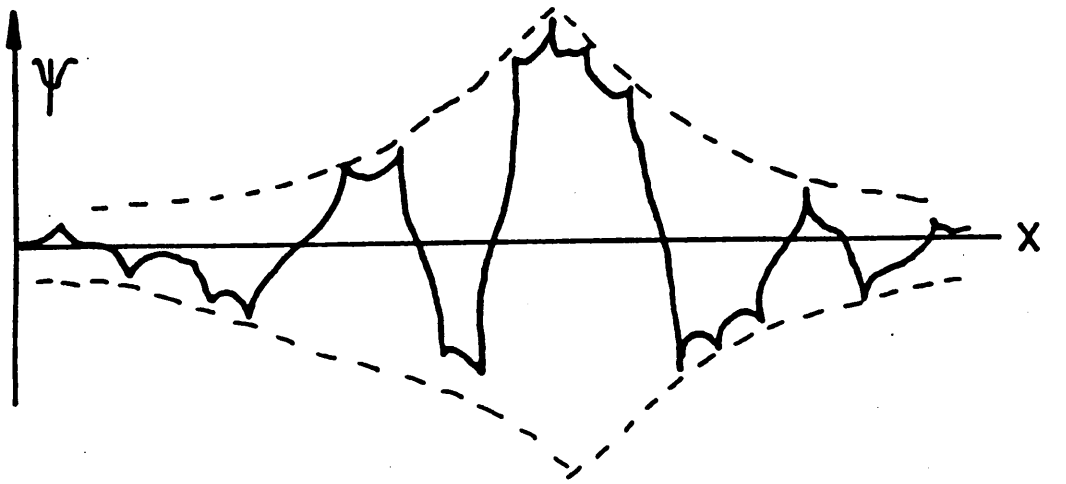

Figure 1.4 Form of localised wavefunction in the Anderson model

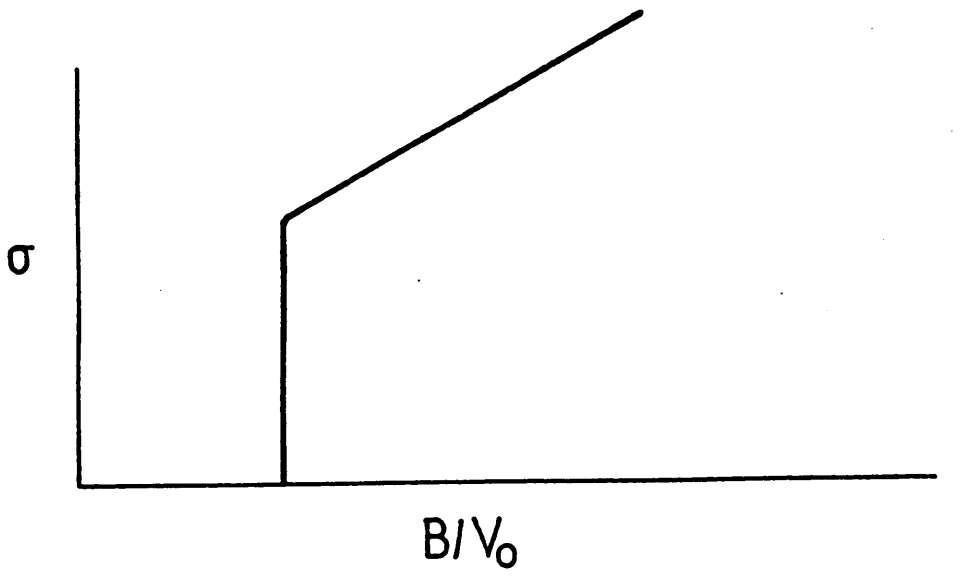

Figure 1.5 The conductivity at zero temperature as a function of B/V_o.

Figure 1.6 shows the density of states, g(E), plotted against energy for an amorphous semiconductor. The important fact to recognise about this distribution is that the two site exchange integral, J, will vary throughout the band, since it is critically dependent upon the separation of the states. The electron wavefunction overlap will be smaller in the "tails" of the band, (where g(E) is small), so that Vo/J will reach the critical value for localisation first in the tail states. States away from the edge of the band will remain delocalised. For the purpose of illustration, consider the conduction band, suppose that localisation sets in when the density of states falls below a value corresponding to the energies, E_c, at the top and bottom of the band. Considering only the bottom of the band (the top of the band being insignificant as far as conduction is concerned), at energies $E > E_c$, there are extended states in which conduction can take place, even at T = 0. For energies $E < E_c$, the ensemble average of the conductivity will be zero at T=0, and the mobility must vanish. The existence of an energy such as E_c, was first pointed out by Mott[15], and its existence in non-crystalline semiconductors implies a " mobility edge" which takes the place of (for many practical purposes) the density of states edge in crystalline semiconductors.

The foregoing description of an "ideal" amorphous semiconductor forms the basis upon which the electrical and optical properties of real amorphous semiconductors may be understood. There is a great deal of experimental evidence to support the existence of valence and conduction bands in amorphous semiconductors dating from

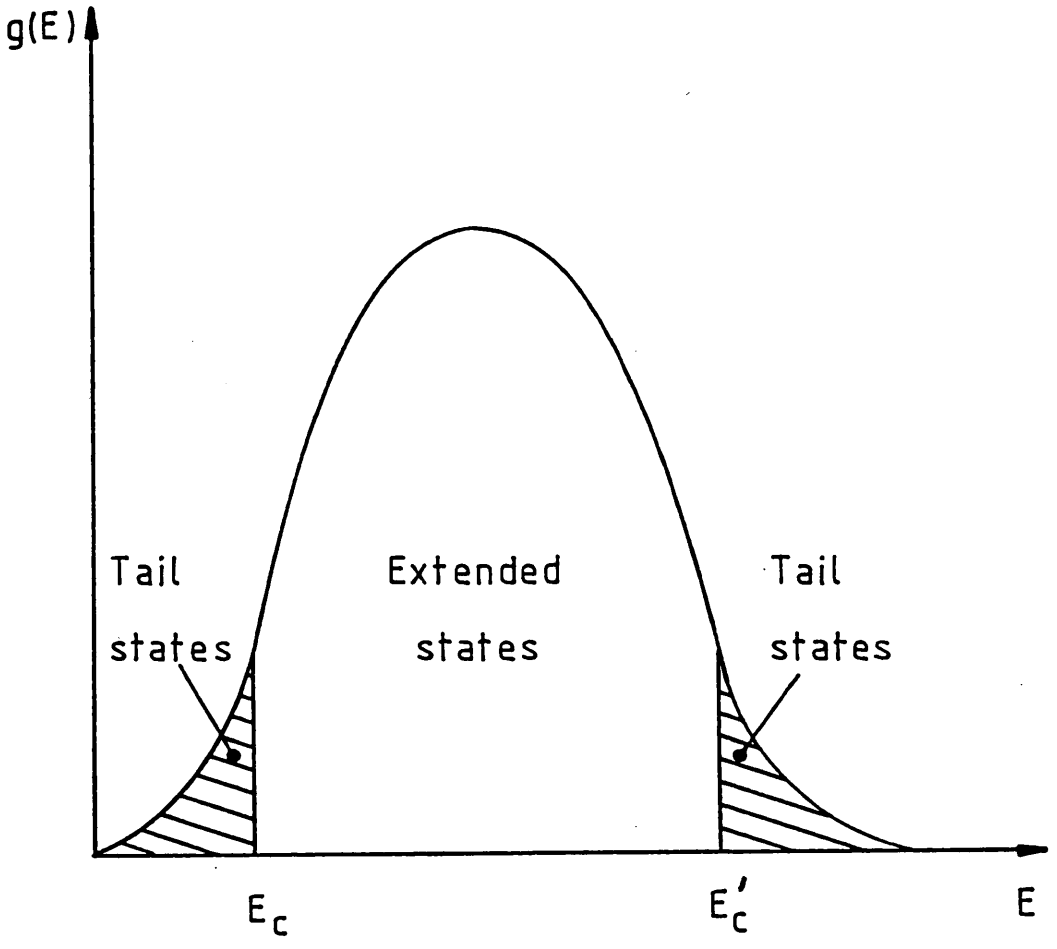

Figure 1.6 Density of states in the Anderson model when states are non-localised in the centre of the band. Localised states are shown shaded.

the pioneering work of Kolomiets and co-workers in the 1950's. There is similarly a large amount of experimental evidence for the presence of mobility edges (the position of which may be temperature dependent), which has been reviewed by Mott et al [16] - although the sharpness of such edges, as well as the presence of a minimum metallic conductivity at low temperatures remain controversial.

Detailed measurements of the drift mobility, field effect, photoconductivity etc. on a variety of materials have subsequently verified the existence of fairly discrete levels or, at least, structure in the distribution of the density of states throughout the mobility gap of amorphous semiconductors. Many models have been proposed to account for this structure, and these will be described in some detail in the next chapter. For the rest of this chapter we need only assume the existence of extended band states and localised gap states.

1.4 The Breakdown of Conventional Transport Theory

The Boltzmann equation formulation of transport theory is based on the idea that the electrons in the solid move freely under the influence of external fields, and that these movements are interrupted by interactions with the lattice such as phonon emission or absorption. Electrons considered in this way are represented by wave-packets using combinations of Bloch functions. These wave-packets must have a smaller extent than does the Brillouin zone in k-space, and hence must extend over several lattice constants in real space. In addition, all other space dependent qualities (such as lattice disorder, external fields etc.) must change slowly along the length of

the wave-packet. Thus, if the mean free path of the electrons starts to approach the dimensions of the lattice parameter this approach breaks down, and $\underline{k}$ ceases to be a good quantum number (as shown in section 1.3). This is the familiar Ioffe-Regel condition which applies in the case of amorphous metals[17].

There is also a restriction placed on the applicability of this approach by the use of the relaxation time approximation. When this approximation is used, the electron is considered to be accelerated like a free particle between two "collisions". Between these collisions it will absorb energy from the field and give it up to the lattice at the next collision. The model will thus fail when the energy absorbed from the external field becomes comparable to the width of the energy band, which is important in the case of narrow bands. This implies that there must be sufficiently weak electron-phonon coupling so that the interaction time during collisions is smaller than the time between collisions.

Another limitation on the applicability of conventional transport theory was pointed out by Frohlich and Sewell[10], who showed that in a narrow band ($B < 2kT$) the uncertainty principle provides the condition

$$\hbar / \tau > 2J \tag{1.5}$$

and because

$$\mu = \frac{eD}{kT} = \frac{e}{kT} \frac{\tau J^2 a^2 \hbar^2}{2} \tag{1.6}$$

it follows that the mobility must be <u>greater</u> than the limited value

shown in equation (1.7)

$$\mu > \frac{ea}{\hbar} \cdot \frac{B}{kT} = \frac{0.1B}{kT} \quad cm^2 V^{-1} s^{-1} \tag{1.7}$$

In a semiconductor with a wide band ($B = 2zJ \gg kT$) we can use the concept of an effective mass, so that

$$\mu = \frac{e\tau}{m^*} \tag{1.8}$$

and the uncertainty principle again provides us with the condition for the applicability of conventional theory

$$\hbar/\tau < kT \tag{1.9}$$

which in turn implies

$$\mu > (m/m^*)(e\hbar/kT) = (m/m^*).30 \ cm^2 V^{-1} s^{-1} \tag{1.10}$$

Summarizing, there are three criteria which must be met if conventional band theory and the Boltzmann equation formulation of transport theory can be applied:-

1). The absence of a disordered potential which changes abruptly over distances of the order of a lattice constant.

2). The absence of a strong electron-phonon coupling.

3). A mobility of greater than about 10 $cm^2V^{-1}s^{-1}$.

These are <u>necessary</u> conditions for the applicability of conventional band theory and the Boltzmann equation, but they do not tell us anything about the conduction mechanisms which will apply if these criteria are not met. In particular they do <u>not</u> imply that the

one-electron states are localised. There are in fact two possibilities:-

1). Extended-state conduction - where $\underline{k}$ is no longer a good quantum number and the Boltzmann formulation fails. Instead the extended motion is a diffusive motion or random walk from one atom to the next. This mechanism does not require phonon assistance and the conductivity ensemble $\langle\sigma\rangle = 0$ at $T = 0$.

2). Localisation and hopping conduction - this will occur for sufficiently low mobilities as a result of either:-

a). Anderson localisation described in the previous section and/or

b). Small polaron formation (or self-trapping), when the local electron-phonon interaction is sufficiently strong to distort the lattice and trap the electron before it moves to another site. Here $\langle\sigma\rangle = 0$ at $T = 0$, and so the processes are thermally activated. These transport mechanisms will now be discussed in greater depth.

1.5 Extended State Conduction

It has been shown in the previous section that for conduction near a mobility edge in an amorphous semiconductor the Boltzmann equation formulation is unlikely to be applicable. Instead, one must start from the more general formulation of conductivity theory developed by Kubo and subsequently simplified by Greenwood (a more detailed discussion of this formalism is beyond the scope of the present work, but may be found in reference[15]). For states involved in conductivity which are several kT from the Fermi-level, the

Kubo-Greenwood formula may be written as

$$\sigma = \int e \mu(E) n(E) \, dE$$

with

$$n(E) = g(E) f_0(E)$$

$$\mu(E) = \frac{\sigma_E(0)}{kT e g(E)} \qquad (1.11)$$

The physical meaning of this formula is that the conductivity is made up of contributions from the individual states, whose localisation or delocalisation is related to the value of the "mobility" $\mu(E)$ at T=0. If one assumes that the Fermi-level is situated near the centre of the mobility gap, and thus sufficiently far from E_c, the energy that separates the extended from the localised states, so that Boltzmann statistics can be used to describe the occupancy of the states, one obtains

$$f(E) = \exp[-(E-E_F)/kT] \qquad (1.12)$$

In the non-degenerate case and under the assumption of a constant density of states and constant mobility (see ref.[18] page 113)

$$\sigma = e N(E_c) kT \mu_c \exp[-(E_c-E_F)/kT] \qquad (1.13)$$

where μ_c is the average mobility. The number of electrons is given by

$$n = N(E_c) kT \exp[-(E_c-E_F)/kT] \qquad (1.14)$$

In order to get an idea of the order of magnitude of σ_{min} Mott's treatment shall be followed (ref.[15] page 31). He defined $\sigma(E_c) = e N(E_c) \mu_c kT$. If $N(E_c) \sim \langle N(E) \rangle / 3$, where $\langle N(E) \rangle$ is the

average density of states over the band, then expression (1.15) is obtained.

$$\sigma(E_c) = e \langle N(E) \rangle \mu_c kT/3 \qquad (1.15)$$

Mott calculated the lowest value of electrical conductivity before the start of the activated process, i.e., just at E_c. This quantity he called the "minimum metallic conductivity". He derived the expression

$$\sigma_{min} = \text{const.}\ e^2/\hbar a \qquad (1.16)$$

where the constant a lies between 0.025 and 0.1. Taking the constant to be 0.025 one finds for the mobility

$$\mu_c = 0.078\, e/\hbar a (\langle N(E) \rangle kT)^{-1} \qquad (1.17)$$

which may be simplified using the nearly-free electron model [18] to expression (1.18)

$$\mu_c = 0.078 \frac{e a^2 B}{\hbar kT} \sim 10\ cm^2 V^{-1} s^{-1} \qquad (1.18)$$

taking a = 2 A and B = 5 eV.

This value corresponds to a mean free path comparable to the inter-atomic spacing. Cohen [19] suggested that conduction in this case would be more properly described as a diffusive or Brownian-type motion. In this regime the mobility may be calculated from the Einstein relation given that

$$D = \frac{1}{6} \nu a^2 \qquad (1.19)$$

where ν is the jump frequency and a is the inter-atomic distance. This yields

$$\mu = \frac{1}{6} \frac{e a^2 \nu}{kT} \qquad (1.20)$$

which has the same temperature dependence as equation (1.18) derived

by Mott.

Optical absorption measurements made on amorphous semiconductors have shown that the band gap decreases with increasing temperature. The energy difference $E_c - E_F$ therefore will show a similar behaviour, and, under the assumption of a linear temperature dependence,

$$E_c - E_F = E(o) - \gamma T \tag{1.21}$$

the expression for the conductivity becomes

$$\sigma = \sigma_o \exp(\gamma/k) \exp\left[-\frac{E(o)}{kT}\right] \tag{1.22}$$

where E(o) is the energy separation at T=0. This may be written in the form

$$\sigma = C_o \exp\left[\frac{-E(o)}{kT}\right] \tag{1.23}$$

where

$$C_o = e N(E_c) kT \mu_c \exp\left(\frac{\gamma}{k}\right) \tag{1.24}$$

As seen before, the mobility is proportional to 1/T, so that the pre-exponential factor C_o is temperature independent. In general σ_o may lie between 10 and 1000 Ω^{-1} cm^{-1}, in most amorphous semiconductors. In chalcogenide glasses, the temperature co-efficient of the optical gap generally lies between 4×10^{-4} and 8×10^{-4}eV K^{-1}. As the Fermi-level is situated near the middle of the gap, values of approximately half this magnitude are expected and hence values of $\exp(\gamma/k)$ in the range 10-100 seem probable.

A different approach based on a 'random phase' model was used by Hindley [20] and Friedman [21] to calculate the mobility in the

extended states near E_c or E_v. In this model a mean free path of the order of the lattice spacing is represented by a loss of phase memory of the electron wavefunction as it moves from site to site. Assuming a constant density of states the following expression for the mobility was derived.

$$\mu_c = \frac{2\pi e a^2 z}{3\hbar} \left[\frac{J}{kT} a^3 J N(E_c) \right] \qquad (1.25)$$

Here z is the co-ordination number, J is the two site exchange integral and a, the interatomic spacing. Equation (1.25) yields a value of 5 $cm^2V^{-1}s^{-1}$ for the mobility at room temperature, a value not significantly different from that obtained from expression (1.18).

1.6 Hopping Conduction

As we saw in section 1.4, there are two possible localisation mechanisms which may lead to carrier localisation and thermally activated transport. These mechanisms are small polaron formation and Anderson localisation. We shall now discuss the transport mechanisms in each case.

1.6.1 Hopping Conduction in Band Tails

If carrier wavefunctions are Anderson-localised, so that $\langle \sigma(E) \rangle = 0$ at $t = 0$, conduction at low temperatures will be by a thermally activated process. One way that this can happen in band tail states is by 'hopping' from one localised state to another, the wavefunction of which overlaps that of the first state. Since the two states have quantized energies, the carrier must exchange energy with a phonon each time it moves. The rate-determining step is that in which the carrier obtains energy from the phonon. Hopping of this

kind was first described by Miller and Abrahams [22] and Twose [23] in their theories of impurity conduction in doped and compensated crystalline semiconductors. They supposed that a carrier on one occupied site would normally jump to a nearest site with energy ΔE above it (see figure 1.7), where

$$\Delta E \sim \frac{1}{\alpha^3 N(E)} \tag{1.26}$$

The hopping probability is then of the form

$$p = \nu_{ph} \exp(-2\alpha R - \Delta E / kT) \tag{1.27}$$

where ν_{ph} depends on the strength of the interaction with the phonons, and α is a measure of the localisation of the wavefunction.

Thus hopping will lead to a thermally activated mobility

$$\mu_{hop} = \mu_0 \exp[-W/kT] \exp(-2\alpha R) \tag{1.28}$$

The pre-exponential μ_0 has the form

$$\mu_0 = \frac{1}{6} \nu_{ph} e R^2 / kT \tag{1.29}$$

where ν_{ph} is the phonon frequency and R the distance covered in one hop [18]. For a typical phonon frequency ν_{ph} = 10^{13}Hz and W=kT this yields a mobility of the order of $10^{-2}cm^2V^{-1}s^{-1}$ at room temperature. Comparison of this value with the one calculated for conduction in the extended states suggests, as postulated by Mott, that the mobility may drop by a factor of at least 100 at the energy which separates the localised from non-localised states, and this can be identified as the mobility edge.

The conductivity being an integral over all available energy states, will depend on the energy distribution of the density of localised states. If one assumes that the density of states N(E) behaves as some power of E, so that $N(E) \sim E^n$ then the following

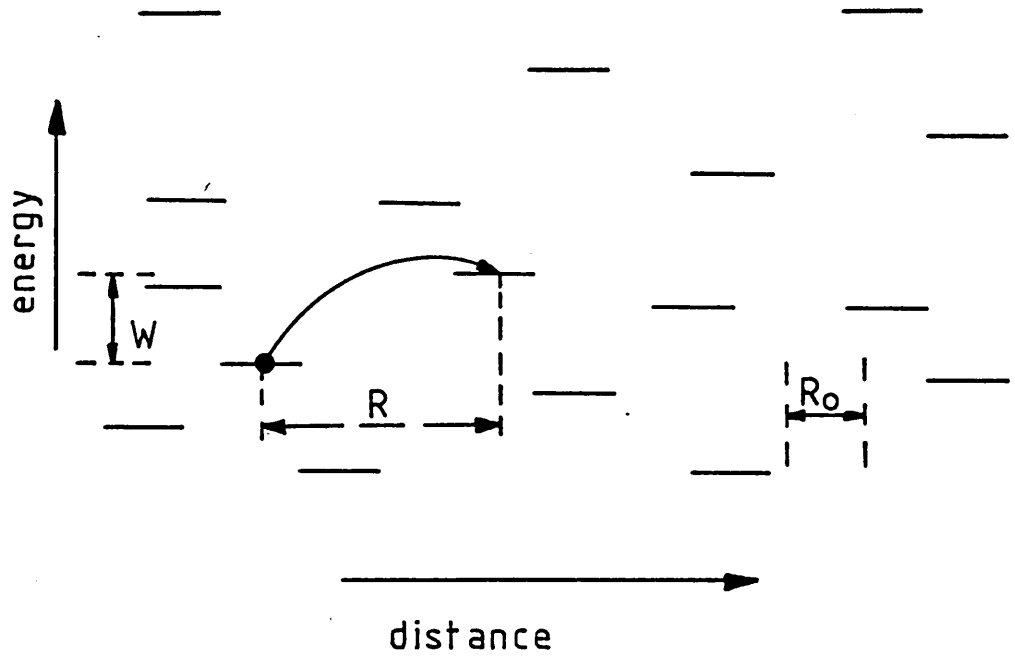

Figure 1.7 Nearest-neighbour hopping in an a-semiconductor

expression can be obtained using equation (1.11).

$$\sigma = \sigma_{o\,hop} \exp\left[-\frac{(E_A - E_F + W)}{kT}\right] \qquad (1.30)$$

Examination of σ_{hop} is not easy, but it is expected to be several decades smaller than σ_{min}, partly because of the lower effective density of states near E_A compared to E_c, and because of the lower mobility μ_{hop}

1.6.2 Hopping Conduction at the Fermi-level

As we have seen in section 1.5, at high temperatures one may observe extended state conduction which follows the expression

$$\sigma = \sigma_o \exp\left[-\frac{(E_c - E_F)}{kT}\right]$$

As the temperature is lowered, we saw in the last sub-section that band tail hopping may take place, with

$$\sigma = \sigma_{o\,hop} \exp\left[-\frac{(E_A - E_F + W)}{kT}\right]$$

At still lower temperatures, the conduction path will move into the localised states deep in the mobility gap, where we expect to obtain a conductivity of the form

$$\sigma = \sigma'_{o\,hop} \exp\left[-\frac{(E_x - E_F + W)}{kT}\right]$$

where E_x is the depth of the localised states in which the conduction path may be found at a given temperature. Finally, the conduction path will reach the Fermi-level. If there is a non-zero single particle density of states at E_F, the phenomenon of variable range hopping is to be expected. For this phenomenon theories that neglect the "Coulomb Gap" caused by interaction between carriers [24, 25, 26], show that the conductivity is given by expression (1.31) for three-dimensional

hopping within a density of states $N(E_F)$.

$$\sigma = A \exp[-(Q/kT)^{1/4}] \qquad (1.31)$$

with

$$Q = 1.5/\alpha^3 N(E_F) \qquad (1.32)$$

However if electron-electron interaction is taken into account, significant changes in this behaviour are predicted especially at low temperatures [27].

1.6.3 Small Polarons

A small polaron may be formed when a charge carrier remains long enough over an atomic site for displacements of the surrounding atoms to occur . A potential well may then be created and can lead to self trapping of the carrier. It is this trapped carrier and the lattice deformation which is called a polaron. The polaron has a lower energy than the free electron but a larger effective mass, since it must carry its induced deformation when it moves through the lattice. The reduction of energy is a net result of two opposite contributions: the first is due to a lowering caused by the displacement of surrounding atoms, the second being an increase (half that of the decrease) due to the strain energy induced in the distortion.

Emin[28] has discussed the likelihood of small polaron formation in non-crystalline materials. He was able to show that several aspects of the transport data can be consistently explained using equations of the transport coefficients originally developed for the motion of small polarons in crystalline materials[29]. For example if carrier motion proceeds via thermally activated hopping, expression

(1.33) is obtained for the conductivity,

$$\sigma = [n e^2 a^2 / kT] \rho \qquad (1.33)$$

where e is the electronic charge, a is the equivalent site spacing and k is the boltzmann's constant.

The mobility is expected to be given by equation (1.34),

$$\mu = [\omega_o / 2\pi] \exp[W/kT] \rho \qquad (1.34)$$

where $\omega_o/2\pi$ is the average phonon frequency and W is the minimum energy necessary to obtain two equivalent sites. As far as ρ in both expressions is concerned, we must distinguish two extreme cases. In the adiabatic regime, the carrier adjusts rapidly to the motion of the lattice and is thus unlikely to miss any chances to hop to a neighbouring site - this means we can set ρ=1. The opposite applies in the non-adiabatic case, where the carrier adjusts itself too slowly and misses many chances to hop. In this case ρ is given by equation (1.35),

$$\rho = \frac{2\pi}{\hbar \omega_o} \left(\frac{\pi}{W kT} \right)^{1/2} J^2 < 1 \qquad (1.35)$$

where J is the transfer integral which is a measure of the wave-function overlap. Equations for the Hall effect and thermopower and many other electrical properties, can also be derived using small polaron theory.

1.7 Thermoelectric Power

The work of Cutler and Mott [30] suggests that a general

expression for the thermopower S exists [31, 30] which is closely related to that of equation (1.11). The thermopower is related to the Peltier coefficient π by expression (1.36).

$$S = \pi / T \tag{1.36}$$

The Peltier coefficient has a simple physical meaning. It is the energy carried by the electrons per unit charge. The energy is measured relative to the Fermi energy. Each electron contributes to σ in proportion to its relative contribution to the total conductivity. The weighting factor for electrons with dE at E is thus $\sigma(E)dE/\sigma$. This yields

$$\pi = -\frac{1}{e} \int (E - E_F) \frac{\sigma(E)}{\sigma} dE \tag{1.37}$$

and

$$S = -\frac{k}{e} \int \frac{(E - E_F)}{kT} \frac{\sigma(E)}{\sigma} dE \tag{1.38}$$

The sign convention is such that $S<0$ for electrons at energies $E>E_F$. The magnitude of an individual contribution to S scales roughly with distance from E_F in units of kT and with its fractional contribution to the total current. Under the assumption of a constant density of states and an energy-independent mobility the thermopower can be readily found by integrating equation (1.38). This yields an expression of the familiar form for band conduction of electrons

$$S = -\frac{k}{e} \left[\frac{E_c - E_F}{kT} + A \right] \tag{1.39}$$

with A=1; in the case of crystalline semiconductors it is well known

that the kinetic term A depends on the scattering mechanism.

From the above results we see that in this regime, S and σ should have the same activation energy. Hindley [20] has found a similar expression for S using the random phase model.

If both electrons and holes contribute to the conductivity then the thermopower is the algebraic sum of the individual contributions S_e and S_h but each is weighted according to the ratio of its conductivity to the total conductivity. Thus we have

$$S = \frac{S_e\sigma_e + S_h\sigma_h}{\sigma_e + \sigma_h} \qquad (1.40)$$

1.7.1 Conduction in Localised States Near the Mobility Edge

For conduction at E_A (or E_B) in an amorphous semiconductor it is generally assumed that equation (1.39) is valid with E_A substituted for E_c, but with n+A substituted for A within the parentheses giving,

$$S = \frac{-k}{e}\left[\frac{E_c - E_F}{kT} + (n+A)\right] \qquad (1.41)$$

if $N(E)\sim E^n$ at the bottom of the band as used in deriving equation (1.30), for the conductivity.

1.7.2 Conduction at the Fermi Level

At low temperatures, charge transport can arise from electrons tunneling between the states at E_F. Cutler and Mott [30] suggested that the thermopower in this regime should be identical to the equation used for metallic conduction,

$$S = \frac{\pi^2 k^2 T}{3e} \left[\frac{d \ln \sigma(E)}{dE} \right]_{E_F} \qquad (1.42)$$

since the thermopower lies in a regime where the density of states is non-zero. The thermopower is small (about 25 μV/K typical of 'metallic' values). Its sign may be positive or negative, depending on whether the major contribution to the current will lie below or above the Fermi energy. However some doubt has been thrown on the applicability of equation (1.42) [32].

1.8 Optical Absorption in Amorphous Semiconductors

Ideally the electron states represented by any two different wave vectors are orthogonal and do not mix. An imperfection in the periodic potential causes a perturbation which can induce scattering or a transition (inelastic scattering). The probability of the transition taking place is proportional to the square of the matrix element of the perturbing potential between the initial and the final states

$$H_{ij} = \langle \underline{k}_i | H | \underline{k}_j \rangle \qquad (1.43)$$

When the perturbing potential arises from the optical radiation the Hamiltonian H can be expressed as $H=\underline{j}.\underline{A}$ where $\underline{j}$ is the current operator and $\underline{A}$ is the vector potential of the electromagnetic field. In the case of phonon-assisted transitions (involving an electron, a photon and a phonon) other matrix elements which arise from the perturbation Hamiltonian of the lattice vibrations are also involved. In the dipole approximation all matrix elements vanish unless both wave vector and energy are conserved. This gives rise to the

k-selection rule. Transitions which are forbidden according to this rule can still take place with a much reduced probability.

Thus in crystals, transitions between states are only allowed if both energy and quantum number $\underline{k}$ are conserved. Photons which have energy of the same order as the band gap have wavelengths in the range 10^3A-10^5A which means that their wave vector is negligible compared to $\underline{k}$ and the initial and final wave vectors must be identical

$$\underline{k}_i = \underline{k}_f \tag{1.44}$$

and

$$E_i \pm h\nu = E_f \tag{1.45}$$

These are termed direct or vertical transitions. If phonons with wave vector $\underline{q}$ and energy $hw_{\underline{q}}$ take part then

$$\underline{k}_i \pm \underline{q} = \underline{k}_f \tag{1.46}$$

and

$$E_i \pm h\nu \pm hw_q = E_f \tag{1.47}$$

Phonon-assisted transitions are called indirect transitions.

The concept of functional E-$\underline{k}$ relationships breaks down when Δk becomes comparable to $\underline{k}$. In amorphous solids, equations (1.44) and (1.46) are no longer thought to apply, at least not near the band edges, because $\underline{k}$ is not a good quantum number. This means that an electron can make a transition between any two sites as long as the energy is conserved. The term non-direct transition is frequently used for these transitions. Since the one-electron Schrodinger equation remains to be solved for amorphous materials it is not possible to

calculate matrix elements for non-direct transitions. In presenting optical absorption data it is generally assumed that the matrix element is nearly independent of photon energy immediately above the onset of interband transitions between extended states. Davis and Mott [33] have argued that transitions where either the initial or the final state is localised and the other is extended should have similar matrix elements as those between two extended states. These assumptions will be used and discussed in this work.

1.8.1 Absorption Edge

In many amorphous semiconductors the absorption edge has the shape shown in figure 1.8. One can distinguish a high absorption region A ($\alpha > 10^4$ cm^{-1}), an exponential region B, which extends over 4 orders of magnitude of α and a weak absorption tail C. Under the assumption of relaxed selection rules and an energy independent matrix element, the absorption can be obtained by integrating over all transitions that satisfy the energy conservation conditions, thus

$$\alpha = \frac{2\pi\nu}{nc}\,\varepsilon_2(\nu)$$

$$= \frac{h^3 e^2 M^2}{2\pi^4 m^2 nc}\,\frac{1}{h\nu}\int_{E_c - h\nu}^{E_v} N_c(E+h\nu)\,N_v(E)\,dE \qquad (1.48)$$

where E_v and E_c are the edges of the valence and conduction bands respectively, M is the matrix element, n the refractive index, c the speed of light , and ε_2 is the imaginary part of the dielectric constant. Assuming that the density of states $N_c(E)$ and $N_v(E)$ vary as

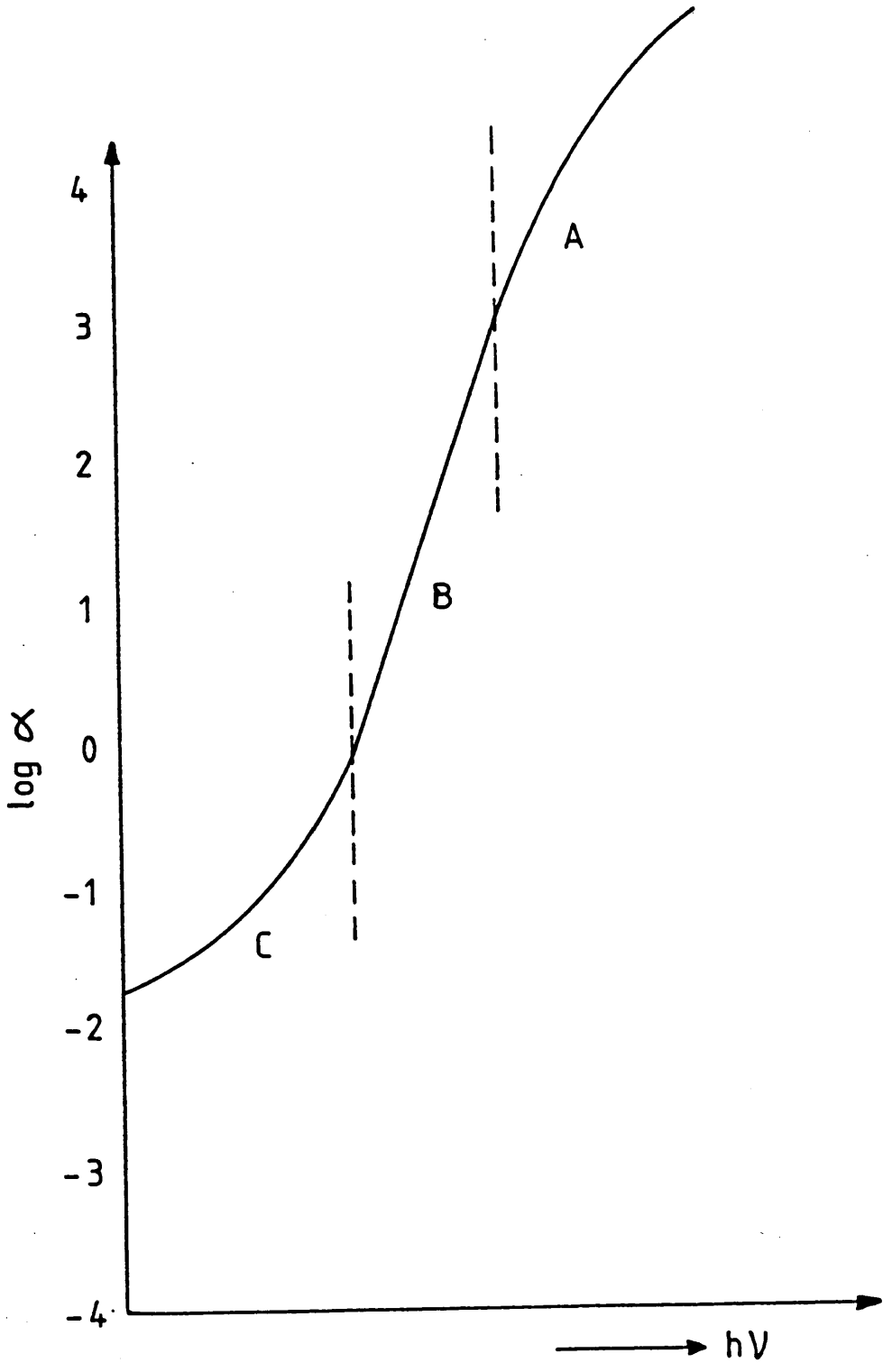

Figure 1.8 The absorption edge found in most amorphous compound semiconductors. Three regions can be distinguished: (A) a power-law region above $\alpha \simeq 10^3$ cm^{-1}, (B) the so-called urback edge (exponential) region, and (C) the absorption tail.

some powers p and s, i.e.,

$$N_c(E) = N_c (E-E_c)^p \tag{1.49}$$

and similarly for the valence band. Equation (1.48) can now be integrated by substituting

$$y = \frac{E_v - E}{h\nu - (E_c - E_v)} \tag{1.50}$$

This gives

$$\alpha h\nu = \frac{h^3 e^2 M^2 N_v N_c}{2\pi^4 m^2 nc} (h\nu - E_o)^{p+s+1} \int_0^1 (1-y)^p y^s \, dy \tag{1.51}$$

where $E_o = E_c - E_v$.

The integral in equation (1.51) can be evaluated by the use of gamma functions and gives a numerical factor $\sim 1/2$.

In amorphous semiconductors the observed behaviour of absorption as a function of energy is of this form in the high absorption region (i.e. region A of figure 1.8). For example the absorption of a-Se is linear with photon energy [15] in the range 2.1 eV $< h\nu <$ 3.1 eV, i.e.

$$\alpha h\nu = \frac{2\pi}{nch} \epsilon_2(\nu) (h\nu)^2 = C_1 (h\nu - E_{o1})$$

This seems to be the exceptional case, however, and the most commonly observed form is the square relation:

$$\alpha h\nu = C_2 \left[h\nu - E_{02}\right]^2 \qquad (1.53)$$

which gives good agreement with the data for example from arsenic triselenide, arsenic telluride, arsenic trisulphide, arsenic, silicon [15] and also many multicomponent glasses (eg, $Ge_{10}As_{40}Se_{50}$ and $Si_{12}Te_{48}As_{30}Ge_{10}$ [15]). Other multicomponent glasses (eg, $Ge_{15}Te_{81}Sb_2S_2$ [15]) have an absorption coefficient that obeys a cubic relation

$$\alpha h\nu = C_3 \left[h\nu - E_{03}\right]^3 \qquad (1.54)$$

There are two different interpretations of these observations. Figure 1.9 outlines the density of states diagrams proposed by Tauc [34] and by Davis and Mott [33] to account for equation (1.53). In both cases the matrix elements are assumed to be the same between two extended states as between one localised and one extended state. Tauc assumes parabolic band edges similar to those in crystals. According to this model p=s=1. The gap that appears in equation (1.53) is not the true gap, but that obtained by extrapolating the parabolic densities of states to zero density. It follows that if the mobility edges do not coincide with the extrapolated edges , then there will be a deviation from equation (1.53) as $h\nu$ approaches E_{02} from above.

In the Davis and Mott interpretation on the other hand, transitions between a linear tail of localised states in one band and extended states in the other band are assumed to dominate, the density of the latter varying slowly enough with energy to be taken as a constant above the mobility edge. Thus p=1, s=0, or vice versa.

The two different expressions for C_2 in the two interpretations are then,

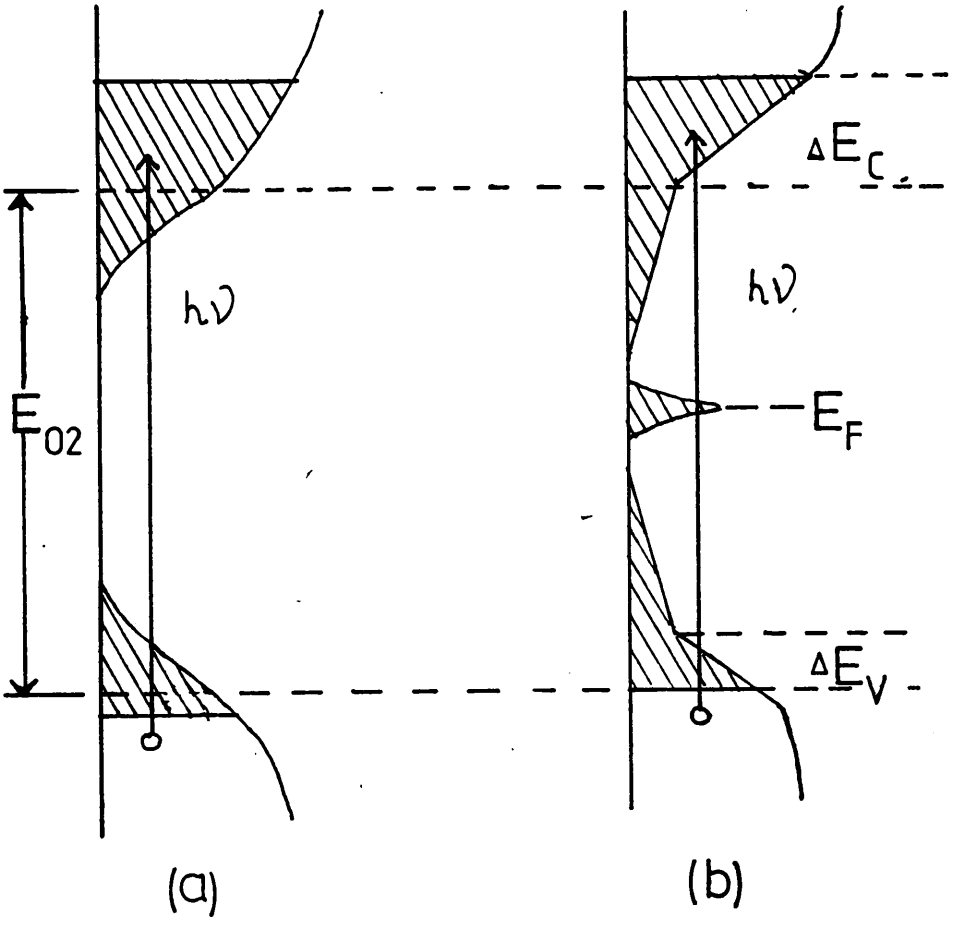

Figure 1.9 Density of states proposed by Tauc (a) and by Davis and Mott (b) to account for square law behaviour showing different interpretations of the extrapolated optical gap E_{o2}.

Tauc: $$C_2 = \frac{\pi}{8} \frac{N_c N_v M^2 D}{n} \quad (1.55)$$

Davis and Mott: $$C_2 = \frac{1}{2} \frac{N_c' N_v' M^2 D}{\Delta E n} \quad (1.56)$$

where D is a constant, n is the refractive index, the numerical factors account for the integral in equation (1.51) and ΔE is the depth of the deeper of the two tails. The linear tails, in the Davis and Mott interpretation are due to disorder and are expected to be 0.1-0.2 eV in extent for the simple chalcogenide glasses like As_2Se_3 [35].

A major objection to the Davis and Mott interpretation as they point out themselves [15], is that it is inconsistent with the relatively wide energy range over which equation (1.53) is observed to hold, eg, 1.5 eV in a-As_2Se_3 [35]. Both interpretations give estimates of C_2 in reasonable agreement with experiment.

The exponential region (region B) of the absorption edge occurs in most amorphous semiconductors. This region could be interpreted as arising from transitions between localised states and indeed, if the densities of states in the deep tails vary exponentially with temperature, such an edge is expected [34]. However, Davis and Mott [33] gave the following arguments as evidence against such an interpretation.

1) The value of γ' in the empirical relation

$$\alpha = \alpha_0 \exp\left[-\frac{\gamma'(E_0 - h\nu)}{kT}\right] \qquad (1.57)$$

appropriate for Urbach edges is observed to be close to 0.5 for a range of amorphous solids. It seems unlikely that the fall-off in the tail of the density of states could be so similar in a wide variety of materials.

2). Urbach edges occur in many crystalline semiconductors. In fact trigonal and amorphous selenium both exhibit Urbach edges with similar slopes at room temperature.

3). The temperature dependences of the slopes frequently follow the above relation at least at high temperatures. Transitions in which the initial or final state is localised should, according to the Frank-Condon principle, show a broadening proportional to $(kT)^{1/2}$.

An alternative explanation for the Urbach edge in amorphous semiconductors was put forward by Dow and Redfield [36]. They treated the problem by calculating the absorption for direct electronic transitions in a uniform electric field. Their calculations show that the variation of the absorption co-efficient with photon energy, obtained in this manner is accurately exponential. The problem that arises, however is where do these electric fields come from in a real material? One possibility is that the electric fields are present due to the inbuilt potential fluctuations within all amorphous materials.

Below the exponential part of the absorption edge an absorption tail is observed (part C in figure 1.8). It's presence has been confirmed by photoacoustic [37], and photothermal deflection

spectroscopy [38], both techniques can measure the absorption coefficient down to small values ($\alpha \lesssim 100 cm^{-1}$). The magnitude of α, and the slope obtained from a plot of α versus $h\nu$, for any given material, are found to depend on preparation conditions, purity and thermal history, Absorption in this region, however has been attributed both to light scattering and to optical transitions between localised states and between localised and extended states.

Chapter 2

REVIEW OF PREVIOUS WORK ON ARSENIC TRISELENIDE

2.1 The Chalcogenide Glasses

Arsenic triselenide (As_2Se_3) is a member of a group of materials called the chalcogenide glasses. The chalcogens are the elements which make up group VI of the periodic table - sulphur (S), selenium (Se) and tellurium (Te). Within certain ranges of composition it is possible to form glasses by combining these elements with one or more of the elements As, Ge, Si, Tl, Pb, P, Sb and Bi among others.

Of the binary glasses, arsenic triselenide, arsenic trisulphide and arsenic tritelluride have been the most extensively studied, and are often regarded as prototypes for the more complicated multicomponent chalcogenide glasses which have been studied in connection with the phenomenon of electrical switching (for a review see ref.[39]). It is also useful to study these binary glasses because comparisons may be made with the properties of the corresponding layered structure crystals[40].

In general, the chalcogenide glasses obey the so-called '8-N bonding rule' proposed by Mott[24], according to which each element is surrounded by 8-N neighbours (N being the number of electrons outside a closed shell) so that all electrons are taken up in bonds, thus large changes of conductivity with small changes in composition do not occur. This was first established by the pioneering work of Kolomiets and co-workers which has been summarized by Kolomiets[1].

In the glassy state, the chalcogen atoms will possess a well-defined co-ordination number. In the glasses of the type

$$A_2^{V} B_3^{VI} \qquad (2.1)$$

(where A = As,Sb; B = S,Se,Te) the structure will consist of a network showing (ideally) complete satisfaction of the two- and threefold covalent bonding requirements of the B and A species. Each chalcogen atom will be bonded to two As atoms while each As atom is linked to three chalcogens. The chalcogen is thus twofold coordinated, and each atom will possess a nonbonding electron pair in a so-called lone pair orbital. This 'ideal' network will of course contain structural defects as in any other crystalline or amorphous semiconductor because of its method of preparation. The position of the localised states deep in the mobility gap which will result from these defects is a difficult theoretical problem, and will be discussed in greater detail in section 2.6.

2.1.1 The Structure of Arsenic Triselenide

Arsenic triselenide crystallizes in the orpiment structure which consists of layers, comprising a cross-linked structure of chains along the a-axis and helices along the c-axis. These layers are stacked together and bonded by weak van der Waals' forces (see for example Weiser[40]). The structure of amorphous arsenic triselenide is not so well characterised. When arsenic triselenide is prepared in either a vitreous form (by quenching from the melt) or an amorphous

form (by evaporation or r.f. sputtering), it will not possess the long range order observed in the crystal. For any binary system A_x,B_{1-x}, analysis of the radial distribution function (RDF) from diffraction studies will be complicated by the difficulty of separating contributions from A-A, B-B and A-B bonds. A review of diffraction studies of the chalcogenide glasses has been given by Wright and Leadbetter[41]. In principle, EXAFS (extended X-ray fine structure) measurements should be capable of making the distinction between bond-types, but problems with the analysis have thus far not allowed conclusive results to be obtained[15]. For arsenic triselenide, most of our knowledge of the local atomic arrangement comes from NQR (nuclear quadrupole resonance) experiments and infrared and Raman spectroscopy. Nemanisch, Connell, Hayes and Street[42] have studied the EXAFS and Raman spectra of arsenic triselenide prepared by evaporation onto substrates held near room temperature - and have studied the effect of annealing the samples near the glass transition temperature on these spectra. Their EXAFS results could not be unambiguously interpreted, but did seem to suggest 10 - 15% more homopolar bonding in the as-deposited films than in the crystal. The amount of homopolar bonding appeared to decrease with annealing, but did not disappear entirely even in bulk glass samples. It has been conjectured that this may be due to the presence of As_4Se_6 molecular units in the as-deposited films - analogous to the molecular ordering observed in As_2S_3 but to a much lesser extent due to the smaller electronegativity difference between As and Se[43]. The structure of the bulk glass has been studied extensively by Taylor, Bishop and Mitchell[44]. In these

experiments, far infrared vibrational modes were observed in As_2Se_3 at temperatures above the glass transition temperature. The results showed that there were layered structural units present even above Tg. Thus as the glass is quenched one would expect a number of these 'rafts' to be frozen into the network, and provide a significant amount of medium range order. The experimental evidence in support of this model has been reviewed by Phillips[45] and Szeftel[46], who propose a structural model consisting of As_6Se_{13} rafts (shown in figure 2.1). In this model, vitreous arsenic triselenide is envisaged as a bundle of polymeric chains, containing these 'rafts' or puckered monomers. The model can thus account for the presence of Se-Se bonds and the presence of two non-equivalent As sites[46], but would lead to a selenium rich glass. Phillips has suggested that this may be overcome by the ad-hoc introduction of a number of As_4Se_4 molecules situated in voids in the structure, but this is not supported by recent NQR measurements[47]. We know of no published work on the structure of r.f. sputtered arsenic triselenide, although one may guess that the layered structures described in the previous section would only occur in films annealed near the glass transition temperature for long periods.

2.2 Band Models

Several models have been proposed for the band structure of amorphous semiconductors which are the same to the extent that they all use the concept of localised states in the band tails. Opinions vary, however as to the extent of this tailing. Figure 2.2 illustrates, schematically, the main features of these various models.

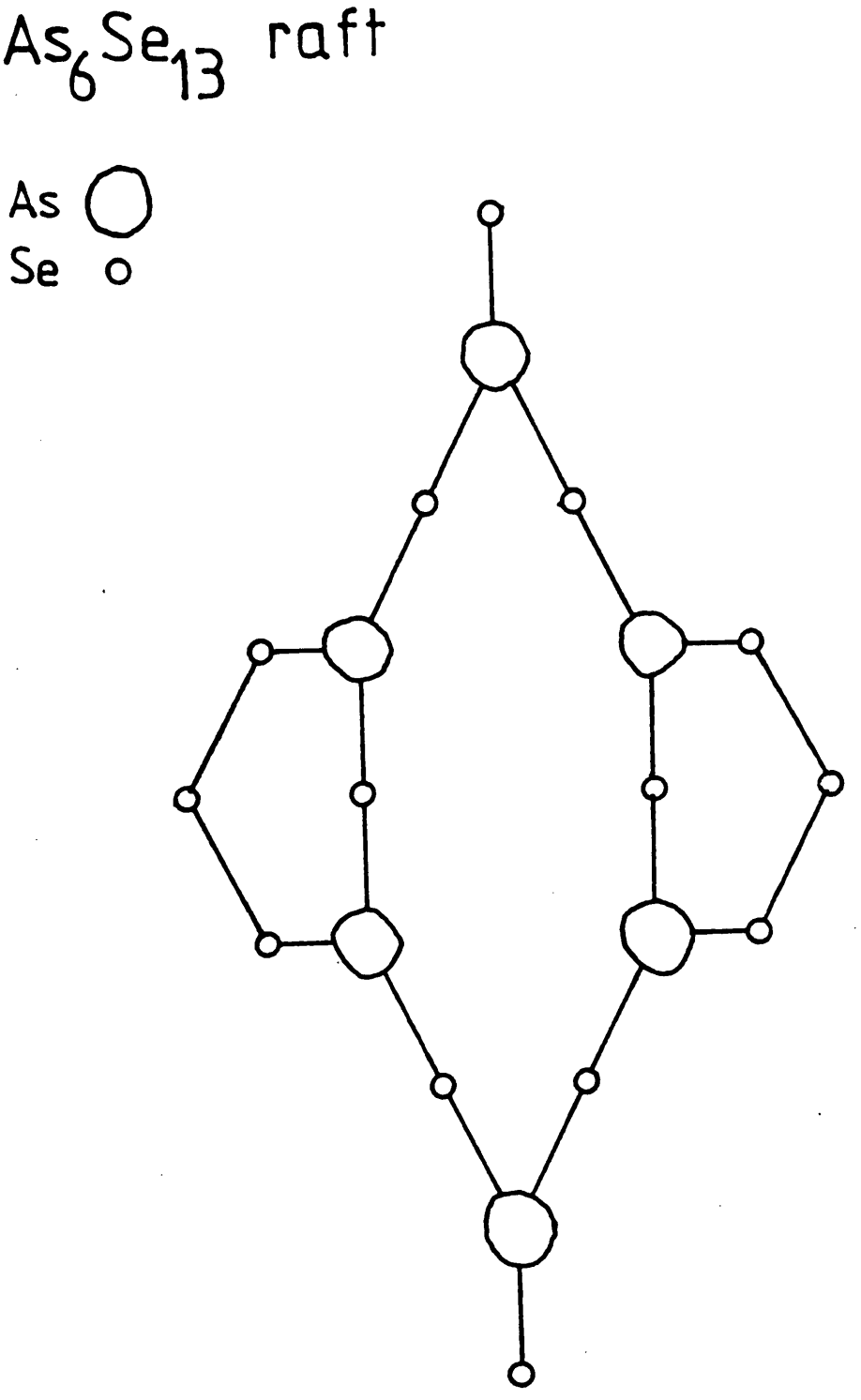

Figure 2.1 One of the $As_6Se_{12}(\frac{1}{2}Se)_2$ rafts thought to occur in vitreous As_2Se_3 from I.R. absorption studies.

2.2.1 The Cohen-Fritzsche-Ovshinsky Model

The CFO model[48], proposed for multi-component glasses, shown in figure 2.2a, assumes that the tails extend across the gap in a featureless distribution. This gradual decrease of the localised states destroys the sharpness of the conduction band and valence band edges. The authors suggested that in the chalcogenide alloys, the disorder is sufficiently great that the tails of the conduction bands and valence bands overlap, leading to an appreciable density of states in the middle of the gap. A consequence of the band overlapping is that there are states in the valence band, ordinarily filled, that have higher energies than states in the conduction band that are ordinarily unfilled. A redistribution of the electrons must take place, forming filled states in the conduction band tail, which are negatively charged, and empty states in the valence band, which are positively charged. This model therefore, ensures self-compensation, and pins the Fermi level close to the middle of the gap.

2.2.2 The Davis-Mott Model

According to Davis and Mott[15] the tails of localised states should be rather narrow and should extend a few tenths of an electron volt into the gap. They proposed furthermore the existence of a band of compensated levels near the middle of the gap, originating from defects in the random network, e.g., dangling bond vacancies, etc. In this model shown in figure 2.2b the centre band may be split into donor and acceptor band, which would also pin the Fermi-level (see figure 2.2c).

In recent years experimental evidence, mainly coming from

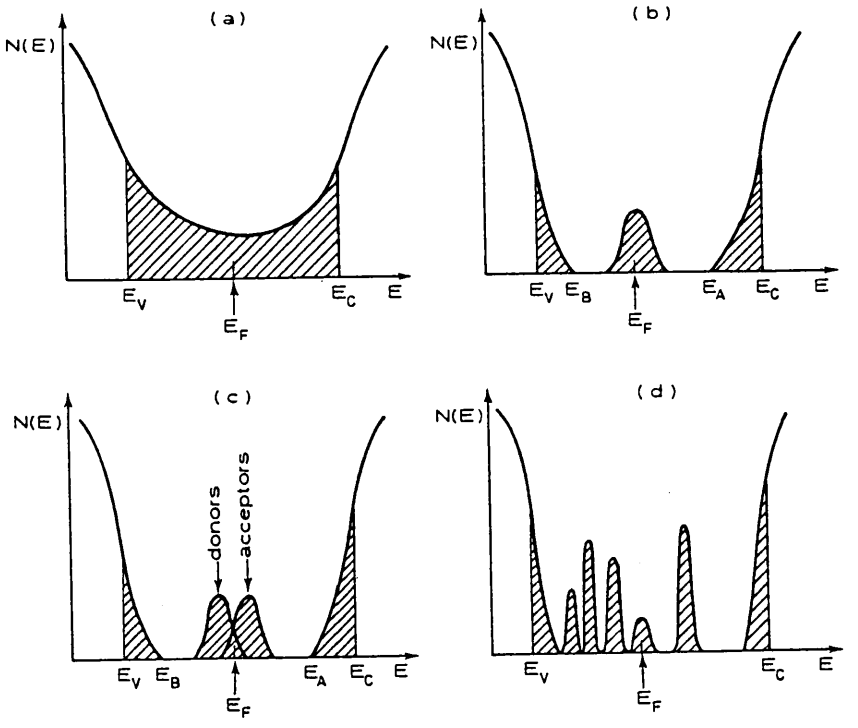

Figure 2.2 Schematic density of states diagrams for amorphous semiconductors. (a) The Cohen-Fritzsche-Ovshinsky model (b) the Davis-Mott model showing a band of compensated levels near the middle of the gap, (c) modified Davis-Mott model, (d) a "real" glass with defect states.

luminescence, photoconductivity and drift mobility measurements, has been found for the existence of various localised gap states, which are split off from the tail states and are located at well defined energies in the gap[49]. These states are associated with defect centres, the nature of which is not always known. A first proposal of a model showing bands of donors and acceptors in the upper and lower halves of the mobility was introduced by Marshall and Owen[50], and is sometimes called the Marshall-Owen model. It is now clear that the density of states of a chalcogenide semiconductor does not decrease monotonically into the gap but shows various peaks which can be well separated from each other. The position of the Fermi level is largely determined by the charge distribution in the gap states. Figure 2.2d illustrates such a picture for the density of states of vitreous As_2Se_3[49].

2.3 The Conductivity and Thermopower

The temperature dependences of the d.c. conductivity and thermopower in amorphous As_2Se_3 observed in a number of previous investigations have been summarised in figures 2.3 and 2.4 (these diagrams have been taken from a paper by Mytilineou and Roilos[51]). The thermopower indicates that undoped arsenic triselenide is p-type, while the d.c. conductivity of vitreous As_2Se_3 obeys the relation

$$\sigma_{dc} = \sigma_0 \exp(-\Delta E/kT) \qquad (2.2)$$

where $\Delta E = 0.95$ eV, and $\sigma_0 = 10^3 - 10^4 \Omega^{-1}cm^{-1}$ [52]. At lower

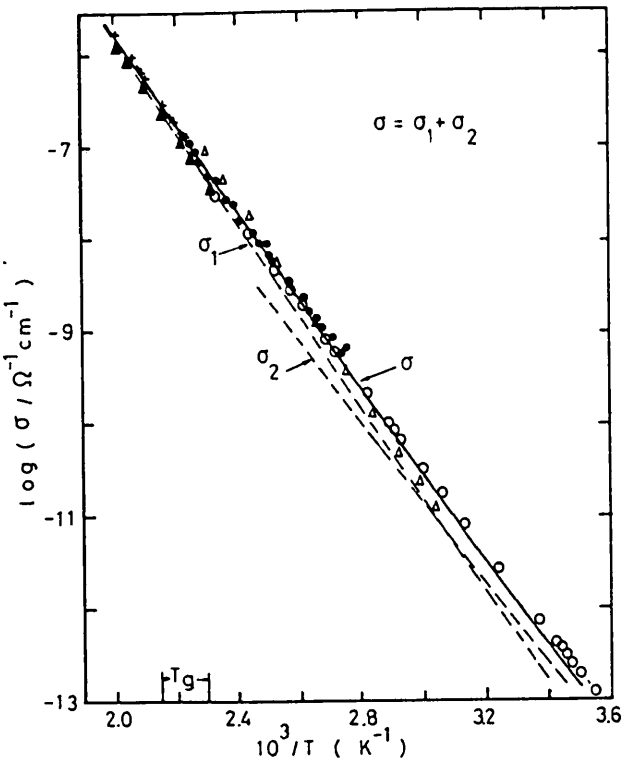

Figure 2.3 Temperature dependence of the d.c. conductivity from the work of various authors as summarized by Mytilineou and Roilios (see reference (51)).

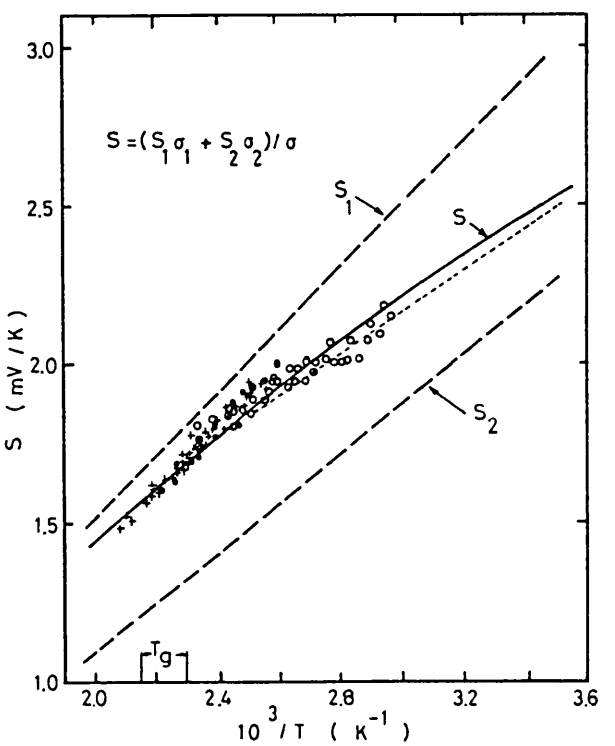

Figure 2.4 Temperature dependence of the thermopower S taken from the same reference as above.

temperatures (T < 300 K), the graphs start to curve away from this straight line, as shown in figure 2.3. Two explanations have been proposed to account for this curvature.

The first model is one which involves two 'conduction channels'. Marshall and Owen[50, 53] Nagels, Callaerts and Denayer[54] and Mott and Davis ([15] p453) consider the high temperature results to be due to conduction at a mobility edge - because of the high value of the conductivity pre-exponent (as discussed in section 1.3 in the previous chapter). Using this model, the reduction in activation energy with decreasing temperature is thought to be due to the contribution made by another conduction mechanism - that of hopping conduction through a set of localised states far from the Fermi-level. Thus the total conductivity may be written as the sum of two terms (drawn as dotted lines in figure 2.3), corresponding to conduction in extended and localised states. A graph of $\ln(\sigma)$ versus 1/T will yield a straight line if $E_c - E_F$ is a linear function of T in the temperature range being studied. As discussed in chapter 1, the gradient of such a graph will be E(0)/k and the intercept will be given by $\sigma_o \exp(\gamma/k)$. At lower temperatures, the conductivity will be given by

$$\sigma_{loc} = \sigma_{hop} \exp\left[\frac{-(E_F - E_x) + W}{kT}\right] \qquad (2.3)$$

as discussed in chapter 1. This will again lead to a straight line on a $\ln(\sigma)$ versus 1/T graph (because the hopping activation energy w is only weakly temperature dependent), with an activation energy of

(E_F-E_x) + w , and once again the slope and intercept will be effected by the temperature dependence of the optical band gap. The magnitude of the intercept in this region is difficult to calculate theoretically, but it is expected to be two to three orders of magnitude less than that expected for extended state conduction.

The thermopower expected on the basis of this model is the weighted sum of the contributions from extended states (S_{ext}) and localised states (S_{loc})

$$S_{ext} = \frac{k}{e}\left[\frac{E_F - E_V}{kT} - \frac{\gamma}{k} + A\right]$$

$$S_{loc} = \frac{k}{e}\left[\frac{E_F - E_x}{kT} - \frac{\gamma}{k} + A\right] \qquad (2.4)$$

such that

$$S_{TOT} = \frac{S_{ext}\sigma_{ext} + S_{loc}\sigma_{ext}}{\sigma_{ext} + \sigma_{loc}} \qquad (2.5)$$

The constant A has been taken as unity and $\gamma = 5.51 \times 10^{-4}$eV/K in the theoretical fit to the curve in figure 2.4. At high temperatures, the activation energy for the thermopower should equal that for the conductivity - whereas at lower temperatures where hopping should predominate the conductivity activation energy may be greater by an amount up to the hopping energy. Unfortunately, previous investigators were in conflict about whether the activation energies were the same at high temperatures or not (see ref.[51] for a review of this problem). The behaviour expected on the basis of this model is

shown as the solid lines in figures 2.3 and 2.4 using the following values:-

$$\sigma_o = 1.5 \times 10^4\ \Omega^{-1}cm^{-1} \qquad \sigma_{hop} = 200\ \Omega^{-1}cm^{-1}$$

$$E_F - E_V = 0.99eV \qquad W = 0.09\ eV \qquad E_F - E_x = 0.78eV \tag{2.6}$$

The other model which can explain most of the details of the results shown in figures 2.3 and 2.4 is that of small polaron hopping. Seager, Emin and Quinn[55], Seager and Quinn[56] and Klaffke and Wood[57] have argued that the graphs are continuously curved, and consequently are best explained by a small polaron model of conduction as described in section 1.6.3 of chapter 1. According to this theory, the conductivity should essentially be thermally activated, the activation energy being the sum of the energy required to generate the carriers plus a small polaron hopping energy W. The conductivity pre-exponent should be in the range 10 - $10^2\ \Omega^{-1}cm^{-1}$, which agrees with experiment if the temperature dependence of the band gap (and mobility edge) are taken into account. The thermopower for small polaron hopping should vary linearly with reciprocal temperature. The thermopower activation energy should yield the the energy for carrier generation, so that

$$\Delta E_\sigma = \Delta E_S + W \tag{2.7}$$

It is clear that this second approach also provides a consistent physical basis for the essential features of these transport properties, and can therefore not be ruled out. To prove in

a definite way the validity of either the two conduction channel model or the small polaron model, one would need to be able to perform these transport measurements at much lower temperatures. This is unlikely to be possible in undoped arsenic triselenide because of its extremely low conductivity, but may become feasible if doping can increase the conductivity appreciably.

The temperature dependence of the d.c. conductivity in evaporated arsenic triselenide has been recently reported by Panasyuk et al[58]. These authors found a room temperature activation energy of 0.7eV decreasing to 0.31eV between 200K and 250K in samples freshly evaporated onto room temperature substrates. After annealing, these activation energies changed to 0.79eV and 0.31eV respectively. For samples of arsenic triselenide prepared by r.f. sputtering, Sharp et al[59] have analyse the d.c. conductivity data shown in figure 2.5 by computer using a program developed by Provencher[60], which is designed to analyse data composed of random noise plus an unknown constant baseline plus a sum of exponential decay functions. These authors[59] find a decrease in ΔE from 0.91 to 0.75eV below 280K.

The field dependence of the d.c. conductivity has been studied by De Wit and Crevecoeur[61], Marshall and Miller[62], Marshall, Fisher and Owen[63], and Hurst and Davis[64]. All these investigations found that the conductivity varied as

$$\sigma = \sigma_0 \exp[\mathcal{E}/\mathcal{E}_0] \qquad (2.8)$$

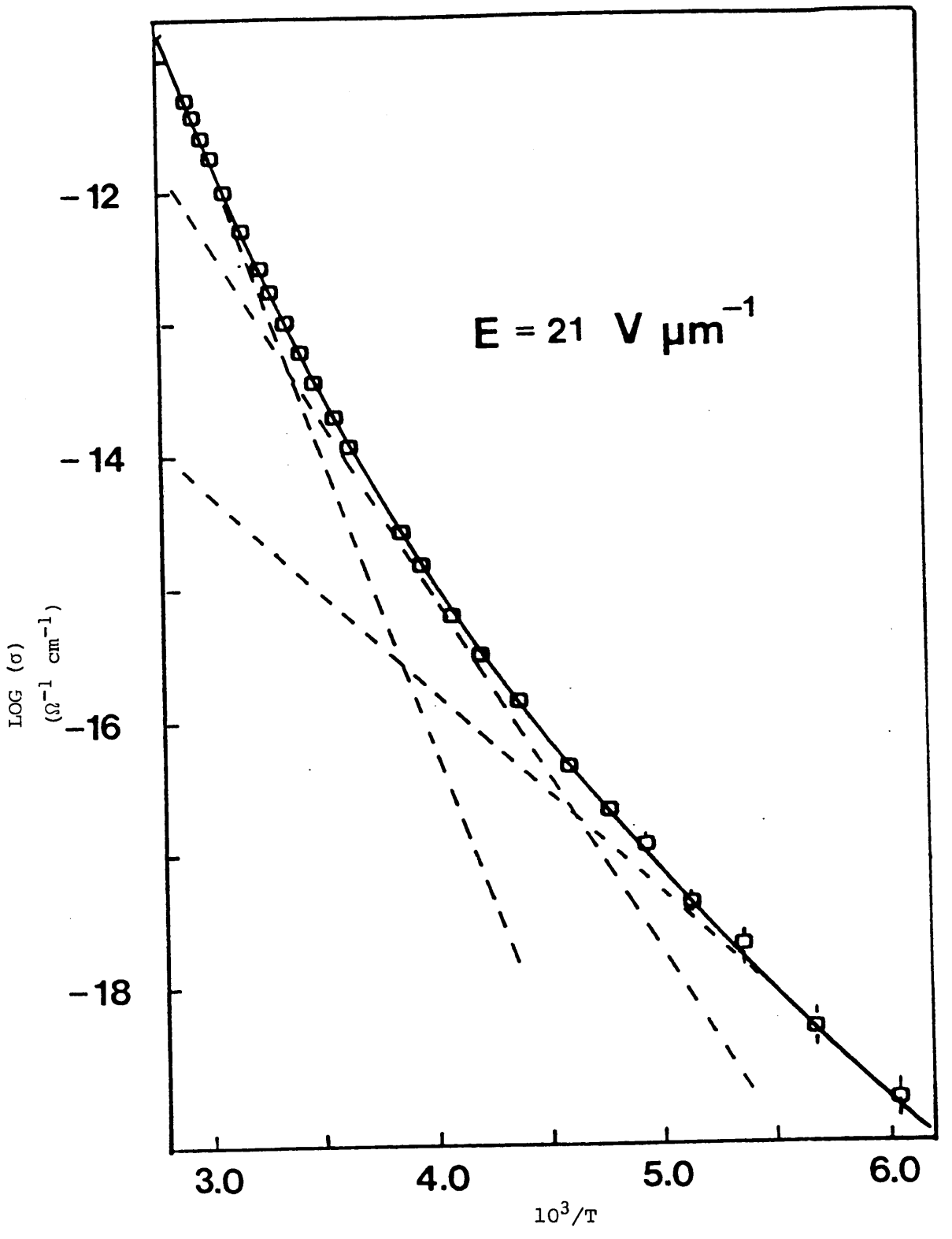

Figure 2.5 Sharp et al's computer fit of three exponentials to the conductivity data as described in the text.

up to fields ($\mathcal{E}$) of the order of 4×10^5 V/cm for various thicknesses of specimen from 5 microns to 1 mm. A remarkable feature of this result is the apparent absence of any ohmic region. Marshall et. al. expressed their results in the form

$$\sigma(\mathcal{E}) = \sigma(0)\exp[ea\mathcal{E}/kT]$$

$$\mu_D(\mathcal{E}) = \mu_D(0)\exp[ea\mathcal{E}/kT] \qquad (2.9)$$

and found that a (which decreases with increasing temperature) is the same for both the mobility and the d.c. conductivity. No full explanation of these results has yet been given, although Mott and Street[65] have indicated how these results may be explained in terms of their model of defect centres (described in detail in section 2.6). They argue that if the ratio between D^+, D^- and D^o centres is independent of the applied field, then the effect of the field on the conductivity and drift mobility should be the same, changing the the equilibrium between the concentration of free holes and D centres. The rate of release of holes should be increased by some factor such as the Poole-Frenkel term $\exp(b\mathcal{E}^{0.5}/kT)$, and the rate of recombination will be proportional to the free hole concentration (because of the large excess of D^- centres into which the holes can drop). However the Poole-Frenkel term, although fairly satisfactory at high fields, gives a term in $1+b\mathcal{E}F^{0.5}/kT$ at low fields instead of the linear behaviour observed experimentally. Mott and Street, however, show that by applying the Onsager[66] mechanism as developed by Pai and Enck [67], some measure of agreement may be obtained

2.4 Drift Mobility

Drift mobility experiments in arsenic triselenide are usually made using the time of flight or transient charge technique described in detail in chapter 3. Many investigations of the drift mobility in undoped arsenic triselenide have been reported in the last decade or so. These include the work of Marshall and Owen[50], Pfister[68], Fisher, Marshall and Owen[69], Pfister and Scher[70, 71] Kolomiets, Lebedev and Kasakova[72], Sharp, Marshall and Fortuna[59] and Sharp and Marshall[73]. In all these investigations, only hole carrier pulses have ever been observed, even for very thin samples and high applied electric fields. The drift mobility of carriers in crystalline As_2Se_3 has been studied by Marshall[74]) - in this case only electron transits could be observed. The experimental data from the above studies are summarised in figure 2.6. The data of Pfister et. al. were obtained from evaporated samples annealed near the glass transition temperature, whereas all the other data were for material prepared by quenching from the melt. The measurements of Marshall and Owen were performed on very thin samples (typically 1 - 5 microns thick) prepared by a bubble blowing technique. For this reason, the transit time of the carrier pulse in this investigation was much smaller than in the other studies. One can clearly see that this had the effect of reducing the observed drift mobility activation energy to about 0.43 eV, as opposed to the value of 0.6 - 0.65 eV observed in all the other investigations. Interestingly, the high temperature measurements of Kolomiets et. al. appear to have a similarly low activation energy.

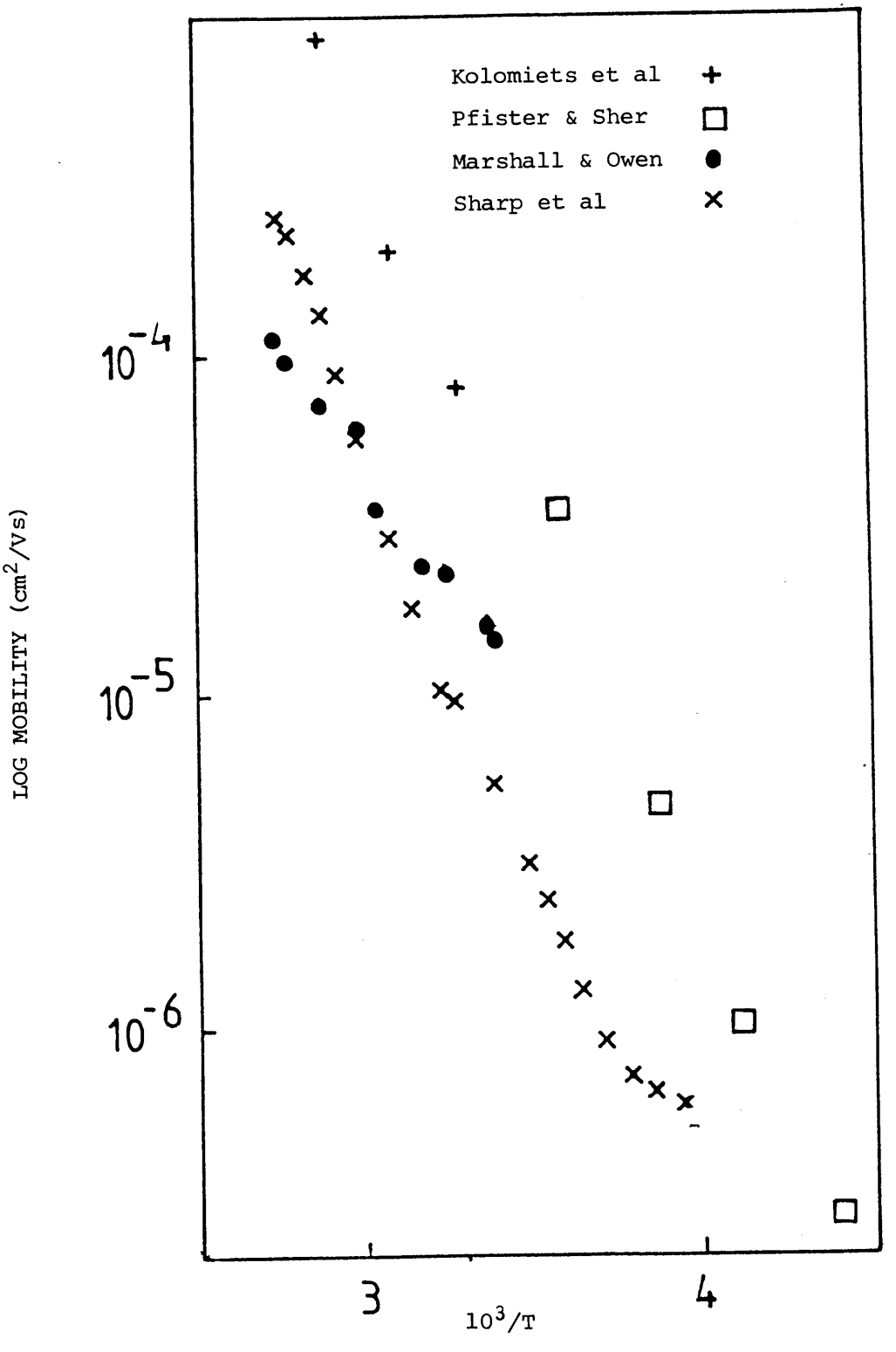

Figure 2.6 The temperature of the hole drift mobility from various studies as described in the text.

The 'anomalously dispersive' transit pulse shape from which the mobility can be calculated is discussed in general terms and in greater detail in section 3.2, page 79, and in subsection 5.5.3.1, page 129. Pfister and Sher[70] observed the value of α calculated from the gradient of the log (I) - log (t) graphs before and after the discontinuity of gradient to be equal (in other words, the gradients sum to two). In addition they found α to be insensitive to both the applied electric field and the specimen temperature. As predicted by the hopping model of Scher and Montroll, these authors found the drift mobility to be thickness dependent such that

$$t_t \sim \left(\frac{\mathcal{E}}{L}\right)^{-1/\alpha} \qquad (2.10)$$

Pfister and Scher did however find it difficult to explain their results on the basis of a pure hopping model, because the large drift mobility activation energy (0.6 eV) could not be accounted for by a hopping energy alone. Similarly, a simple hopping model could not account for the small number of localised states (about $10^{16}cm^{-3}$) which are observed in photoinduced ESR and thermally stimulated depolarisation experiments - to get the required mobility by hopping alone would require about $10^{20}cm^{-3}$ localised states. They therefore considered either trap-limited band transport or trap-limited hopping to be more likely, and because they observed a temperature independent α, they concluded that trap-limited hopping was the most likely mechanism. This conclusion was supported by the pressure - dependence of the drift mobility and conductivity reported by Pfister (1974). It

should however be pointed out that these measurements were made at room temperature, and that for films prepared in slightly different ways the transition from extended state conduction to hopping is likely to occur at slightly different temperatures. In contrast Kolomiets, Lebedev and Kasakova (1978) observed a temperature dependence of the transit pulse shape in arsenic triselenide. It should be borne in mind that the method of sample preparation in these two studies differed significantly The samples used by Pfister and Scher were prepared by evaporation of the bulk glass onto aluminium foil which was subsequently removed by flexing the foil, whereas Kolomiets et. al. used thin slices of arsenic triselenide cut from the bulk glass. The Kolomiets group actually observed a rather complicated variation of pulse shape with temperature - they saw dispersive behaviour below 280K and above 350K, but fairly well defined transits at intermediate temperatures.

Sharp et al[59] also observed a temperature dependence of the transit pulse in both vitreous and evaporated samples. They found that changing the field did not significantly affect the shape of a pulse at a given temperature, but the transit pulses became more dispersive as the temperature was lowered. The degree of dispersion observed in the evaporated specimens depended much less on temperature. Figure 2.7 shows the value of dispersion parameter α_1 calculated from the initial slope of the log(I)-log (t) graphs as a function of temperature for both vitreous and evaporated samples. The data indicate that a spread of trap energies (for a trap-limited transport mechanism where the traps have a Gaussian distribution) of about 0.07eV would be necessary

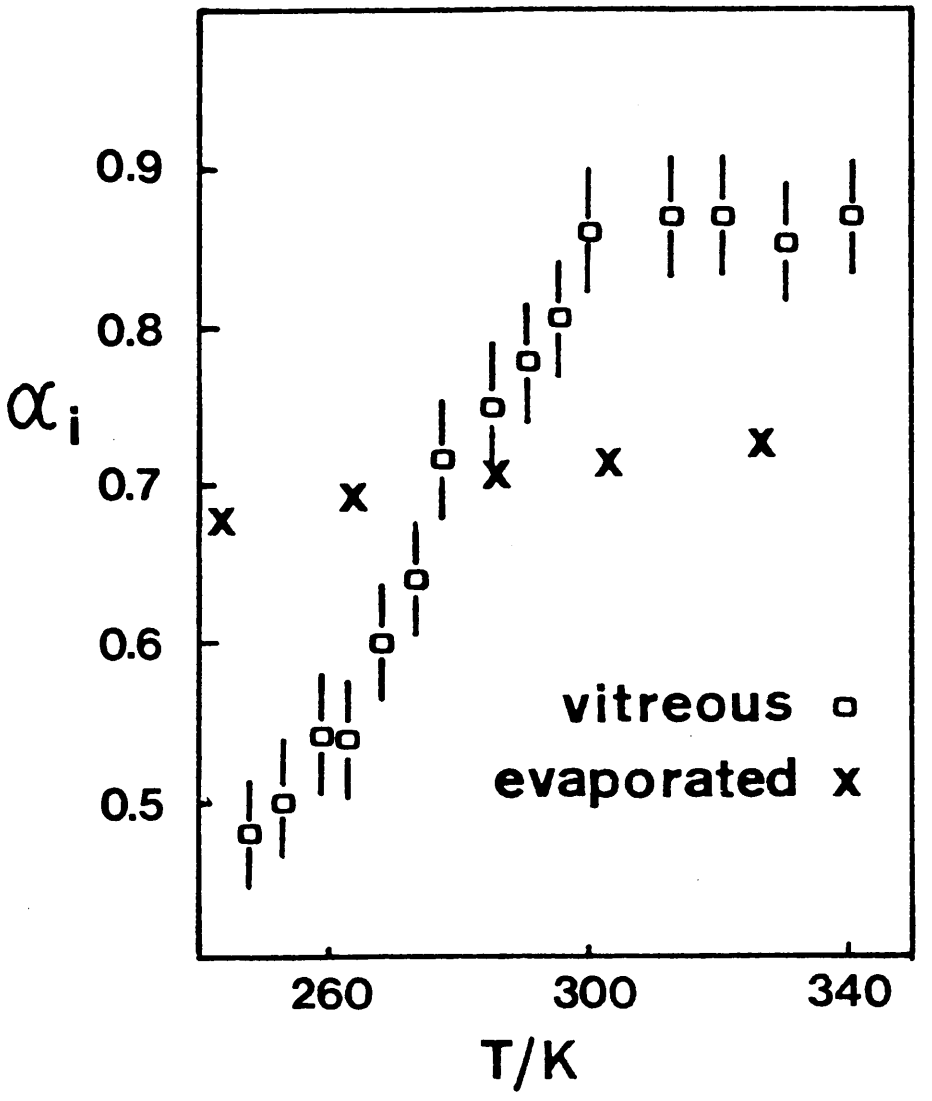

Figure 2.7 Temperature dependence of the dispersion parameter calculated from the initial slopes of log (I) vs log (t) graphs for vitreous and evaporated arsenic triselenide (from the work of Sharp et al. [59])

to account for the dispersion observed in the evaporated samples. The almost linear dependence of α observed for the vitreous specimens indicates a trap distribution of only about 0.03eV. These authors also investigated hole (and electron) current transients observed in r.f. sputtered samples. These transients did not exhibit a discontinuity of gradient, but appeared to decay exponentially down to noise level.

The drift mobility measured as a function of temperature for the vitreous specimen exhibits three activated regimes of energy 0.62eV above 300K, falling to about 0.5eV between 300K and 270K. An abrupt change in activation energy to 0.15eV was also observed by Sharp et al[59] below 265K. The drift mobility in evaporated specimens was observed down to 190K, and for these samples ΔE_μ decreases from 0.65eV to 0.45eV below 290K. Sharp et al then interpret these results in conjunction with the d.c. conductivity results discussed in section2.3 via a model in which the hole carriers interact with three distinct sets of traps centered on energies 0.3 eV, 0.4 eV and 0.6 eV above the valence band mobility edge.

The field dependence of the drift mobility in evaporated arsenic triselenide has been studied by Pfister[75], who explained it on the basis of the CTRW theory of Scher and Montroll. He found that if an exponential field dependence for the probability of nearest neighbour hopping of

$$prob \sim \exp[epE/2kT] \qquad (2.11)$$

is introduced, one would expect a field dependence of the transit time of the form

$$t_t \sim L^{1/\alpha} (\sinh.espE/2kT)^{-1/\alpha} \exp\left[\frac{E_o}{kT}\right] \qquad (2.12)$$

where p is the average hopping distance in the real system, α is the dispersion parameter and Eo is the activation energy at zero field.

Although Pfister's results exhibited such sinh behaviour for very thin samples (less than about 10 microns), for thicker samples it was very difficult to distinguish between this behaviour and the exponential behaviour reported by Marshall and Miller[62].

2.5 Transient Photoconductivity Measurements

The transient photoconductivity can also provide valuable information on localised states, and in particular Main[49] has shown that a drift mobility may be derived from the transient rise of the photocurrent. In some cases it has been possible to observe three regimes of transient rise in a single sample of arsenic triselenide, corresponding to trap depths of 0.3eV, 0.44eV and 0.65eV. Unlike the time of flight technique however, the derivation of a mobility from the transient photoconductivity does not determine the sign of the carriers. It is assumed that they refer to the trap-limited drift mobility of holes and this seems reasonable because of the consistency with time of flight measurements. In addition to the above investigations there have been a number of studies of the transient photoconductivity and photocurrent decay by Orenstein and Kastner

(1979, 1981), Monroe, Orenstein and Kastner (1981), which are closely related to the mobility studies summarised in the previous section. In these experiments, a bulk sample of vitreous As_2Se_3 about 1mm thick equipped with coplanar graphite electrodes was used. The photoconductivity (PC) and photoinduced absorption (PA) in the samples were excited by a pulse from a dye laser - the photocurrent was detected as the voltage drop across a series resistor, while the PA was simultaneously monitored by measuring the transmission of a probe beam from a tungsten lamp. These experiments showed that the PC decays much more quickly than the PA for the same excitation pulse. Orenstein and Kastner argued, however, that both effects were due to the same density of photoexcited carriers at all times after the laser pulse. This result is in conflict with measurements on thallium doped arsenic triselenide by Pfister et al[76] who observed no correlation between PA or photoinduced ESR and drift mobility measurements. Orenstein and Kastner explained their results in terms of the Tiedje/Rose model discussed in section 3.2.2 page 89.

2.6 Defects in Chalcogenides

States in the energy gap of these materials undoubtedly do exist, there being extensive evidence that these materials are not "intrinsic" but that the Fermi level is pinned(see ref[15] page 287). This was a puzzle for many years because pinning would involve the existence of states with spin, and no electron spin resonance or paramagnetism of Curie type at low temperatures was observed.

In an attempt to explain this Anderson[77] proposed that the localised electronic states commonly thought to exist within the gap

consisted of paired electrons and were hence diamagnetic in agreement with experiment. Following this proposal, in which the electron-electron attraction was provided by distortions in local bonding, several detailed models have been presented[78, 28, 79, 80]. Mott, Davis and Street[78] (MDS), and Kastner, Adler and Fritzsche[80] (KAF), have focused on specific electronic states, usually related to a postulated defect in the solid, in an attempt to account for the detailed facts obtained from the various transport, optical and ESR experiments.

In the MDS model, applied to "dangling bonds" (e.g chain ends in selenium), it was assumed that the transfer of an electron from one site to another would be an exothermic process. The energy (the Hubbard U) required to put another electron into the singly occupied lone-pair selenium orbital, to form a D^-, was more than compensated by the energy gained when the D^+ centre formed a bond between its empty lone pair orbital and the fully occupied lone-pair on a neighbour. The bond formed is called dative because both electrons come from the same orbital. These centres would then pin the Fermi energy, but give no spin signal. The term "negative Hubbard U" donates the hypothesis that the energy to take an electron from the dangling-bond state and put it in another is negative ;and this can only occur through a distortion of the D^+ centre. KAF were responsible for the following:

1) They called the defects valence alternation pairs (VAP), the D^- was named C_1^- and the D^+ named C_3^+, the suffixes donating the

coordination (see figure 2.8)

2) They differ from MDS in their description of the neutral state D^o, which they write C_3^o, implying it to is threefold coordinated. The account of the origin of the Hubbard U is therefore not the same. The energy needed for the reaction

$$2C^o \rightarrow C_1^- + C_3^+$$

is about 1.3 eV in arsenic triselenide or selenium, which implies that one does not have to break a bond to form C^o.

3) KAF point out that to form the pair C_3^+, C_1^- (see figure 2.8), the number of bonds is not changed, so the pair may well be the defect of lowest energy.

4) KAF also considered "intimate valence alternating pairs" (IVAP), a pair of C_1^-, C_3^+ centres bound close together by their electrostatic attraction.

Although one cannot deny the existence of defects in real amorphous solids any more than one can in crystalline solids, an explanation of experimental properties exclusively in terms of these defects is not within the spirit of the original Anderson model. Ngai and Taylor[79] have suggested that the configurational entropy characteristic of an amorphous solid makes possible the formation of abnormal bonding configurations not present in the corresponding crystal. The defect states suggested by MDS and KAF represent only a small subset of the possible localised states in an amorphous solid and they introduced a formalisation which facilitates the enumeration of these states. They consider states that lie deep within the gap

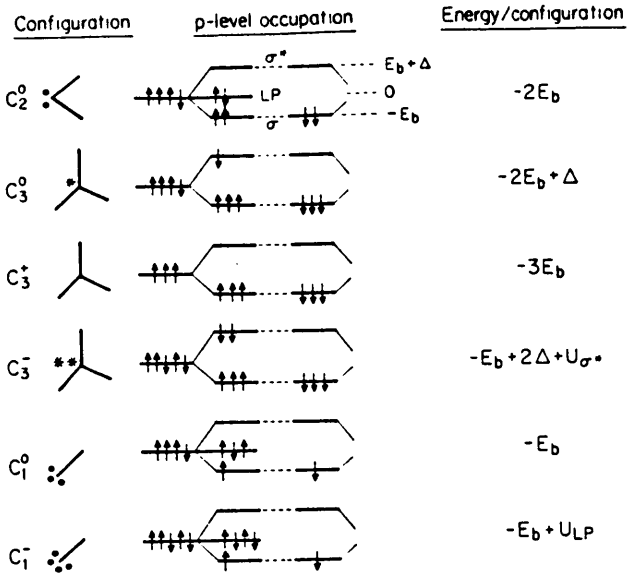

Figure 2.8 Structure and energies of various defect configurations in a chalcogenide as suggested by Kastner, Adler and Fritzsche (KAF)[80].

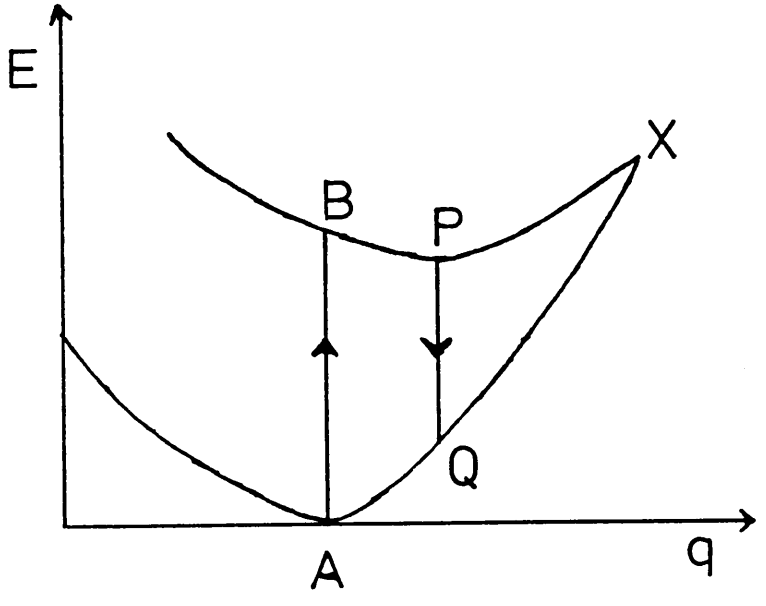

Figure 2.9 Configurational coordinate diagram of energy(E) versus distance (q) for a C_1^- centre. The election is excited into a localised state near the band edge, and the centre then relaxes, and radiates in a transition P to Q.

and employ the language of molecular orbitals in order to compare with the MDS, KAF approaches.

The KAF model considered only those bonding configurations that can be obtained from broken and rearranged bonds, called the "normal bonding configuration", where the relative energies of the bonding, non-bonding and anti-bonding p orbitals are fixed in a given solid. This description is true for the vast majority of atoms in an amorphous semiconductor, but the legitimacy of applying normal bonding energetics for those few (10^{16} - 10^{17} cm^{-3}) highly distorted sites giving states that lie deep within the gap is undoubtedly in question.

In Ngai and Taylor's "abnormal bonding" approach one can, even under a limited set of assumptions, show that there exists an astonishingly large number of distinctly different deep gap states possible in a simple binary chalcogenide glass. For example in arsenic triselenide one can construct, ten abnormal sites or pairs of sites involving only Se atoms, eight involving As atoms, and 18 involving pairs of abnormal As-Se sites. Certainly some of these sites will be less energetically favourable than others, but it is impossible to anticipate which ones these will be by invoking arguments involving normal bonding energies for the abnormal sites.

A second important feature of the abnormal bonding description is that a great number of diamagnetic gap states are theoretically capable of yielding metastable paramagnetic sites with properties matching those inferred from optically induced ESR experiments.

In the MDS and KAF models the occurrence of metabolic gap states is linked to the presence of non bonding electrons on the normally bonded chalcogenide atoms. In the group V elements, of which arsenic is a member, there are no non-bonding electrons at the normal As sites. It is only after a complicated procedure involving hybridisation, argue Kastner and Fritzsche[81], that non-bonding s-electrons become available for use in the framework of the KAF model. On the other hand the occurrence of similar gap states for both group VI and group V materials is a natural consequence of any abnormal bonding model.

It is suggested[79] that the experimental data cannot be explained by a unique defect of well defined energy, but rather a hierarchy of distorted sites on which some of the paired electrons are bonded in an abnormal fashion. In this respect the abnormal bonding model is closer to Anderson's original idea of a set of intrinsic, disordered induced states within the gap of which the defects of MDS and KAF are a subset.

2.7 Photoluminescence and Photo-Induced ESR

Photoluminescence in the chalcogenides was investigated first by the Leningrad school (Kolomiets et al[82, 83], then in a series of papers by Street, Searle and Austin (for a review and references see ref.[84], by Cernogora et al[85], Mollet et al[86] and by Bishop and Mitchell[87]. Briefly they observe the following.

(a) The luminescence is most efficient when excitation occurs in the tail of the optical absorption edge ($\alpha \sim 10\text{-}10^2$) and therefore is

almost certainly associated with localised defect states. Excitons or free carriers recombine non-radiatively.

(b) The emitted radiation consists of a band with its peak at about half the band gap; according to Street and co-workers this is due to a large Stokes shift.

(c) The efficiency of photoluminescence falls off rapidly with T, as $\exp(-T/T_o)$ with $T_o \sim 50K$ in As_2Se_3.

Street proposed that the radiation is due to C_1^- centres (or in some cases C_3^+). The electron is excited into a localised state near the band edge, and the centre then relaxes, and radiates in a transition from P to Q in figure 2.9. He[84] interpretated the temperature dependence as due to the escape of the electron from the weakly bound excited state. This conclusion was criticised by Hudgens and Kastner[88] who found that the excitation efficiency η was not sensitive to the electric field implying that the excited state must be strongly bound. They argue that some temperature-dependent non-radiative recombination mechanism must be responsible for the temperature dependence of η. They then propose that to give deep enough excited states, the luminescent centre must be neutral (an IVAP, namely C_1^- and C_3^+ very close to each other). The assumption has been criticised by various authors[89], the most decisive evidence that the centres are charged comes from the observation by Street[90] of shifts in the maximum of the band to lower energies with increasing time delay after excitation. Street supposes that the mechanism is the same as in a-Si; i.e., fast luminescence is due to electrons,

which are attracted to holes trapped in deep band-edge localised states, but have not yet thermalised. The holes must be trapped in centres deeper than in silicon, so that they are not, at low temperatures removed by an electric field. This is evidenced by the fact that the rise of luminescence peak energy with time, attributed to the coulomb term $e^2/\epsilon R$, where R is the distance between two trapped carriers, is absent. This suggests, in Street's view, that the electron is not attracted by a charged carrier, so that the initial centre is C_1^-, not an IVAP.

A related phenomenon of considerable interest is the optically induced ESR investigated by Bishop et al[91, 92], and Bishop and Taylor [93]. They report that the effect saturates at 10^{17} spins cm^{-3} in As_2Se_3 and 10^{16} in Se. They conclude that two types of spin are present corresponding to the predominantly p-like orbitals on As and Se atoms respectively. The data are consistent with the centre being a dangling bond, but it is not as yet possible to say with certainty whether is is best described by a dangling bond, or a configuration such as C_3^0 (an electron at a threefold-coordinated chalcogen).

2.8 Modification of Arsenic Triselenide

It is known that with a few exceptions the chalcogenides cannot be effectively doped by quenching from the melt, the independence of conductivity on the presence of impurities being considered a distinctive feature of vitreous semiconductors. There is some evidence, however, that introduction of such metals as Ag or Cu into complex chalcogenides causes quite large changes in the

electrical properties. Only recently has promising progress been made in controlling the electrical properties by introducing foreign atoms. A number of new methods for control of the electrical properties have been developed, known as "cold" methods. These are photodiffusion[94], electrodiffusion[95] and r.f cosputtering[96, 97], the latter being the most convenient method. This method was used by Ovshinsky and co-workers[96] and called chemical modification of the chalcogenides. They succeeded in preparing high conductivity films of a material of complex composition $Ge_{32}Te_{32}Se_{32}As_4$ by the introduction of transition metals such as Nickel, Copper and Iron.

Kolomiets[98] considered this finding very important and carried out similar experiments on As_2Se_3. He cosputtered As_2Se_3 with transition metals (Ni,Cu,Fe) and non-transition metals (Bi,Sn). Figure 2.10 shows the influence of chemical modification with various metals, observed by Kolomiets, on the room temperature conductivity. He found that the conductivity activation energy decreased more rapidly than the optical gap energy with increasing dopant concentration in a manner that suggested that the Fermi-level had shifted from 'mid-gap' and concluded that it was possible to change both the type of conduction and the magnitude of conductivity over a broad range in all cases. The results of this study are difficult to overestimate, since they open new possibilities for applications of the chalcogenides. It was found that the transition metals whose atoms have completely filled electron shells influence the conductivity most.

Kolomiets[98] proposes that the following mechanisms are

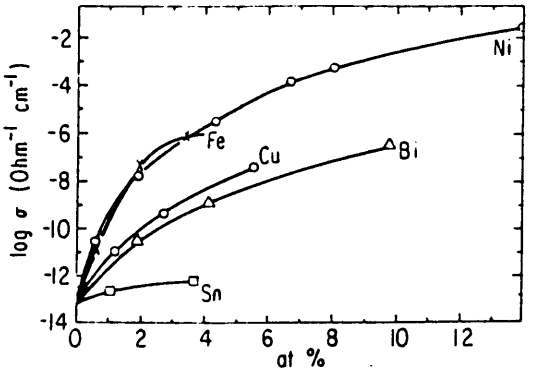

Figure 2.10 Concentration dependence of the conductivity of modified films after Kolomiets.

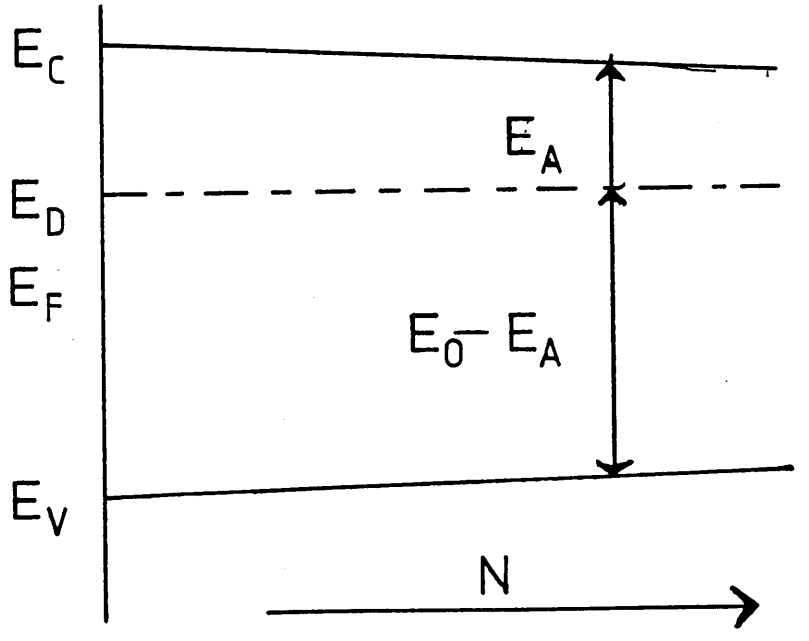

Figure 2.11 Band diagram of a transition metal doped chalcogenide as proposed by Kolomiets; N represents the donor impurity concentration; E_D - donor level, E_o - optical gap.

responsible for the high extrinsic conductivity. In the course of cosputtering, elements such as Ni, Cu and Fe, enter the glass in an unusual way. Some of these atoms become incorporated into the glass structure in a normal manner with all their electrons taken up in bonds with the chalcogen atoms, while the others interact with the chalcogens with only a fraction of their electrons, some of which remain free. In filling local states in the gap, these free electrons shift the Fermi level, with the consequences easy to predict.

The proposed band diagram of the chalcogenides doped with a transition metal is shown in figure 2.11. One readily sees that as the impurity concentration rises, the Fermi level shifts from mid-gap towards the donor level and the energy gap decreases, while the quantity (E_o-E_A) remains constant, which indicates that the donor level is pinned to the top of the valence band.

This hypothesis has found confirmation in a study of the Mossbauer spectra of Fe doped As_2Se_3 which reveal the presence of peaks corresponding to both the Fe^{+3} and Fe^{+2} states[98].

An interesting case is As_2Se_3 doped with bismuth. Introducing bismuth permits one to vary the conductivity within 5-6 orders of magnitude without changing the position of the Fermi level in the gap. It is remarkable that starting with a certain concentration, the As_2Se_3 films exhibit n-type conduction. The first to announce the observation of n-type conduction in the chalcogenides were the Japanese scientists Tohge, Yamamoto, Minani and Tanaka[99]. The growing interest to this feature is reflected in the studies of

Nagels [100] and Batia[101].

Another interesting study of the effects of bismuth has been made by Sarsembinov et al[102], who found that deposition of bismuth electrodes on irradiated bulk samples of vitreous As_2Se_3 increases the conductivity by six orders of magnitude. This is due to the fast bulk diffusion of this metal into the sample.

2.8.1 Mobility Measurements in Doped Arsenic Triselenide

Pfister and Morgan[103] have measured hole transit times and d.c resistivities for films of As_2Se_3 doped with Li, Na, K, Mn, Fe, Ni, Cu, Zn, Ga, In and Tl. The samples were prepared by co-evaporating the dopant metal and the bulk glass onto aluminium substrates which were held close to the glass transition temperature $T_g \sim 458K$. They found that the hole transit time increases or decreases by as much as two orders of of magnitude depending on the dopant and concentration. For example figure 2.12a shows the concentration dependence of both the transit time and the d.c. resistivity for Ni, Mn and Cu, whereas figure 2.12b shows these same parameters plotted for Tl, Na, K, In and Ga. They found well defined but field dependent activation energies in all the doped films. The field dependence varied somewhat, but no systematic dependence on either the type of impurity or its concentration was observed. They accounted for the results they found by suggesting that

(1) Mn, Fe, Ni, (10^{17}-10^{18} atoms per cm^3) and Cu (>10^{19} atoms per cm^3) introduce hole traps extending from an intrinsic trapping level located at 0.6 eV above the transport states to the middle of the

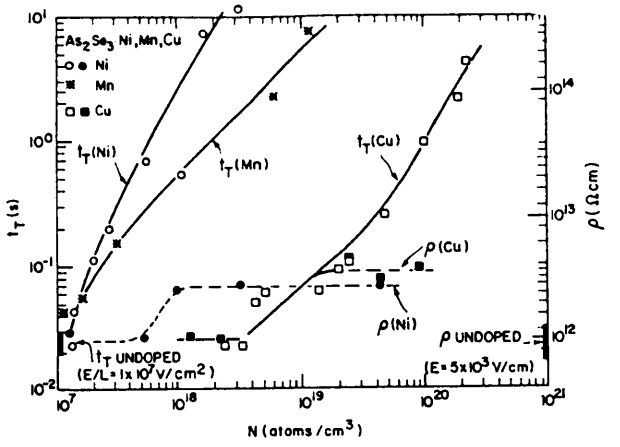

Figure 2.12(a) Log-log plot of transit time (t_T) and resistivity (ρ) versus the concentration N of Ni, Mn and Cu doped As_2Se_3. T = 296K. The transit-time data were plotted for fixed $\mathcal{E}/L = 1 \times 10^7 V/cm^2$. The d.c. resistivity data were measured at a field of $5 \times 10^3 V/cm$ (after Pfister and Morgan [103])

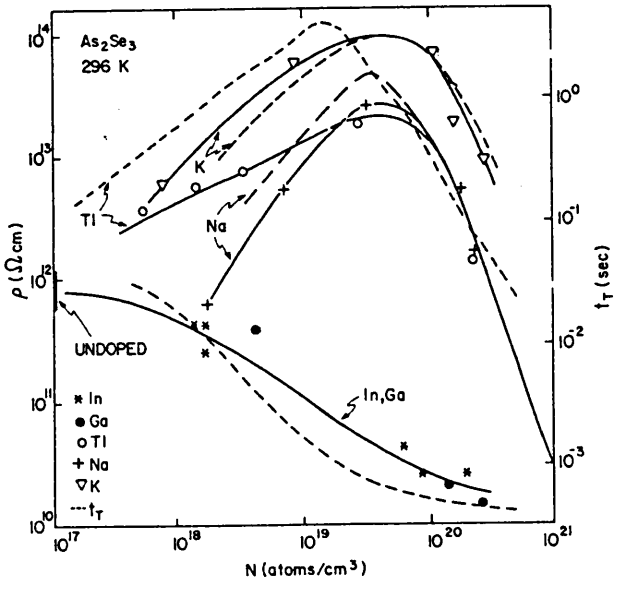

Figure 2.12(b) The same parameters plotted for Tℓ, Na, K, In and Ga-doped As_2Se_3. The dashed lines indicate the concentration of the transit time.

mobility gap as shown in figure 2.13.

(2) Ga, In, and Zn (10^{18}-10^{20} atoms per cm^3) and high concentrations of alkali metals and Tl (10^{19}-10^{20} atoms per cm^3) lead to additional (neutral) states 0.1 eV above the intrinsic transport states.

(3)Low concentrations of Tl (10^{16}-10^{18} atoms per cm^3 and alkali metals (10^{18}-10^{19} atoms per cm^3) generate hole traps approximately isoenergetic with the intrinsic trapping level (see figure 2.13). These latter results are generally consistent with the expectations from current models of charged defects in chalcogenide glasses[103].

Vaninov et al[104] have performed transient photocurrent measurements on a-As_2Se_3 doped with Cl, Br, I, Ge, In, Tl, Na, K, Ag and Cu. The samples used were prepared in the bulk form, adding the impurities to the As_2Se_3 melt in the form of the Se salt or in the elemental form. The glass was air-quenched then polished into plates approximately 1mm thick. The time dependence of the average mobility observed for pure As_2Se_3 and that doped with (1 at. %) Tl, Cl, Br, and In is shown in figure 2.14. For these samples which show no deviation from the power law decay $t^{1+\alpha}$ of the average mobility, the change in mobility can be entirely accounted for by a variation in α. These authors claim that the power law decrease of the average mobility requires a distribution of localised states which decreases exponentially away from the mobility edge (assuming multiple trapping is the correct description). The width of the exponential density of states is kT_c, and T_c was found to be 550K for pure a-As_2Se_3, somewhat higher than the glass transition temperature. For the doped material

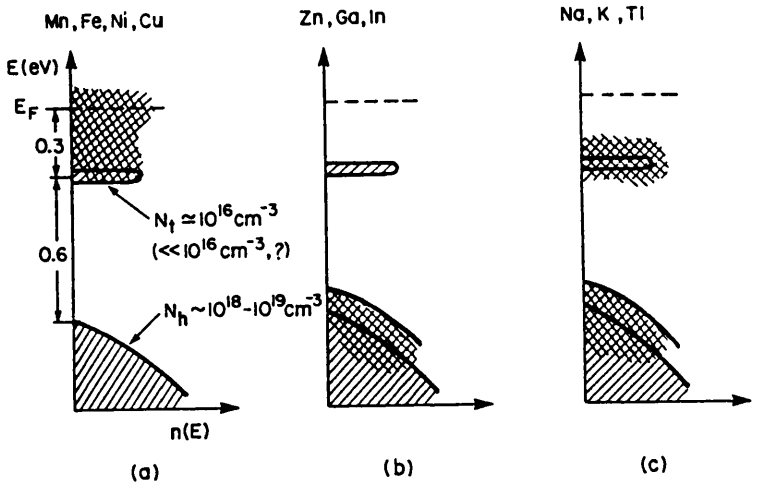

Figure 2.13 Schematic energy level diagrams for As_2Se_3 doped with (a) Mn, Fe, Ni, Cu, (b) Zn, Ga, In and (c) Na, K, Tℓ.

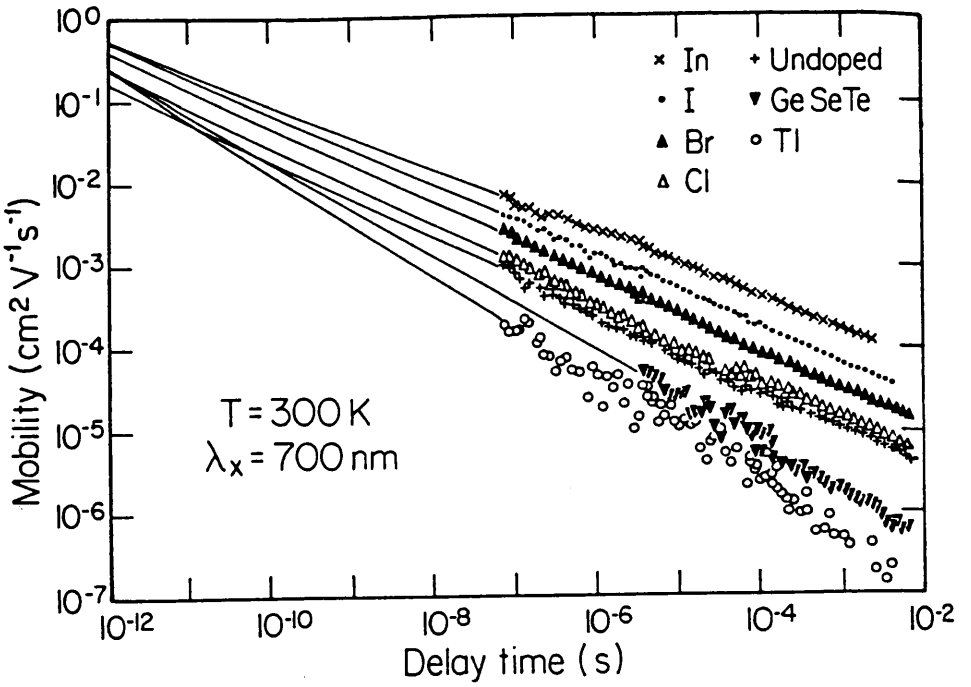

Figure 2.14 Mobility vs delay time for doped and undoped As_2Se_3 as well as a-GeSeTe. Note that all the power laws intercept at $\sim 10^{-12}$s (after Vaninov et al [104]).

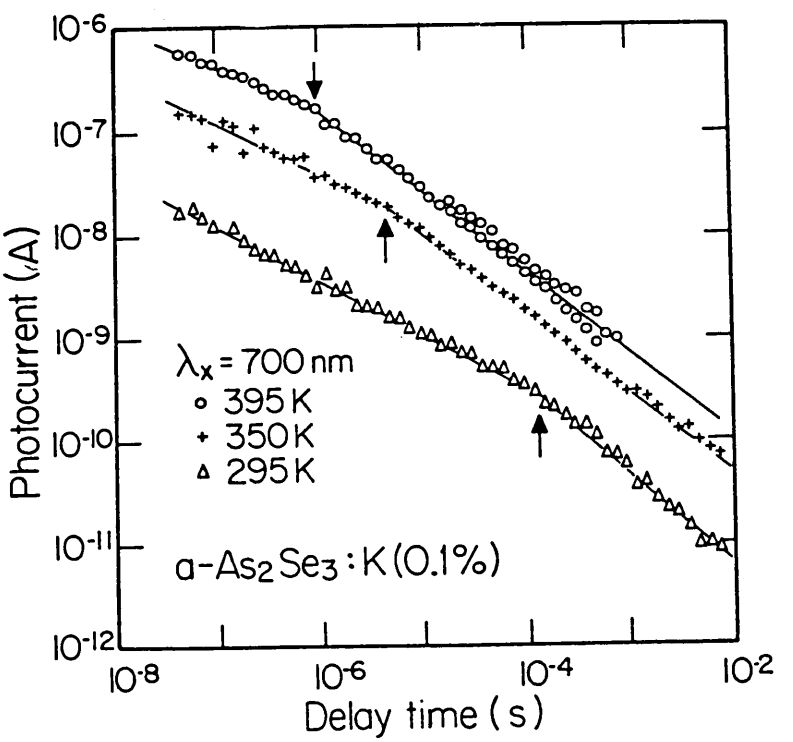

Figure 2.15 Photocurrent vs delay for a-As_2Se_3 doped with 0.1 at % potassium. Note that the kink at each temperature (arrowed) occurs at the same value of $kT\ell n\nu_0 t \simeq 0.5$ eV.

the values of T_c vary over a wide range: from 490K for I-doped to 670K for Tl doped a-As_2Se_3. Since no change in T_g was found from differential thermal analysis, they concluded that there was no simply relationship between T_c and the glass transition temperature. They then state that the origin of this density of states is not fully understood, but whatever the explanation of the exponential density of states, it must also explain these doping effects.

The effect of doping with potassium (0.1 at. %) was more interesting since in this case, a kink can be seen in the current transient (see figure 2.15). As the temperature is raised, the kink shifts to shorter times in such a way that $kTln\nu_0 t$ remains constant (approx. 0.5 eV), as shown by the arrows in the figure. Vaninov et al claim that the presence of the kink supports the multiple trapping interpretation of dispersive transport, stating that potassium introduces new states at an energy of 0.5 eV above the mobility edge for holes.

Chapter 3

PHOTOCONDUCTIVITY AND DISPERSIVE TRANSPORT

3.1 Photoconductivity

When optical absorption by a semiconductor or insulator produces additional free carriers, the electrical conductivity of the material is enhanced in the phenomenon of photoconductivity. Suppose that such a material has a dark conductivity

$$\sigma_0 = n_e e \mu_0 \tag{3.1}$$

where (for simplicity) we here consider a material in which electrons alone contribute to the to the transport of the charge. In the presence of photoexcitation

$$\sigma = n e \mu \tag{3.2}$$

where $\sigma = \sigma_0 + \Delta\sigma, n = n_0 + \Delta n$, and $\mu = \mu_0 + \Delta\mu$ If we substitute into equation (3.1), we obtain for the photoconductivity

$$\Delta\sigma = \sigma - \sigma_0 = e\mu_0 \Delta n + n_e \Delta\mu e \tag{3.3}$$

3.1.1 Lifetimes

The relationship between the change in carrier density Δn and the rate of excess carrier generation ΔG can be expressed in terms of a lifetime.

$$\Delta n = \Delta G \tau_n \tag{3.4}$$

In using this expression care is needed, since a change in n can come about via changes in either ΔG or τ_n, both of which may be produced by appropriate optical excitation. Where τ_n is independent of ΔG, the

change in Δn with ΔG constitutes 'normal' or linear photoconductivity, whilst the influence of τ_n can give rise to either sublinear or superlinear forms of response. Substitution of equation (3.4) into equation (3.3), and assuming a constant value of carrier free mobility gives

$$\Delta \sigma = e \Delta G \tau_n \mu_o \tag{3.5}$$

so that the magnitude of the photoresponse for a given excitation intensity is proportional to the lifetime.mobility product.

The term lifetime may be used in more than one context, the two most important referring to free and shallow-trapped carriers (see next section), i.e.

Free lifetime - the lifetime of a free carrier, not including any time which it may spend in trapping centres prior to recombination. The parameter τ_n defined above refers to a free lifetime.

Excited lifetime - the total lifetime of an excited carrier, including both time spent free and in trapping centres. Where such a term is employed for shallow traps, the free carrier mobility should be replaced in equations (3.3) and (3.5) by the appropriate trap-limited mobility.

3.1.2 Trapping and Recombination

Electron and hole motion within the bands of real crystals and amorphous semiconductors is interrupted by scattering events and the average distance between scattering is the mean-free-path.Thus the motion is of a diffusive nature and one can define a free mobility

which is the average velocity of the carriers per unit field. The free mobility may depend on energy, field and temperature. When localised states are present they act as capture centres for the free carriers. The captured carriers can either be re-emitted to the band or recombined with carriers of the opposite sign. When re-emission is more likely than recombination the localised states are called traps, otherwise they are recombination centres.

Release of a captured carrier back to the band requires energy and is therefore not likely when the energy difference is large. Traps can be subdivided into shallow traps which can establish thermal equilibrium with the band during the time of measurement and deep traps which have release times that are longer than the time of measurement.

3.1.3 Capture Cross Sections

In the case of capture of a free carrier, the capture coefficient of the centre involved can often be written

$$C = vs \tag{3.6}$$

where v is the mean thermal speed of the free carrier, and s is the 'capture cross section' of the centre for that carrier

If the electron and hole effective masses are taken to be isotropic and equal to that of a completely free electron (m_o) then $v_n = v_p \sim 10^7 cms^{-1}$. Radiative capture of a free carrier, usually gives a value for S of about $10^{-19} cm^2$ [104].

Radiationless or phonon involved capture can result in a

wide range of capture cross-sections, depending on the type of centre involved. For such a process to have a high probability, the carrier must be strongly coupled to the lattice in its initial and final state - i.e. localised. Radiationless interband transitions are therefore very unlikely.

If the binding energy or 'depth' of the localised state is >> kT, then a number of phonons are involved in the transitions. Simultaneous emission of several phonons has a low probability (s << $10^{-15}cm^2$). Lax[105] has proposed a model where a carrier is first captured into a highly excited state of the centre, followed by a 'cascade' process through the excited states, to the ground state, each step requiring one or two phonons only.

The cross-section for coulomb-attractive centres can thus be as high as $10^{-12}cm^2$. For neutral centres Lax calculates a capture cross section of $10^{-15}cm^2$ for centres that are 0.5 eV deep in the mobility gap.

3.1.4 Quantum Efficiency

The fraction of absorbed photons that generate carriers, i.e., electrons or holes that can take part in the photoconductivity, is called the quantum efficiency . For a photon flux F

$$\Delta G_n = \eta_n \alpha F$$
$$\Delta G_p = \eta_p \alpha F \qquad (3.7)$$

where ΔG_n and ΔG_p are the generation rates of the excess electrons and holes respectively, η_n and η_p the quantum efficiencies and α is

the absorption coefficient.

An interesting factor in the behaviour of some disordered materials is that the quantum efficiency of generation is found to depend upon photon energy and also upon temperature and electric field. In fact, a value approaching unity is only achieved for high values of these parameters. The most probable explanation of this type of behaviour is that the electron-hole pair is initially generated in the form of an exciton. Since an exciton, once generated, is electrically neutral, it will not contribute to the photoconductivity until its constituent carriers are able to separate from one another. Classical analysis of the separation process is reviewed by Mott and Davis[11]. The features of this type of model are illustrated in figure 3.1.

The excess kinetic energy of the carriers is

$$K.E. = (h\nu - E_g) + \frac{e^2}{k_r} \qquad (3.8)$$

where k is the permittivity. The excess energy is rapidly lost by thermalization (i.e. emission of photons) .The rate of emission of phonons is expected to be of the order of the maximum phonon frequency (10^{12}-10^{13} sec^{-1} when the k selection rules are relaxed, so that the thermalization time can be found.

Random walk theory gives the separation of the carriers achieved in this time. If the coulomb binding energy at that distance is kT or less, then it is assumed that ionisaton of the exciton will take place, giving a quantum efficiency of unity.

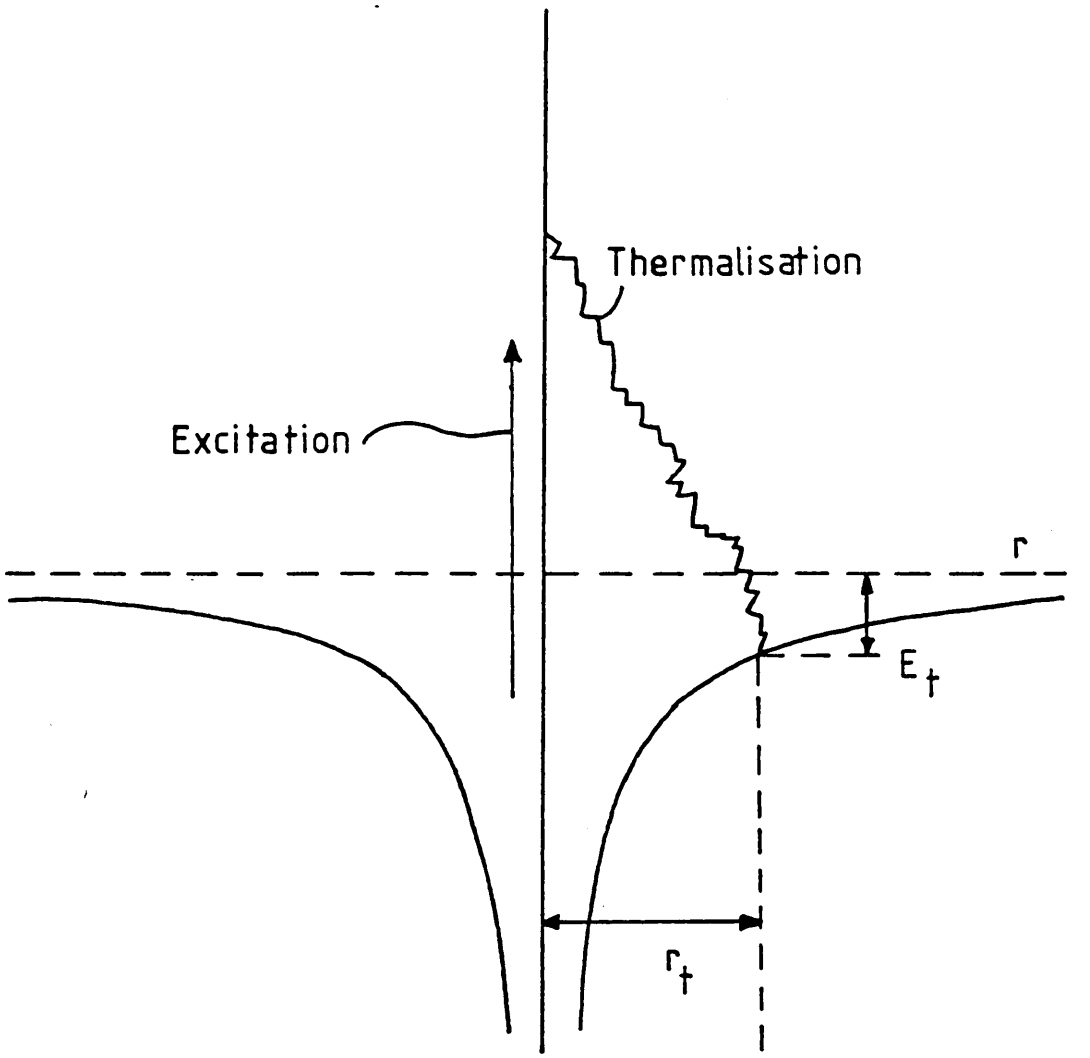

Figure 3.1

Thermalisation of electron-hole pair in their mutual Coulomb field

3.1.5 Simple Rate Equations

Two very important ideas of photoconductivity kinetics are those of DETAILED BALANCE and of CHARGE NEUTRALITY.

The principle of detailed balance states that, at equilibrium, the rate (number of carriers per unit time) at which carriers enter a particular set of states, by operative input paths (see figure 3.2), must be equal to the rate at which the carriers depart from the states by the relevant exit paths.

The principle of charge neutrality states that internal thermal or optical carrier generation will yield equal numbers of holes and electron carriers, so that the material will remain (overall) electrically neutral.

Now let us consider how the above concepts are applied to a semiconductor containing one discrete set of traps (see figure 3.2). In the absence of optical illumination, the various process indicated in the diagram represent:

G -interband generation of an electron-hole pair.

R -interband recombination of C.B. electron and V.B. hole.

a -thermal release of trapped electrons.

a' -trapping of free electrons

d -generation of trapped electron and free V.B. hole.

d' -recombination of trapped electron with V.B. hole. It is now

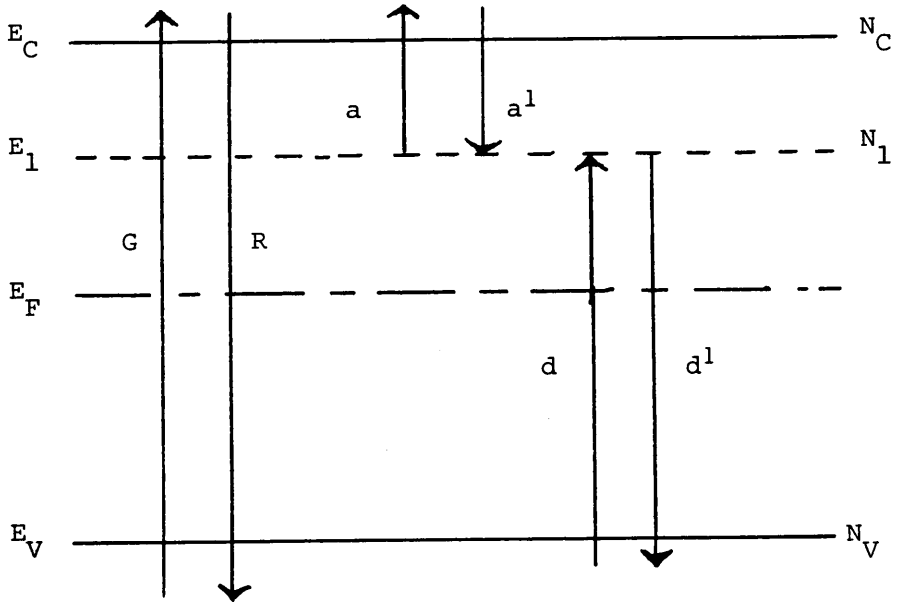

Figure 3.2

Transition diagram for model with one discrete set of traps

possible to proceed via the process of detailed balance and via the charge neutrality condition. Therefore, G=R, a=a′ and d=d′.

The rate a can be expressed as

$$a' = n_1 \nu \exp\left[-(E_c - E_1)\right] / kT$$
$$= N_1 f(E_1) \nu \exp\left[-(E_c - E_1)/kT\right] \qquad (3.9)$$

and similarly

$$a = n_0 s N_1 (1 - f(E_1))$$
$$= N_c f(E_c) s N_1 (1 - f(E_1)) \qquad (3.10)$$

Hence, by equating (3.9) and (3.10) and making the appropriate substitutions

$$\nu = N_c s \qquad (3.11)$$

which us a useful expression for the attempt-to-escape frequency for a trapped carrier, in terms of the more readily calculable parameters N_c and s.

The above treatment of the situation of a material with only one set of traps is, of course, only concerned with the 'dark' conductivity, and does not tell us what to do about the photoconductivity. A major obstacle here is that under illumination the occupancies of states are no longer determined by the Fermi-Dirac distribution function. Hence, equations (3.9) and (3.10) cannot be carried over without a detailed consideration on their relevance.

3.1.6 Quasi Fermi Levels

Under optical excitation the increased free electron and hole densities may be expressed formally in terms of two Quasi Fermi

levels or 'IMREFS', E_{Fn}, and E_{Fp}, respectively, closer to the relevant bands than the equilibrium Fermi level, E_F

$$n = N_c \exp\left(\frac{-E_c - E_{Fn}}{kT}\right) \quad E_{FN} > E_F \tag{3.12}$$

$$p = N_v \exp\left(\frac{E_{FP} - E_v}{kT}\right) \quad E_{FP} < E_F \tag{3.13}$$

These energies may also be used in a limited way to describe trap occupancies, but Simmon's[106] 'trap Fermi levels' provide a more general description, as will be shown in subsection 3.1.8.

In the 'small signal' case, E_{Fn}, $E_{Fp} \sim E_F$, and the trap occupancy function is approximated by the equilibrium function $f_o(E)$.

3.1.7 Demarcation Levels

The occupancy of levels in effective thermal equilibrium with one of the bands is given in terms of the corresponding steady state Fermi level. The demarcation level defines the boundary between these states and those whose occupancy is determined by recombination kinetics. The location of the demarcation level depends upon the specific values of capture coefficients C_n and C_p for the particular type(s) of localised state present. However, it is always true that $D_n + D_p = E_{Fn} + E_{Fp}$ where D_n and D_p are the electron and holes demarcation levels (for a specific trap species).

3.1.8 Analysis of Photoconductivity Data

As with other transport parameters, the analysis of photoconductivity data requires the presumption of a particular model of the disordered state, followed by the use of any simplifying

assumptions which are deemed to be justified, and finally by the comparison of theoretical and experimental photoresponse data. Clearly the conclusions reached by this type of process are not by any means unambiguous, and it is highly desirable to compare the model not only with photoresponse data but also with measurements of as wide as possible a range of other experimental data.

When measured as a function of temperature, the photoconductivity of the chalcogenide glasses shows a typical behaviour shown in figure 3.3. At high temperatures, the photoconductivity is small compared to the dark conductivity, and increases exponentially as 1/T and linearly with the incident light intensity. At lower temperatures, the photoconductivity exhibits a maximum, and subsequently decreases exponentially with 1/T. In this regime, the photoconductivity is proportional to the square root of the incident light intensity. At still lower temperatures, the curves seem to level off to a constant value.

To explain these characteristics two fundamentally different types of model have been applied to experimental measurements.

(a) The classical type of model with discrete sets of localised states in the energy gap[49, 106, 107].

(b) Models with trapping centres distributed throughout the mobility gap [108, 109, 110].

Experimental evidence suggest that models with discrete trap levels are more appropriate to arsenic triselenide[49, 106]. The best

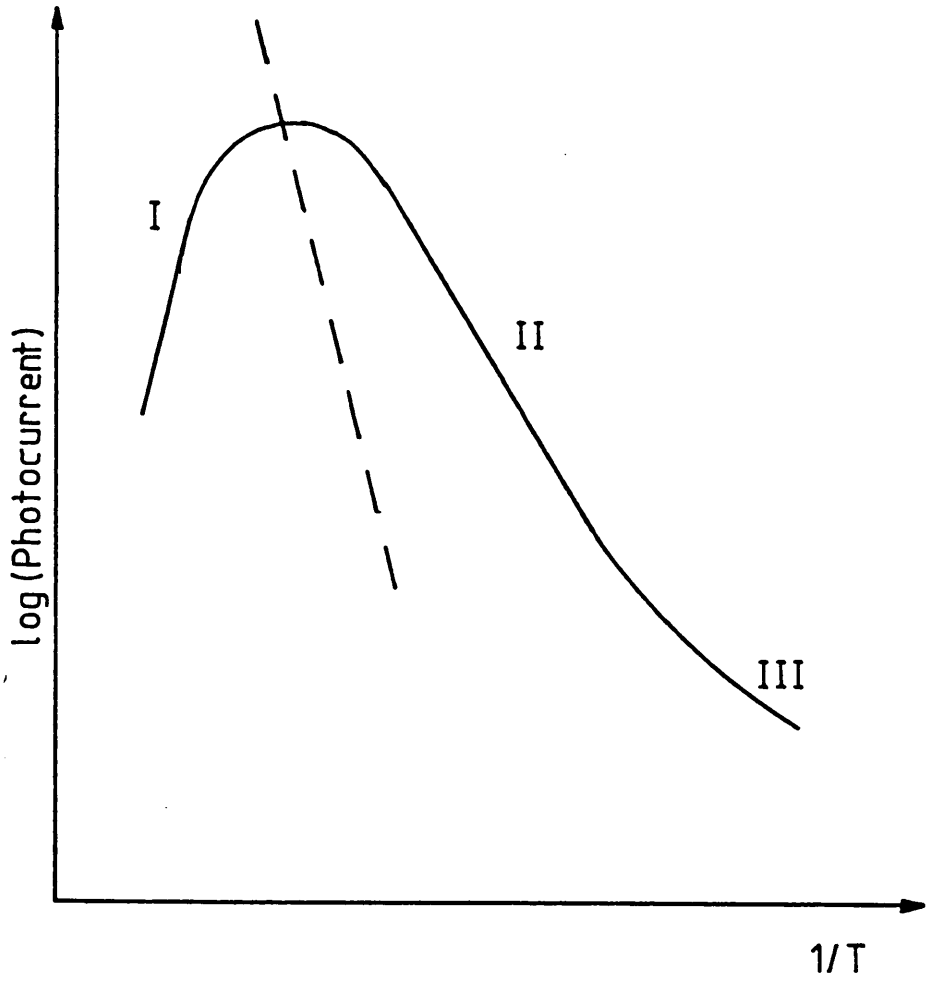

Figure 3.3

Schematic diagram of the temperature dependence of the photocurrent in most amorphous semiconductors. The dashed line represents the dark current.

fit to the experimental data is obtained with band-localised recombination of holes as the dominant mechanism.

Analysis (a) proceeds by assuming the presence in the energy gap of the minimum number of sets of localised states necessary to account for the transport data. In arsenic triselenide, the photoconductivity data appears to require only two sets of localised states in order to account for the response characteristics in detail. However, it should be realised that this does not rule out the occurrence of other localised states, so long as these would not tend to dominate the photoresponse behaviour.

The two level model is shown in figure 3.4. G represents interband generation and R represents interband recombination. Rate analyses may be applied to the various processes and a serious of equilibrium detailed balance equations constructed for the density of free holes and electrons. Main[49] also introduces some band tailing and states at the Fermi level E_F, effectively pinning it; both have some influence on the charge neutrality condition but do not take part in the recombination traffic, i.e., the transitions labeled No. 3 in figure 3.4 do not occur. It is assumed that the traps are in quasi-thermal equilibrium with the nearer band and lie outwith the appropriate trap quasi-Fermi levels under all experimental conditions; and that where possible, rates that are very small compared to others can be eliminated in determining the equilibrium conditions. Using these, assumptions, combined with the charge neutrality condition, Main arrived at a solution of the form (for holes):

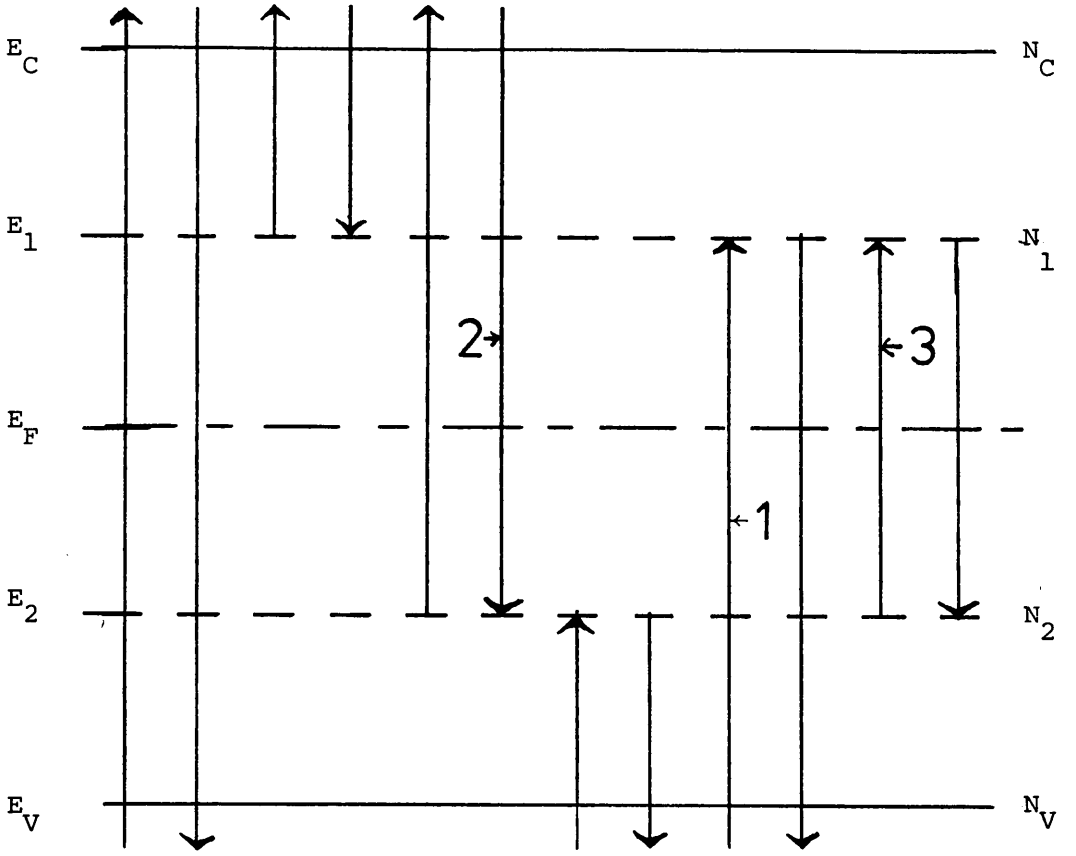

Figure 3.4

Diagram showing all the possible carrier transitions in Main's two level model[49]. The main recombination paths 1, 2 and 3 are shown as described in the text.

Table 3.4.1

Nomenclature

Parameters specific to trap energy levels E_1 and E_2 as shown in figure 3.4 and as used in Main's analysis described in the text.

E_1, E_2	trap energies $E_1 > E_F$ $E_2 < E_F$
N_1, N_2	trap densities
f_1, $\bar{f}_2$	trap occupancies
n_1, n_2	electron emission - effective densities
P_1, P_2	hole emission - effective densities
C_{n1}, C_{n2}	electron capture coefficients
C_{p1}, C_{p2}	hole capture coefficients
K_{12}, K_{12}	L-L transition coefficients

$$\Delta G = [2p_o\Delta p + \Delta p^2]\left\{C_{p1}\frac{N_2}{P_2} + C_{n2}\left(\frac{N_2}{P_2}\right)^2\frac{n_1}{N_1} + K_{12}\left(\frac{N_2}{P_2}\right)^2\right\} \quad (3.14)$$

where $p - p_o = \Delta p$ and p_2 and n_1 are the 'effective densities' of free holes and electrons which would exist if the Fermi level were coincident with the traps E_2 and E_1 respectively. This equation can then be solved for Δp and clearly there is a small signal case where $\Delta p << P_o$, and $p \sim \Delta G$ and a large signal case where $p >> p_o$ and $p \sim \Delta G^{0.5}$. The three terms in the curly brackets represent the three recombination paths, 1, 2 and 3 shown in figure 3.4 and in a particular material it is likely that one of the three recombination modes will dominate the other two.

Equation (3.14) can be solved for each path separately and the solutions checked against experimental data. The activation energy of each solution is a combination of two or more of the energies E_c, E_1, E_2 and E_v. To determine which solutions are appropriate to the experimental observations it is necessary while analysing the data to make comparisons with other electrical properties, e.g., dark conductivity, transient photoconductivity, etc (see subsection 3.1.12, page 76).

3.1.9 Distributed Trapping Centres

Several variants of the 'C-F-O' type of model have been advanced to analyse photoconductivity data on amorphous semiconductors.

In the model proposed by Weiser et al[109] the excess carriers thermalize in the tails of the localised states with decreasing

probability as the depth increases. It is assumed that the probability of recombination (via localised transitions) decreases more slowly than the thermalization probability. Hence an energy will be reached where the two are equal and below that energy (for electrons) the probability of recombination is greater. Weiser et al[109] call this critical energy the 'recombination edge'. An important consequence of the model is that the trap occupancy is at a maximum at the recombination edges.

To obtain agreement with the experimental data it is necessary to assume that the thermalization probability decreases with energy (for electrons) much more rapidly than seems likely and as a result the trap occupancy would peak very sharply at the recombination edges. This model is then almost indistinguishable from a discrete-trap-level model, with levels situated at energies corresponding to the recombination edges. Moreover, the spatial separation of localised levels will make localised-to-localised transitions much less likely than transitions between a band and a localised state.

Arnoldussen et al[108], used a band tail model precisely as envisaged by C-F-O with overlapping valence and conduction band tails. They invoked both band-to-localised and localised-to-localised transitions between the recombination edges and the Fermi level, i.e., effectively a five level model, as illustrated in figure 3.5.

Arnoldussen et al interpret their photoconductivity data for As_2SeTe_2 in terms of this scheme. In the high temperature region

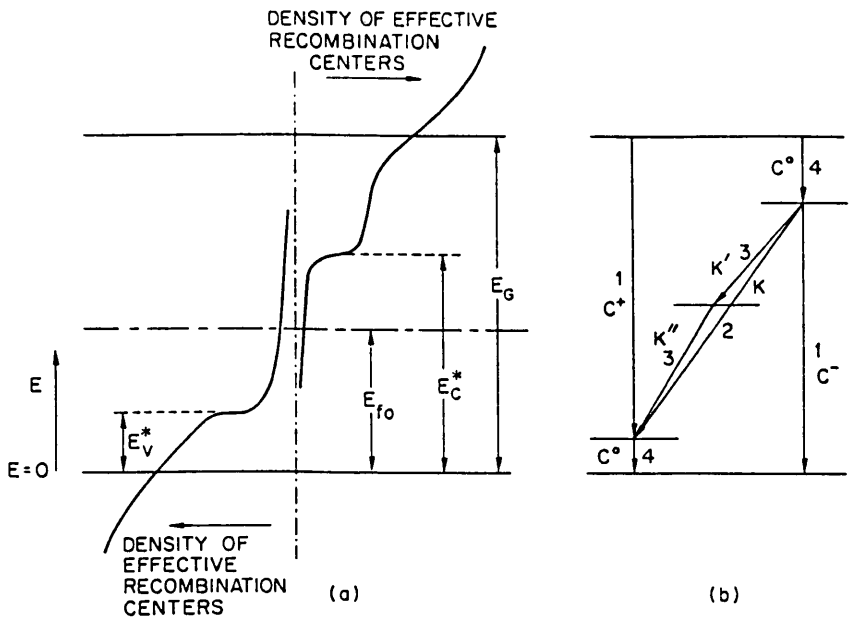

Figure 3.5

(a) Schematic energy level diagram for the model proposed by Annoldussen et al[108]. (b) Typical transitions between individual states in the distribution shown in (a). They assume that the states near the valence edge are neutral when occupied and positively charged when unoccupied, and that states near the conduction edge are neutral when unoccupied and negatively charged when occupied.

either transitions 1 or 2 may govern the recombination. In the intermediate region transitions 2 dominate at high intensities and transitions 3 at low intensities. At low temperature transitions 4 control the recombination. Their modified model [111] is effectively a discrete level model plus a 'chaotic potential' which causes spatial fluctuations of the bands. Averaging of the spatial fluctuations, gives a continuum of states on both sides of the Fermi level and localised band-edge states. In the high temperature region the number of excess carriers, both in traps and in bands, is much smaller than the number of thermally generated carriers. Since the capture rate depends on the product of occupied states at one level (or band) and unoccupied at the other, it will increase linearly with increased generation until the excess generation becomes comparable to the thermal generation. After that, the increase in capture rate becomes proportional to the square of the carrier density. This results in the steady-state densities increasing with the square root of the generation rate.

3.1.10 Exponential Tail Model

In this particular study the variation of the photoconductivity with light intensity obeyed the relationship $I_p \sim \Delta G^{\gamma}$, but in some instances γ did not equal 0.5 as expected from bimolecular recombination, but varied in value between 0.5 and 1 i.e., $(0.5<\gamma<1)$.

One can find attempts to account for such an odd power in terms of a mixture of monomolecular and bimolecular processes but such a mixture does not account for non-integer powers extending over

several powers of ten of light intensity. A model which may explain this behaviour has been put forward by Rose[110] who presents a simple picture to account for exponents less than unity based upon a distribution of trapping states, N_t (see figure 3.6). He states that as the light intensity is increased, more and more of the N_t states are converted from trapping to recombination states. The conversion takes place as the quasi-Fermi level E_{Fn} sweeps through the N_t states towards the conduction band. As p_r, the density of recombination states for electrons, increases, the electron lifetime decreases.

The model differs from that used in the previous section in two respects:(1) the p_r states are negligible or absent at zero light intensity, (2) the trapping states N_t have an exponential distribution in energy such that

$$N_t(E) = N_0 \exp\left[-\frac{(E_c - E_t)}{kT_c}\right] \tag{3.15}$$

The temperature, T_c, is a formal parameter that can be adjusted to make the density of states vary more or less rapidly with energy. Rose takes $T_c > T$, where T is the ambient temperature. He uses the following relation

$$N_r > \int_{E_F}^{E_c} N_t(E)\, dE \tag{3.16}$$

and lets the capture cross sections of the N_t states be the same as those for the N_r states, where N_r equals the total number of recombination centres p_r+n_r. Actually, the capture cross sections of the N_t states may differ markedly from those of the N_r states without

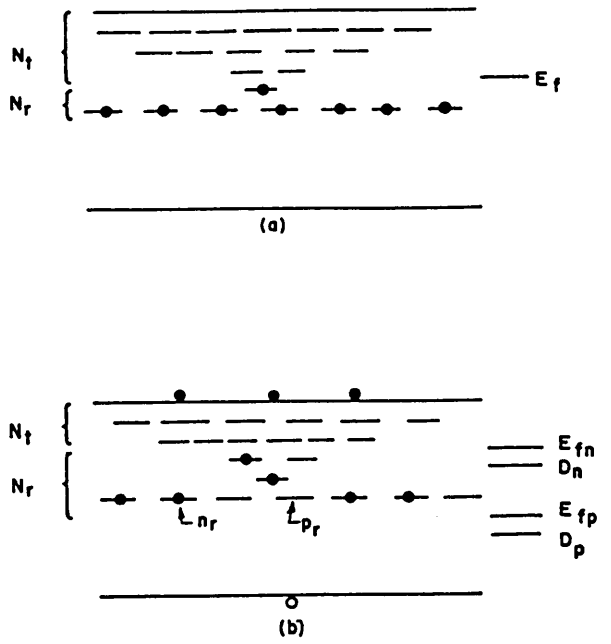

Figure 3.6
Model for exponents of current - light curve lying between 0.5 and 1.0 (a) Unilluminated (b) Illuminated

affecting the main argument. For definiteness, Rose takes $s_n << s_p$ so that the density of photoexcited electrons is much larger than that of photoexcited, holes, i.e, $n >> p$.

Figure 3.6 shows the conditions at some intermediate light intensity. The demarcation levels D_n, D_p are slightly shifted down from the Fermi levels E_{Fp} and E_{Fn} because $p_r << n_r$. For example, if $n_r = 10^2 p_r$, the shift is about 0.1 eV at room temperature. The distribution of electrons and holes in the states lying between D_n and D_p is homogeneous and independent of energy.

To a good approximation, the density of empty states p_r is given by the number of N_t states lying between E_F and E_{Fn}. These were originally empty states that have now been brought into the category of recombination centres. A more accurate treatment would make correction for the states lying between E_{Fn} and D_n. The correction however, would not alter p_r by more than the fraction p_r/n_r. Since this ratio was taken to be small, the simple estimate of P_r is justified

$$p_r = \int_{E_F}^{E_{FN}} N_t(E)\, dE$$

$$= \int_{E_F}^{E_{FN}} N_o \exp\left[-\frac{(E_c - E_t)}{kT}\right] dE \qquad (3.17)$$

Hence one can write

$$P_r = kT_c N_t(E_{FN})$$

$$n = \Delta G \tau_n = \Delta G \left(\frac{1}{P_r V S_n}\right)$$

$$= \Delta G \cdot \frac{1}{kT_c N_o \exp\left[-\frac{(E_c - E_{FN})}{kT_c}\right] V S_n} \qquad (3.18)$$

By definition

$$n = N_c \exp\left[\frac{-(E_c - E_{FN})}{kT}\right] = N_c \exp\left[\frac{-(E_c - E_{FN})T_c}{kTT_c}\right] \qquad (3.19)$$

Insertion of equation (3.19) into equation (3.18) leads to

$$n = \left[\frac{\Delta G N_c^{T/T_c}}{kT_c N_o V S_n}\right]^{T_c/(T+T_c)} \qquad (3.20)$$

Since $T_c > T$, the exponent $T_c/(T + T_c)$ lies between 0.5 and unity.

We have in equation (3.20) a simple mechanism to account for photocurrents that increase with increasing light intensity as any power lying between 0.5 and unity. While the model assumes an exponential distribution of states lying between E_F and E_c, the distribution need only extend over a small range in energies through which E_{Fn} moves, since the largest contribution to P_r comes from states near E_{Fn}. Further, the distribution need only be approximated by an exponential form over this short range of energies. Hence almost any distribution of states will lead to exponents of the current-light curve lying between 0.5 and unity.

3.1.11 Photomobility

Consider a step-function illumination applied to a sample in thermal equilibrium

$$\Delta G(x) = \eta \alpha F(x) \tag{3.21}$$

In times shorter than the trapping time for the shallowest traps

$$\frac{d\Delta p}{dt} = \Delta G \tag{3.22}$$

$$\therefore \quad \frac{dI_{ph}}{dt} = e\mu_{p_0} \mathcal{E} \frac{d\Delta p}{dt} \tag{3.23}$$

Such short measurement times have not been experimentally possible so far.

If the probability of trapping in a set of traps N_{t1}, with trapping time τ_{t1} and release time τ_{tr1}, per unit time is much greater than the probability of trapping in deeper traps N_{t2} (or recombination), then quasi-thermal equilibrium will be established with the first set and will prevail for some time so that equations (3.24) and (3.25) apply.

$$\Delta p + \Delta p_t = \Delta G \times t \tag{3.24}$$

and

$$\frac{\Delta p}{p} = \frac{N_v}{N_t} \exp\left[\frac{-E_t - E_v}{kT}\right] \ll 1 \tag{3.25}$$

where Δp_t is the increase in holes trapped at the level E_t. It follows

that

$$\frac{dI_{ph}}{dt} = e\mathcal{E}\Delta G\mu_{po}\frac{N_V}{N_t}\exp\left[-\frac{(E_t-E_v)}{kT}\right]$$

$$= e\mathcal{E}\Delta G\mu_d$$

$$= e\mathcal{E}w\eta F(1-R) \qquad (3.26)$$

where μ_d is the trap limited hole drift mobility, w is the width of a specimen electrode (coplanar configuration see chapter 5, figure 5.10b) and R is the air/film reflectance. Figure 3.7 shows how the photocurrent is expected to grow with time. The steep slope in part (a) corresponds to the short interval before any trapping occurs, part (b) to band-trap quasi-equilibrium and part (c) shows the turnover resulting from recombination. In theory there could be linear regions corresponding to other trap levels.

3.1.12 Photocurrent Decay

Using the two level trap model (see figure 3.4) described in section 3.1.8, page 68, Main[49] has shown that solution of equation (3.14)in the small signal case gives an exponential decay of the form.

$$\Delta p(t) = \Delta p_{ss}(-t/\tau_{cm}) \qquad (3.27)$$

where Δp_{ss} is the steady state hole concentration and

$$1/\tau_{cm} = 2p_o\left(c_{p_1} + c_{n_2}\frac{N_2 n_1}{p_2 N_1} + K_{12}\frac{N_2}{p_2}\right) = 2p_o\theta \qquad (3.28)$$

The temperature dependence of the decay time is an important means of distinguishing B-L and L-L recombination.

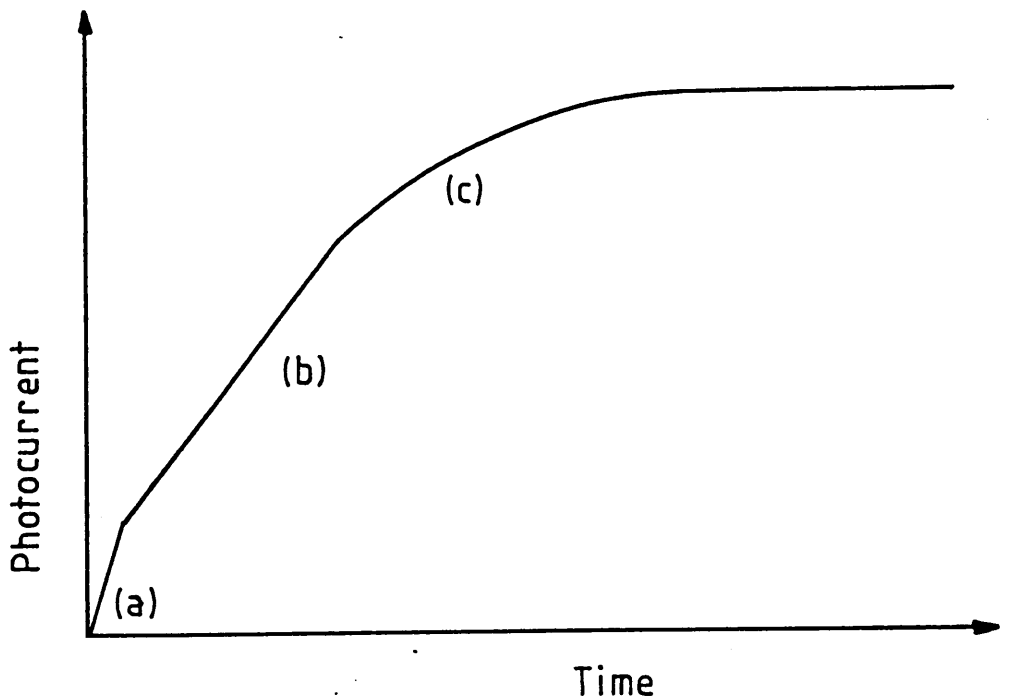

Figure 3.7
The response of photocurrent to a step function illumination (a) before trapping, (b) after quasi-equilibrium has been established with a set of traps but before recombination becomes significant, (c) recombination limited growth.

$$\text{path 1} \quad \tau_{cm(1)} \sim \exp\left(\frac{[E_2-E_v]+\frac{1}{2}[E_1-E_2]}{kT}\right) \tag{3.29}$$

$$\text{path 2} \quad \tau_{cm(2)} \sim \exp\left(\frac{[E_c-E_1]+\frac{1}{2}[E_1-E_2]}{kT}\right) \tag{3.30}$$

$$\text{path 3} \quad \text{L-L} \quad \tau_{cm(3)} \sim \exp\left(\frac{\frac{1}{2}[E_1-E_2]}{kT}\right) \tag{3.31}$$

All exponents are positive, but the L-L path gives a smaller temperature dependence. The greater temperature dependence in the B-L cases arises from the fact that a small temperature dependent fraction of one of the reservoirs is active in recombination, (hence the (E_2-E_v) and the (E_c-E_1) terms).

In the large signal case it is difficult to measure a lifetime because the decay of the steady state photocurrent in the bimolecular regime is hyperbolic and not exponential as in the monomolecular regime. However an instantaneous decaytime can be calculated using relation (3.32)

$$\tau = \frac{-\Delta P_{ss}}{d(\Delta p)/dt} \tag{3.32}$$

where Δp_{ss} is the steady state "hole" concentration.

From Main's, analysis[49] the "quasi hyperbolic" decay follows relation (3.33).

$$\Delta p(t) = \frac{\Delta p_{ss}}{1 + \Delta p_{ss}\theta t} \tag{3.33}$$

where θ is defined in equation (3.28).

A bimolecular decay time τ_{cb} may be defined as the time for the excess density to decay to half the steady state value

$$\tau_{cb} = \left(\frac{\theta \Delta G p_2}{N_2} \right)^{-0.5} \tag{3.34}$$

The decay time is now dependent upon light intensity, and again, B-L and L-L paths give rather different temperature dependencies.

Path1. $$\tau_{cb}(1) \sim \exp\left(\frac{\frac{1}{2}[E_2 - E_v]}{kT} \right) \tag{3.35}$$

Path2. $$\tau_{cb}(2) \sim \exp\left(\frac{\frac{1}{2}[E_c - E_1]}{kT} \right) \tag{3.36}$$

Path3. Temperature independent (3.37)

If the steady state photocurrent ΔI_{ss} is obtained and then modulated by a small percent of this value, δi_{ss} say,(similar to the experimental method described in chapter 5) and if Δp_{ss} is used as the new p_o value then expression (3.38) is obtained.

$$\frac{d(\delta p)}{dt} = \delta G \left(\frac{P_2}{N_2}\right) - \left[2\Delta p_{ss}\delta p + \delta p^2\right]\theta \qquad (3.38)$$

Since δp^2 is small and can be neglected a solution in this case gives expression (3.39),

$$\delta p(t) = \delta p_{ss} \exp(-t/\tau') \qquad (3.39)$$

which is an exponential decay.

In this case $\tau' = 1/(2\Delta p_{ss}\theta)$, and Δp_{ss} is dependent upon illumination and temperature.

The above two level trap model (see figure 3.4), even if conceptually correct, is clearly 'idealised' in the sense of assuming discrete trapping centres. Clearly, in an amorphous semiconductor the levels are not discrete but spread in energy by a few kT. The density of states distribution for an amorphous solid may even consist of tails extending from the conduction/valence band with features superimposed upon them[112]. It is thought that if the features in the density of states are such (as in the case of amorphous arsenic triselenide) that they dominate the trapping/recombination traffic, then the above solutions may be applied where appropriate.

3.2 Anomalously Dispersive Transport

It had been observed that the transport of holes through samples of arsenic triselenide in drift mobility experiments cannot be described by conventional gaussian broadening of the carrier packet. In other words, the dispersion σ of the carrier sheet and its mean displacement ℓ from the excited surface do not obey the well-known

relations $\sigma \sim t^{1/2}$ and $\ell \sim t$ which are expected from gaussian statistics. This led to the phenomenon being termed anomalously dispersive transport.

Scharfe[4] reported that the anomalously dispersive transport indicated a very broad spread of individual carrier transit times and that two distinct power law regimes were present in such transit pulses, obeying the relations (3.40)

$$I_1 \sim t^{-(1-\alpha_1)} \qquad (t < t_t)$$

$$I_2 \sim t^{-(1+\alpha_2)} \qquad (t > t_t) \qquad (3.40)$$

He also reported the UNIVERSALITY of pulse shape when it was observed that transit pulses obtained from measurements upon a given specimen at various values of applied field, exhibited almost identical degrees of relative dispersion. This universality of pulse shape was also suggested to extend to variations in specimen thickness, and (in some cases such as that of hole transport in As_2Se_3) to variations in temperature.

Figure 3.8 displays experimental data for As_2Se_3, illustrating both the (approximate) universality of pulse shape, and the occurrence of the two regimes. The experimental data are usually displayed using logarithmic axes conforming to such functional behaviour. Scharfe had suggested that α_1 and α_2 were equal, and a first serious attempt by Scher and Montroll[5] to explain anomalously dispersive behaviour predicted such equality. Their analysis also

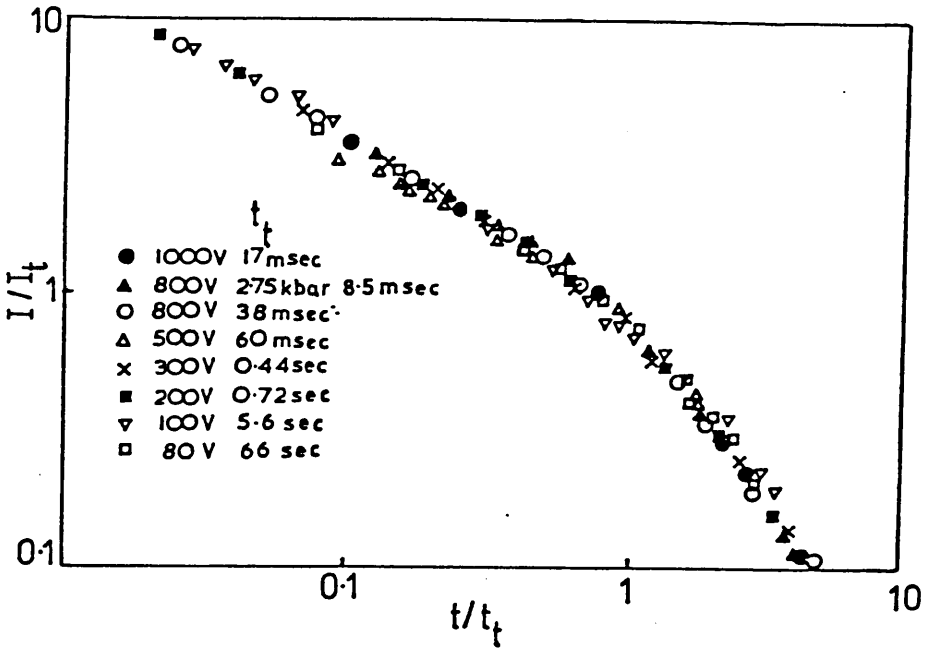

Figure 3.8

Superimposed transit characteristics for hole carriers in a-As_2Se_3 at room temperature, under various values of applied electric field (data as presented by Scher and Montroll[5])

predicted the universality of pulse shape (see next subsection).

3.2.1 The Scher-Montroll Model of Anomalous Dispersion

A major advance the study of anomalous dispersion was achieved in 1975, with the publication of the first detailed model capable of predicting the various features of the experimental behaviour. Scher and Montroll[5] (SM) advance a model based upon the transport by hopping between isoenergetic sites with a random position distribution ('r-hopping'). The analysis of the transport characteristics expected for this process has proved to be a daunting theoretical problem, and to date no exact solution has been advanced.

Scher and Montroll approached the problem in the following manner.

(1) A global 'waiting time distribution function', $\psi(t)$, was evaluated by averaging over all individual sites in the system. For any particular occupied centre, transitions are possible to various neighbouring sites, and the probability of each (per unit time) varying with intersite distance R as $\exp(-2R/R_o)$. If the mean site separation $\bar{R}$ is large compared to R_o, then various sites within the random array will be characterised by widely different escape probabilities. Taking into account the combined probabilities of transitions to various neighbours, it is possible to represent the probability that a carrier which reaches a given site at time t=0 should remain localised there for time t and then escape within the the time interval dt, in the form

$$p(t)\,dt = \gamma'' \exp(-\gamma'' t)\,dt \qquad (3.41)$$

where γ'' is the nett release coefficient for the centre (comprising an appropriate combination of the transition coefficients to the various neighbours).

The Scher-Montroll function $\psi(t)$ represents an average of p(t) taken over all sites in the array, so that $\psi(t).dt$ represents the probability that if a carrier became localised somewhere at t=0, it will be released during the time interval t to t + dt.

(2) having computed a form for the function $\psi(t)$, SM then introduced the significant assumption that, since the waiting time distribution function contained all the necessary information concerning the random nature of the r-hopping system, the behaviour could be transferred to a regular lattice of sites. Each individual centre of this array was assumed to possess a release time distribution function equal to $\psi(t)$, as computed for the random system, rather than a distribution function appropriate to the array or to the individual site concerned.

The averaged waiting time distribution function for the topologically-random array of sites was evaluated by SM to be of the form

$$\psi(t) \sim \text{const}\,(\ln \Upsilon)^2 \Big/ \Upsilon^{1+(\eta'/3)(\ln \Upsilon)^2} \qquad (3.42)$$

where Υ is a normalised time and $\eta' \sim (R_o/R)^3$. SM then suggest that since the logarithmic terms in equation (3.42) vary rather slowly with

time , it is appropriate to approximate $\psi(t)$ (over the time range accessible in a 'time of flight' experiment) by the function

$$\psi(t) \sim \text{const } t^{-(1+\alpha)} \tag{3.43}$$

where

$$\alpha = \frac{1}{3}\eta' (\ln T)^2 \tag{3.44}$$

giving a value of α which is envisaged as being approximately constant over the experiment time scale.

SM further demonstrate that, for the algebraic form of $\psi(t)$ given in equation (3.43), the mechanism of continuous time random walk on a regular lattice yields an excess carrier transit pulse possessing two power law regimes, in agreement with the experimental observation indicated in equation (3.40). Moreover, the values of α_1 and α_2 are equal to each other and to the parameter α in equation (3.44), again in agreement with the Xerox group's observation of the experimental behaviour in a-As_2Se_3 and other materials.

3.2.2 Trap Limited Band Transport and Anomalous Dispersion

Whilst the SM analysis successfully mirrors some of the features which were originally ascribed to the anomalously-dispersive transport, it is none the less the case that subsequent experimental studies have frequently identified characteristics which are rather different than those initially suggested. That is to say deviations from the SM predictions of equality of α_1 and α_2, and of universality

with temperature have been reported in an increasing number of materials[113, 72, 114, 115, 116] including a-As_2Se_3. These authors note, that whilst transit pulses observed at low temperatures may be characterised to a first order as involving two power-law regimes, there are detectable deviations from such algebraic behaviour within the experimentally accessible time range.

It rapidly became clear in 1977 from a number of studies [117, 118, 119, 120, 121, 122] performed either by computer simulation or by theoretical analyses on model systems that a suitable $\psi(t)$ can arise from the case of trap limited band transport. All that was required for the generation of anomalous dispersion was for localised states to be distributed over a sufficient range of energy.

In the simulation studies, various distributions of trapping centres were examined, as illustrated in figure 3.9, and it was established that in each case, highly dispersive transit pulses could be generated if the localised states extended (in significant numbers) over more than a few kT. Of the distributions the rectangular distribution is of particular interest because it is rather easier to evaluate the function $\psi(t)$ for this case. Marshall [117] has shown $\psi(t)$ to be of the form

$$\psi(t) = \text{const.}\left[\exp(-Ct) - \exp(-Dt)\right] \cdot t^{-1} \qquad (3.45)$$

where $C = \lambda_0' \exp(-\Delta E/2kT)$, and $D = \lambda_0' \exp(+\Delta E/2kT)$, and λ_0' is the release coefficient for states at the centre of the energy

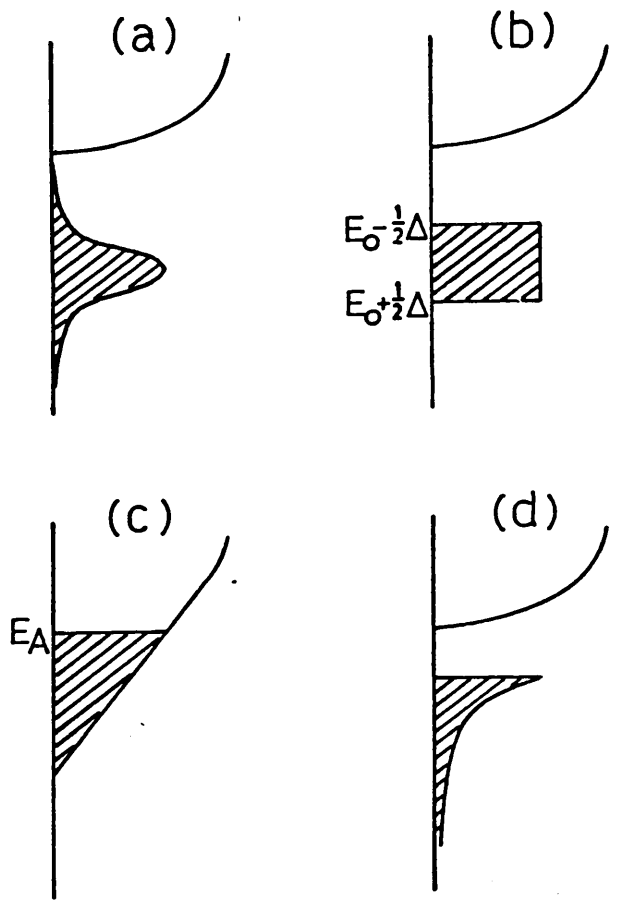

Figure 3.9

Various forms of localised state distribution which have been employed in Monte Carlo simulation studies of the transient response for trap-limited band transport of excess charge carriers (after Marshall[134])

(a) Gaussian distribution $N(E) = N_o \exp(-[(E-E_o)/kT]^2)$

(b) Rectangular distribution $N(E) = N_t \; (-\frac{1}{2}\Delta\varepsilon < E < +\frac{1}{2}\Delta\varepsilon)$

(c) Linear distribution $N(E) = N_o (\Delta - E)/\Delta$

(d) Exponential distribution $N(E) = N_o \exp(-E/kT_c)$

distribution. This dwell time distribution function is displayed, for various values of $\Delta E/kT$, in figure 3.10.

Upon examination of equation (3.45) and of figure 3.10 it is clear that $\psi(t)$ does not possess the algebraic form adopted by SM for the r-hopping case, except in the limit of a very wide distribution of traps. Consequently, assuming the validity of the SM relationship between $\psi(t)$ and I(t), algebraic forms would not be expected for the latter parameter in either the initial or the final regime of the transit pulse.

In the analytical investigation of trap-limited transport performed by Noolandi [121], the multiple-trapping equations were written in the form

$$\frac{dp}{dt}(\vec{x},t) = g(\vec{x},t) - \vec{\nabla}.\vec{f}(\vec{x},t) \qquad (3.46)$$

$$p(\vec{x},t) = p(\vec{x},t) + \Sigma_i P_i(\vec{x},t) \qquad (3.47)$$

$$d\frac{(\vec{x},t)}{dt} = p(\vec{x},t)\omega_i - P_i(\vec{x},t)\tau_i \qquad (3.48)$$

where $\vec{x}$ $(=x_1,x_2,x_3)$ is the position in space, t is the time, $g(\vec{x},t)$ is the local photogeneration rate, $f(\vec{x},t)$ is the flux of mobile carriers, $p(\vec{x},t)$ is the free carrier density, and $p_i(\vec{x},t)$ is the density of carriers localised in the i^{th} set of a group of different trapping centres. w_i and r_i are respectively the capture and release rate for this set of traps. Neglecting diffusion, and considering the case of flash excitation of excess carriers by a short pulse of

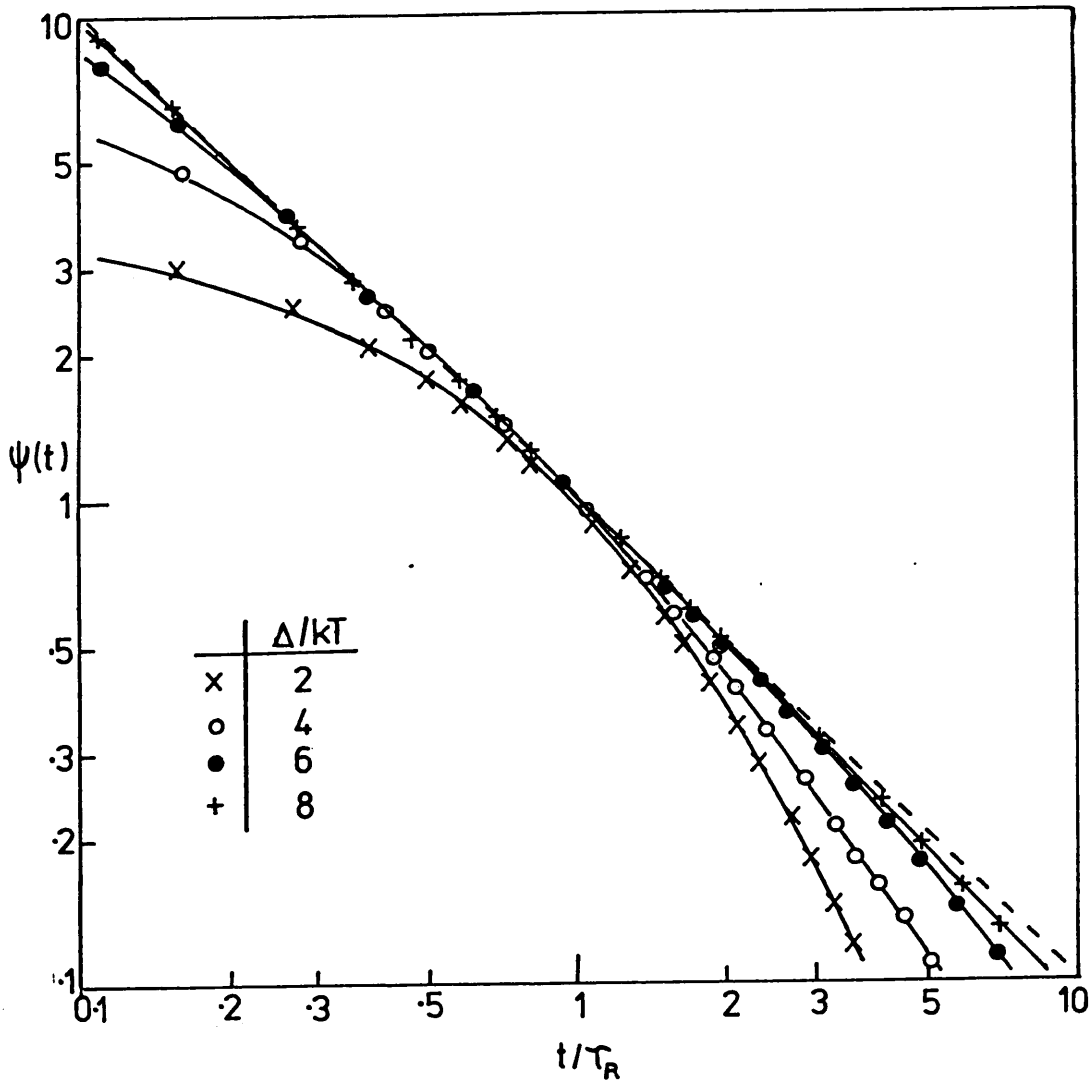

Figure 3.10

Form of the dwell time distribution function $\psi(t)$ for a rectangular distribution of localised states, $\tau_R (=\lambda_o^{-1})$ represents the release time constant for states at the centre of the distribution. (After Marshall [117]).

strongly-absorbed light, Noolandi was able to solve (3.46) to (3.48) using Laplace transform techniques. He obtained the following expression for the transform of the photocurrent

$$\bar{I}(s) = (e\eta'/t_o)\left[1-\exp(-a(s)t_o)\right]/a(s) \tag{3.49}$$

where s is the variable of the transformation, η' is the photogeneration efficiency, $t_o = L/\mu_o E$ is the free carrier transit time, and

$$a(s)t_o = s\left(t_o + \Sigma_i \frac{M_i}{s+\gamma_i}\right) \tag{3.50}$$

with $M_i = \omega_i t_o$ representing the number of times on average that a carrier is captured in traps from the i^{th} set, during its passage across the sample.

The significance of equation (3.49) is that it is identical in form to a corresponding equation derived by SM at an equivalent stage in the analysis of continuous time random walk. This suggests an equivalence between the multiple trapping formalism and the SM hopping approach, and the correspondence was established by both Noolandi[121, 122] and Schmidlin [119, 120].

Schmidlin advanced a "Critical Trap Criterion", that, for anomalous dispersion to be generated, a set of localised states must be present in such a concentration that (a) the carrier is likely to be trapped in the set approximately once during transit ($M_i = 1$), and (b) the release time constant for traps in this set should be

comparable to the transit time t_T.

Thus, such centres would be able to influence the transit time of some carriers , whilst others would complete their transit without trapping in the set, giving a considerable overall dispersion.

In comparing their models with experimental data, Schmidlin[119] examined the case of hole transport in a-As_2Se_3, whilst Noolandi [121] considered hole transport in a-Se. In the former case, because of the suggestion of a temperature-independent degree of dispersion, Schmidlin concluded it to be necessary that all the localised states be situated at the same energy, with the dispersion originating from differences in the unactivated component of the release coefficient - i.e. the attempt to escape frequency ν. More surprisingly, Noolandi (using a model with three set of traps), also concluded that all three possessed the same release activation energy. The strong temperature dependence of the degree of transit pulse dispersion was assigned to variations in the trap capture process.

The r-hopping model has been criticised by several authors [117, 123, 118] for a variety of reasons. The major criticism is that hopping sites with very long dwell times must be considered as isolated sites which will consequently be avoided by the fastest carriers. Pollak[123] has provided a criterion for the observation of dispersive transport:that the sites which have long release times must be correspondingly difficult to enter. This criterion is clearly not met for a spatially random hopping system, as has been confirmed by Monte-Carlo computer simulation[117, 118]. It was shown using this

technique, that the SM model may give anomalous dispersion at short times, but is not expected to show highly-dispersive transit pulses in specimens of experimental dimensions. However, whereas it is now well established that anomalous dispersion involves a waiting time distribution function $\psi(t)$ which varies only slowly with time, the question of whether such a distribution is appropriate for "r-hopping" is still a subject of controversy[123, 117, 124, 125].

One of the implications of Schmidlin's work described above was that transient photoconductivity could have spectroscopic applications, in the sense that information concerning the density and capture or release parameters of the localised states could, in principle, be obtained from the time and temperature dependence of the transient excess current in the case of multiple trapping transport. Schmidlin showed that the ratio of trap to transport state densities can be determined from trap parameters, which in turn can be determined by fits to the experimental current traces using the formula

$$\frac{N_i}{N_v} = \text{const.}\ \nu_i^{\alpha-1} \exp\left[\frac{-(\alpha E_i - \Delta_i)}{kT}\right] \qquad (3.51)$$

where N_i/N_v is the ratio of the density of traps to the density of transport states, E_i is the energy difference between trap and transport states, Δ_i is a possible activation energy for a capture event and ν_i the attempt to escape frequency which is related to the capture coefficient C_i through microscopic reversibility. He pointed out that many features could complicate such an analysis, e.g., a distribution of ν_i if E_i = const, a distribution of E_i if ν_i = const,

a distribution of Δ_i, or a combination of all three.

Despite these complications attention has turned in recent years towards the possibility of utilising the transient photoresponse characteristics in the identification of the energy distribution of localised states in these materials. A different but related technique to the time of flight, called transient photoconductivity (TP) has been used in these studies. In this technique the carriers are generated within a specimen fitted with coplanar electrodes[126, 127]. The current/time response for this TP configuration should be identical to the initial regime of the TOF experiment, provided that only one type of carrier is mobile and that effects associated with transport close to the surface in coplanar cells are not important. The mechanism of trap-limited band transport is assumed to take place in those materials for which an identification of localised state distributions have been attempted by Tiedje and Rose[115, 128] and Orenstein and Kastner[126, 127] (the Tiedje/Rose analysis). These investigators further assumed the presence of an exponential distribution of trapping centres; having demonstrated that this yields a power law decay with time, as observed (approximately) in various experimental studies. Results typical of these experiments are shown in figure 3.11.

The thermalisation, involved in this process, causes a progressive decrease in the density of free carriers, and thus of transient current. An "intuitive thermalisation" model, has been introduced in the Tiedje/Rose analysis of TP. This model concerns the

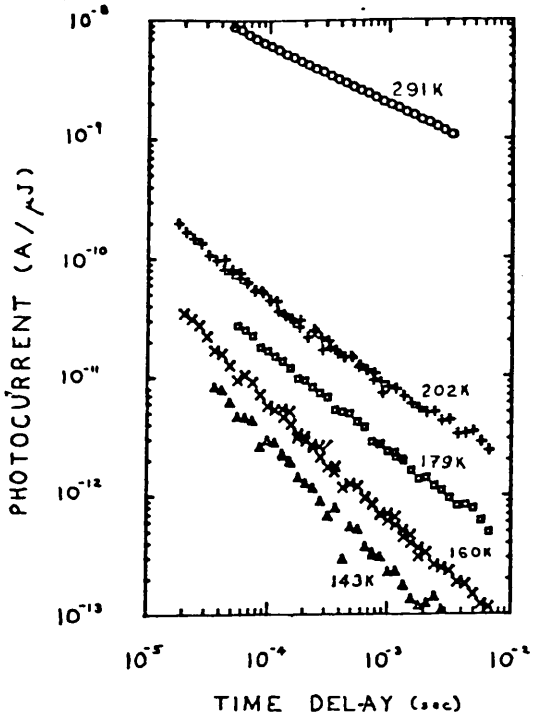

Figure 3.11(a)
Results from the work of Orenstein and Kastner [127], showing that the decay of the photocurrent in As_2Se_3 obeys a power law.

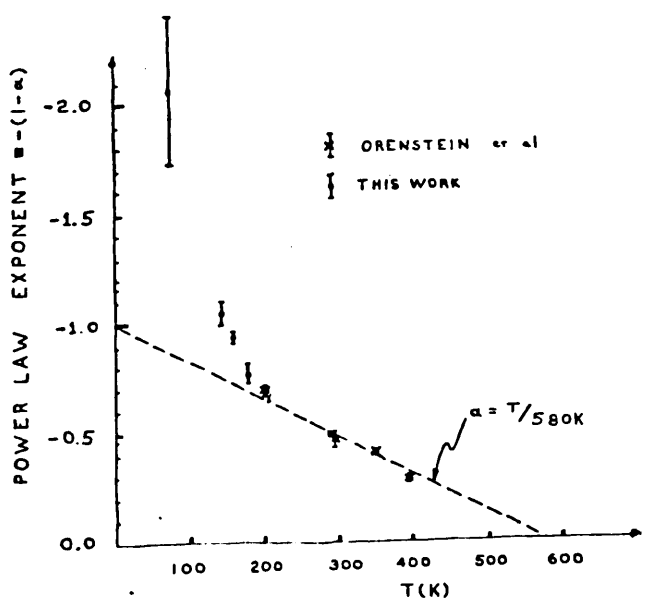

Figure 3.11(b)
Results taken from the same reference showing the variation in power law exponent with temperature.

introduction of a thermalisation energy E_D separating "shallow " from "deep" traps situated at energy E_A. The occupancies of the two types of centres are envisaged as being determined by radically different considerations. The energy E_d, measured relative to E_A, is specified by the criterion that a trap of this depth has a release time constant equal to the total elapsed time since the creation of the excess carriers, i.e.,

$$t = \nu^{-1} \exp(E_D/kT) \tag{3.52}$$

giving

$$E_D = kT \ln \nu t \tag{3.53}$$

They argue that trapping centres with release energy less than E_D have had sufficient time to <u>both</u> trap and release carriers, and thus should attain an occupancy in quasi-thermal equilibrium with the extended states. On the other hand, deeper-lying centres are envisaged as being populated purely in terms of trapping kinetics, since insufficient time has occurred for appreciable release to occur. Thus, under the assumption of an energy-independent capture cross section, such deep traps are seen as containing numbers of excess carriers in linear proportion to their density $N_t(E)$.

This model has been criticised by Marshall and Main[129], who demonstrate that the thermalisation process is a complicated function of trapping and release time constants, and that the influence of deep traps can prevent the establishment of quasi-thermal equilibrium for shallow centres. It is also demonstrated that the model will yield

erroneous results for the energy distribution of localised states in the general case.

Apart from this criticism of the thermalisation process involved in the above analysis, it has been shown[129], that other distributions of localised states in the gap can also lead to a linear dependence of α upon temperature. In a recent paper, [129]Monte Carlo simulation techniques were employed to study various energy distributions of localised states shown in figure 3.9. For each of the four distributions studied, α was shown to vary linearly with temperature in the low temperature regime. This clearly showed that such behaviour does not constitute evidence for a particular (e.g exponential) energy distribution of traps. They found α_2 to be more sensitive than α_1 to the changes in distributions (see figure 3.12 for an exponential distribution and a "skewed" gaussian distribution), and that comparison between experimental and simulated data suggest a comparatively structured distribution of trapping centres in those amorphous semiconductors for which α_1 and α_2 data are presently available.

A more accurate analysis which allows spectroscopic examination of transient photodecays that deviate from power law behaviour (observed in many cases, e.g. refs.[126, 59 and 130]), has been given by Michiel et al[131]. In this paper the authors examine the intimate relationship that exists between the time dependent current, I(t), and the statistical parameter, $\psi(t)$. For the case of trap-limited band motion, the following relationship exists,

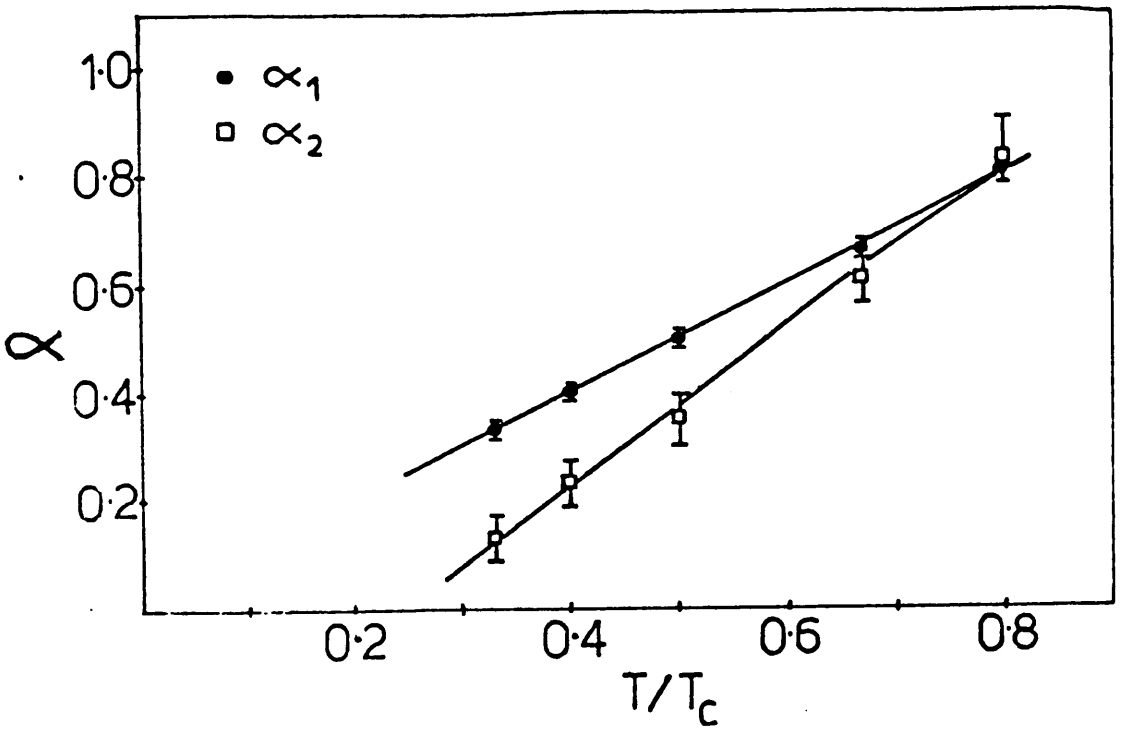

Figure 3.12(a)
Temperature dependence of dispersion parameters for the exponential-tail distribution of localised states.

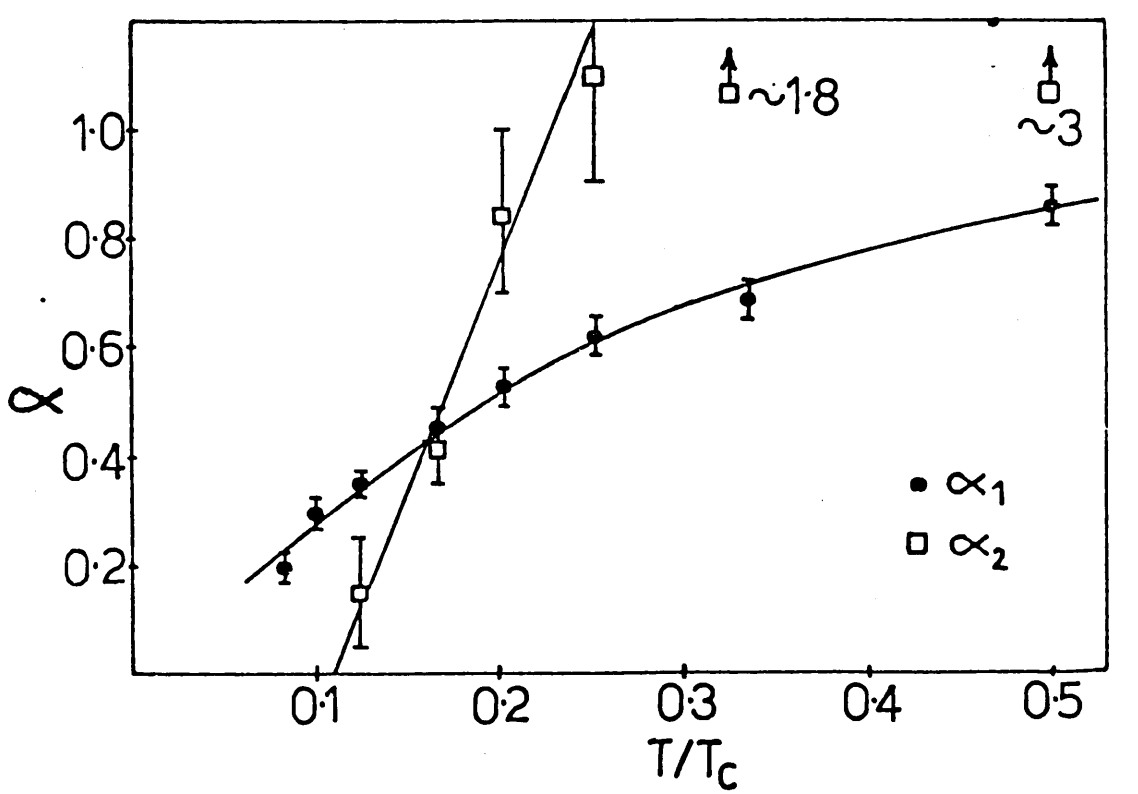

Figure 3.12(b)
Same plot as in (a) for a 'skewed' gaussian, $E\exp[-(E/kT_c)^2]$, distribution of localised states. (From the same reference as fig 3.9)

$$\psi(t) = \int_{\substack{\text{all} \\ \text{Traps}}} \left(N(E)/N_o\right) p(E)\, dE$$

where $(N(E)/N_o)dE$ is the fraction of localised states within the energy range dE, and $p(E)$ is the release probability function,

$$p(E) = \lambda(E) \exp\left(-\lambda(E)t\right)$$

The authors demonstrate that I(t) is related to the energy distribution of localised states, through the waiting-time distribution function $\psi(t)$ and that this relationship which involves a Volterra equation of the first kind, may be solved numerically.

The $\psi(t)$ is also related to the relative density of states N(E) via a Friedholm equation of the first kind, whose solution becomes straight forward using an approximation which should not introduce more than a small degree of distortion. Michiel et al consider all centres at depth E_t to release trapped carriers after a dwell time exactly equal to the release time constant $\lambda^{-1} = \nu^{-1} \exp(E_t/kT)$. This assumption is identical to that made by Tiedje/Rose, but does not in this case carry any identification of a 'demarcation energy'. Using this assumption it is possible to show that,

$$N_t(E_t) = (N_o/kT)\psi(t).t \qquad (3.54)$$

which can be readily computed. As in the case of the Tiedje/Rose

analysis, the introduction of the simplifying assumption results in a blurring of the computed distribution of localised states over a range of energy $\pm$ kT. In amorphous semiconductors, it is anticipated that disorder effects will usually be such that any localised states will be spread out over a range well in excess of kT, so that distortion introduced by the approximation should be acceptable.

The validity of the above technique has been demonstrated by its application to transient current data generated for known trap distributions by Monte Carlo techniques[131]. Figure 3.13 demonstrates the results of its application to the case of three discrete sets of localised states. In addition to the broadening effect noted above, there are some minor distortions of the distribution, which are associated with the limitations of the numerical techniques employed for the solution of the Volterra equation. The technique has been applied to a-As_2Se_3; for which material the data suggest a feature in the density of states at about 0.45 eV[132]. It has also been employed in the analysis of transient photoconductivity data for As_2Se_3 crystals, in which disorder has been induced by bombardment with high energy electrons. Here, the measurements clearly indicate the presence of specific energy features in the density of states distribution[133].

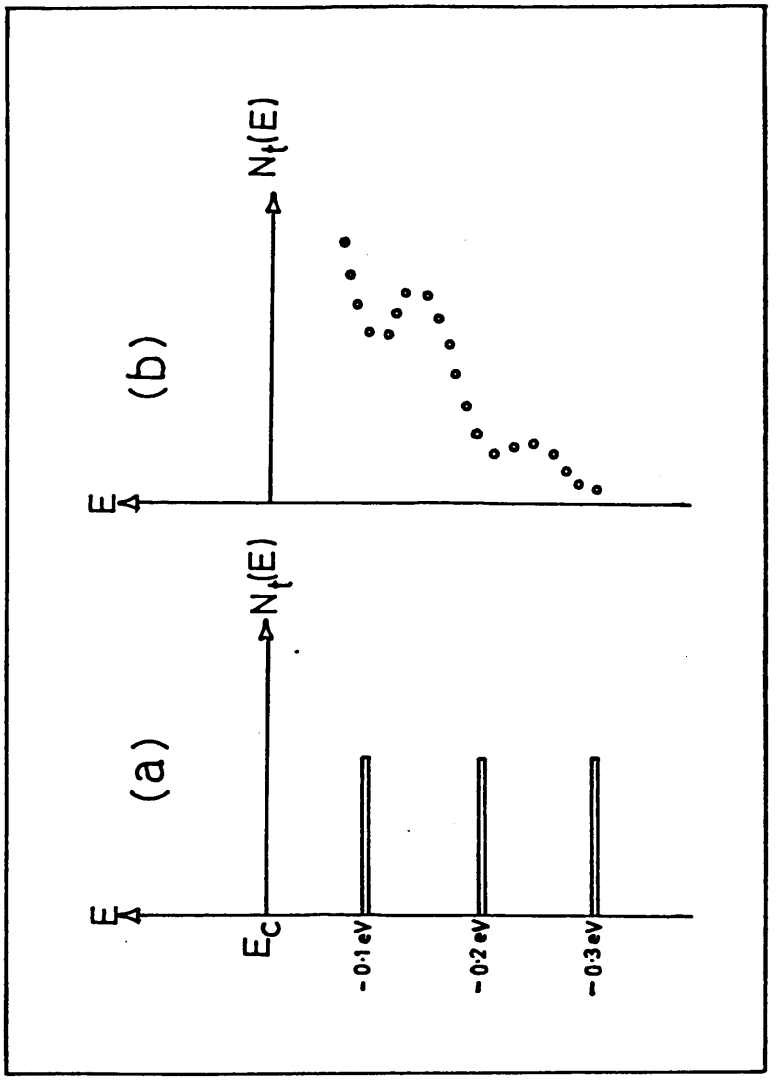

Figure 3.13

Comparison of the actual (a) and calculated (b) distributions of localised states for the case of three discrete sets of traps. The computed distribution was evaluated by applying the thermalisation concept of Tiedje/Rose to data obtained by Monte Carlo simulation of the response of the actual system. (After Marshall and Main ref [129]).

Chapter 4

COMPUTER SIMULATION STUDY OF AMORPHOUS SEMICONDUCTORS

As discussed in chapter 3, the density of localised electronic states is of considerable interest in the exploration of the electronic properties of amorphous semiconductors. Despite this there is a lack of straightforward methods for spectroscopic interpretation of dispersive transient photodecay data. Of the techniques available the Tiedje/Rose approach, based on the concept of a thermalisation energy, has been subject to controversy [129]. The more accurate analysis given by Michiel et al [132] is not very practical owing to the considerable complexity of solving an integral equation, and further refinements such as the inclusion of recombination, are quite unrealistic for the same reason. A simpler way of solving the problem would therefore be most useful. In this particular study a multilevel analogue solution of thermalisation was developed and is presented below.

4.1 Multilevel Analogue Solution

The system shown in figure 4.1 is the electrical analogue of the conduction band with trapping levels $N_t(1)$, $N_t(2)$ and $N_t(n)$ shown in figure 4.2. The model assumes that unipolar (electron) transport occurs via extended states at a specific energy (the mobility edge), and is intermittently interrupted by trapping/release events involving the localised states. The charge Qo stored in capacitor C represents the total number of electrons entering the conduction band as switch S is closed. The rate of change of charge with time for the first, second and nth component of the analogue model can be written as

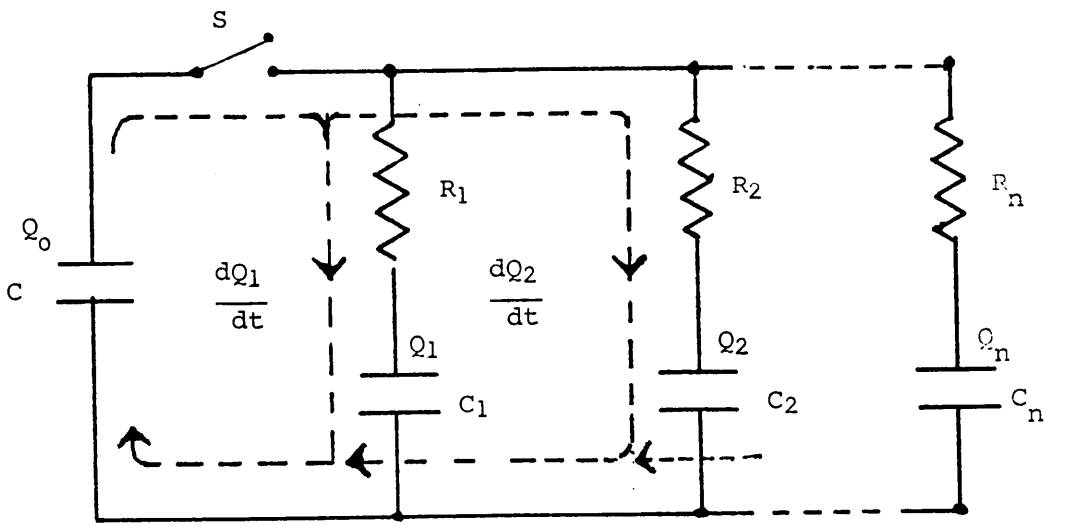

Fig. 4.1

Electrical analogue of the conduction band with trapping levels $N_t(1)$, $N_t(2)$ and $N_t(n)$ shown in figure 4.2a. Each RC network represents a specific discrete trapping level. The following differential equations are appropriate.

$$\frac{dQ_1}{dt} = \frac{Q_o}{CR_1} - \frac{Q_1}{C_1R_1} \qquad \frac{dQ_2}{dt} = \frac{Q_o}{CR_2} - \frac{Q_2}{C_2R_2}$$

$$\frac{dQ_n}{dt} = \frac{Q_o}{CR_n} - \frac{Q_n}{R_nC_n}$$

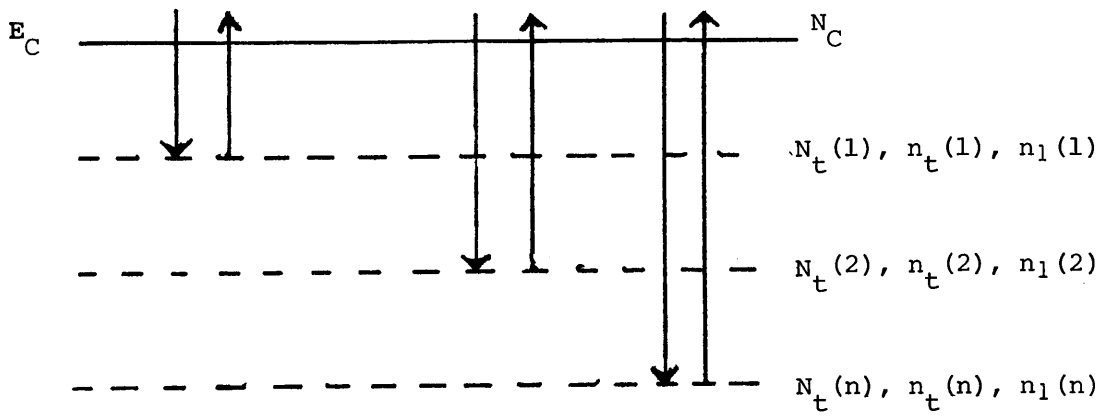

Figure 4.2a

Discrete trapping model used in the simulation study as described in the text. $N_t(n)$ represents the nth trap level, $n_t(n)$ the trapped electron density at E_n and $n_1(n)$ the 'emission density'.

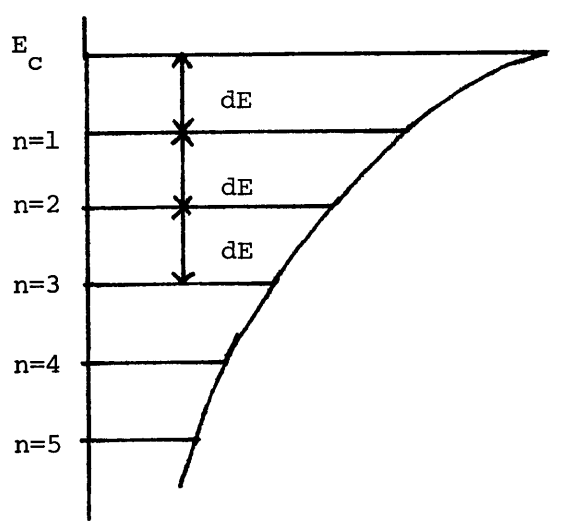

Figure 4.2b

Simulation model of an exponential tail. The continuous distribution is split into a set of n discrete levels, spaced dE apart.

follows (see figure 4.1)

$$\frac{d\varphi}{dt} = \frac{\varphi_0}{CR_1} - \frac{\varphi_1}{C_1R_1} \qquad \frac{d\varphi_2}{dt} = \frac{\varphi_0}{CR_2} - \frac{\varphi_2}{C_2R_2}$$

$$\Rightarrow \frac{d\varphi_n}{dt} = \frac{\varphi_0}{CR_n} - \frac{\varphi_n}{C_nR_n} = \frac{\varphi_0}{\tau_{tn}} - \frac{\varphi_n}{\tau_{rn}} \qquad (4.1)$$

Similarly the expression for the nth level of the physical model can be expressed as

$$\frac{dn}{dt} = -nC_{tn}N_{tn} + n_{tn}C_{tn}n_{1n}$$

$$= \frac{n}{\tau_{tn}} + \frac{n_{tn}}{\tau_{rn}} \qquad (4.2)$$

with the nomenclature being as indicated in figures 4.1 and 4.2. The capture coefficient for the nth level is defined as $C_t(n)$ and $n_1(n)$ the 'emission density' is given by

$$n_1(n) = N_c \exp \frac{-(E_c - E_n)}{kT} \qquad (4.3)$$

From these equations it can be seen that the following relations between the physical and the analogue parameters exist.

$$\text{TRAPPING} \quad \tau_{tn} = R_nC = 1 \Big/ C_{tn}.N_t(n)$$

$$\text{RELEASE} \quad \tau_{rn} = R_nC_n = 1/C_{tn}.n_1(n) \qquad (4.4)$$

If capacitance C is set =1, which is arbitrarily allowed for the conduction band then

$$R_n = \frac{1}{C_{tn}N_{tn}} \qquad C_n = \frac{1}{n_1(n)} \qquad (4.5)$$

4.1.1 R.C. Analogue for an Exponential Tail

A consequence of the above idea is that different model

distributions can readily be generated. For example the density of states for a continuous exponential distribution of states (which is often assumed to occur as a fundamental consequence of disorder in a specimen film) can be written as

$$g(E) = N_o \exp\left[\frac{-(E_c - E)}{kT_c}\right] \quad cm^{-3}\,eV^{-1} \tag{4.6}$$

where T_c is the characteristic tail temperature. If follows from this equation that since $g(E_c) \sim N_c/kT$ then $N_o \sim N_c/kT$.

4.1.2 Discrete Levels

The distribution can be approximated with discrete levels dE apart in energy units of kT (i.e. 0.025eV at room temperature). This method is not unique and has been used before in representing model densities of states[134, 119]. At the nth level the approximate density is given by

$$N_t(n) = dE \cdot g(n.dE)$$

$$= \frac{N_c}{kT} . dE \exp -\left[\frac{n.dE}{kT_c}\right] \tag{4.7}$$

The conduction band density can now be set to N_c=1 for computational convenience. Equations (4.3) and (4.7) can be substituted into equation (4.5) to obtain the following expressions for R_n and C_n,

$$R_n = \frac{kT}{C_{tn}.dE} \exp\left[\frac{n\,dE}{kT_c}\right]$$

$$C_n = \frac{\frac{dE}{kT}\exp -\left[\frac{n dE}{kT_c}\right]}{\exp -(n dE/kT)} = \frac{dE}{kT}\exp\left[n.dE\left(\frac{1}{T}-\frac{1}{T_c}\right)\right] \quad (4.8)$$

It is now convenient to make the <u>total</u> trapping time into the distribution equal to one unit. This is achieved as follows. The trapping time for the nth level can be written

$$\tau_{tn} = R_n C = 1/C_{tn}.N_t(n)$$

and the total trapping time

$$\tau_t = [\Sigma_j 1/\tau_{tj}]^{-1} = [1/R_j]^{-1}$$
$$= [\Sigma_j C_{tj} N_t(j)]^{-1}$$

and if the capture cross section C_{tn} is taken to be be the same for each level $C_{tn}=C_t$ then

$$\tau_t = 1/C_t \Sigma_j N_t(j) = 1$$

by choice so $C_t=1/\ N_t(j)$. Thus now one can write $R_n=1/C_tN_t(n)$ and therefore

$$R_n = \Sigma_j \frac{N_t(j)}{N_t(n)} \quad (4.9)$$

Expression (4.9) applies for an arbitrary distribution if the capture coefficient is fixed and ensures a total trapping time equal to one unit. For an exponential tail this gives,

$$R_n = \frac{\Sigma_j \frac{dE}{kT} \exp -\frac{j\,dE}{T_c}}{\frac{dE}{kT} \exp -\frac{n\,dE}{kT_c}} = \frac{\Sigma_j \exp -\frac{j\,dE}{T_c}}{\exp -\frac{n\,dE}{kT_c}} \qquad (4.10)$$

4.1.3 Other Distributions of Localised States

The above procedure can be applied to other distributions of localised states, e.g., a RECTANGULAR distribution. The density of states can again be split up into discrete levels as shown in figure 4.3. Thus, as before, $N_t(E)=dE.g(E)$ and for this particular distribution $g(E)=G(\text{const})$ and energy depth $E=E_x+ndE$. For ease of calculation it is necessary to ensure a given ratio of [total trap density]$/N_c$ i.e., $\Sigma N_t(n)/N_c$ = const.b. Thus one can write $N_t(n)=de.G$ which is fixed for $E_x<E<E_y$ so $\Sigma_j\{de.G\}/N_c=b$ and for the total number of levels L,

$$\frac{L.dE.G}{N_c} = b \qquad (4.11)$$

giving $G=bN_c/L.dE$. For any other distribution a characteristic constant must be found in this way by using $\Sigma N_t(j)/N_c=b$.

As before the general expression (4.9) for the capacitance and the resistance can now be applied giving,

$$C_n = dE.G \,/\, N_c \exp\left[-\frac{(E_c-E)}{kT}\right]$$

$$\therefore \quad C_n = \frac{b}{L} \exp\left(\frac{E_1+ndE}{kT}\right) \qquad (4.12)$$

and

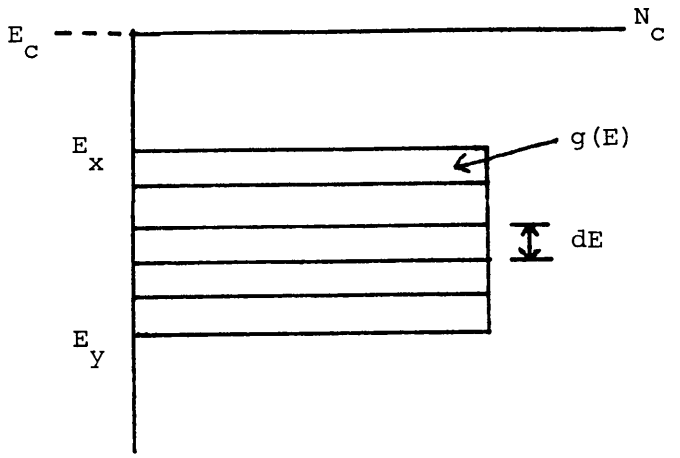

Figure 4.3
Model of rectangular localised state distribution used in the simulation study.

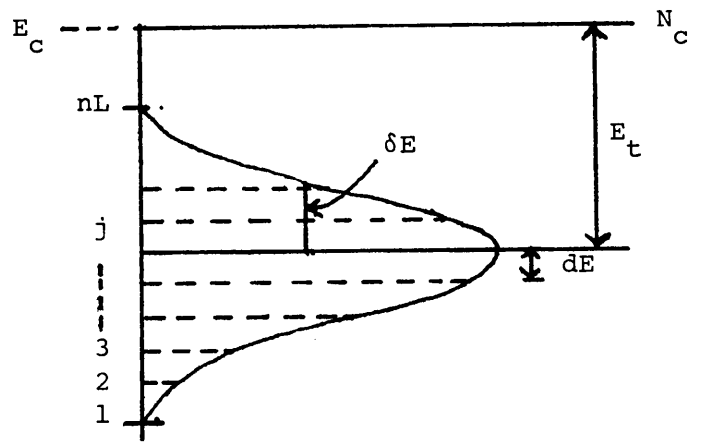

Figure 4.4
Gaussian distribution of localised-states, as employed in the simulation study. E_t represents the energy depth of the gaussian and δE the characteristic energy.

$$R_n = \frac{b\,N_c}{N_t(n)} \tag{4.13}$$

again by setting τ_t=1 and N_c= 1. It can be seen from expression (4.13) that R_n=L since $N_t(n)$=dE.G = bN_c/L.

For the GAUSSIAN distribution shown in figure 4.4 an expression for the density of states is

$$g(E) = G \exp\left[-\{(E-E_o)/\delta E\}^2\right] \tag{4.14}$$

and $N_t(j)$=g(E)xdE

If the total trap density equals $b.N_c$ as for the rectangular case then $\Sigma N_t(j)=b.N_c=b$. Therefore

$$G = \frac{b}{\sum_{j=1}^{nL} \exp\left[-\left(\frac{E-E_o}{\delta E}\right)^2\right] dE} \tag{4.15}$$

and since energy E_o at the centre of the distribution equals (nL/2).dE, E in this case is given by $E=\{E_o-[n.dE/2] + jdE\}$ leading to the expression

$$G = \frac{b}{\sum_{j=1}^{nL} \exp\left[-\left(\frac{jdE - n/2\,dE}{\delta E}\right)^2\right]} \tag{4.16}$$

It is now possible to obtain an expression for the nth level density, e.g.,

$$N_t(j) = G \exp\left[-\left(\frac{j dE - n/2\, dE}{\delta E}\right)^2\right] \qquad (4.17)$$

Similarly the general emission equation (4.3) in this case can be expressed in the form

$$n_1(E) = N_c \exp\left\{-\left[E_c - E_o + (j - nL/2)dE\right]\right\} \qquad (4.18)$$

if $E_c - E_o$ is in the same energy units as dE (in this case units of kT). Again from $N_t(n)$ and $n_1(n)$ it is easy to obtain expressions for R_n and C_n.

4.1.4 Methods Used To Solve the Differential Equations

The differential equations (4.1) were solved in the first instance using a fourth-order Runge-Kutta method. This method is widely used in computer solutions to differential equations[135].

Solutions of the differential equations for each component of the model were obtained for a step-length (time increment) h. From these solutions the change in charge Q after time h can be calculated since

$$Q(t+h) = Q(t) + \frac{h}{6}\left(D_1 + 2D_2 + 2D_3 + D_4\right)$$

where

$$D_1 = f(t_o, Q_o)$$

$$D_2 = f(t + 0.5h, Q + 0.5h D_1)$$

$$D_3 = f(t + 0.5h, Q + 0.5h D_2)$$

$$D_4 = f(t + h, Q + h D_3)$$

with t_o and Q_o being the initial starting parameters. The charge Q(t+h) can therefore be computed step by step for a number of time-steps X (see appendix 1), giving the variation of Q with time (t=Xh)).

While running the program the step-length was set to 0.5τ, half the trapping time constant of the model system. This meant that Q(t+h) had to be calculated for $2x10^6$ steplengths in order to obtain a charge decay down to $1x10^6\tau$ (i.e. the equations (4.1) had to be solved $2x10^6$ times in the program). This used up a great deal of computer time, on the DEC20 computer, and methods of decreasing the computational time were investigated. This revealed that increasing h from 0.5τ to 1.0τ after t=100 and from 1.0τ to 2.0τ after t=1,000 gave the most stable solution and there was no loss in accuracy when calculating Q(t+h). Despite this, programs took on average two hours to run.

A faster method, with similar accuracy to that of the Runge-Kutta, was applied to the model of figure 4.2 during the course of the study by Dr C. Main[136]. The rate equations were set up as previously and a time stepping procedure was also used i.e., in short time δt, changes δn and $\delta n_t(j)$ are:

$$\delta n = - \Sigma_n C_n(j) N_t(j) \delta t + \Sigma n_1(j) C_n(j) n_t(j) \delta t \qquad (4.19)$$

and

$$\delta n_t(1) = nC_n(j)N_t(j)\delta t - n_1(j)C_n(j)n_t(j)\delta t \quad (4.20)$$

so for step i to step i+1

$$n^{i+1} = n^i + \delta n$$

and $$n_t^{i+1} = n_t^i(j) + \delta n_t(j)$$

The expressions (4.19) and (4.20) can be written in transition matrix form as follows $[n^{i+1}] = [A][n^i]$ where [A] is an (nL+1)x(nL+1) matrix called a stochastic matrix. Once the transition probabilities have been set up in matrix form a multiple stepping method can be applied since

$$[n^{i+2}] = [A][n^{i+1}] = [A][A][n^i]$$

which can be written

$$[n^i] = [A]^i[n^o]$$

where $[A]^i$ is the i^{th} power of matrix [A]. This implies rapid generation of very long time steps by successive squaring. i.e

$$[B] = [A]^2$$

$$[C] = [B]^2 = [A]^4$$

$$[D] = [C]^2 = [A]^8$$

This procedure thus produces a doubling in the time interval for each squaring i.e. in terms of step t we get a sequence

$$1,2,4,8,16 \text{ --------- } 2^i$$

Therefore after twenty squarings 10^6 step lengths are obtained. If δt

< 1, then continued squaring of [A] leads to a 'stationary' solution corresponding to $t=\infty$ where Boltzman statistics will prevail, no matter what the initial conditions are! In practice small truncation errors will propagate and instability eventually results (even for $\delta \ll 1$) eg, for 9 figure precision, instability starts at approximately 30 squarings (approx. 10^9 steps). Results obtained from the computer simulation studies will be presented in the next section.

4.2 Computer Simulations:-Results and Discussion

As discussed in section 4.1, thermalisation in a model distribution of states can easily be examined in terms of computer simulations. To illustrate the usefulness of the method and to demonstrate it's consistency, differential equations were generated for a system of discrete levels (i) with exponentially decreasing N_i, spread 0.025eV apart, with a characteristic tailing temperature T_c=600K (this is the tailing parameter estimated from fitting power-laws to the photocurrent decay data obtained from the vitreous sample (see section 6.4; Orenstein and Kastner obtained a value T_c=580K)[137].

According to dispersive transport theory, carrier interaction in an exponential tail, should yield a pre-transit current and a band occupation function as follows

$$I(t) \sim n_o(t) \sim t^{-(1-\alpha)}$$

where $\alpha=T/T_c$. Figure 4.5 shows the simulation data calculated at four different temperatures. The initial rapid decay represents the trapping time, one time unit in this simulation, into the exponential

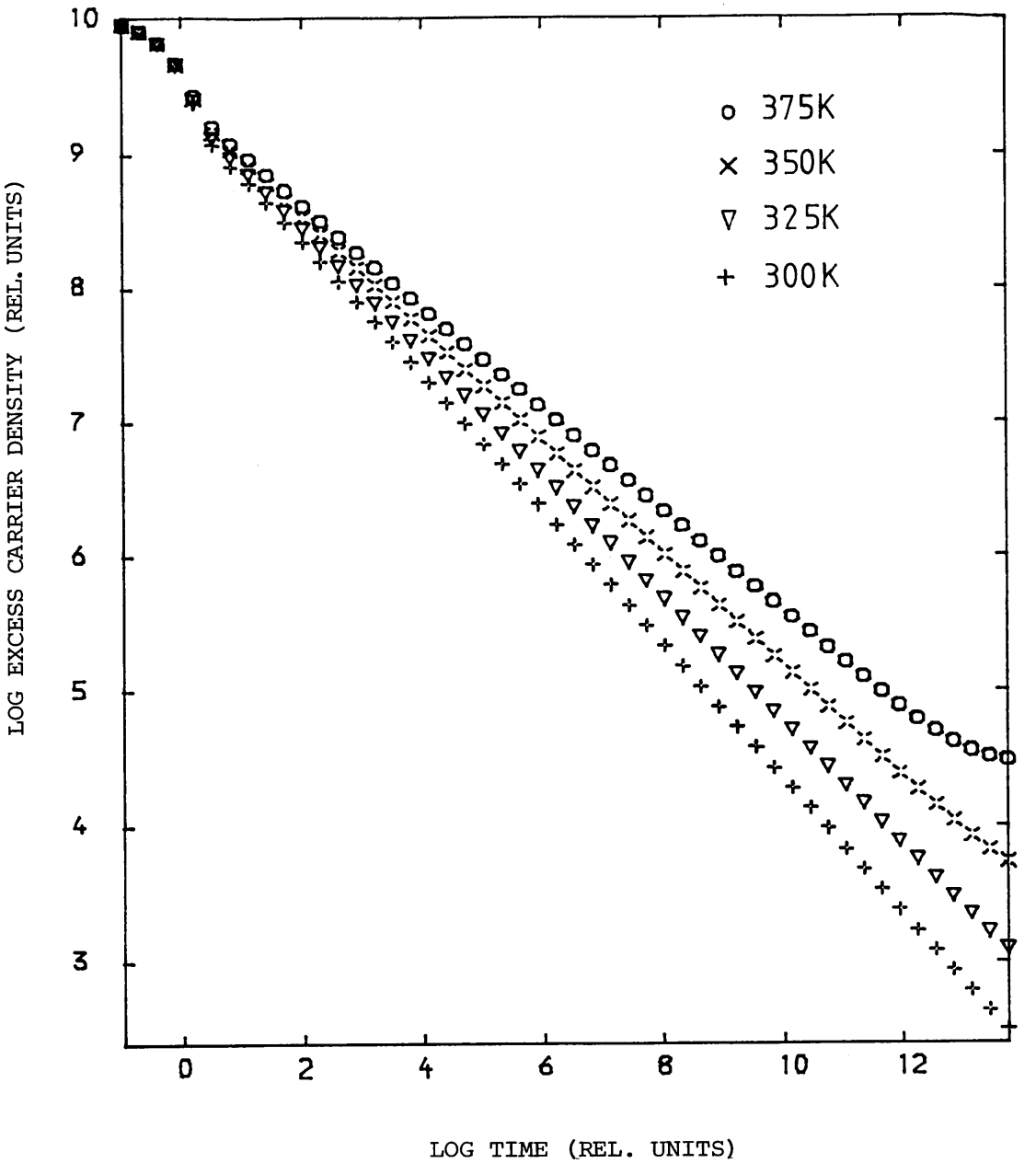

Figure 4.5

Computed transient photodecay for the exponential tail of localised states shown in figure 4.2, at four different temperatures. T_c = 600K; dE = 1 kT (0.025 eV).

density of states before thermalisation occurs, evidenced by the power law behaviour that ensues. A value of α was calculated for each temperature using $\alpha = T/T_c$ and a value also calculated by fitting a power law to the data. Figure 4.6 shows that good agreement is obtained when comparing α calculated using the two methods (an almost exact match).

It was found that increasing the resolution,i.e., decreasing dE (dE<0.025eV), did not alter the results. In fact when the energy step was increased to 0.05eV no significant change in the power law decay occurred. Only on increasing the energy step further to 0.1eV (i.e. 10 energy segments in a 1.0eV deep tail) did the effects of using discrete levels become observable. The decay in this case appears as a sum of 10 exponentials spaced 0.1 eV apart, as shown in figure 4.7, but despite this a power-law can be fitted to the data giving little variation from the predicted value of α expected from anomalously dispersive transport theory. Thus these simulation results show that a continuous distribution of localised states can be represented by discrete levels.

For the simulation of carrier motion at the mobility edge periodically interrupted by trapping events in a gaussian distribution of localised states, figures 4.8, 4.9 and 4.10 are representative of the results obtained. For the results shown in figure 4.8 the following parameters were used. The gaussian was split up into forty discrete levels, each 0.2 kT apart, representing a total spread of 8 kT. The characteristic gaussian energy was set at 2kT, with the total

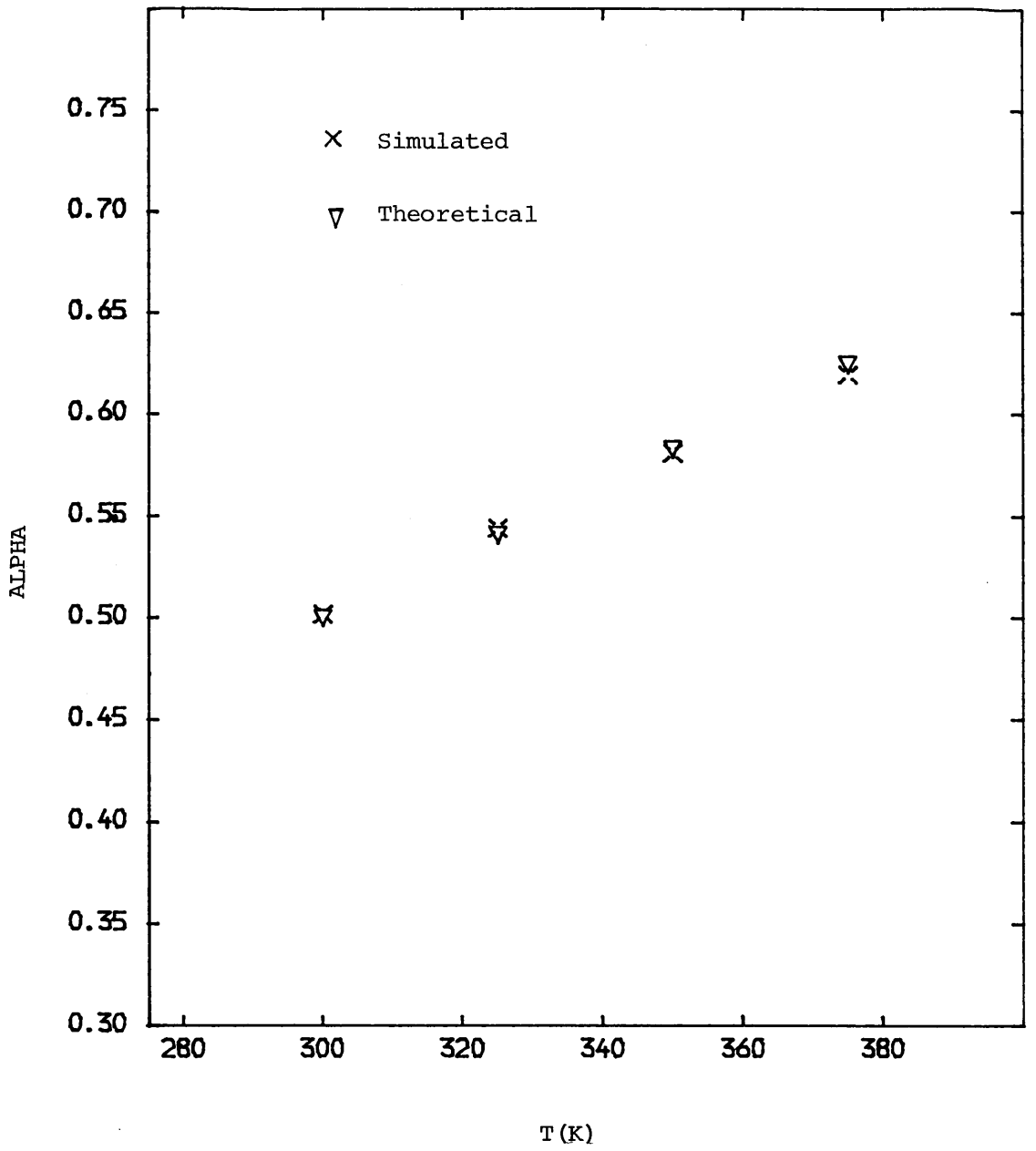

Figure 4.6

Comparison of the variation of the dispersion parameter α with temperature, calculated both theoretically and from fitting the power law $-(1-\alpha)$ to the simulated photodecay as discussed in the text.

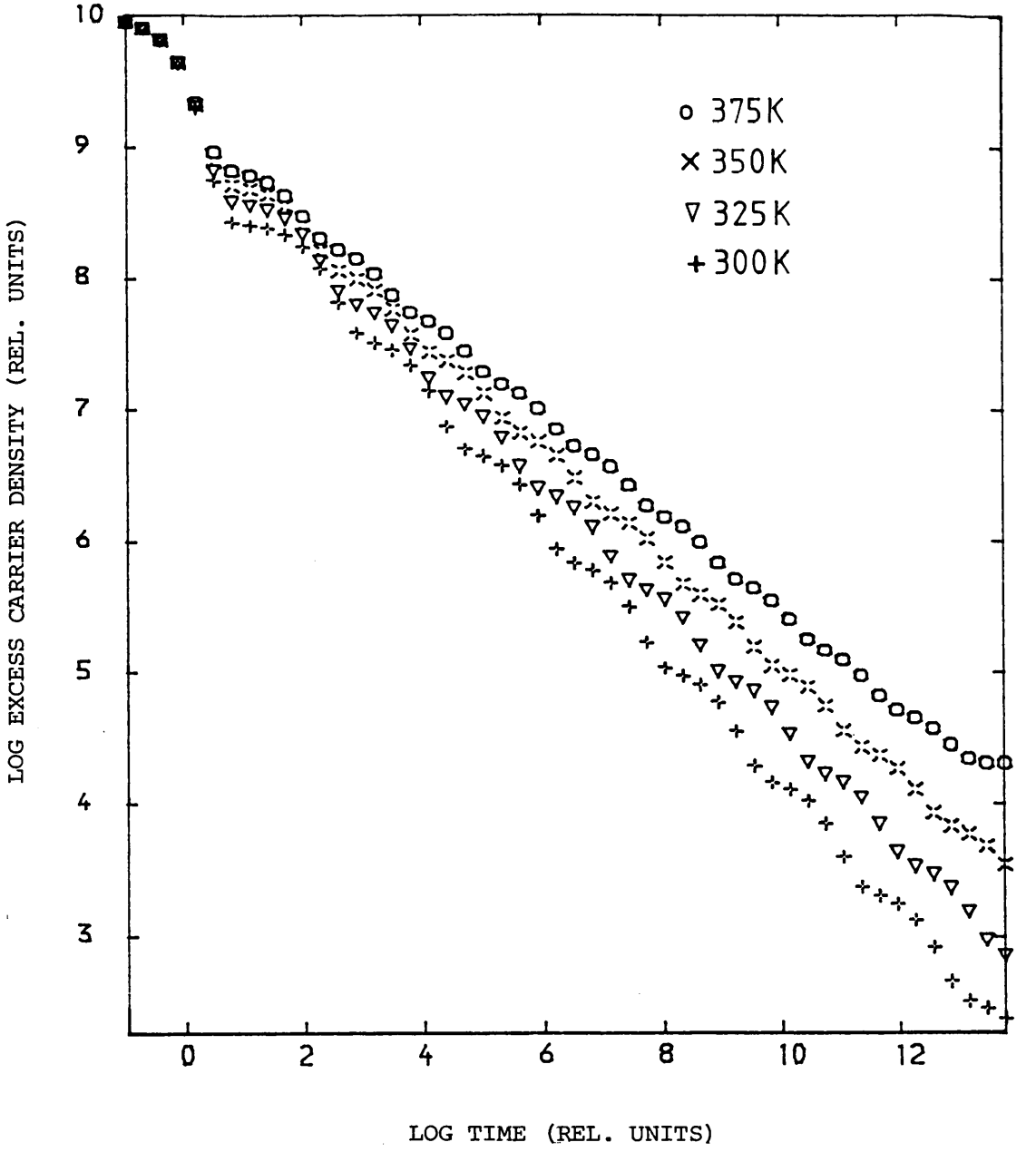

Figure 4.7

The effect of decreasing the resolution, i.e., increasing dE from 0.025 eV to 0.1 eV on the form of power law decay shown in figure 4.6

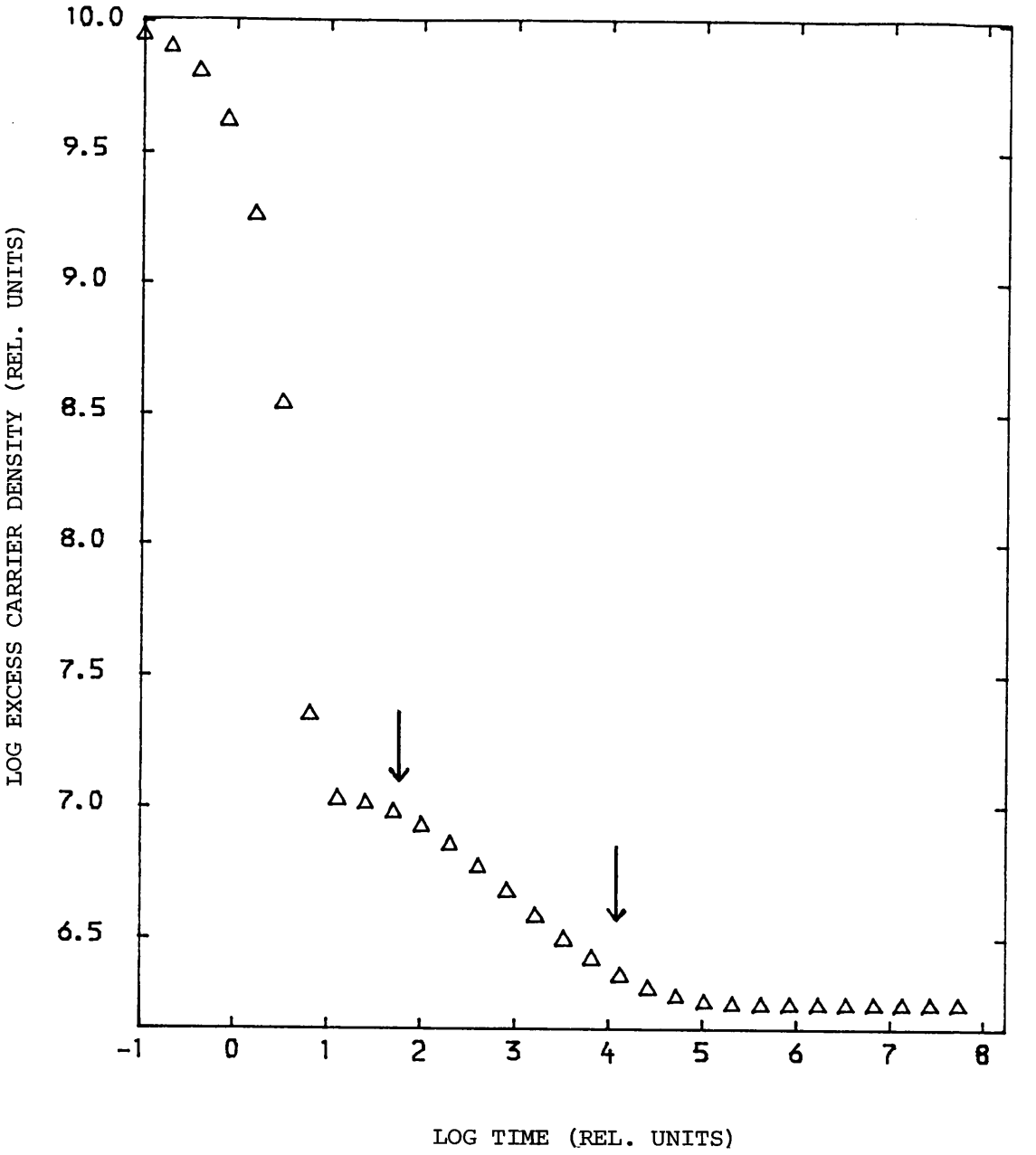

Figure 4.8

Computed transient photodecay for the gaussian distribution of localised states shown in figure 4.4. E_t = 10 kT; dE = 0.2 kT; δE = 2 kT; b = 0.1. The extent of the power law regime is arrowed as discussed in the text.

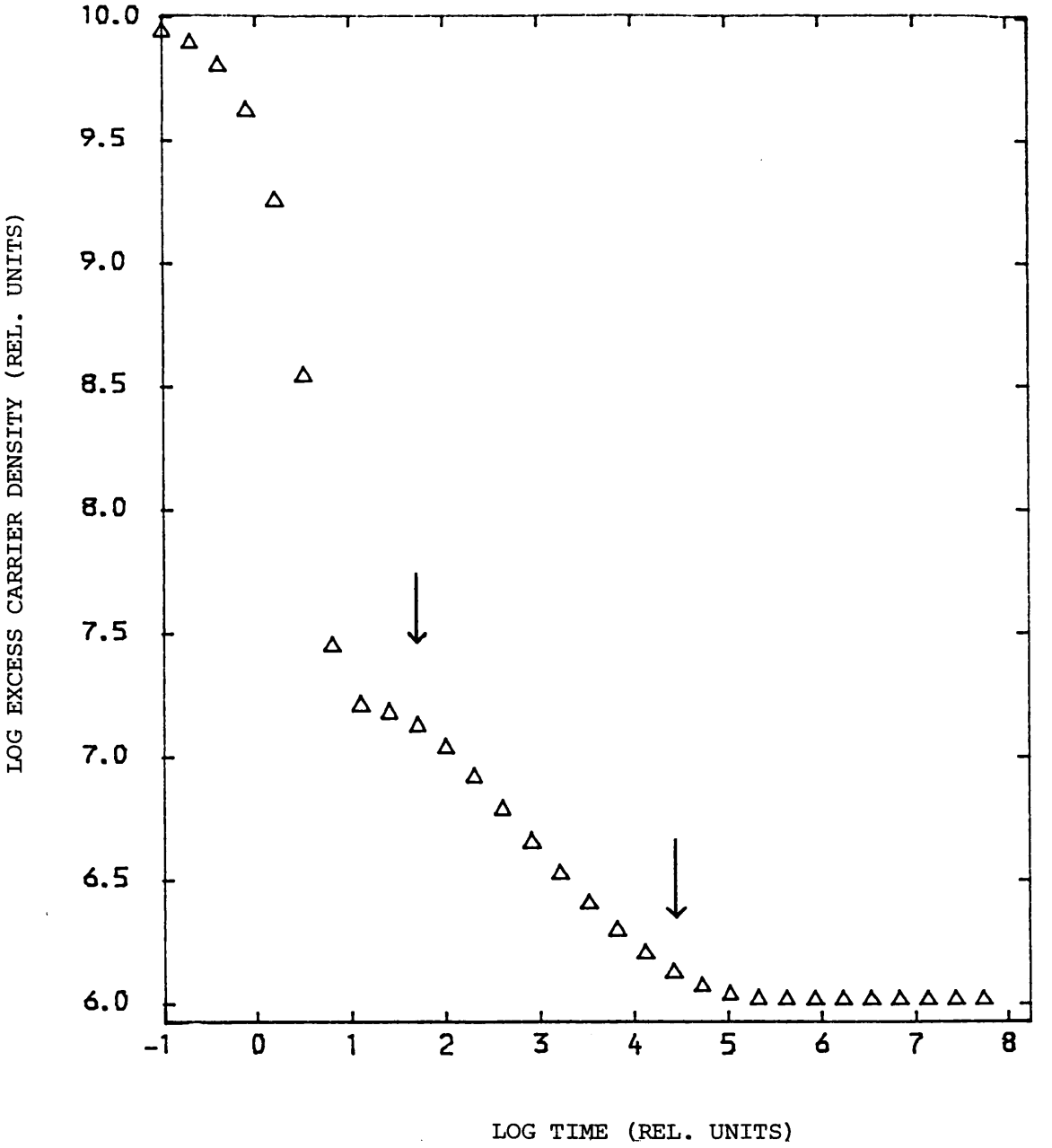

Figure 4.9

Same plot as figure 4.8 except $\delta E = 3$ kT. An increase in the extent of the power-law can be observed when comparing both figures.

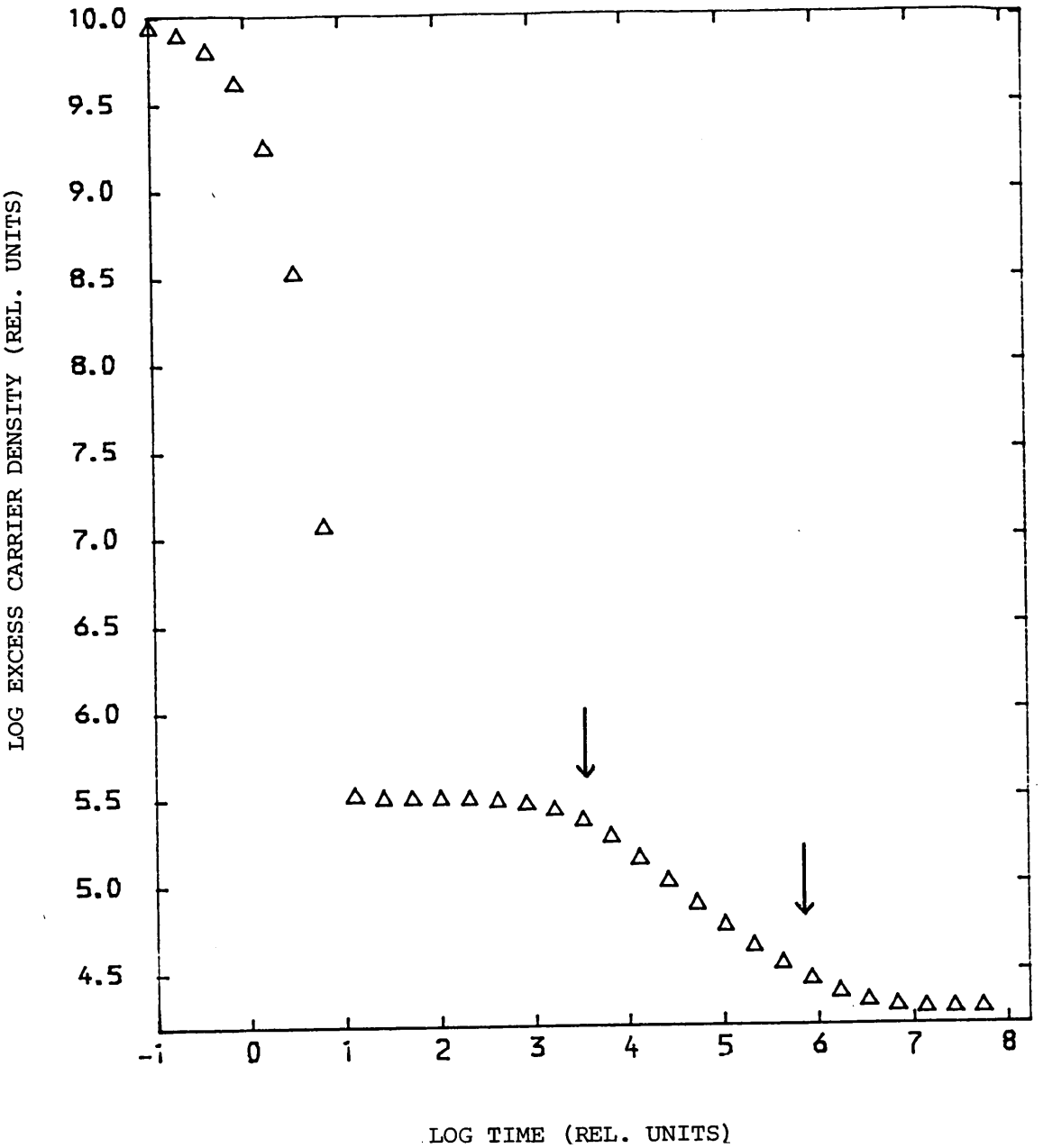

Figure 4.10

Same plot as figure 4.9 except E_t = 14 kT compared to 10 kT.

further check this parameter was set to 3kT(see figure 4.9), keeping the other parameters the same. Again rough agreement was obtained since from this figure $2\sigma E$ was calculated at 5.9kT.

Figure 4.10 shows the simulation results obtained from a gaussian distribution with the simulation parameters keep the same as above except the energy depth was changed from 10kT to 14kT (σE=3kT). From the figure it can be seen that the initial rapid decay is steeper dropping to a plateau in about 10 trapping time constants. The extent of the plateau region is larger, lasting about 1000 trapping units, before thermalisation occurs. The extent of the power-law in this 'thermalisation region' is is in rough agreement with a similar region observed in figure 4.9 for the gaussian centered around 10kT (this is expected since the energy depth was the only parameter changed).

From the central position of this power-law region, a change in energy depth can be calculated as previously for gaussians centered at 10kT and 14kT, and a change in energy depth of approximately 4kT was calculated in agreement with the expected shift.

It has thus been demonstrated in these two fundamentally simply distribution of states that a continuous distribution of states, be it exponential or gaussian can be represented by discrete energy levels.

The considerable simplification of the simulation model obtained by the use of discrete levels allows for the inclusion of features, such as, capture cross sections that vary with energy,

linear or monomolecular recombination etc. Since most calculations are essentially matrix manipulations, they may be easily and efficiently performed on a computer.

Another advantage is that simulation of model distributions of states incorporating two or three of the above distributions superimposed upon one another can be easily performed. In this particular study it was necessary to simulate such a model density in order to examine experimental results obtained from arsenic triselenide samples. Figure 4.11 shows the model density of states used. It consisted of an exponential tail, with an additional rectangular feature of total density (b) and energy breath ΔE superimposed on top of it. It is proposed that such a simulation would allow an examination of the influence of structure upon the transient photocurrent of the slowly decaying type encountered in the experimental study section 6.4 of this report.

Marshall and Street[112] have reported on the extent to which structure in the density of states may be detected from photodecay measurements. They computed the transient photocurrent using a somewhat different technique, that of Monte Carlo simulation, and show that a rectangular component of energy width kT must protrude from the background exponent tail by a factor of about 5 in density, in order to exert a readily detectable influence on the photodecay. They also assume that the capture cross-sections in the exponential and rectangular component are equal.

Using the matrix simulation method described in section 4.1,

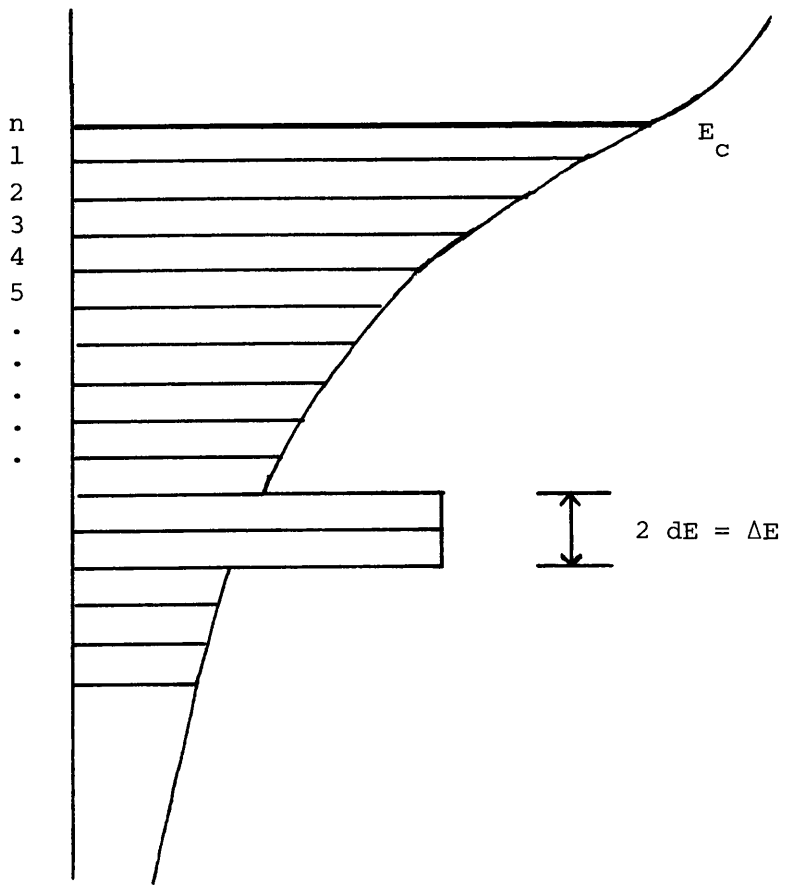

Figure 4.11

Model density of localised states consisting of an exponential tail, plus an additional sharp rectangular feature of total density (b) and energy breath ΔE. For this particular case ΔE was set to 2 dE (2 kT or 0.05 eV).

photodecays were obtained for such a model distribution of states. The computer program was arranged so that the density states at the feature (a width of 0.05eV was used, representing two discrete levels), could be varied compared to the background density of states. The energy depth of the feature was varied as required. Using this particular simulation method the current decay down to 10^{12} time units could be generated in less than one minute C.P.U time on the College's D.E.C. 20 computer.

Figure 4.12 shows the simulation results for the superimposed rectangular feature incorporated at an energy 0.45 eV, with a density of ten times the background level for four different temperatures. Looking at the figure, in the time range $2<t<10^4$, the transient decay deviates only slightly from the power-law form. However, even at these relatively short times there is some carrier interaction with the rectangular feature. At times $10^4<t<10^7$ the decay becomes more rapid, due to carrier interaction with the rectangular component. In the 'intermediate' time regime ($10^7<t<10^9$), the rate of decay decreases. Carriers have now reached some degree of quasi-thermal equilibrium with shallow centres in the exponential tail, and with the rectangular feature. Finally at times greater than 10^9 simulation units the decay regains the power law form expected for anomalously dispersive transport as thermalisation becomes dominated by states deeper than the rectangular feature in the exponential tail.

From the different temperature decay data shown in figure 4.12 some interesting features emerge. The curves follow the basic

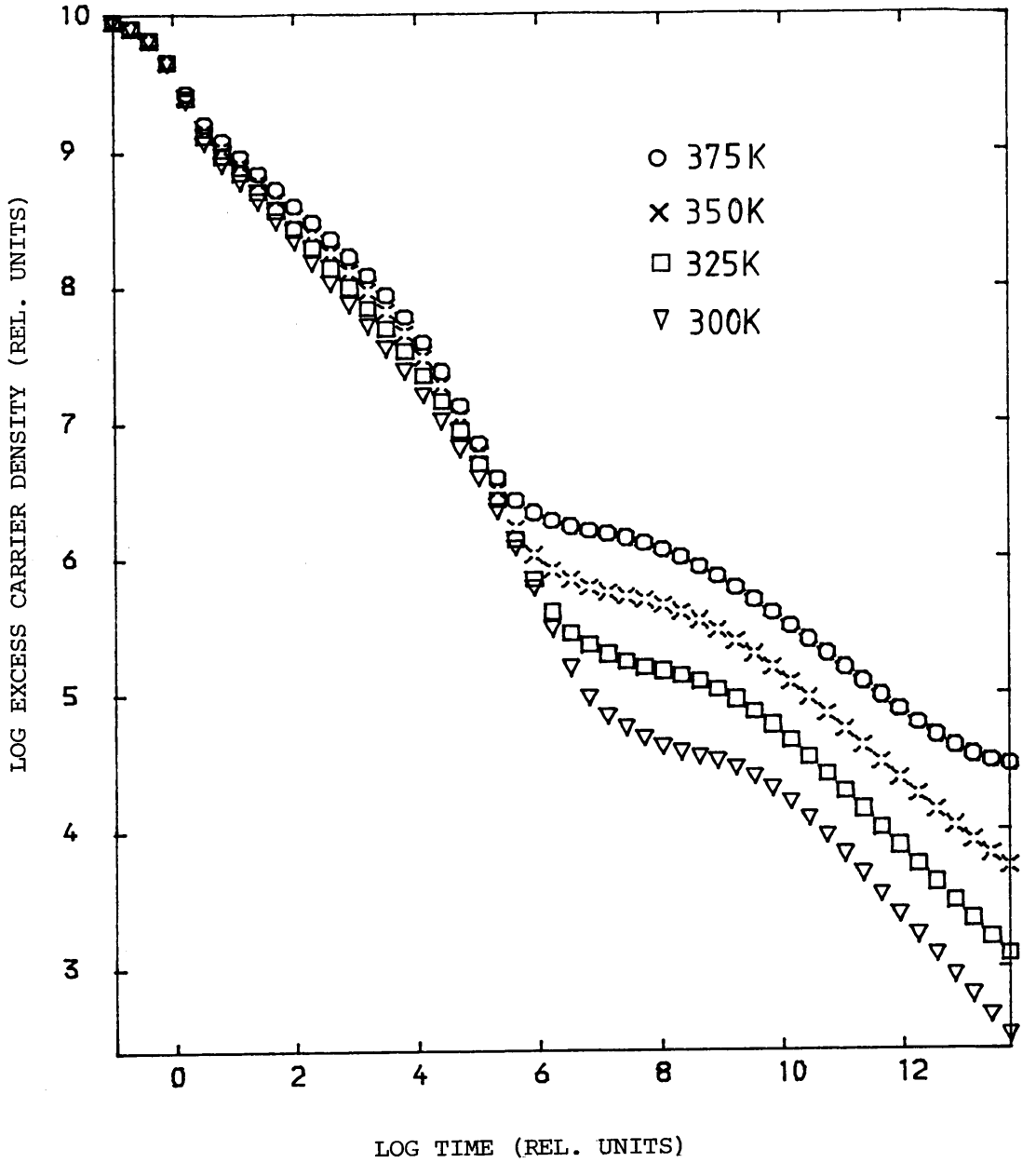

Figure 4.12

Computed transient photodecay at four different temperatures for the model shown in figure 4.11. The density of the feature being set at 10x the background. T_c = 600K; E_t = 0.45 eV; dE = 0.025 eV; ΔE = 0.05 eV.

trends described above, but it is noticeable in the time region, $10^4<t<10^6$ that the decay becomes more rapid at higher temperatures. This leads to a point in time, approximately 10^5 time units, where the the curves appear to merge. After this quasi-thermal equilibrium is reached with the rectangular feature. The onset of this region occurs at progressively longer times as the temperature is lowered. From the shift of the onset of this 'plateau' region with temperature an activation energy of 0.45eV was obtained using equation (4.21) in agreement with the energy depth of the rectangular feature.

On decreasing the relative density of the feature, from 10x to 6x to 3x the background density, the transient photodecay characteristics become less pronounced (see figures 4.13 and 4.14). The rate of decay in the regime, 10^4 to 10^6 time units, decreases and the time extent for which the carriers are in quasi-thermal equilibrium with the feature also decreases. One interesting observation is that the time at which the onset of quasi-thermal occurs remains constant while varying the relative density of the feature at a particular temperature.

Further studies of the above density of states using a narrower distribution of states (0.025eV) shortened the extent of the equilibrium regime (by about half) at each relative density. In fact for a relative density of only 3x the background level, the transient decay deviates only slightly from the power-law form found in the case of an exponential tail. Only when the ratio was increased to 6x did significant variation from the power law occur.

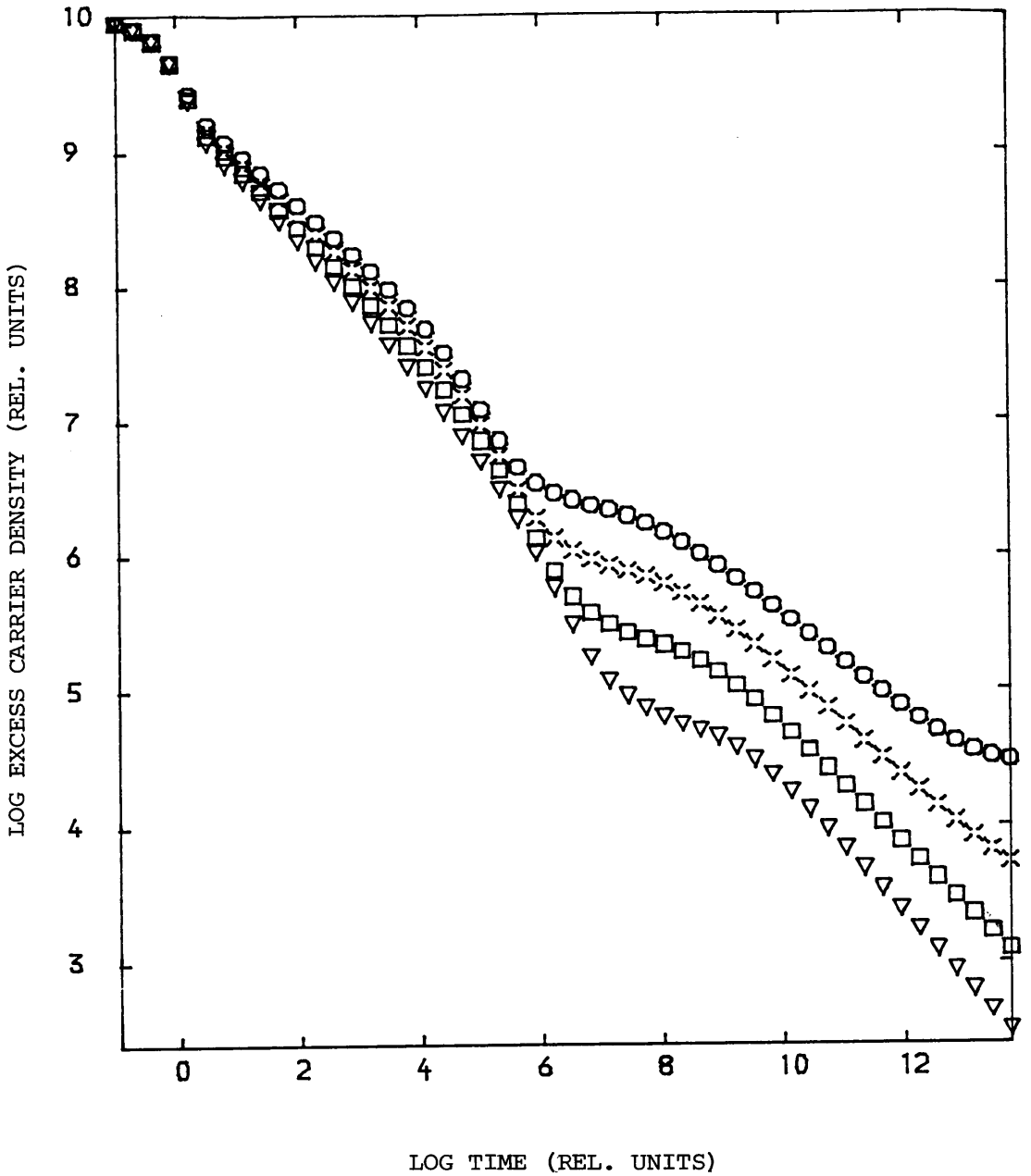

Figure 4.13

Same plot as figure 4.12, except b = 6x the background density.

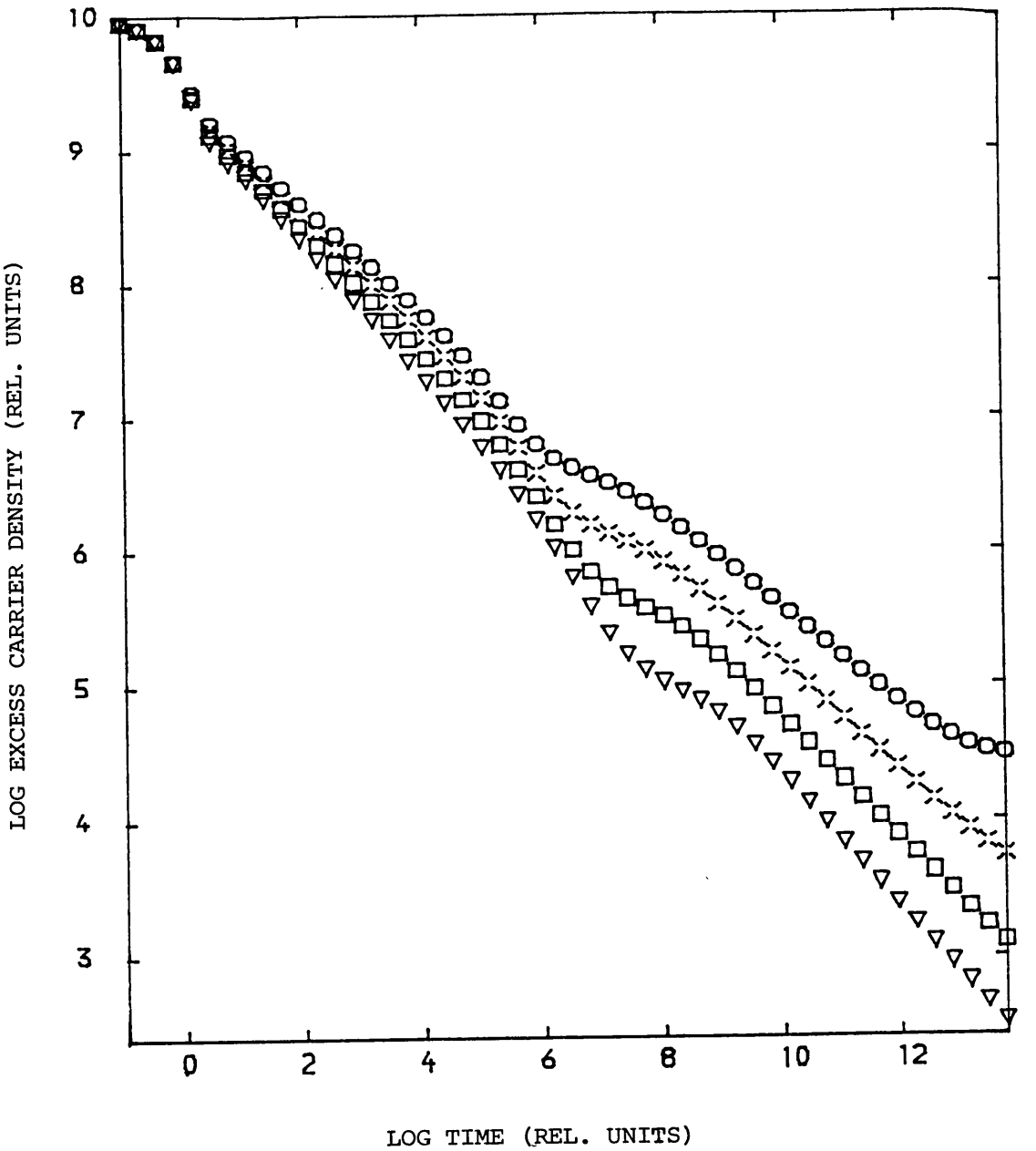

Figure 4.14

Same plot as figure 4.12 except b = 3x the background density.

In conclusion it has been demonstrated that simulation of the transient photodecay technique is capable of detecting the presence in the energy distribution of localised states of a 'sharp' feature superimposed on a continuous distribution of states. However, the rectangular feature must protrude by about six times the background density for a feature width of order 0.025(kT). If the width is adjusted to 0.05eV , the influence on the photocurrent is observable at 3x the background density.

In some experimental studies of the transient photodecay in amorphous arsenic triselenide, the decay data do exhibit deviations from signal power law decay[126, 127]. In one particular study, the data have been analysed to determine the energy distribution of the localised states[132]. In other cases a featureless decay has been observed which suggests the presence of an exponential distribution of localised states. The simulation studies performed in this report provide a means of interpretating transient photocurrent decay data and also a way of assessing an upper limit to any structure in the trap distribution. This may also enable one to obtain information about the very relevant basis parameters of multiple trapping, such as ν_0 and the variation of ν_0 with energy (see section 7.4).

Chapter 5

EXPERIMENTAL TECHNIQUES

5.1 Introduction

This chapter gives a brief description of the methods used to produce samples, of the equipment used for experiments and of the experimental techniques themselves. Most of these methods have been used by other workers in this laboratory and elsewhere, although some modifications have been made for the present work.

5.2 Preparation of Samples

5.2.1 Preparation of the Bulk Glass

The samples used in this study were prepared from bulk glass starting material. The glass was prepared in batch weights of approximately 80g by melting 5N purity elemental arsenic and selenium in an evacuated sealed tube of fused silica. The silica tube was carefully cleaned in a ultrasonic bath in which a strong detergent solution had been placed. After about 30 minutes the tube was removed from the ultrasonic bath and rinsed in isopropyl alcohol for several minutes. The tube was dried by overnight baking at 100 C. When all the constituents had been weighed out, in predetermined amounts placed into small trays, the silica tube was weighed and the contents of one tray placed into it. The tube was then placed on the balance pan again and any weight loss was made up by gradually adding the extra with tweezers. This procedure was repeated until all the required material was in the tube. During weighting of the constituents disposable gloves were worn to avoid contamination of the outer surface of the tube because finger-marks can cause weighting errors.

Powered material was not used since oxygen contamination increases with the surface to volume ratio. When using pure As it was left in the open air for a short a time as possible to minimize oxidation. It was estimated during the weighing process that variations in stoichiometry should be no greater than

$$As(2 \pm 0.0002)\ Se(3 \pm 0.0003)$$

With all the materials loaded, the silica tube was connected to a rotary vacuum pump, and the tube evacuated to approximately 10^{-5} Torr. The bottom section of the tube was then heated gently using a bunsen burner to accelerate outgassing of any adsorbed gases. When such outgassing was judged to be complete, the tube was allowed to cool under continuous evacuation. The tube was then sealed at the neck using an oxy-acetylene blow torch. This process is aided by the tendency of the neck of the tube to collapse inwards as the silica softens. The tube was then put in a rocking furnace and heated slowly up to 800 C over a period of 4 hours. This allowed the arsenic to react slowly with the selenium. It is essential that the elemental arsenic reacts before the temperature of 800 C is reached because the high vapour pressure of arsenic at this temperature might have caused the tube to explode. After continuous agitation in the rocking furnace for about six hours, the tube was removed and quenched in air. The author is grateful to Dr J T Edmond of Dundee University who perform this part of the preparation in the early stages of this research program before our own furnace was constructed.

The ignots of glassy arsenic triselenide thus prepared were

removed from the silica tube by scribing the tube with a diamond stylus and giving a sharp tap. This usually resulted in a clean break, after which the arsenic triselenide could be easily removed.

5.2.2 The Preparation of Vitreous Specimens

Thin 'platelet' vitreous samples in the 30-100 μm thickness range were produced by a 'compression' technique. A small pellet of bulk material, 2-3 mm across, was placed on a quartz plate which was heated, on a hot plate to the glass transition temperature. Aluminium capacitor foil, approximately 0.5 μm thick, was placed on top of the pellet followed by another quartz plate. The 'soft' glass deforms and can be pressed into a film between the quartz plates. The pressing was done on a hot plate using a preheated pressing tool. The sample parted easily from the glass when cooled, due to differences in the expansion coefficients, and the aluminium foil was peeled from the sample, leaving a sample of glass with high quality surfaces.

5.2.3 Evaporated Films

Thin samples of evaporated arsenic triselenide (0.5 μm - 40 μm) were prepared by evaporating the bulk glass onto aluminium which was subsequently removed by flexing. The evaporation was performed in a large evacuated bell jar. The glass to be evaporated was placed in a small perpex beaker or silica crucible which was then placed on a titanium boat in the chamber. The chamber was evacuated to a pressure of less than 10^{-6} Torr using a diffusion pump prior to the evaporation. The foil was placed about 8 cm above the crucible containing the bulk glass, and was shielded from the source by a brass paddle which could be swiveled out of the way by means of a lever

outside of the chamber. The brass paddle was used to prevent deposition of the evaporated material whilst the source was heating up or cooling down. No attempt was made to control the temperature of the aluminium foil during deposition - the foil was at room temperature prior to the start of all deposited runs.

In the next section an introduction to the process of r.f. sputtering will be given and the preparation of the r.f. sputtered samples discussed.

5.3 Introduction to the Sputtering Process

The process of r.f. sputtering is commonly used in the semiconductor industry to etch or deposit a wide range of insulating and conducting material. A schematic diagram of the essential features of an r.f. sputtering system is shown in figure 5.1. The dielectric target which is to be sputtered is positioned so that it forms a boundary of a plasma. A radio frequency (r.f.) voltage is applied to the metal backing electrode and, as a result of capacitive coupling through the target, an r.f. voltage is induced on the front surface of the target. Electrons are more mobile than positive ions, therefore more electrons are attracted to the front surface of the target during the positive half cycle than positive ions in the negative half cycle. The resultant electron current causes the dielectric surface to acquire an increasing negative bias voltage during successive cycles until a stage is reached when the substrate surface is positive with respect to the normal wall potential for only a short period of the r.f. cycle. During this time, enough electrons are attracted to the surface to neutralize the positive ion charge accumulated during the

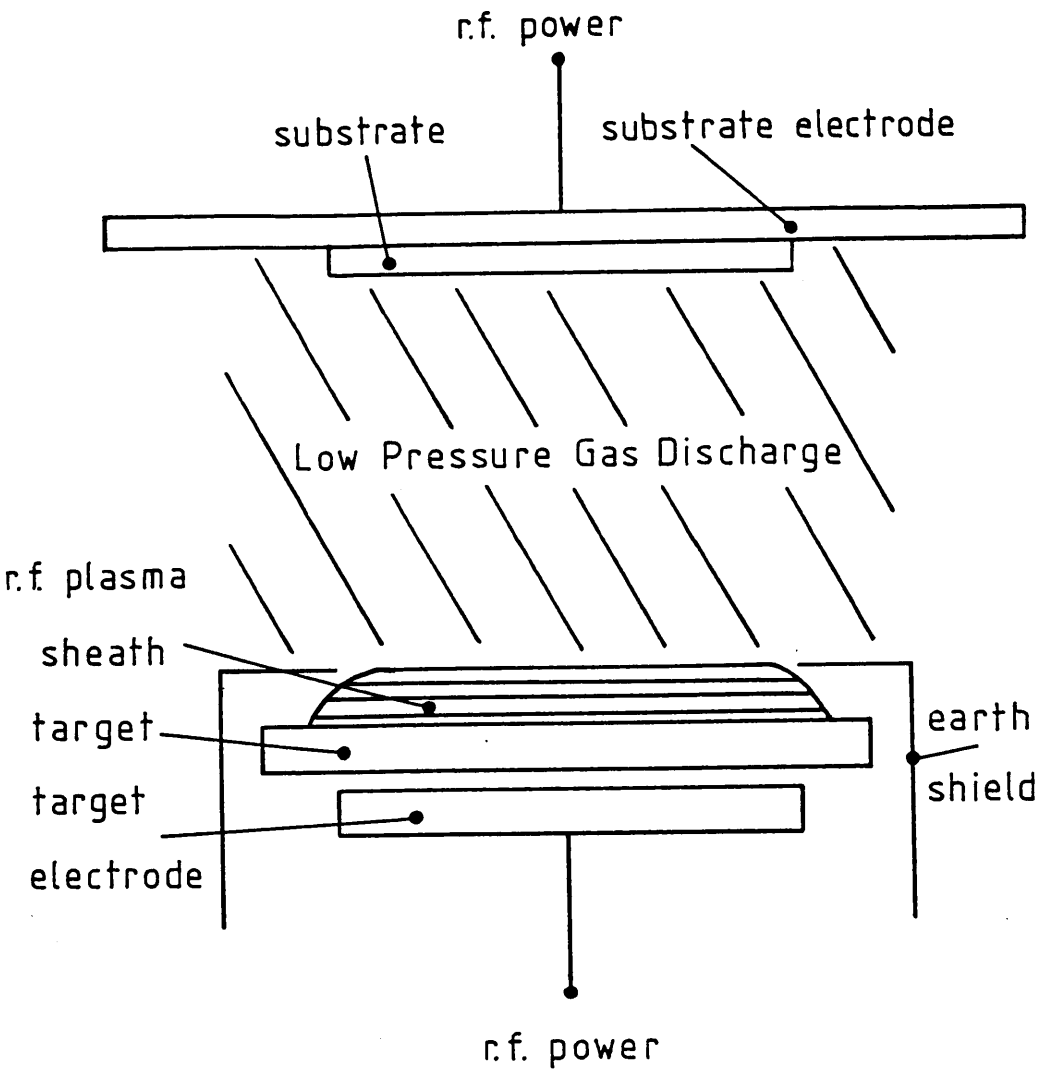

Figure 5.1

Elements of an r.f. bias sputter deposition system

rest of the cycle. The bias potential is close to half the value of the peak to peak r.f. voltage appearing on the target surface (see for example Jackson [138]). The ions are accelerated essentially by the bias potential (V_b) rather than the r.f. potential and bombard the target with an energy of the order of V_b electron volts. Sputtering is generally carried out using ions of a few keV, thus r.f. voltages of a few kV are required. The drop in bias voltage experienced during each half cycle is a function of the r.f. frequency. For the frequency used in this study (13.56 MHz), this drop in bias voltage should be less than 100V.

5.3.1 The Nordiko Sputtering System

All doped and undoped arsenic triselenide films were deposited using the Nordiko sputtering unit shown in figure 5.2. The chamber was evacuated using a 20 cm oil diffusion pump backed by a suitable mechanical rotary pump. Gases were admitted into the chamber under the control of automatic gas flow equipment, the gas flow rates being controlled to maintain a constant pressure. Three, 10 cm targets could be accommodated by the system, the target chosen for deposition being rotated underneath the substrates. The substrates were held in contact with a 19 cm diameter copper plate which could be heated electrically, or cooled by water or liquid nitrogen.

A solid target was fabricated in the following way. A stainless steel base 8mm thick was placed on a heater taken from a small diffusion pump. Pellets of the bulk glass were placed on this base, and the whole system placed in a bell jar containing nitrogen gas at slightly less than atmospheric pressure. The steel disc was

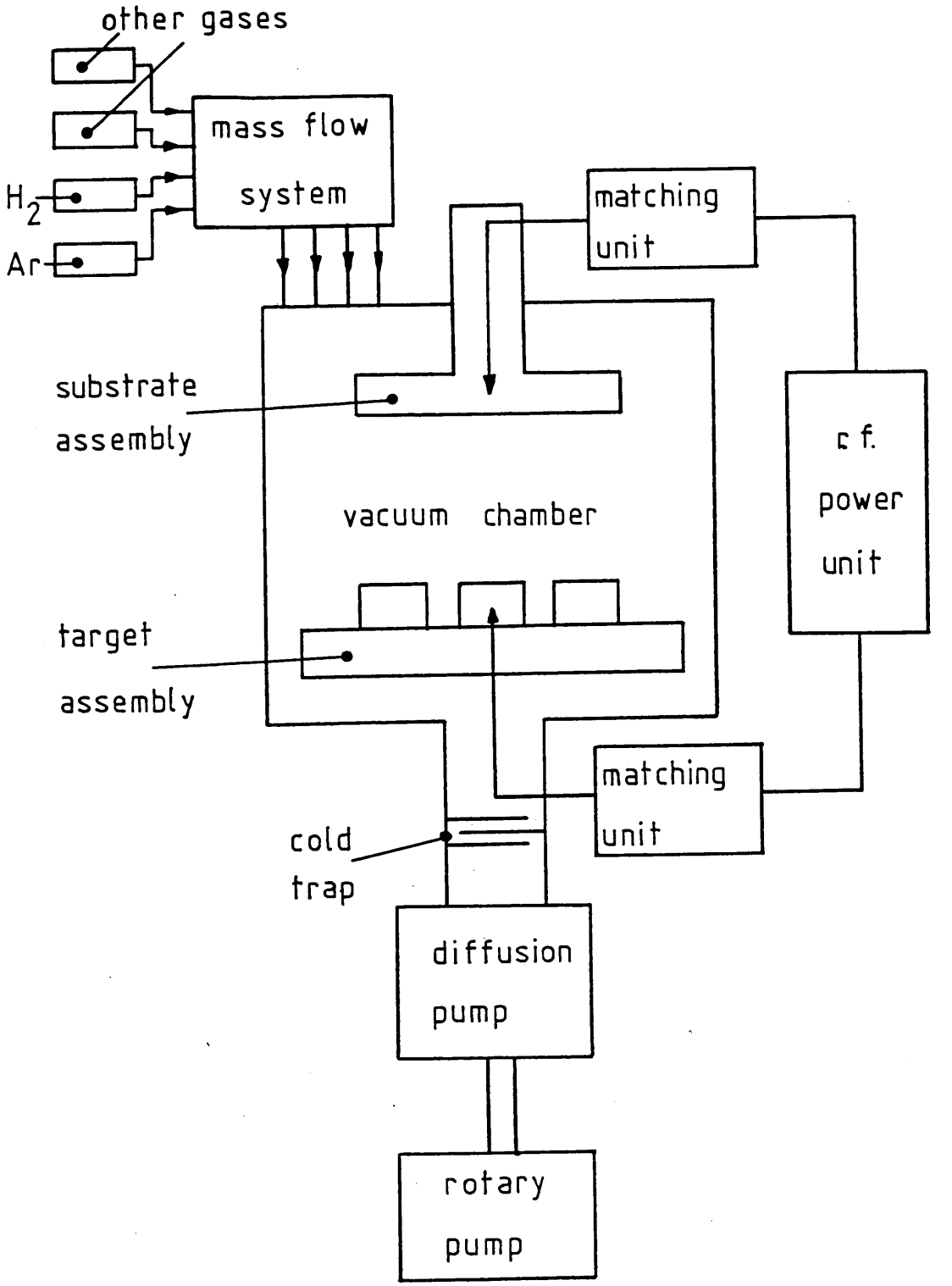

Figure 5.2

Schematic diagram of Nordico bias sputter deposition system. The r.f. power is split between the target and substrate via the matching units.

then heated to just above the glass transition temperature, and the molten As_2Se_3 allowed to flow until it covered the base to a depth of 5mm. The target was then allowed to cool in the nitrogen atmosphere before being removed and placed in the sputtering system.

Several different substrate arrangements were used to give both supported and unsupported films. Unsupported films were obtained by sputtering onto thin aluminium capacitor foil which was subsequently removed by flexing. This method could produce films thicker than about 20 μm - for thinner films the aluminium had to be removed by dissolving in HCl. Supported film were deposited onto corning 7059 glass substrates 25mm x 12mm x 0.8 mm. Eight of these substrates could be loaded into the sputtering unit for each deposition, the substrates being held in good thermal contact with the copper substrate plate in a brass specimen holder. The copper plate could be removed from the sputtering system, facilitating substrate and mask position. The copper plate was located directly above the target and was kept in good thermal contact with a 1.5 kW electric heater element by a large copper o-ring.

The arsenic triselenide samples investigated in this study were all produced using bias sputtering deposition. In this arrangement the r.f. power is split between the target and substrate. This technique has the advantage of removing most of the gas trapped from the plasma in the deposited film, leading to films with more repeatable characteristics which are closer to those of the bulk target (see figure 5.2). For all the samples used in this study the

power was split in the ratio 5:1 between the target and the substrate respectively.

As already mentioned, gases were removed from the sputtering chamber using a 20 cm oil diffusion pump, backed by a mechanical rotary pump. A pneumatically controlled baffle plate was used to control the rate at which gases were removed from the chamber. Prior to a deposition run, the background pressure was reduced to between 10^{-5} and 10^{-6} Torr.

During the term of this project the sputtering system was upgraded and as a result two methods of admitting gases into the chamber were employed. The first method involved the use of a needle valve to control the flow of argon . The Argon pressure in the chamber could be controlled upstream of the chamber by the sensitive needle value or downstream of the chamber using the baffle plate. The gas pressure was measured using a Hastings thermocouple gauge, which could be read to an accuracy of $\pm$0.2 millitorr in the pressure range 5 - 20 millitorr. Unfortunately the reading on this gauge could also be affected by the presence of the r.f. discharge - it was therefore assumed that the true pressure during deposition corresponded to the pressure which the gauge read immediately after the discharge was switched off.

In order to remedy this problem, automatic gas flow equipment was obtained for the system. The equipment operated by adjusting the rate of flow of the gases. Flow rates were adjusted by applying three term control to the difference signal between a

setpoint pressure and the chamber pressure obtained from a Baratron manometer. Upto four gases could be controlled simultaneously, their flow rates being kept constant by the controller. This equipment was thus capable of maintaining a fixed ratio between the flow rates of the gases.

Doped and undoped a-As_2Se_3 were deposited from the above prepared bulk glass target. The undoped material was deposited directly from the arsenic triselenide target, while the doped material was deposited by co-sputtering the arsenic triselenide with small percentages of dopant material (either nickel or indium wire) being distributed evenly over the target surface. The concentration of the dopant in the film was controlled by varying the amount of dopant material placed on the target.

Typical sputtering conditions, for the undoped specimens, were 12 millitorr of argon, a bias voltage of 300V and a power of 30 watts. Under these conditions, deposition rates of 0.5μm/hour were produced. The substrate electrode assemble could be water cooled or heated. All the films used in this study were deposited with the substrate held at room temperature.

5.3.2 Thickness Measurements

The thickness of the above mentioned samples can be measured in two different ways.

1). The samples can be broken up and the thickness of several pieces measured with a micrometre screw gauge. This technique is only useful for samples thicker than about 40 microns.

2). For thinner samples, i.e samples evaporated or sputtered onto a substrate, a Taylor Hobson model 3 "Taly-surf" was employed. This machine works on a principle similar to a gramophone pick-up, i.e., a diamond stylus is moved across the sample and its vertical movements give a proportional electrical output which is amplified and displayed on a recorder. The thickness could accurately be measured with a maximum error of 0.05 μm for submicron samples to within 5% for thicker samples.

5.4 Deposition of Electrodes and Their Geometry

For time of flight and d.c. conductivity measurements vitreous samples were equipped with thin, semitransparent gold electrodes onto the top and bottom surfaces to form the 'sandwich' configuration shown in figure 5.3. This configuration was also used for samples produced by thermal evaporation and those produced by r.f. sputtering. In this case, however, the gold electrodes were firstly evaporated onto a 7059 corning glass substrate by masking the substrate. An arsenic triselenide film was then deposited onto the substrate/electrode configuration, followed by evaporation of the top semi-transparent electrodes. Electrical contact to the electrodes was by means of thin aluminium wire (60 μm in diameter). The wire was dipped into silver dag, then brought into contact with the narrowest part of each electrode (as shown in figure 5.3). The silver suspension was kept as far away as possible from the region of overlap of the electrodes because silver diffuses fairly rapidly through arsenic triselenide even at room temperatures [139]. This electrode configuration was used for both dark d.c. conductivity and time of

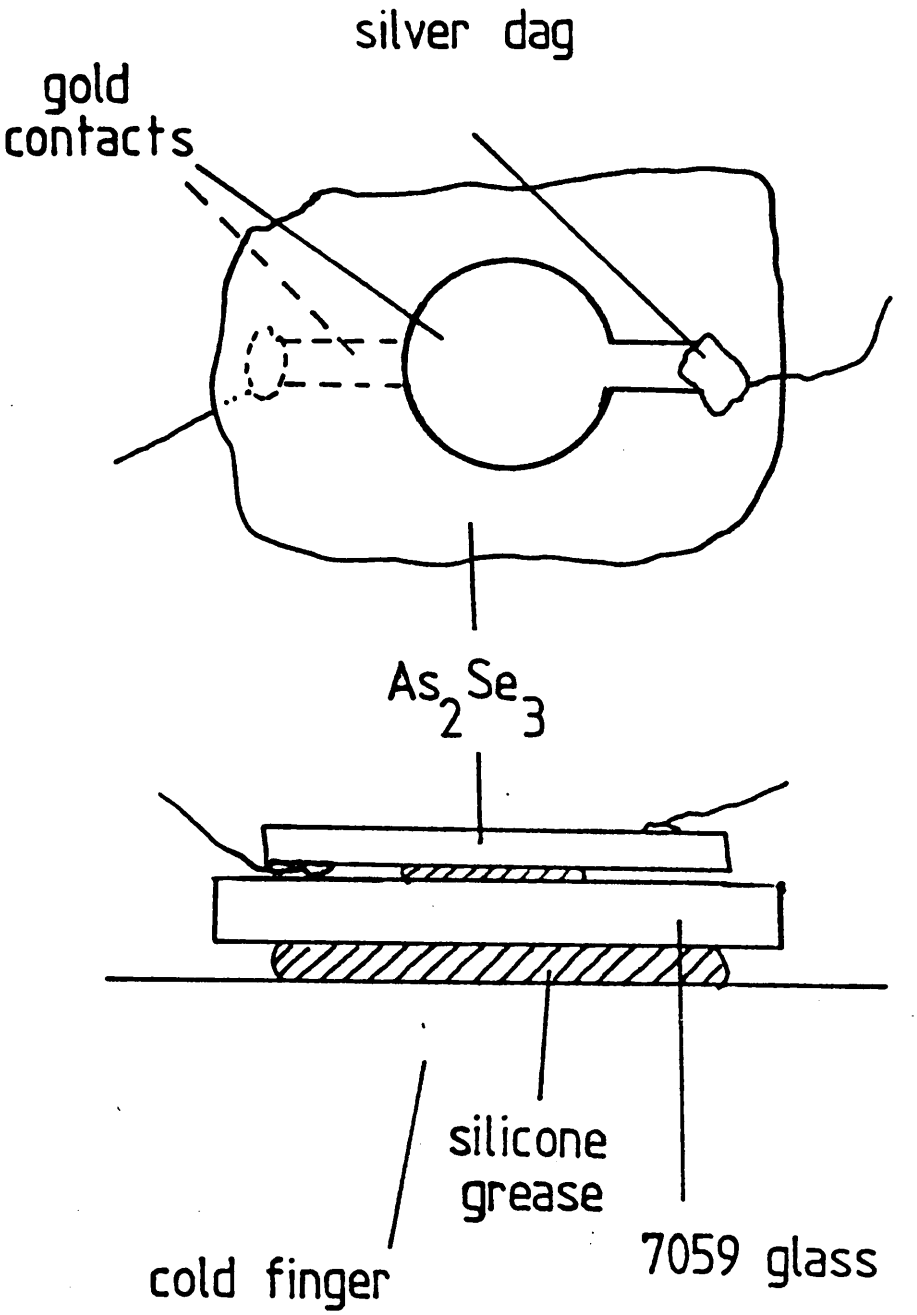

Figure 5.3

Sandwich cell configuration (top) and contact to cold finger (bottom)

flight measurements.

For the purpose of transient photoconductivity, steady state photoconductivity, photomobility and thermopower measurements, the gap cell configuration shown in figure 5.11b, was used. Gap's of various sizes (from 60 μm to 4 mm) were produced by either stretching wire (aluminium 60 μm in diameter or tungsten 200 μm in diameter) across the specimens, or by masking off a set gap size using brass foil, to give well defined electrodes, of length 2-10 mm. Gap's were also produced by first depositing gold onto a masked substrate, after which the masking wire was removed and the arsenic triselenide film deposited.

When the gold is deposited first it is possible to use either the above method or photolithography to produce the desired electrode configuration. The latter method makes it possible to produce electrodes of different gap sizes of exactly known width. These electrode configurations were produced as follows. Firstly a thin layer of gold was evaporated onto clean glass substrates. Next the substrate was placed on a, Headway Research Inc. Spinner (EC101D), and a few drops of Shipley microposit 1350H positive photoresist placed on the gold layer. The sample was then spun at a rate of 4000 rpm for 20s producing an even distribution of photoresist, approximately 2 μm thick, across the gold. The photoresist was dried for 10 minutes in an oven held at a temperature of 80 C. After placing the desired mask on top of the substrate in the, Kasper 17A, wafer mask alligner, the substrate was exposed to ultraviolet light for 1 minute. To develope the photoresist the sample was steeped in a

mixture of microposit developer and water (in the ratio 1:1) for a period of one minute. After washing thoroughly, the slide was placed under an infra-red lamp to hard-bake for about 5 minutes at a temperature of 120 C. Next the gold was etched away in a mixture of 5g potassium iodide, 1g iodine and 40 ml of water. The photoresist layer was removed in acetone after thorough washing with water. This process removes all the gold in the areas exposed to the ultraviolet light but leaves the rest untouched. The slide was then cleaned in Propan-2-ol.

5.5 Electrical Measurements

5.5.1 Sample Holder for D.C. Conductivity and Photoconductivity Measurements

The samples were mounted on a sample holder isolated from a coldfinger with four spacings (as shown in figure 5.4). The only thermal contact being through four screws which can be either brass or nylon. For the purpose of performing different experimental techniques, the holder can be attached to the coldfinger in different positions, normally facing upwards for dark d.c. conductivity measurements, or rotated by 90 facing one of the vacuum chambers windows, for photoconductivity measurements. To measure the temperature a platinum resistance temperature sensor was used. The sensor was embedded in the holder directly under the sample. This configuration may cause a slight discrepancy between the actual and measured temperature of the sample which may be observed as a hysteresis (a difference in the measured conductivity between heating and cooling cycles) in a dark d.c. conductivity measurement for

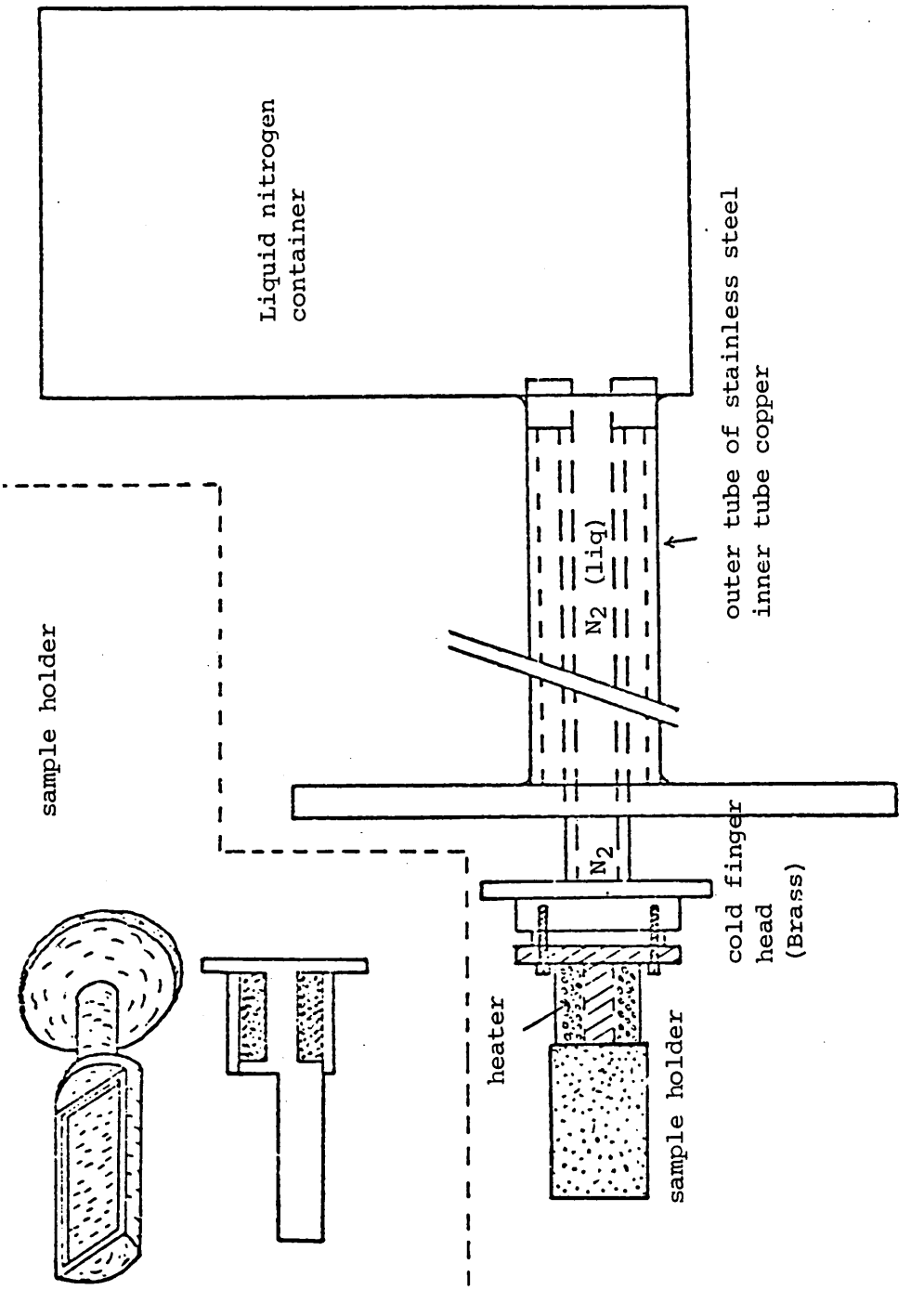

Figure 5.4

Cold finger and sample holder arrangement used for d.c. conductivity and photoconductivity measurements.

example. In practise this effect was found to be slight, corresponding to a temperature difference of less than 0.5K.

The specimen holder and heating head were placed in a vacuum chamber and pumped down to pressures less than 10^{-6} Torr with a rotary/diffusion pump vacuum system, before any experimental measurements were taken. The resistance of the heater shown in figure 5.4 was 30Ω giving an output power of 30 watts with a 1 amp supply current. This power was more than sufficient to counteract the cooling effect of the liquid nitrogen (78 K), which was used to lower the overall temperature of the heating head. Thus the temperature of the specimen holder could be controlled at the desired temperature by balancing the heating power against the cooling effect of the liquid nitrogen.

For thermoelectric power measurements a different heating head was used. The main block of the heating head is shown in figure 5.5. It consists of the main heater (1), with resistance of 30Ω (maximum power of 30 watts), and a smaller 15Ω (maximum power 15 watts) heater (2) at the front end of the block. Thermal contact between the brass bar and the heater was made through mica and copper discs to give electrical isolation. The specimen was placed between the brass section and heater (1) as shown in the figure.

A copper/constantan thermocouple circuit was designed to measure the temperature at either side of the sample as shown in figure 5.6. The thermocouple junctions at T1, T2 and T3 were made by soldering the copper and constantan wires together, then electrically

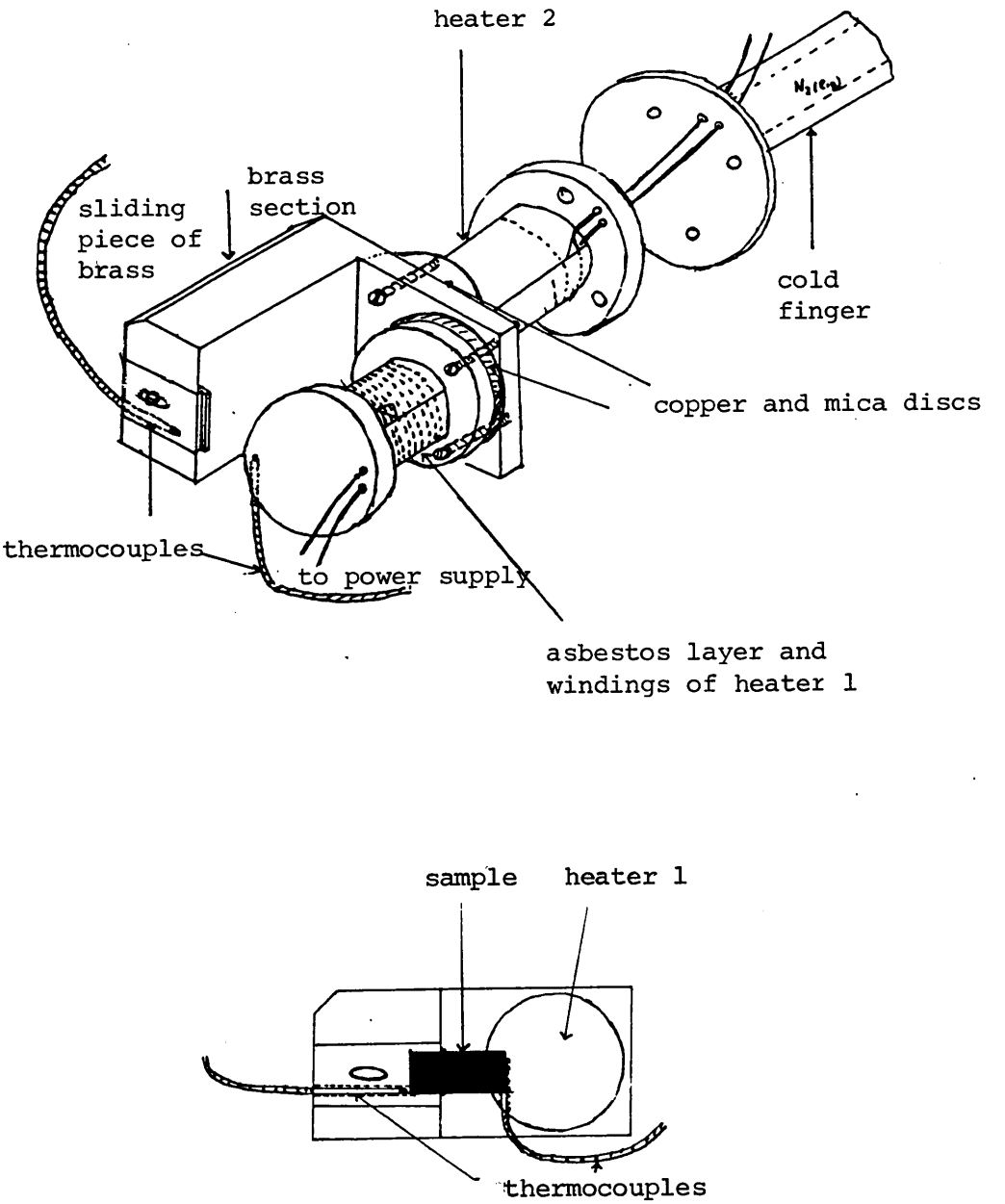

Figure 5.5
Main block (top) and frontal view of heating head (bottom) used for thermopower measurement.

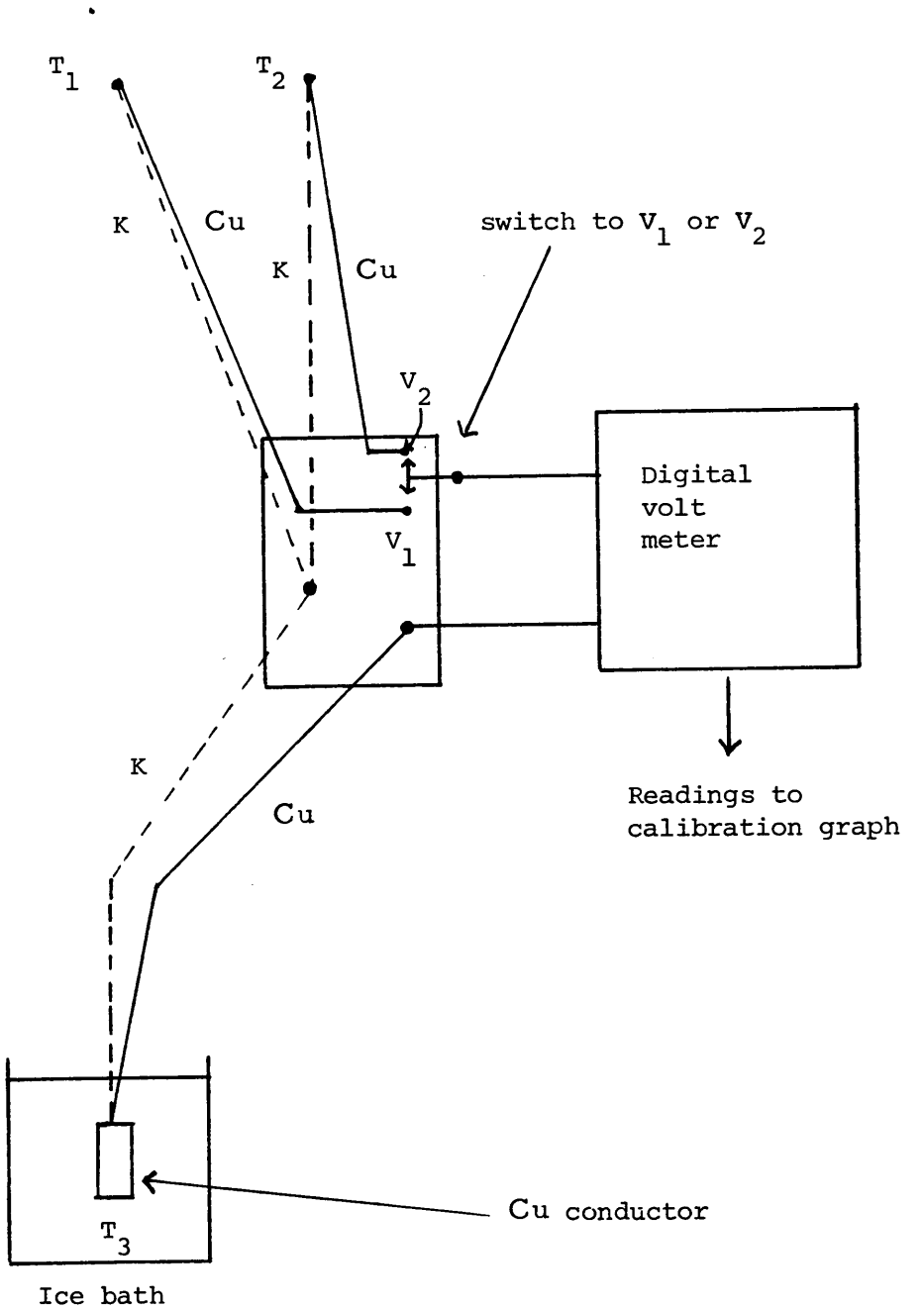

Figure 5.6

Schematic diagram showing the thermocouple circuit used. The temperatures T_1 and T_2 represent the temperatures measured at either end of the specimen. The readings from the digital voltmeter (mv) were calibrated to K using a calibration graph.

insulating them with high temperature resistant plastic (PTFE). The circuit included a switch which when in position 1 enabled the temperature at T1 on the sample to be measured. Similarly, when in position 2 the temperature at T2 could be measured. The technique used to measure the thermoelectric power will be discussed in section 5.8.

5.5.2 d.c. Conductivity

Prior to the TOF and photoconductivity work, straight forward electrical measurements were made with the same samples kept in the dark. The samples were kept in a light-tight evacuated box during runs. The voltage across the sample was maintained by a Fluke 415B power supply which is capable of providing 0 - 3000 V $\pm$ 0.1%. The steady state current flowing through the samples was measured using a Keithley 610C solid state electrometer, in 'fast' mode, which could detect currents down to 10^{-13} amps. The dependence of the dark conductivity on temperature at low and high fields was studied. The electrometer was always switched on several hours before measurements were made to minimize possible drift during cooling cycles.

5.5.3 The Time of Flight Technique

The measurement of drift mobility by the time of flight or transient charge technique provides a physically direct method of transport measurement which is particularly suited to the combination of high specimen resistivity and low carrier mobility found in arsenic triselenide. The technique has been reviewed in detail by various authors [140, 141]. The technique essentially involves detecting the drift through the semiconductor of a sheet of excess carriers

generated near one electrode by a pulse of electrons, a strongly absorbed light flash, or some other excitation. The principle underlying drift mobility measurements on insulating solids will now be discussed.

Consider a sample in the form of a thin platelet, thickness d, fitted with metallic electrodes T and B as shown in figure 5.7. The top electrode is connected to a steady or pulsed source of potential. For the sake of the present discussion we shall assume that T is kept at a positive potential V_a with respect to ground. The bottom electrode is returned to ground through the resistor R which is normally much smaller than the specimen resistance. Excess carriers are generated by some form of transient excitation. It is essential that the duration of the excitation pulse, t_e, should be considerably shorter than the transit time t_t of the generated carriers across the specimen. More easily interpretable results are obtained if the absorption depth δ of the excitation is kept very much smaller than the specimen thickness d. In that case a narrow sheet of charge carriers of one sign is drawn across the specimen (see reference [140]). Suppose that N of the carriers generated in a surface area A escape recombination between x=0 and $x=\delta$. The drifting sheet of charge at $x=x'$ will modify the applied field $\mathcal{E}_a=V_a/d$ and elementary electrostatics show that $\mathcal{E}_1$ and $\mathcal{E}_2$, indicated in figure 5.7, are given by

$$\mathcal{E}_1(x) = \mathcal{E}_a - \frac{4\pi Ne}{kA}\left(1 - x'/d\right) \tag{5.1}$$

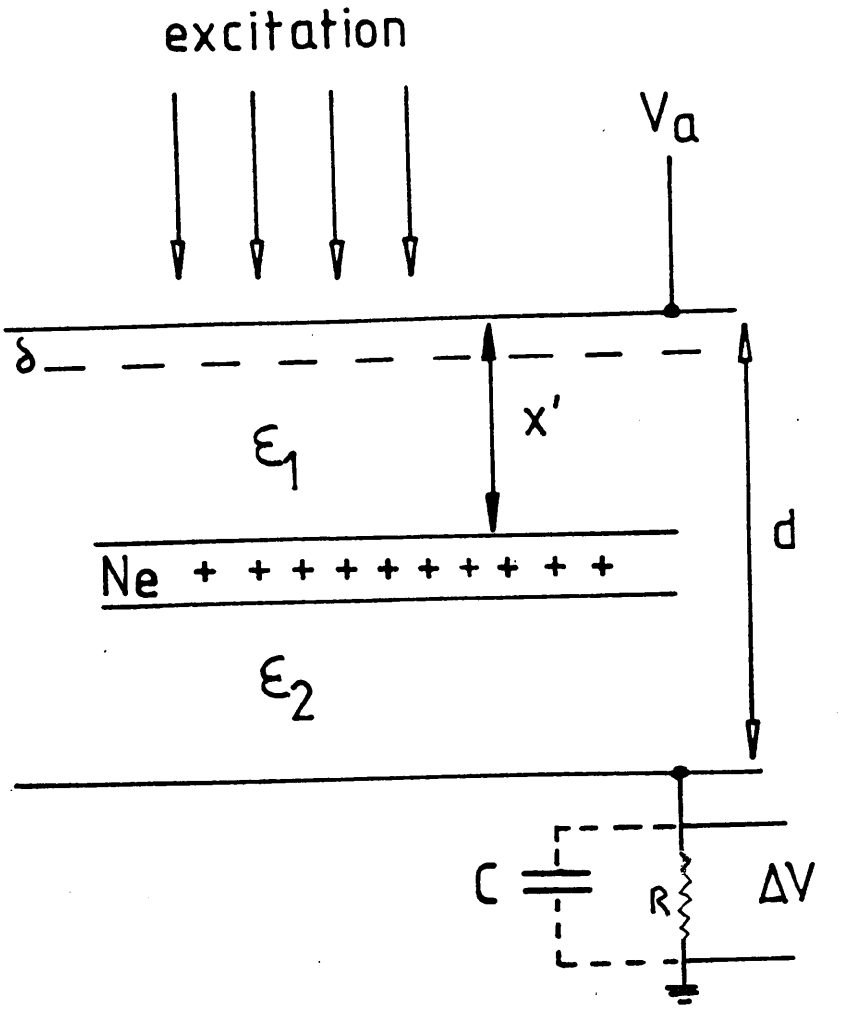

Figure 5.7
Schematic diagram of time-of-flight drift mobility experiment.
(After Spear [140]).

$$\mathcal{E}_2(x') = \mathcal{E}_a + \frac{4\pi Ne}{kA}\left(\frac{x'}{d}\right) \qquad (5.2)$$

where k is the dielectric constant of the solid.

Thus the drifting carriers alter the field within the solid. However, if N is kept sufficiently small so that the self field $4\pi Ne/kA$ is much less than $\mathcal{E}_a$, it is a good approximation to take the internal field as V_a/d. It must be remembered that this description of carrier transport applies to a low conductivity solid in which the dielectric relaxation time τ_{rel} is very much longer than the transit time. In this respect the situation is fundamentally different from standard Haynes-Shockley mobility measurements on the drift of minority carriers in an extrinsic semiconductor, in which the condition of charge neutrality must remain during the transit. The highly resistive sample has an advantage over the semiconductor in this respect, because drift mobility measurements on both types of carrier are possible (in principle) simply by reversing the polarity of the applied electric field.

There are essentially two ways in which the transit time of the carriers can be determined. The first relies on charge integration and in this method the time constant CR must be much larger than the transit time t_t. C donates the total capacitance across the resistor R and includes that of the specimen, the leads and the input of the detecting system. As the generated carriers drift across the specimen, the changing fields $\mathcal{E}_1$ and $\mathcal{E}_2$ will cause a re-distribution of charge on the electrodes. On the bottom electrode this is

$$q = Nex'/d \tag{5.3}$$

The potential across R is then

$$V(t) = Nevt/Cd \tag{5.4}$$

during $0<t<t_t$, where $v=d/t_t$ donates the drift velocity. For $t>t_t$, V remains equal to Ne/C as long as $t<<CR$. The typical pulse shape from which t_t can be obtained is shown in figure 5.8a. The linear rising edge implies that N remains constant during the transit, and that the drifting carriers do not interact appreciably with deep traps.

Alternatively, t_t can be measured from the duration of the current pulse produced by the drifting carriers (see figure 5.8b). In this case it is necessary to reduce R so that $CR<<t_t$. Equation (5.2) leads to

$$I = Nev/d \tag{5.5}$$

Therefore

$$V = RNev/d \tag{5.6}$$

for $0<t<t_t$ and V=0 when $t>t_t$ (see figure 5.8).

Carrier transit times for a vitreous As_2Se_3 sample 50 μm thick are typically hundreds of microseconds at room temperature and low applied electric fields. Therefore detector rise times are not critical and large values of R may be used. For this reason all our

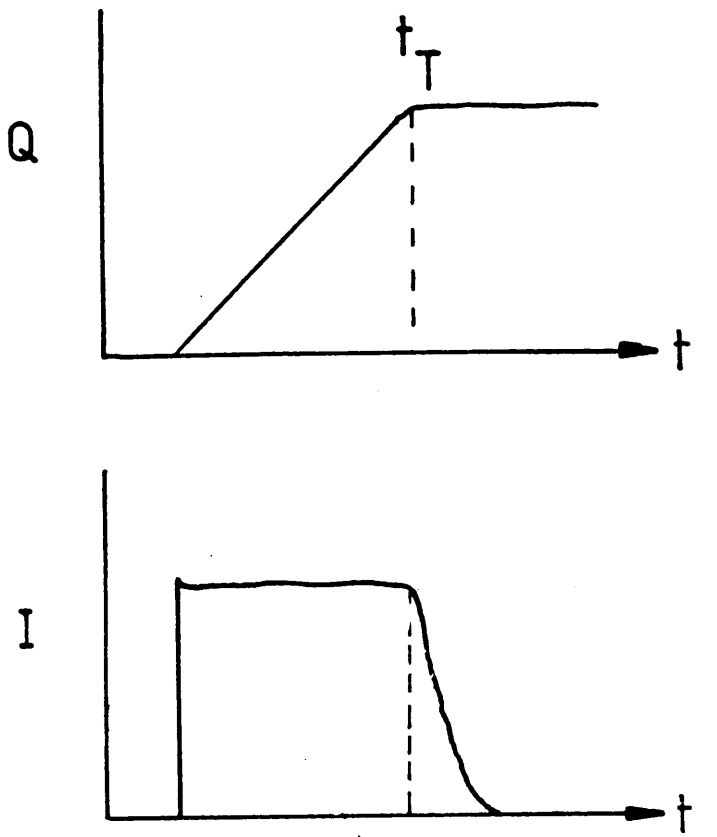

Figure 5.8
Transit pluses observed in a time-of-flight mobility experiment. Top-charge integration transient. Bottom - idealised current transient.

drift mobility measurements were made using the current pulse mode, which has several advantages if deep traps are present.

Once the transit time has been measured, the drift mobility may be obtained from

$$\mu_d = \frac{d}{\mathcal{E}_a t_t}$$

The safest procedure is to determine t_t over as wide a range of applied fields as possible. A graph of $1/t_t$ versus $\mathcal{E}_a$ should be a straight line , and the mobility may be obtained from the gradient. This line will not however pass through the origin if a trapped surface charge layer builds up near the top electrode. Obviously such a technique cannot be used if a field dependent mobility is present.

The time-of-flight technique relies on a well defined pulse of generated carriers and any effects which tends to appreciably broaden the sheet of carriers must be avoided. This applies particularly to the injection of excess charge from the electrodes during the generation and transit of the carriers. In an extreme case, the position of the transit pulse may be totally obscured if this occurs. Therefore, ideally, the top electrode should be blocking to the charge carrier under investigation and extracting to that of the opposite sign. In fact the observation of a well defined transit pulse is usually taken to imply that the top electrode is at least partly blocking in character. Unfortunately such contacts usually impede the extraction of carriers of the opposite sign. This tends to produce polarization effects which must be carefully minimized using

techniques which will be described in the next section.

5.5.3.1 Minimization of Space-charge

There are two kinds of space-charge effects which are of importance in drift mobility experiments. The first is connected with the presence of deep trapping centres in the volume and particularly near the surface of the specimen, whilst the second effect is due to the space-charge associated with the carriers themselves.

In the first case, the gradual build-up of charge in deep traps during successive transits will modify the internal field, so that the assumption of an essentially uniform field is no longer valid. Experimentally, one observes slow polarization effects in which the transit signal gradually diminishes in size during the first few transits after switching on the excitation pulses. Occasionally the signal disappears completely, and it must be concluded that the resultant field has become very small in part or all of the specimen.

To eliminate effects of this kind two precautions are essential. Firstly, the density of generated carriers must be kept as low as is consistent with the sensitivity of the detection apparatus. Secondly space-charge neutralization techniques must be employed. A simple neutralizing technique employed, by Spear, to minimize such effects involves running the excitation pulses at a frequency of about one Hertz while the top and bottom electrodes are earthed. The presence of an internal charge distribution, particularly near the top surface, is then indicated by the appearance of a reverse signal caused by the displacement of the generated carriers in the

space-charge field. The signal will decrease as the trapped charges are removed by recombination, and normally disappears after a few seconds. The external field is then applied across the specimen, but is removed as soon as the transit is recorded. The sequence of excitation pulses, field pulses and observed signals are shown in figure 5.9. This technique has been used by Spear and his co-workers with considerable success in their work on the rare gas solids, where surface polarization presents a particular problem [140]. In the experimental set-up used throughout this study the excitation and field pulses were enabled using logic circuits present in an Advance Instruments PG52 pulse generator. The field pulse was produced from a Fluke 415B H.T. supply using a mercury wetted relay gated by the output of the PG52.

The second effect is connected with the space charge of the carriers themselves. If N is increased sufficiently, the self field can be made to approach the value of the applied field $\mathcal{E}_a$. Equations (5.1) and (5.2) show that the fields behind and in front of the drifting charge sheet will be very different, and marked changes will occur in the observed signal shape. Figure 5.9 shows a typical electron transit pulse in the current mode when $4\pi Ne/\mathcal{E}A = \mathcal{E}_a/2$, and is taken from the review by Spear [140]. The most prominent feature is the cusp at about $0.8' t_t$. The physical reason for this pulse shape is as follows: electrons near the leading edge of the carrier packet experience the larger field $\mathcal{E}_2$ and "run away" from the slower moving carriers. The current will increase until the extraction of the faster carriers causes it to drop beyond the cusp. The position of the cusp

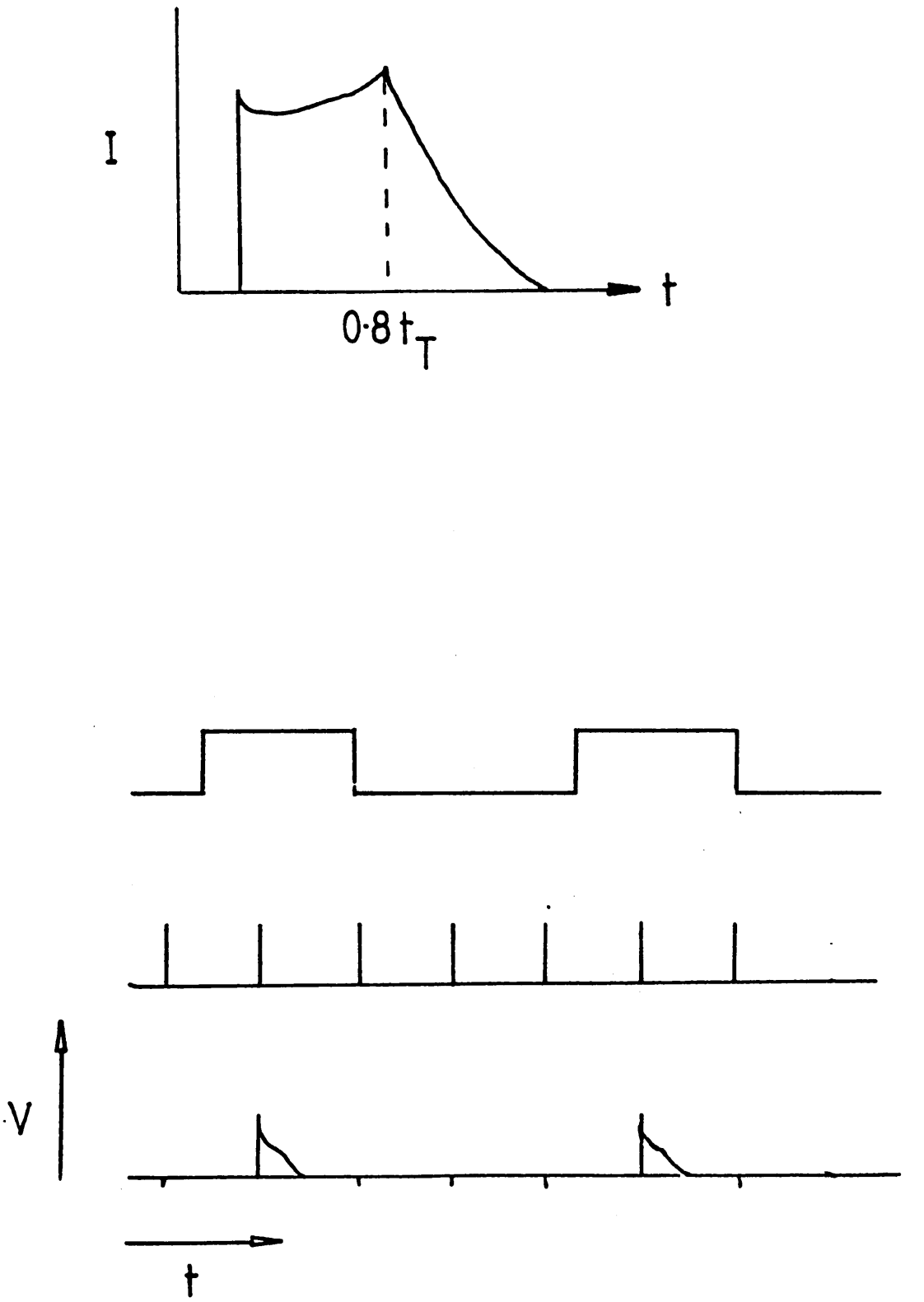

Figure 5.9

Top - current transient with space charge perturbation. Bottom - diagram showing timing relationship between field, excitation pulse and transit pulse used by Spear in the minimization of space-charge (After ref [140]).

in terms of the transit time depends somewhat on the ratio of applied to self-field. If N is kept reasonably constant during the experiment, the cusp forms a useful feature for the accurate measurement of the transit time. However, the larger the number of generated carriers, the more important effective space-charge neutralization between excited pulses becomes. In this investigation light flash excitation was employed. Free carriers , generated by a 5 ns light flash from a nitrogen laser, constructed at the College, impinged upon the top surface of the sample. The current transients, produced by the drift of the carriers through the sample under the influence of the applied field, were captured using a DL905 transient recorder, and then transferred to a computer for storage and analysis.

In this particular study it was found that the conventional technique led to distortions (despite using the neutralization technique described above in an effort to minimise space charge) in the pulse shape due to space charge accumulation and polarization effects, therefore a modification of the conventional technique was used. The sample was raised in temperature to 100C, and held at this temperature for about 30 minutes to rid it of space charge accumulation, then lowered to the desired temperature and flashed once with laser light. It was found that this did change the transit pulse shape for all temperatures investigated.

5.6 Transient Photoconductivity

The technique of transient photoconductivity (TP) is different from TOF in several respects. In TP the sample is illuminated uniformly in a direction transverse to the electrodes,

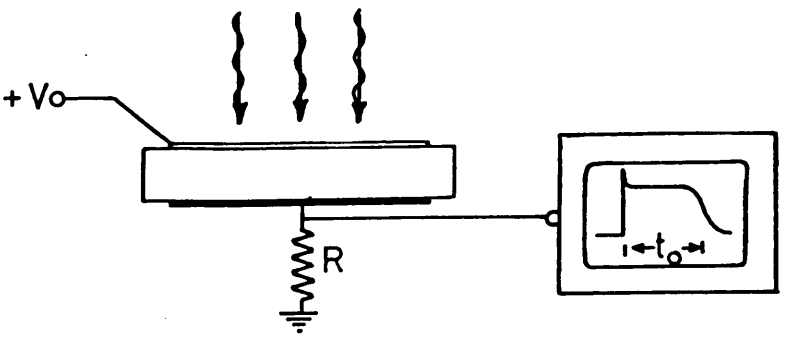

(a)

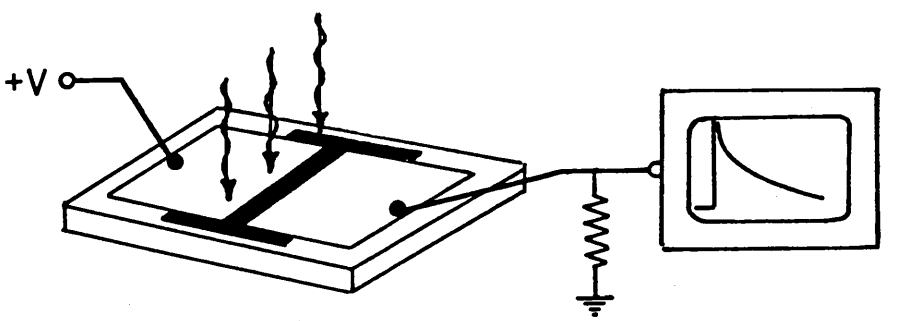

(b)

Figure 5.10

(a) Diagram showing the Spear technique used in this study for the excitation of carrier drift mobility.

(b) The transient photodecay technique using the gap cell electrode configuration.

creating an excess conduction G (see figure 5.10), Injecting contacts supply the excess current, i = GV for bias voltage V. With the use of the gap cell configuration, there is no build up of charge at the electrodes so that measurements can be made at $t > \tau_{rel}$. Furthermore the excited region between the two electrodes remains electrically neutral permitting the sample to be pulsed repetitively. For example using a 5 ns laser pulse, with a repetition rate low enough to allow complete decay of the current pulse, it is possible to measure i(t) from 10 ns to 10 ms and beyond. In addition, the effects of high excitation intensity (Q>CV) can be explored.

Using the transient photoconductivity technique it is impossible to distinguish between electron and hole motion. This is of no consequence in vitreous and evaporated arsenic triselenide since even in TOF only hole motion can be observed[5]. For the coplanar electrode geometry used, we may write the excess induced photocurrent as

$$i_p(t) = N(t) \langle \mu(t) \rangle e w \mathcal{E} \tag{5.7}$$

where N(t) is the areal density of photocarriers, $\langle \mu(t) \rangle$ is the average drift mobility at time t after excitation, and w, e and $\mathcal{E}$ are the width of the illumination region, the electronic charge and applied electric field respectively. In general, N(t) may decrease with time following the laser pulse, due to recombination of photo-excited electrons and holes. In the present experiment,it was assumed that the laser intensity was such that bimolecular recombination was negligible over the time scale of the measurement

(see reference [142]). Under these conditions the initial excess density N(o) replaces N(t) and the photocurrent becomes accurately proportional to $\langle \mu(t) \rangle$ at times shorter than τ_{MR} at which monomolecular recombination becomes prominent.

5.7 Steady State Photoconductivity Techniques

The basic requirement of a photoconductivity experiment, steady state or the rise and decay of the photoconductivity, is to observe the change in conductivity when the specimen is illuminated with photons. The light sources used in this study will now be discussed.

5.7.1 High Power Light Emitting Diodes

Two light emitting diodes were chosen for use both in steady state and in transient photoconductivity measurements. The diodes were manufactured by the Stanley Electric Company, the ESPY5501 model emitted in the yellow region of the visible spectrum, and the 591519G model emitting in the red region. The relevant manufacturers specifications for the diodes are given below.

	I_F (mA)	Lumimious Inten.(mcd) (min.)	(typ.)	λp(nm)	$\Delta\lambda$
ESPY5501	50	80	160	570	30
591519G	20	400	500	660	30

5.7.2 Modulation of Steady State Photoconductivity

The experimental set up used for the steady state photoconductivity measurements is shown in figure 5.11. The light-pipe is an optical fibre rod and it extends into the vacuum chamber to within a few mm from the sample. The incident flux was obtained from the calibration graphs shown in figures 5.12 and 5.13.

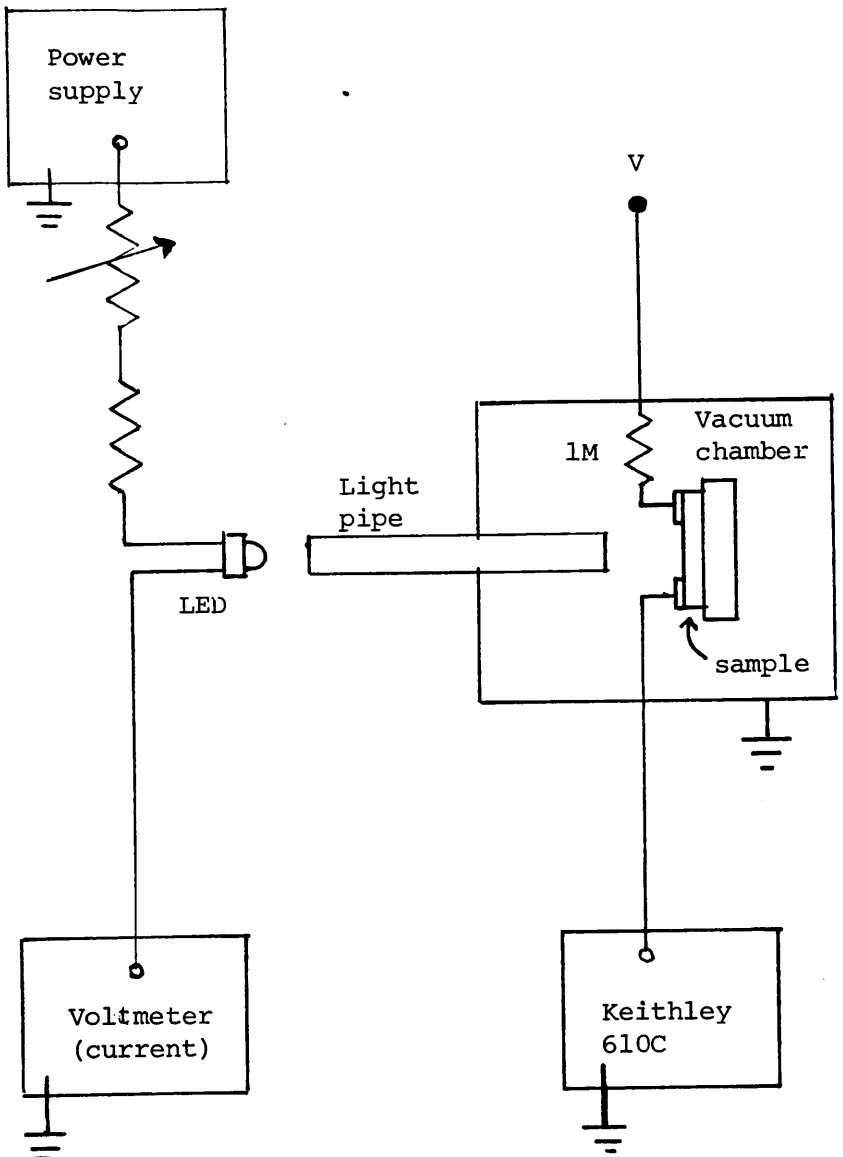

Figure 5.11

The system used for the steady-state photoconductivity measurements.

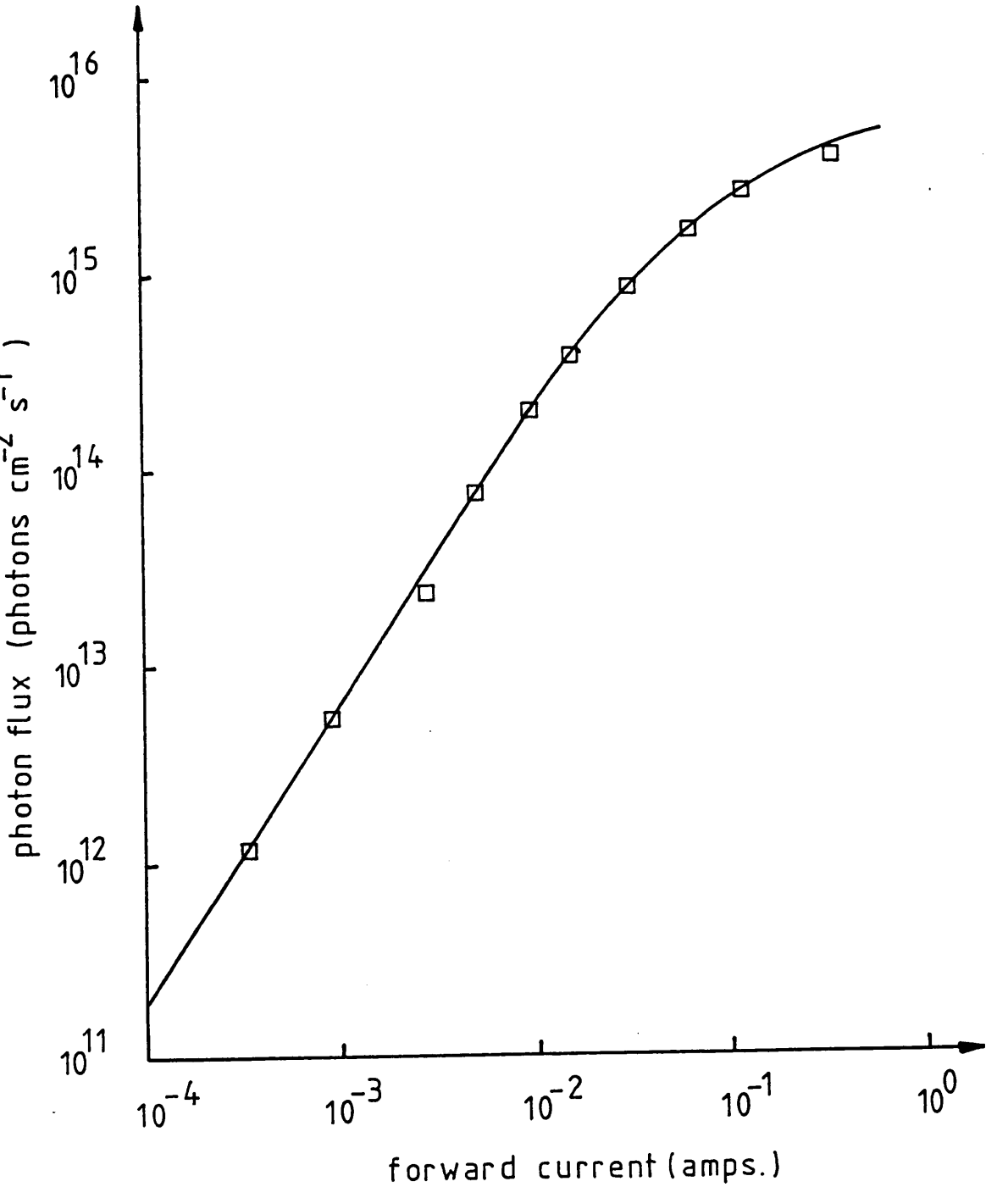

Figure 5.12

Photon flux output from light pipe versus diode forward current for the red l.e.d. (59151G)

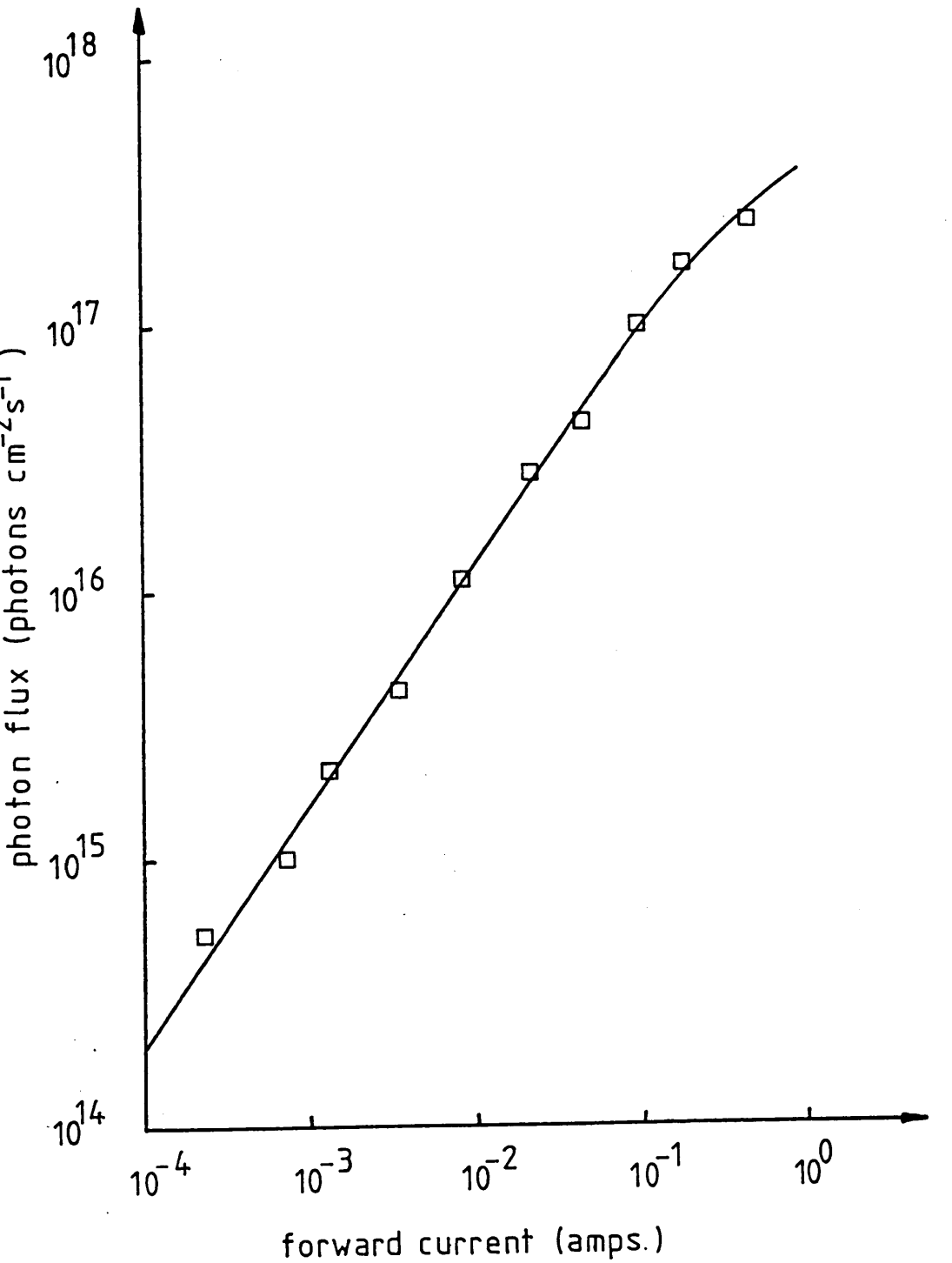

Figure 5.13

Same plot as figure 5.12 for the yellow l.e.d. (ESPY 5501).

A silicon photodiode was used in the calibration. The calibration curves were obtained for the red and yellow light emitting diodes when operating under steady steady state d.c conditions. At all times during calibration and subsequent use the diodes were held in a fixed position against the fibre-optic light pipe, and the calibration curves shown refer to the photon output from the end of the light pipe. It can be seen that a wide range (10^{11} to 10^{17} photons $cm^{-2}s^{-1}$) of photon flux density was available, which could be easily controlled and monitored.

To study photomobilities and decay lifetimes, the steady state photocurrent ΔI_{ss} was modulated by less than 5%. This was achieved by superimposing a square wave upon the constant d.c. voltage across the LED. The pulse rep-rate was adjusted to ensure that the modulation decayed back to the previously attained steady state level between pulses. The modulated signals were recovered from background noise by a Brookdeal 9415/9425 box car noise recovery system (see figure 5.14). The averaged output signal was then plotted using a graph plotter.

In sputtered and vitreous samples the steady state photocurrent was allowed to decay down to the dark level and the half decaytime was obtained as described in subsection 3.1.12.

5.8 Thermoelectric Power

The thermoelectric power was determined by measuring the thermal e.m.f., ΔV, existing between two electrodes on the specimen when a temperature difference ΔT, was maintained between them. We

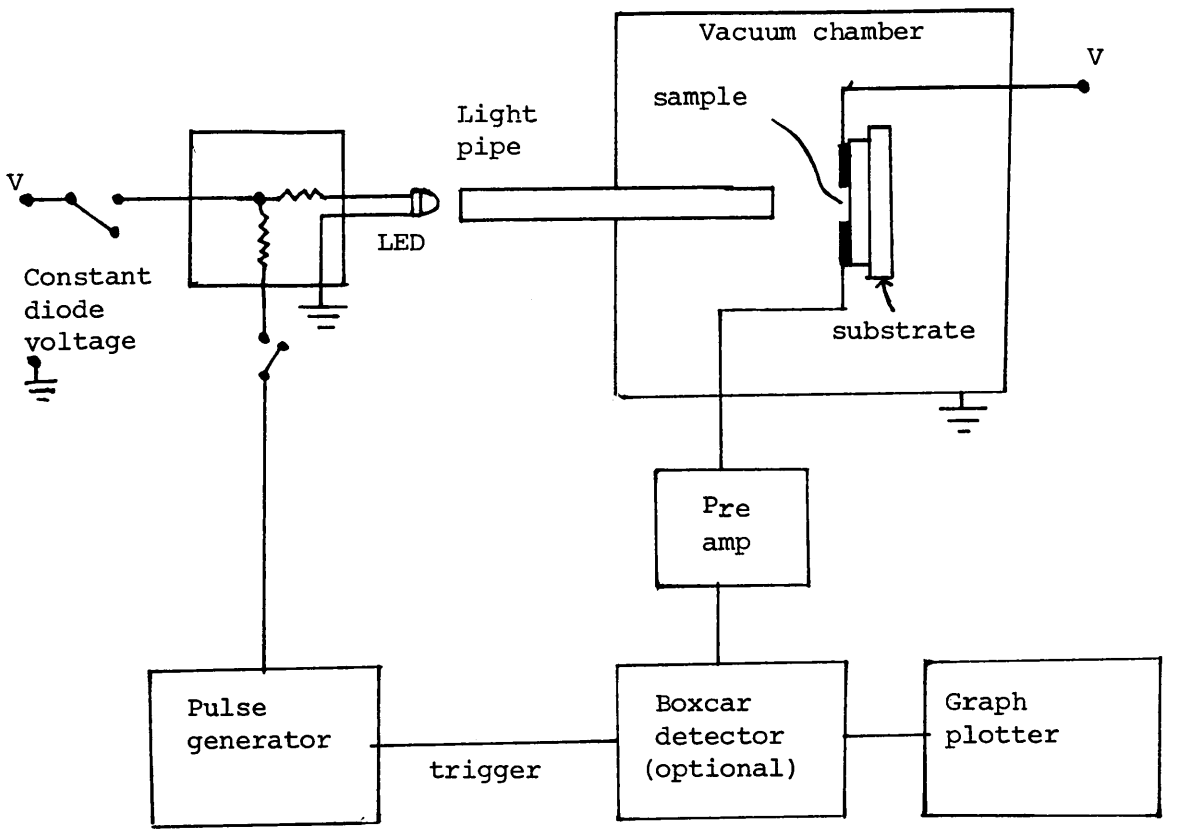

Figure 5.14
Arrangement used for transient photoconductivity experiment

then have $S=\Delta V/\Delta T$.

The Keithley electrometer was used to measure ΔV. For the case of the nickel doped samples where the signal was small (about 10 $\mu V/K$), the voltage was first amplified with a high input impedance amplifier (approx. $10^{12}\Omega$) before measurement with the Keithley.

Problems arose in the voltage measurements due to electrical noise pick-up, and precautions were taken, such as removing any wires in the chamber not used in the measurement, re-earthing the chamber and making sure that the thermocouples were properly isolated. Wide band electrodes were used successfully to decrease these noise effects.

Voltage measurements were recorded for various ΔT values with the temperature at the centre of the specimen being kept as constant as possible. A graph was then plotted of ΔV against ΔT for the set temperature at the centre of the specimen: the gradient being equal to the thermopower. This eliminated any problem caused by a background voltage. The thermopower was calculated using this method over a temperature range similar to that of the conductivity.

5.9 Optical Absorption

Measurements of optical transmission using thin films were carried out to determine the optical absorption coefficient (α) for various photon energies using a Pye Unicam S.P. 6-550 Spectrophotometer. Wavelengths of incident light ranging from 1000 nm to 195 nm could be used as required. The transmission T was measured at room temperature, and the absorption coefficient, at each photon

energy, was calculated using the following expression .

$$\alpha = \frac{1}{t} \ln (I/I_o)$$

Where t is the sample thickness and I the measured intensity.

The measurements were simply to give information about possible changes in the optical band gap with sample doping; for this reason absolute measurements were not attempted. Losses due to reflection and so forth were estimated by averaging a number of readings taken at long wavelengths (greater than 900nm) and taking this average as an estimate of the maximum transmitted intensity (Io). For thin films of nickel doped arsenic triselenide this method was unsuitable because the absorption co-efficient was high (about 10^4 cm^{-1} at 900nm for the 4.5% doped sample). For these specimens a unicam Spectrophotometer type S.P. 700., with a wavelength range of 500nm to 2500nm, was used. The author is grateful to Dr J T Edmond of Dundee University for performing these measurements. Losses due to reflection were again estimated by taking a number of readings at long wavelengths (greater than 2400nm).

Chapter 6

EXPERIMENTAL RESULTS AND DISCUSSION

6.1 Optical Absorption

Absorption data of the type described in subsection 1.8.1 page 25, have been obtained for r.f. sputtered and for annealed evaporated samples. The range of absorption coefficients obtained was typically from below $5x10^2$ cm^{-1} to $3x10^5$ cm^{-1}. This was achieved by using samples of varying thicknesses. The room temperature results are shown in figure 6.1.

It was found that the square law equation $\alpha h\nu = C_2(h - Eo_2)^2$ applied to all specimens. Results typical of this region are shown in figure 6.2 which is a plot of $(\alpha h\nu)^{1/2}$ v $h\nu$ for a sputtered and an annealed evaporated sample . For all specimens there was found to be no deviation from the square law at the highest absorption values measured. The values of Eo_2 and C_2 calculated from the graphs and values from the literature are presented below

	Eo_2	C_2
annealed (evaporated)	1.75eV	$6.1x10^5$
r.f. sputtered	1.75eV	$6.3x10^5$
r.f. sputtered[143]	1.76eV	$6.2x10^5$
bubbles [143]	1.73eV	$6.3x10^5$
$As_{43}Se_{57}$[143] (evaporated)	1.80eV	$8.1x10^5$

It was found for the sputtered samples that Eo_2 and C_2 did not vary for batches of samples prepared during different deposition 'runs', using the same sputtering conditions.

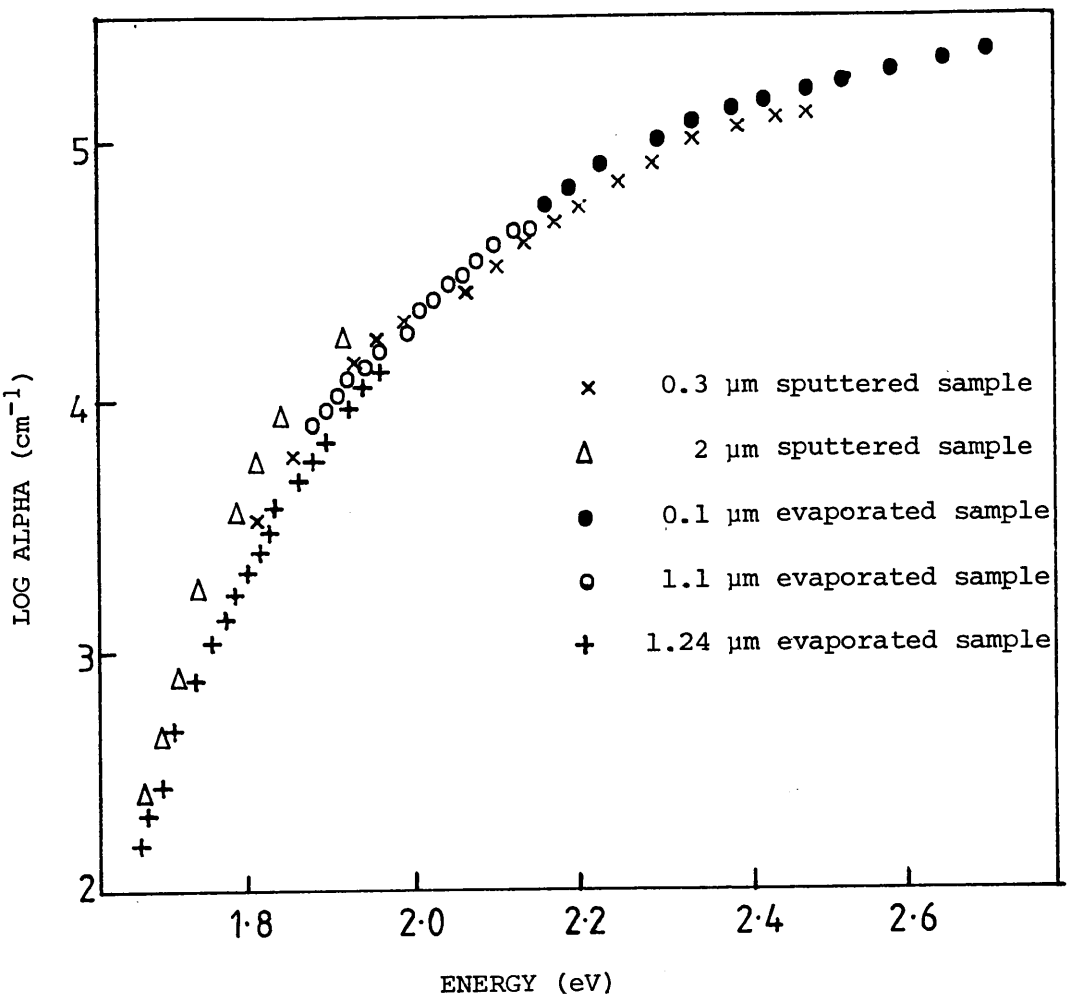

Figure 6.1

Graph showing the variation of the optical absorption coefficient with photon energy for various samples.

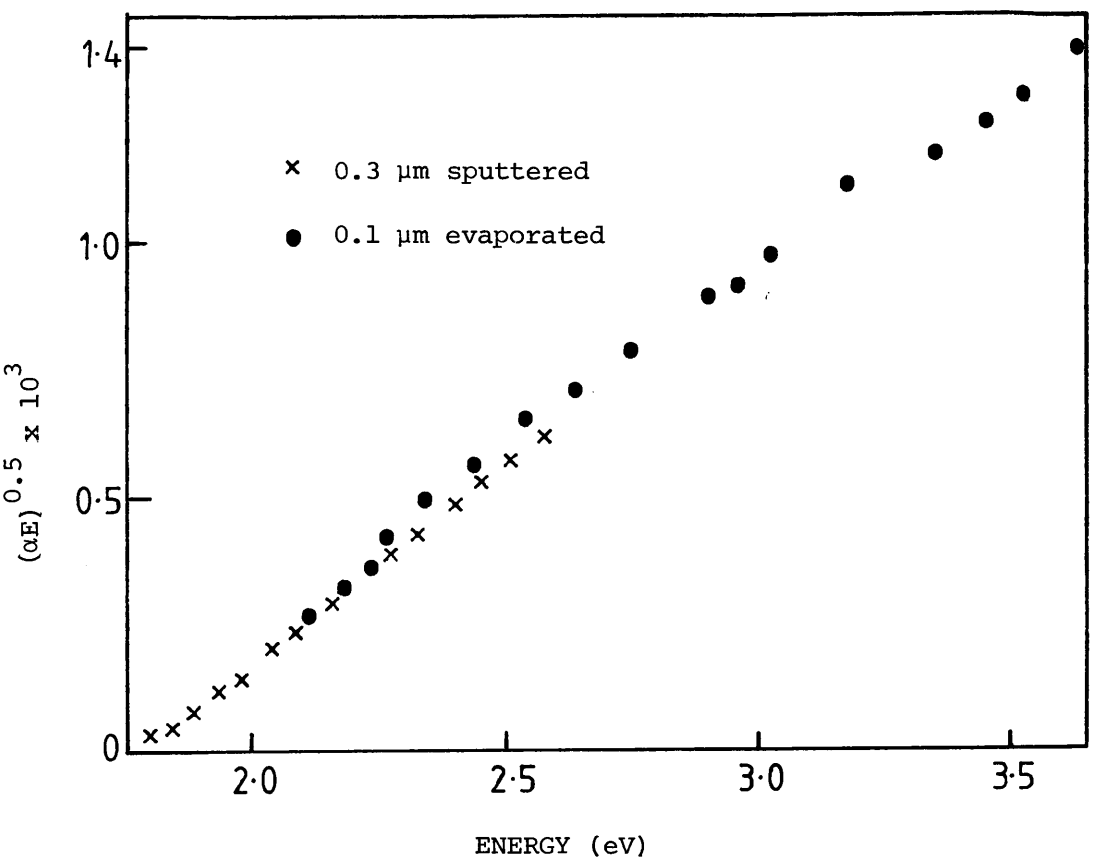

Figure 6.2

Graph showing square law behaviour over a wide range of photon energies.

6.2 Dark d.c. Conductivity

Dark d.c. conductivity measurements were made on both sandwich cell samples (as used for drift mobility experiments) and coplanar gap cell specimens. Figure 6.3 shows the temperature dependence of the d.c. conductivity for a 24 micron thick specimen of sputtered arsenic triselenide equipped with gold electrodes. This sample was prepared at an r.f power of 30 watts and an argon pressure of 12 microns, with the specimen substrate holder being held at room temperature.

At low applied field, the graph of $\log \sigma$ versus 1000/T is to a good approximation a straight line. The gradient of the 9.4×10^3 V/cm line corresponds to an activation energy of $0.91 \pm .02$eV calculated using a weighted least squares fit. The activation energy was found to depend on applied field in the manner shown in the insert of figure 6.3. The activation energy decreased linearly over the range of fields investigated. On extrapolation of these results to zero field an activation energy of 0.93eV is obtained.

At higher electric fields, there is strong evidence for a regime, below 298K, with an activation energy of $0.48 \pm .03$eV when extrapolated to zero field. An example of this is shown in figure 6.3 for measurements taken at a field of 1.25×10^5 V/cm.

Also shown in figure 6.3 is the variation of d.c. conductivity with temperature, obtained from measurements taken on a vitreous specimen. The applied electric field in this case is only slightly smaller than for the sputtered specimen being 1.22×10^5 V/cm

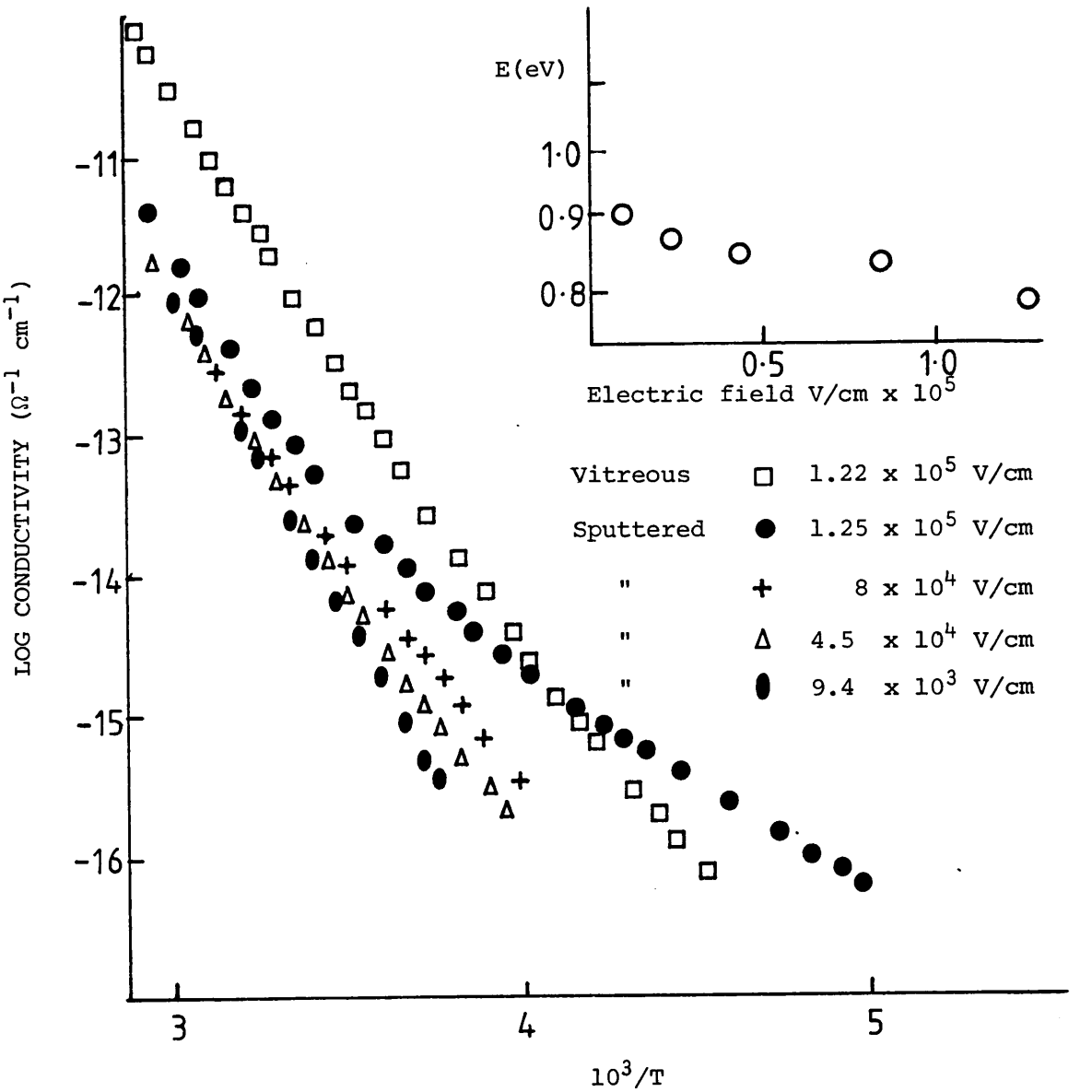

Figure 6.3

The temperature dependence of the conductivity for a sputtered sample and a vitreous sample. Insert shows the field dependence of the activation energy for the sputtered sample. The field at which the conductivity was measured is shown for each sample.

compared with 1.25×10^5 V/cm. There is also a second regime in this graph but this occurs at the lower temperature of 250K, compared with 298K in the sputtered sample. The activation energy is also higher, having a value of 0.65 ± 0.03eV when the field dependence is taken into account. In one of the conductivity curves, plotted from measurements on a sputtered sample taken at a field of 8×10^4 V/cm, there is also evidence of a regime with a similar activation energy of $0.63 \pm .03$ eV commencing at a temperature of 280K.

The conductivity vs 1/T graphs for annealed evaporated samples exhibited more curvature than in the case of vitreous samples making it difficult to distinguish between any regimes. In all the specimens studied, sputtered, vitreous and evaporated, the conductivity graphs exhibited continuous curvature at fields higher than 1.5×10^5 V/cm, down to the lowest current values measurable.

A computer analysis of the experimental d.c. conductivity vs 1/T curves was performed in order to determine whether they might reasonably be represented as a sum of pure exponentials. This analysis will be discussed in the next section of this report.

The field dependence of the conductivity at room temperature for sputtered, vitreous and annealed evaporated samples is shown in figure 6.4. This field dependence is in agreement with the dependence obtained by previous authors[61, 69, 71]. The conductivity is found to increase more steeply above 2.2×10^5 V/cm for the vitreous specimen. In the evaporated and the sputtered samples no sudden increase in conductivity was observed over the range of applied fields studied.

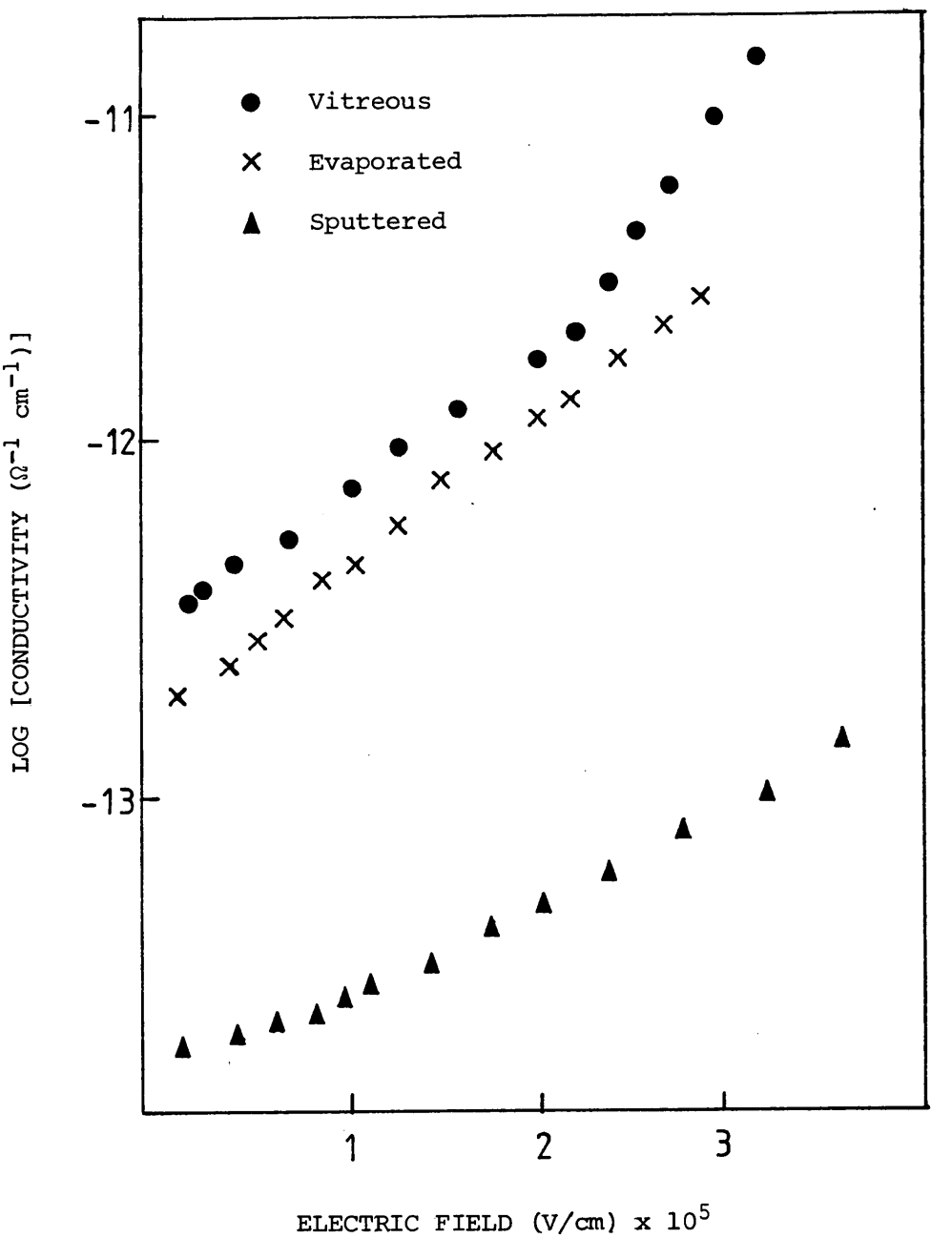

Figure 6.4
Graph of the field dependence of the d.c. conductivity for samples prepared by three different methods.

6.2.1 Analysis Of Conductivity Data

Most of the analysis in the previous section assumed the conductivity to be a sum of pure exponential functions with different activation energies and pre-exponential factors. Certainly in the graphs of figure 6.3 these exponential regions can be seen quite clearly. At higher fields the d.c. conductivity shows a continuous curvature which may contain more than two different exponentials. Halpern,[144] pointed out that a careful computer analysis of these conductivity curves might determine whether the conductivity was indeed a sum of pure exponentials. If so, this would support the view that a mobility edge model was more appropriate than a small polaron model.

The computer analysis was performed using a program developed by Provencher[60] at Heidelburg University. The program was designed to analyse data composed of random noise, plus an unknown baseline and a sum of exponential decay functions. The analysis of the sputtered sample data in figure 6.3 gave two components with zero field activation energies of 0.93$\pm$.02eV and 0.48$\pm$.03eV, the intercepts being 50-100 /Ωcm and 2.55×10^{-8} /Ωcm respectively. The program could not resolve the conductivity data (figure 6.3) for the vitreous specimen into two components, but when data taken at a lower applied field were used it gave an activation energy of 0.92$\pm$.02eV and intercept of 715 /Ωcm when corrected for zero field. All the analyses of the high field data failed to show that the curves were sums of pure exponentials.

The electric field dependence of the conductivity has been investigated by previous authors (for a review see chapter 2, section 2.3). The results presented in this report (figure 6.4) show exponential behaviour over the range of fields investigated in sputtered and annealed samples, but indicate a transition to much steeper behaviour at about 2.2×10^5 V/cm. Equation (2.9), page 42, was applied to the room temperature experimental data and values of a(T), corresponding to 20Å, 18Å and 22Å, were obtained for sputtered, vitreous and evaporated samples respectively. These results are similar within experimental error to the value of approximately 20Å obtained by Marshall, Fisher and Owen[63] at room temperature.

6.3 Drift Mobility Data

6.3.1 Vitreous Specimens

Drift mobility measurements were made by the TOF technique (described in Chapter 5). As in all previous investigations, no electron transit pulses could be detected.

Graphs of logI v logt for different temperatures are displayed in figure 6.5. The shapes of the transit pulses were found not to vary significantly with field, provided t_t was less than the dielectric relaxation time. If t_t were allowed to approach the dielectric relaxation time, the transit pulse would become more dispersive and the amount of dispersion would vary with applied field.

It is clear from figure 6.5, that the transit pulse becomes less dispersive with increasing temperature, the specimen being held at a field of 1.22×10^5 V/cm. The dispersion parameter was calculated

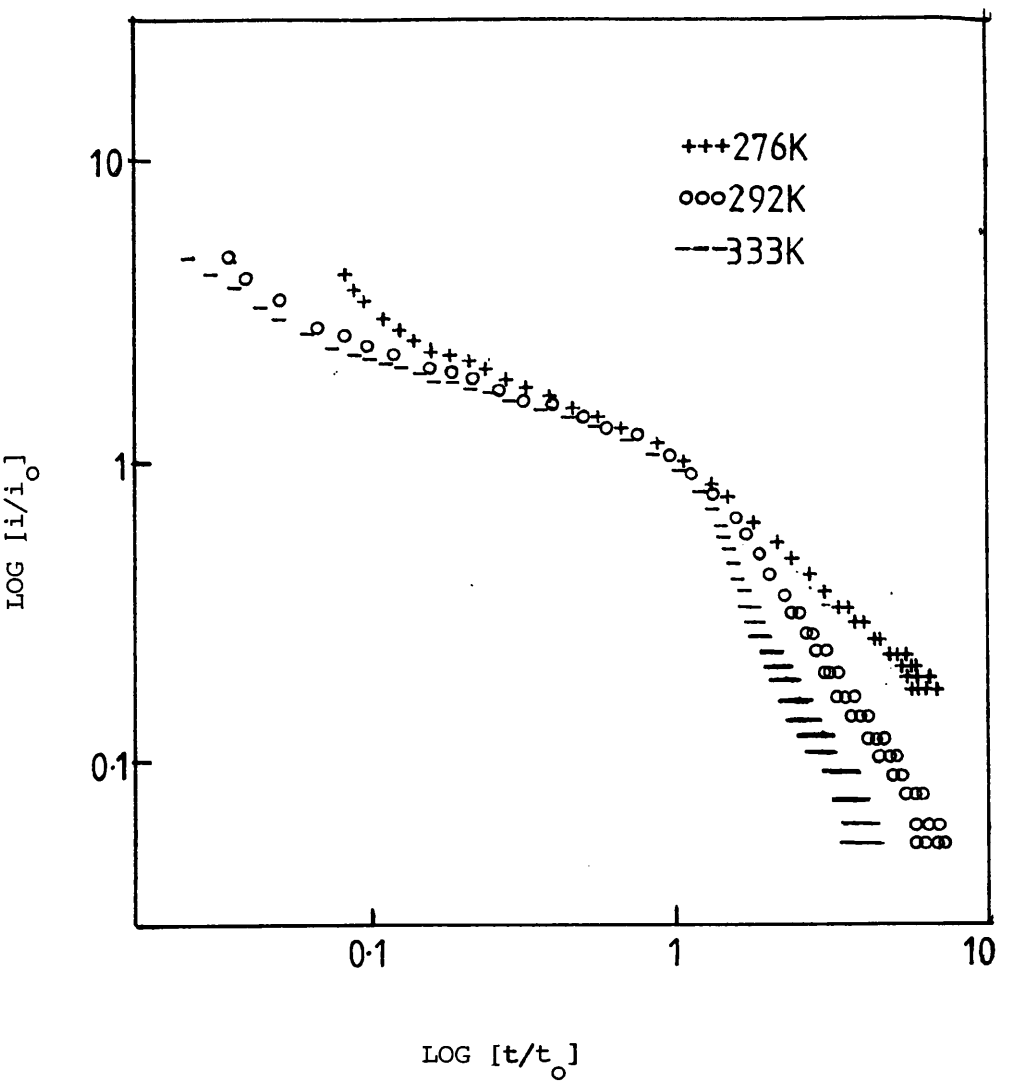

Figure 6.5

Logarithmic plot of transit pulses in vitreous As_2Se_3

from the initial slope as described in section 3.2. The value of α_2 obtained from the second slope is very sensitive to choice of current baseline and also to baseline noise. Nevertheless if the experimental procedure is arranged so that the background dark current is used as the baseline, reproducible results can be obtained. Figure 6.9 shows that α_2 varies more rapidly with temperature than α_1.

Figure 6.6 shows the temperature dependence of the hole drift mobility, as calculated using t_t obtained from the break in the log/log graphs. This gave an extrapolated zero field activation energy of 0.61±.02 eV with a pre-exponential of 11,000±1000 $cm^2V^{-1}s^{-1}$ over the range of temperatures for which an accurate determination of the transit time could be obtained. Below 280K, baseline noise became more prominent and distorted the shape of the transit pulse giving a false reading of t_t.

6.3.2 Annealed Evaporated Specimens

In these specimens the "knee" in the transit pulse was more prominent than in the vitreous samples and the transit pulse time could easily be obtained from the end of the plateau region. Thus at a particular temperature the variation of drift mobility with applied field could be obtained and extrapolated back to zero field. Figure 6.7, which shows the variation of zero field mobility with temperature, exhibits three regimes. The first for temperatures up to 305K, has an activation energy of 0.43±.03 eV, the second from 305K to 350K has an activation energy of.62 ±.02 eV and the third is an artifact showing the effect of further annealing on the sample. The pre-exponentials of the first two mentioned regimes are 200 $cm^2V^{-1}s^{-1}$

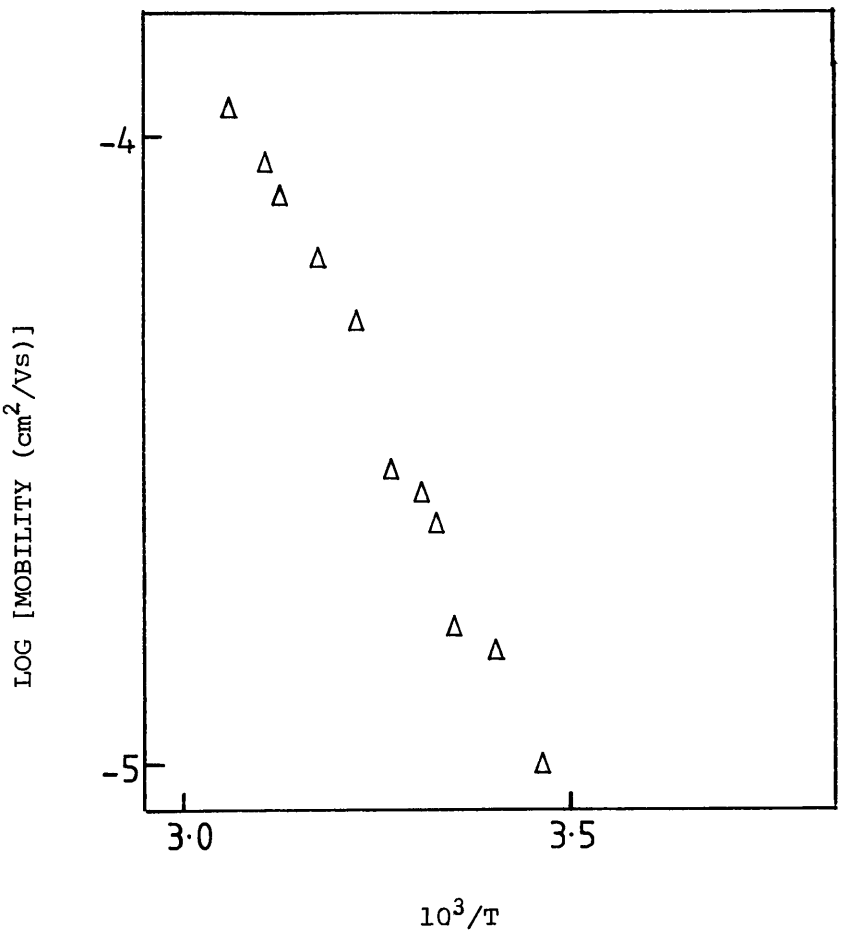

Figure 6.6

The temperature dependence of the hole drift mobility in vitreous As_2Se_3

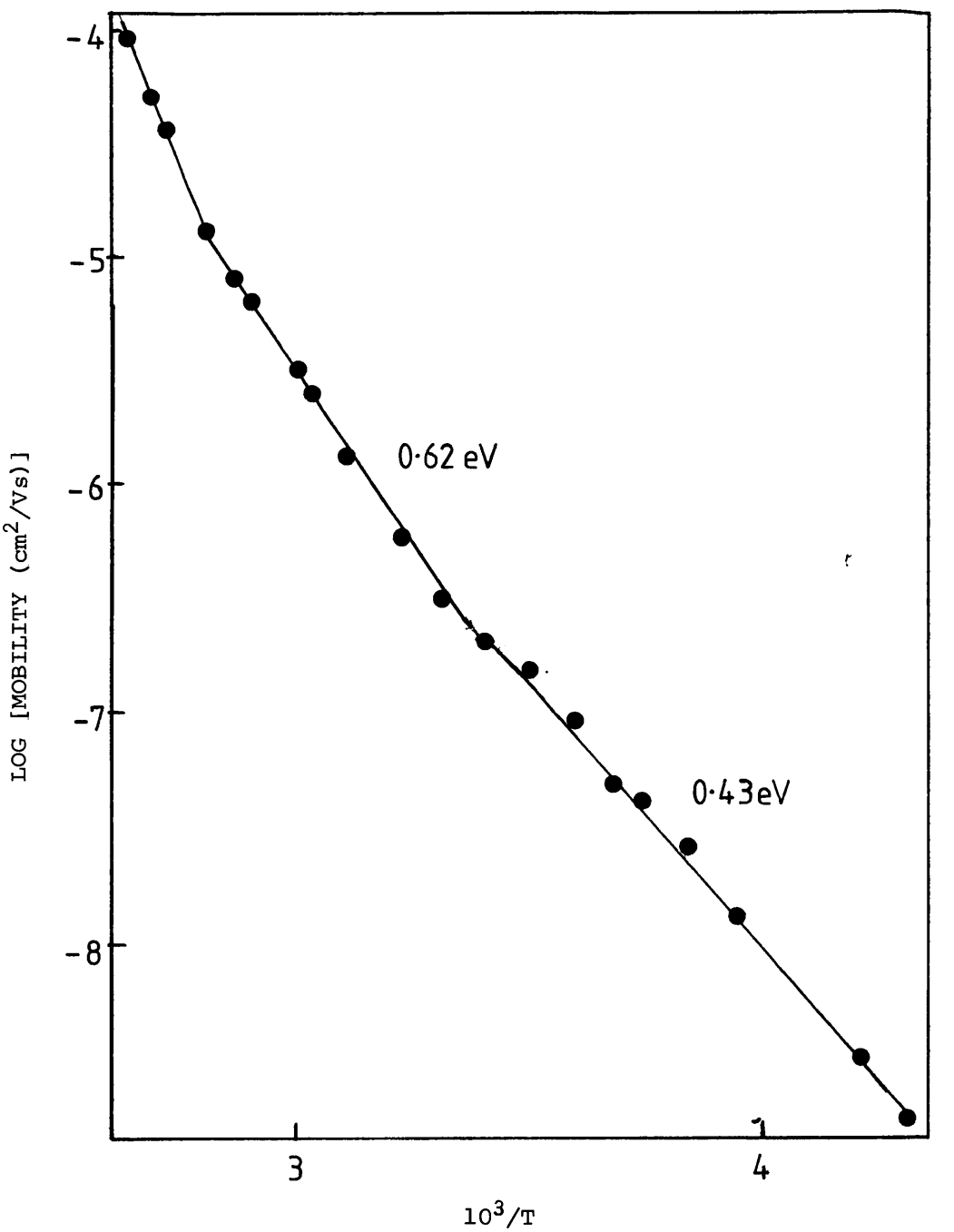

Figure 6.7

Temperature dependence of the drift mobility in an annealed evaporated specimen showing three activated regimes.

and 8200 $cm^2V^{-1}s^{-1}$ respectively.

6.3.3 Sputtered Specimens

It proved extremely difficult to observe transit pulses in sputtered material. Many samples were investigated and in the few cases where transit pulses were observed, the transient response obtained for both polarities of applied field decreased rapidly specimens and measurement was very difficult. Even with a detection network response time of about 0.5xEμs, using the oscilloscope amplifier (bandwidth 1MHz), the transient response appeared to have decayed to zero in a shorter time. From the few measurements that were performed in the temperature range 200K to 350K, it was found that the pulse duration and pulse shape did not change with temperature. Also the pulse amplitude scaled approximately linearly with field strength while the pulse duration remained unaffected.

This type of fast decaying transit pulse could originate from one of two sources. Firstly, the carriers could recombine (geminate recombination), or they could become trapped at the surface of the specimen. The traps at the surface would be 'deep' (in terms of energy) causing a gradual build up of charge in such centers during successive transits which will modify the internal field, so that the assumption of a uniform field is not valid. The precautions suggested in chapter 5 to eliminate such an effect were applied but did not alter the shape of the observed transit pulse. One can can only therefore assume that the traps at the surface are of fairly high density and of such a 'deep' nature that they have the ability to hold charge for a considerable period of time (in which recombination may

occur before the carriers are released). Thus during the first transit most of the carriers are trapped in these surface states giving a resultant electrical field which is extremely small at this part of the specimen. The chances of observing a transit pulse would therefore depend on the density of these 'deep' surface states, which would vary from sample to sample. This could explain why no transit pulse was observed in some samples.

Secondly, the observed current pulse may be due to rapid trapping and recombination of the carriers in the bulk sample. This again would involve centres with very long release times. The traps concerned would be deep, preventing the thermal release of carriers back into the extended states to recontribute to the conductivity, over an experimentally realistic time period: i.e until recombination processes become dominant.

In order to gain insight as to which of the above two mechanisms is occurring (if any), it is concluded that information must first be obtained about carrier lifetimes and mobilities, using an independent experimental technique. Both transient and steady state photoconductivity measurements were performed in order to extract this information. We shall return to the discussion later (see section 7.6).

6.4 Transient Photocurrent

6.4.1 Vitreous Specimens

Measurement of the photocurrent following excitation by a short flash was performed over a wide range of temperatures from 390K

to 106K. Two gold electrodes 1.5 mm apart provided electrical contact on a 0.5mm thick sample. In figure 6.8 the photocurrent is plotted against time for five different temperatures, the voltage across the specimen being 1000 V. It is interesting to note that the decays are not featureless as suggested by Orenstein et al[137], but there is some evidence of structure. It is clear that the current does not decrease as a power law over all the temperatures for which the photocurrent was studied. This is especially noticeable in the 383K and the 336K curves in which one has difficulty in fitted a power law over more than two decades. Below approximately 298K one can easily fit a power law to the results and calculate the dispersion parameter α(TP). Figure 6.9 shows the variation of the dispersion parameter with temperature calculated using this method. A break in the log/log plot of the 383K photodecay also occurs at approximately 6ms. These deviations from power law behaviour may be due to either discrete trapping or recombination. An investigation of decaytimes from the steady state photoconductivity is capable of giving evidence as to which mechanism is responsible (see section 7.5).

6.4.2 Evaporated Specimens

Figure 6.10 shows the decay of the photocurrent for an evaporated sample at four different temperatures. The sample had a 60 micron gap and a field of 5×10^4 V/cm was applied. Above room temperature, the photocurrent clearly deviates from a power law dependence at shorter times. For the 368K decay there appears to be a feature between 10 ms and 100 ms, but this is probably due to some recombination mechanism. The other curves below 345K appear quite

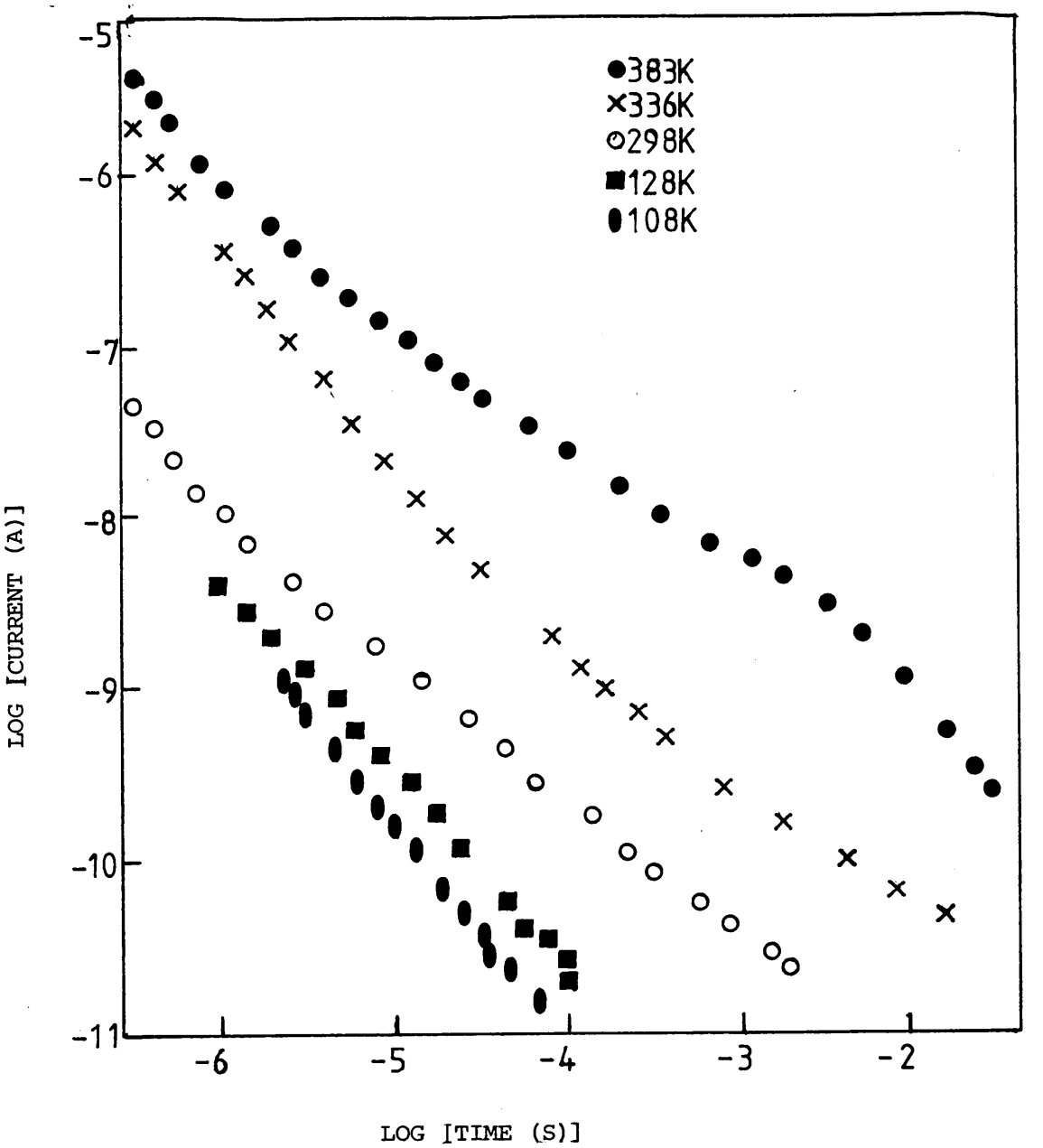

Figure 6.8

Decay of the transient photocurrent showing deviations from power law behaviour for a vitreous specimen.

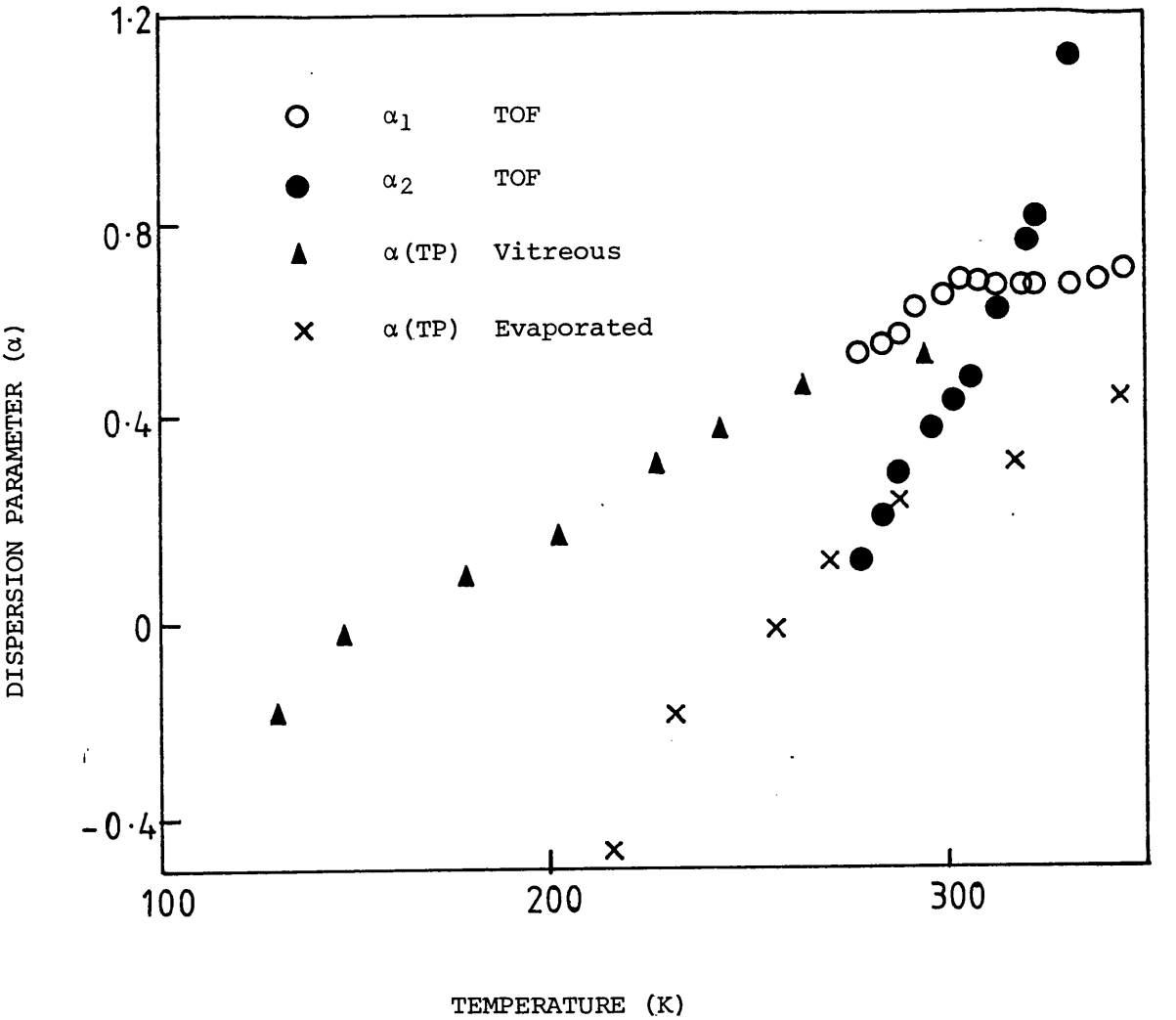

Figure 6.9

The variation of the dispersion parameter (α) with temperature as measured using the TOF and TP techniques.

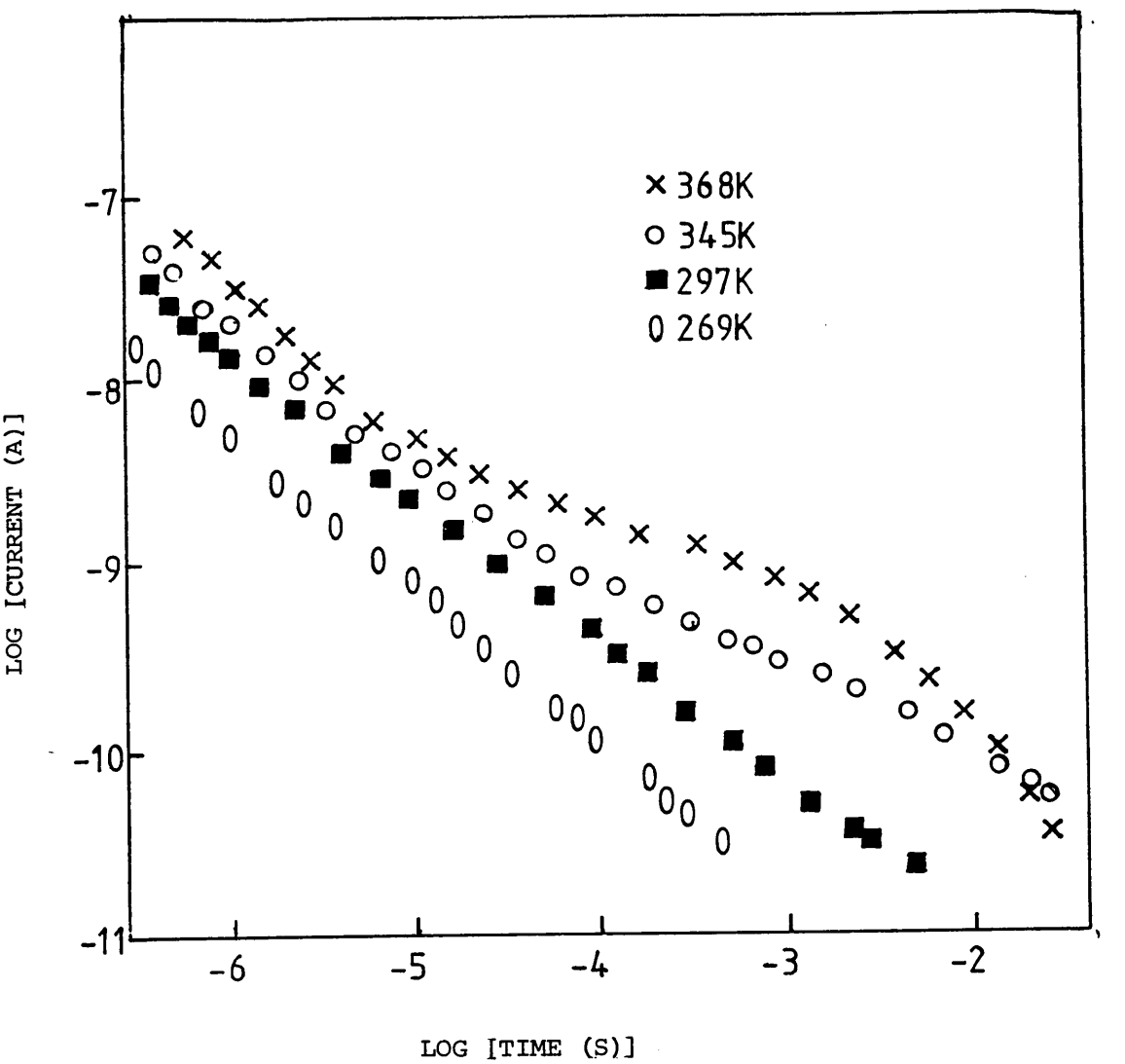

Figure 6.10

The decay of the photocurrent for an evaporated sample at four different temperatures.

featureless. The best straight line was drawn through the decays below room temperature and the dispersion parameter (α) was calculated. It can be seen from figure 6.9, which is a plot of (α) v T, that is much smaller in the evaporated sample than in the vitreous sample.

6.4.3 Sputtered Specimens

At low applied fields it was very difficult to measure the TP because of the small magnitude of the signal over the accessible time range. Measurements were made on a 60 micron gap cell at a field of $5.x10^4$ V/cm and these results are shown in figure 6.11 for three different temperatures. There is a "bump" present in the decay of the photocurrent, the position in time of which varied significantly with temperature, changing from 0.7ms at 300K to 0.08ms at 345K. An activation energy of $0.38\pm.03$ eV was calculated from the temperature variation of this time, using all the results obtained experimentally. This gives an activation energy of $0.42\pm.03$ eV when corrected to zero field. Again this suggests the presence of structure in the density of states in the absence of recombination.

The magnitude of the signal decreased rapidly as the temperature was lowered until it became experimentally inaccessible (below room temperature). An amplifier with a very fast response time and a non-integrated output would aid in obtaining results at these temperatures and also in measurements of TOF (unfortunately such an amplifier was not available during the period of this study).

6.5 Photomobilities, Decaytimes and Steady State Photoconductivity

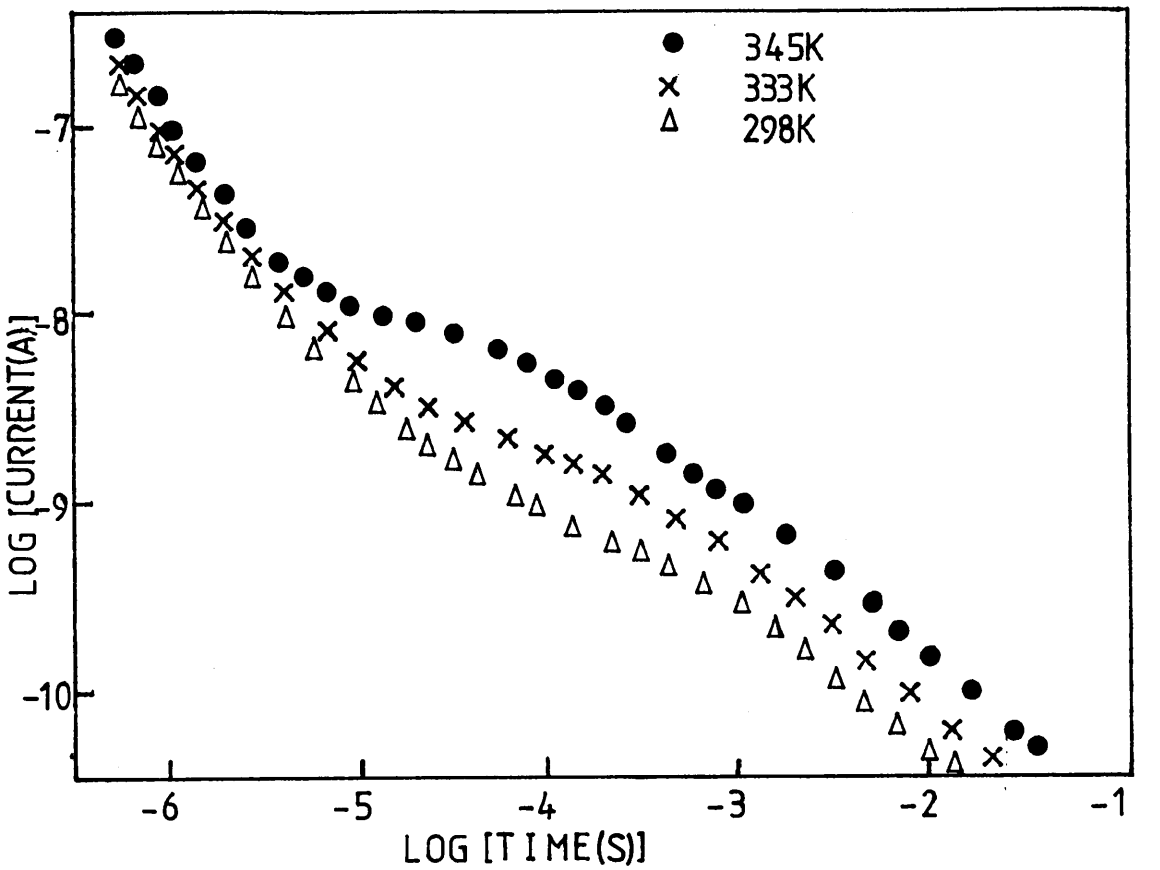

Figure 6.11

The decay of the photocurrent measured at three different temperatures for the r.f. sputtered sample. The position of the 'bump' varies with temperature.

6.5.1 Sputtered Specimens

Films approximately 2-10 microns thick with coplanar gold electrodes (typical gap 60 μm) were investigated.

The Steady State photocurrent versus photon flux, for temperatures 293K and 333K, presented in figure 6.12., illustrates that the square root behaviour, indicative of the bimolecular regime, obtained over the range of photon flux employed. Figure 6.13 shows the temperature dependence of the steady state photocurrent ΔI_{ss} and the increment value ΔI_{ss} for a steady state photon flux of $2x10^{15}cm^{-2}s^{-1}$ with the incremental photon flux being $2x10^{14}cm^{-2}s^{-1}$. The zero field activation energies obtained were 0.24 $\pm$.02 eV and 0.25$\pm$.02 eV respectively. Thus they agree within experimental error. The activation energy of ΔI_{ss} varied only by about 0.03 eV over a photon flux range of $8x10^{13}cm^{-2}s^{-1}$ to $1x10^{15}cm^{-2}s^{-1}$. An upper limit of temperature of 343 K was set so that erroneous results were not obtained due to annealing effects [103]. This meant that the change from square root to linear behaviour, expected at higher temperatures [49], could not be investigated.

Photomobilities were calculated from the rise of the increment, using equation (3.26), assuming a quantum efficiency of 1 and a (1-R) value of 0.75 [49]. The trap limited mobility has a room temperature value of $3x10^{-5}$ cm^2/Vs and an activation energy of 0.33$\pm$.03 eV as can be observed in figure 6.14. The dependence of photomobility on applied field was measured at four different temperatures and a zero field photomobility was obtained by

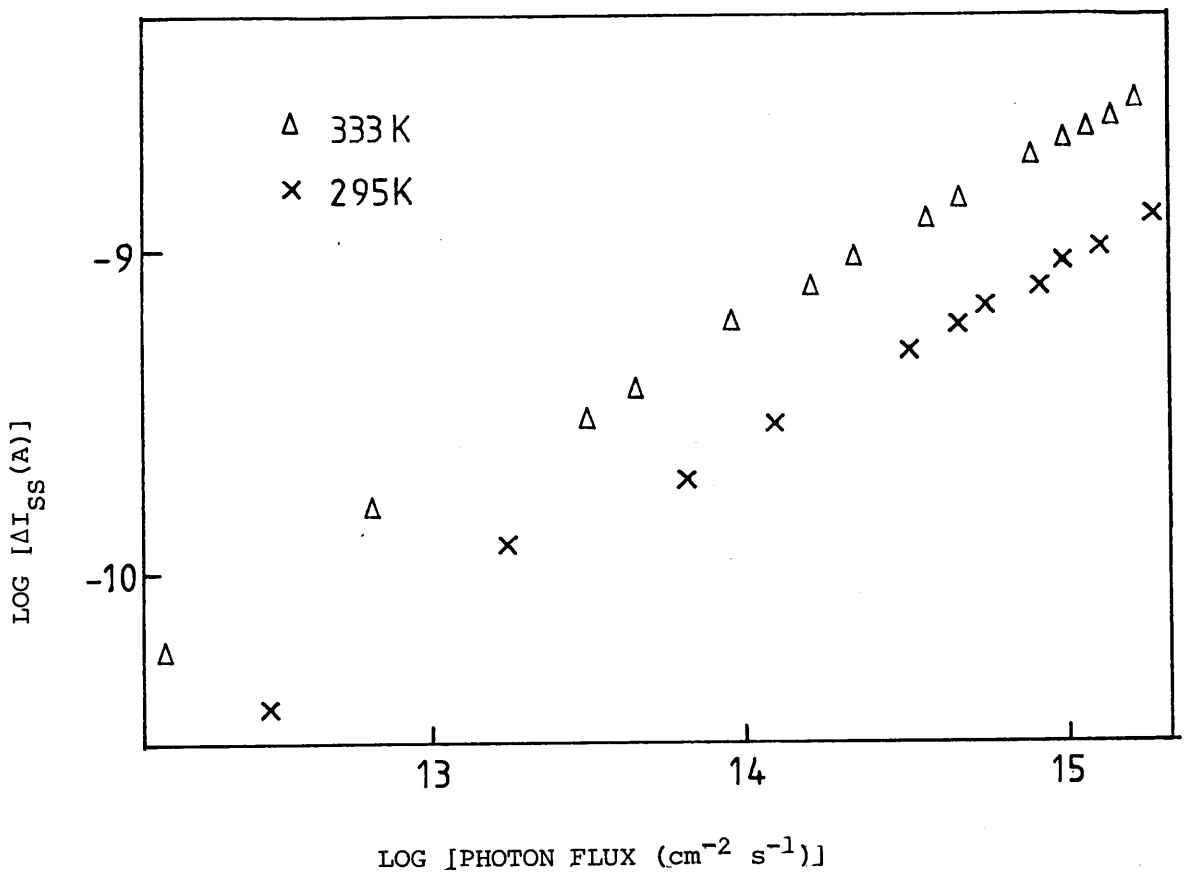

Figure 6.12

Variation of photocurrent with photon flux density.

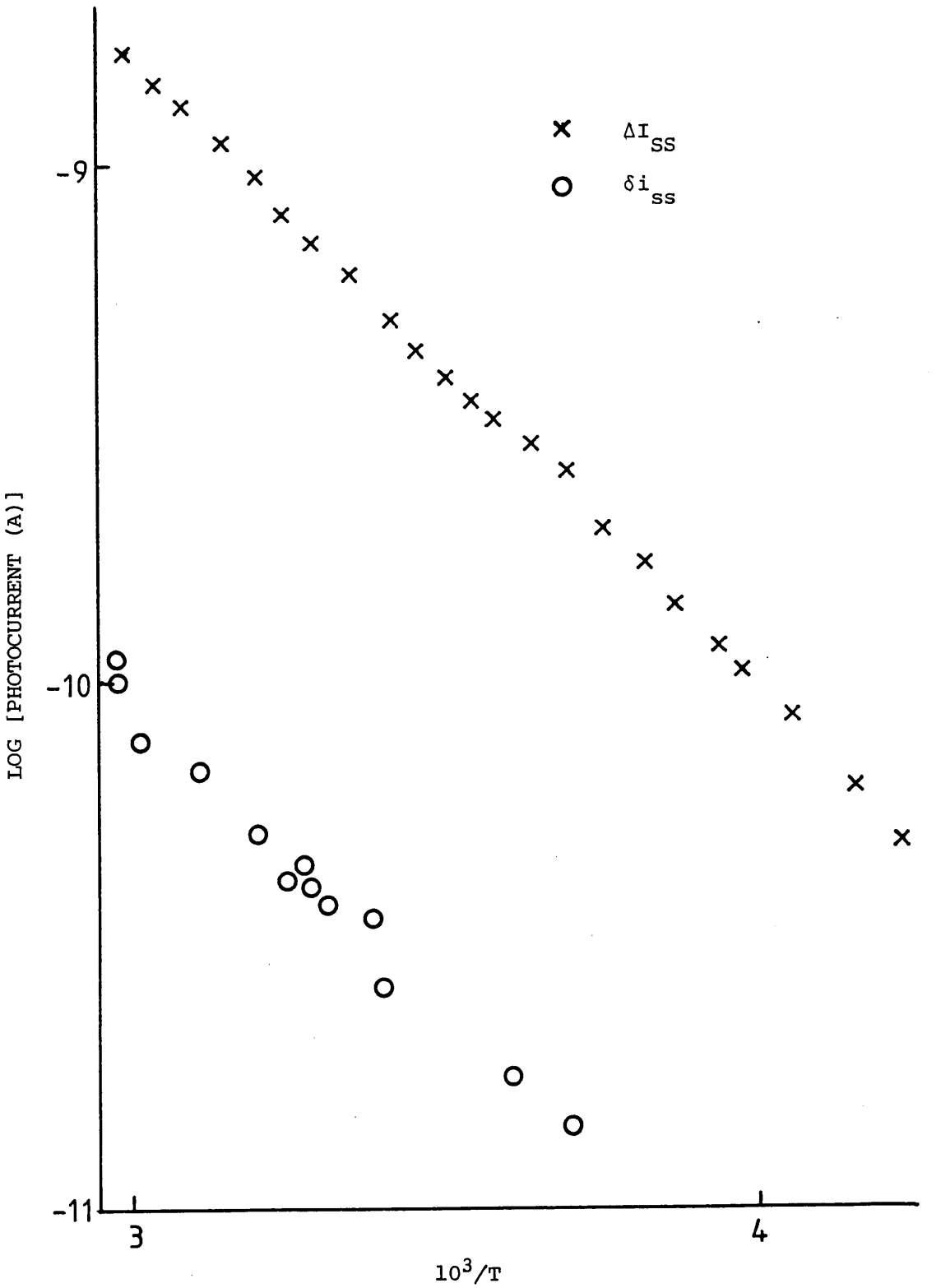

Figure 6.13

The temperature dependence of the steady state photocurrent.

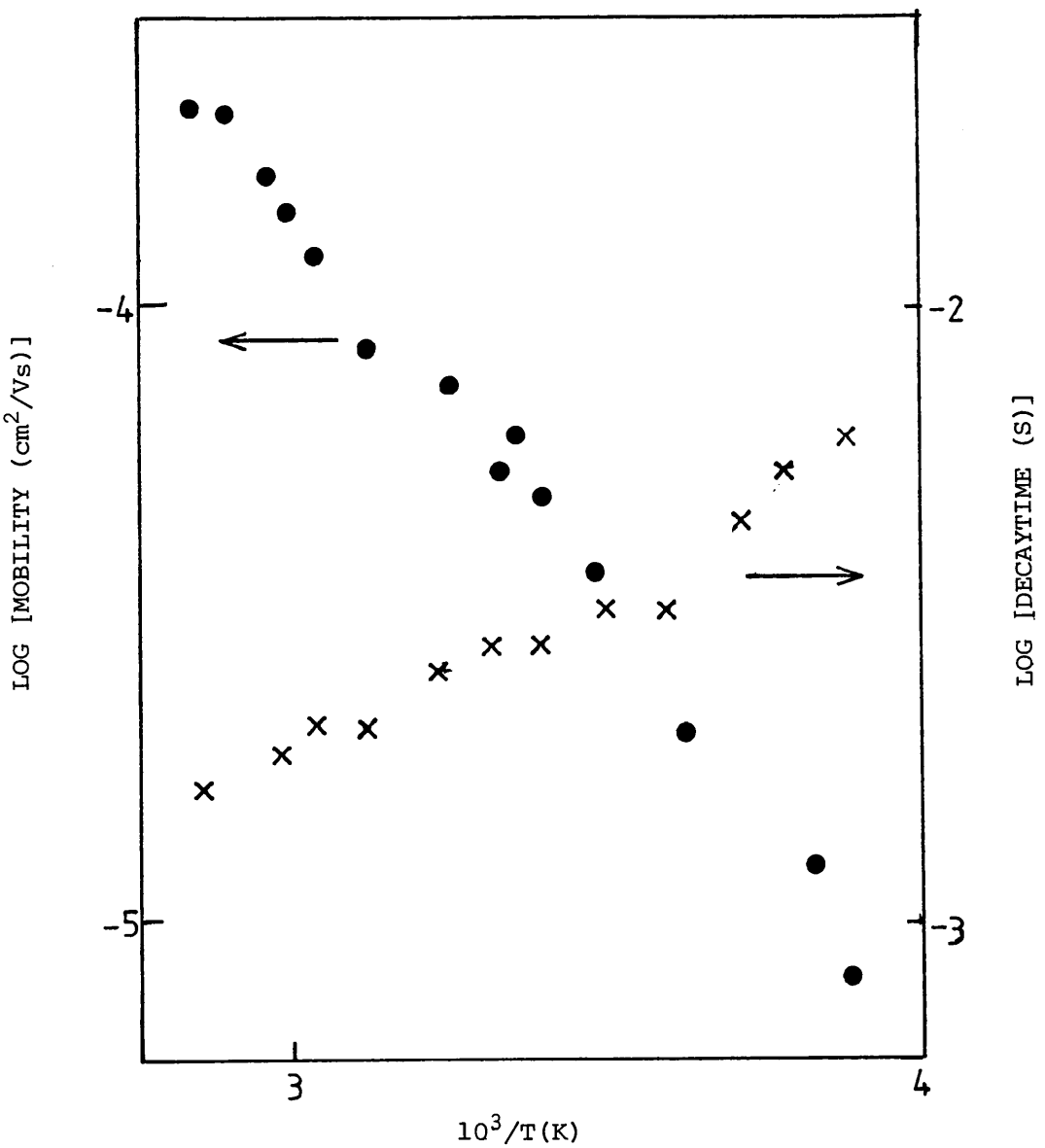

Figure 6.14

The temperature dependence of the photomobility and the decaytime in sputtered As_2Se_3.

extrapolation. This zero field mobility had an activation energy of 0.44eV with a pre-exponential factor of 10 ± 5 cm^2/Vs. To obtain a decay time an exponential law was fitted to the decay of the increment and equation (3.39) was used to calculate τ. The variation of decaytime with temperature is shown in figure 6.14 and gives a calculated activation energy of $0.11\pm.01$ eV. The decaytime activation energy appeared to be almost independent of applied field and intensity varying only by about 0.01eV over the whole range of fields and intensities investigated.

6.5.2 Vitreous Specimens

Measurements of ΔI_{ss} and the half decaytime were performed on the 1.5 mm gap cell sample described in section 6.4, page 143. Figure 6.15 shows the temperature dependencies of ΔI_{ss} and τ_{cb} measured at a photon flux of $2x10^{15}cm^{-2}s^{-1}$ and a field of $7x10^3V/cm$. These graphs exhibit activation energies of $0.31\pm.02$ eV and $0.14\pm.01$eV respectively. It is interesting to note that the 293K value of decaytime, is about 10 times smaller than that measured at an equivalent temperature in the sputtered specimen.

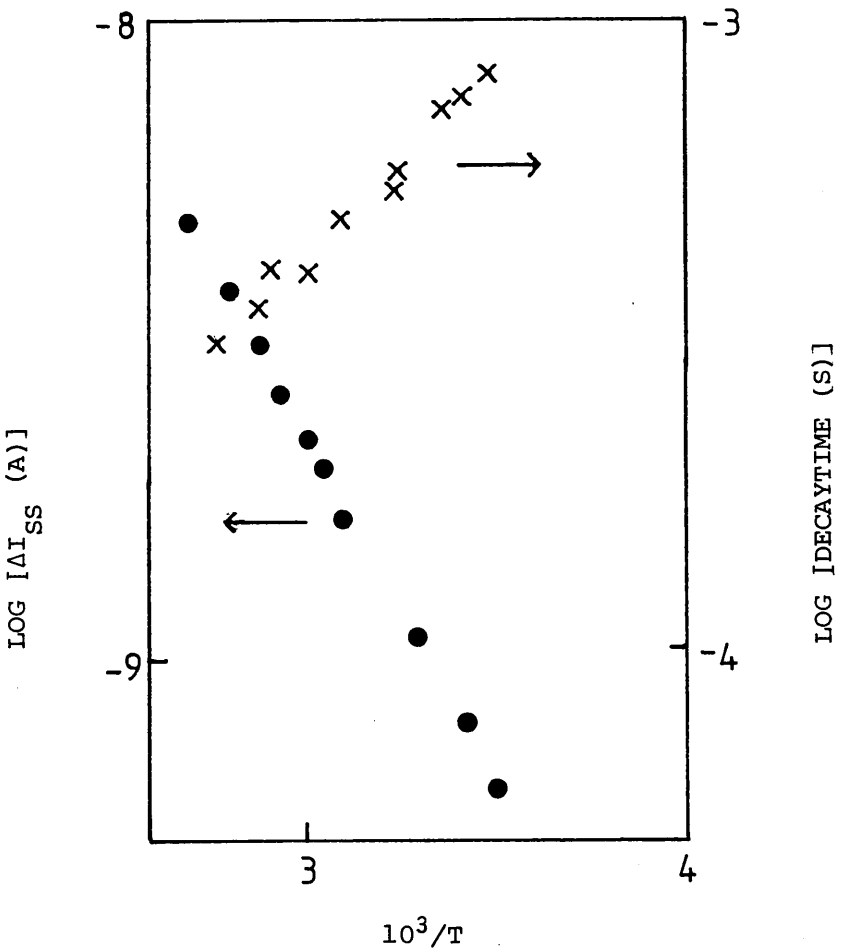

Figure 6.15
The variation of the steady state photocurrent and the half decaytime with temperature in the vitreous specimen.

Chapter 7

DISCUSSION OF RESULTS

7.1 Optical Absorption

It can be seen from figure 6.1 that the optical absorption coefficient α rises exponentially with increasing photon energy up to a value approximately $5x10^3$ cm^{-1} for both evaporated and sputtered specimens of varying thicknesses.

At higher values of absorption coefficient the square law is shown to hold over the experimentally accessible range of photon energies. The results, from page 136, show remarkable agreement of Eo_2 and C_2 between the samples despite vastly different preparation conditions. In a detailed study, of AsSe complexes, Petursson [143] found Eo_2 and C_2 to vary with composition and temperature. The good agreement between the values, shown on page 136, suggests that the composition of the evaporated and sputtered does not vary significantly from that of the bulk material.

7.2 Conductivity and Drift Mobility

Previous attempts to explain electronic transport in arsenic triselenide have been based on four models.

1) Trap-limited band motion (multiple trapping).

2) Trap-limited hopping conduction.

3) Hopping conduction between localised states.

4) Small polaron hopping conduction.

The experimental results obtained in this study will be explained mainly in terms of trap-limited band motion but arguments for and against the other models will be given.

In all specimens studied, vitreous, evaporated and sputtered the, low field, high temperature, conductivity data obeys the relationship

$$\sigma = \sigma_o \exp.(-\Delta E/kT)$$

Knowing that $\sigma_o = \sigma_{min}.\exp[\gamma/2k]$, and that γ is in the range $4.5\text{-}6\times10^{-4}$eVK^{-1}, σ_{min} can be calculated.

In vitreous and annealed evaporated specimens the magnitude of σ_o was found to be similar, being in the range 550-750/Ωcm and this value is in good agreement with that obtained from previous measurements[69, 59]. Thus the magnitude of σ_{min} is in the range 20-60/Ωcm. This value suggests that carrier transport occurs in the extended states rather than by a process of thermally activated hopping between localised states in the mobility gap, σ_{min} being two to three orders of magnitude greater than one would expect for hopping conduction. It must also be stressed, at this point, that the value of σ_o is also compatible with small polaron hopping. The conductivity activation energy in this case, ΔE, is attributed to being the sum of energy required to generate the carriers and the hopping energy W. In this regime, the adiabatic regime, $\rho = 1$, (see subsection 1.6.3, equations (1.33) and (1.34)) and Emin [28] has predicted σ_o to be in the range 10^2-10^3

It was shown in section 6.3 that the hole drift mobility for

vitreous specimens had a zero field activation energy of 0.61eV and a pre-exponential of 11000 $cm^2V^{-1}s^{-1}$ above 280K. The evaporated sample had an activation energy of 0.62eV between 305K and 350K and 0.43 below 305K; the pre-exponentials being 8200 $cm^2V^{-1}s^{-1}$ and 200 $cm^2V^{-1}s^{-1}$ respectively. These values of pre-exponentials are again compatible with trap-limited band transport, but because the pre-exponential contains ratios such as N_c/N_t (see next paragraph), in addition to the 'free' mobility itself, it must again be stressed that they are also compatible with small polaron hopping motion.

The exact form of drift mobility from a trap controlled transport mechanism depends upon the energetic distribution of localised states within the material. In the case of a well defined set of traps of density N_t situated at an energy E_t from the edge of the conduction band, the drift mobility is given by expression (7.1).

$$\mu_d = \mu_0 (N_v/N_t) \exp(-E_t/kT) \quad (7.1)$$

To get meaningful quantitative estimates of the densities of traps and transport states in a multiple trapping mechanism from measurements of the d.c. conductivity and drift mobility, it is necessary to make the assumption that the carriers involved in the mobility and conductivity measurements move through the same conduction path. This assumption can only really be justified by comparing how well the trap densities calculated on the basis of this model compare with other estimates from different experiments. Using expression (7.1) it is possible to determine the trap density from combined conductivity and mobility measurements , since $\sigma_0 = N_v e \mu_0$ (if we assume that the conduction is by

holes only). Then one obtains expression (7.2)

$$N_t = \frac{\sigma}{e\mu_d} \exp\left[(E_\sigma - E_t)/kT\right] \qquad (7.2)$$

From a graph of $\log(\sigma/\mu_d)$ versus 1/T drawn for data from the vitreous specimen, a value of N_t was obtained from the intercept on the 1/T=0 axis on extrapolating the high temperature results. Values of $N_t = 4 \pm 1 \times 10^{16} cm^{-3}$ and $\mu_o N_v = 4 \pm 1 \times 10^{20}$/V cm s were obtained (since $\mu_o N_v / N_t = 11{,}000$ $cm^2 V^{-1} s^{-1}$). To take account of the temperature dilation of the mobility gap the $\mu_o N_v$ value was corrected by the factor exp.(γ/2k) (where $\gamma = -6 \times 10^{-4} eVK^{-1}$) and the N_t value by an approximate factor exp.(γ/4k) to allow for the traps being closer to E_F than the mobility edge. Values of $\mu_o N_v = 1.4 \times 10^{19}$/V cm s and $N_t = 1 \times 10^{16} cm^{-3}$ were obtained for the trap densities.

In the annealed evaporated sample, three activated regions of mobility were observed, but it was impossible to distinguish between any regimes in the conductivity graph which exhibited continuous curvature. If one assumes $\mu_o N_v$ to be similar to that obtained in the vitreous specimen one can calculate trap densities from the mobility pre-exponentials. A trap density of $1.3 \times 10^{16} cm^{-3}$ was calculated for the 0.62 eV trap level, again taking into account temperature dilation of the mobility gap. Below 305K the 0.43eV trapping level dominates and exhibits a trap density N_t of $9 \times 10^{17} cm^{-3}$, after adjusting N_t via a factor of exp(γ/6k) to take account of temperature dilation of the mobility gap.

In r.f. sputtered specimens σ_o was found to be in the range

$50\text{-}100\Omega^{-1}cm^{-1}$. This is about two orders of magnitude higher than one would expect for hopping conduction and seems somewhat lower than one would expect for a trap limited band mechanism. Unfortunately the drift mobility could not be measured in these samples via the time of flight experiment, but a photo-mobility with an activation energy of 0.44eV and a pre-exponential factor of 10 $cm^2V^{-1}s^{-1}$ was measured. This value of pre-exponential is again three to four orders of magnitude higher than one would expect from hopping between localised states. Interpretation of this data using the trap limited band transport mechanism, assuming $\mu o=1cm^2V^{-1}s^{-1}$ in the random phase region, and using equation (7.1) yields a trap density of $8x10^{18}$ to $2x10^{19}$ cm^{-3} giving values of $N_v=8x10^{19}\text{-}2x10^{20}cm^{-3}$ This trap density is higher than but in order of magnitude agreement with, the density calculated for the 0.43eV trap level in the evaporated sample. This density is large, but is an order of magnitude less than the effective density of states at the edge of the valence band.

7.3 Dispersive Transport

Figure 6.9 shows how the dispersion parameters α_1 and α_2 vary with temperature in vitreous arsenic triselenide. It can be seen quite clearly from the graph that α_1 and α_2 are not similar in magnitude as predicted by Scher and Montroll[5] for R and E hopping mechanisms, but α_2 varies more rapidly with temperature than α_1. A similar variation in α_1 has been seen previously,[73] but such a rapid variation in α_2 has never been reported before in arsenic triselenide.

It was stated in section 3.2 of this report that the mechanism of trap limited band transport is now widely accepted as

giving rise to anomalously dispersive transport and that this form of transport has been assumed to take place by various authors who claimed that the power law behaviour constituted evidence for an exponential distribution of localised states. It has since been shown that various distributions of localised states can give rise to power law behaviour, and that only a detailed study of the variation of the dispersion parameters with temperature allows the possibility of differentiating between specific distributions of localised states. The variation of α with temperature presented in this study suggests that definite structure exists in the density of states at an energy level of 0.61 eV, as obtained from the temperature dependence of the drift mobility. Further evidence against an exponential distribution of states can be seen in figures 6.8, 6.9 and 6.11, showing clearly that the transient photocurrent does not decay as a power law over the time scale of the experiment for vitreous, evaporated and sputtered specimens. For the measurements taken from vitreous and evaporated samples, power laws can be fitted over at least two decades, but at temperatures above 300K the power law is preceded by a region of more rapid decay.

Deviations from power law behaviour can also be observed in the initial regions of the time of flight transit pulses shown in figure 6.5.

It has very recently been suggested by Khan, Kastner and Adler[145], that this deviation at shorter time is due to contact induced effects. These authors claim to find consistent results from

the TOF and TP, provided genuinely blocking contacts are used. The films used in that particular study were 1-2 microns thick with a gap of 33 microns being used in the TP experiment. The results presented show power law behaviour over three orders of magnitude from 10 μs to 1 ms. No TP data are presented at times shorter than 10 μs, and from the TOF data only data taken at 350K include measurements taken at times shorter than 10 μs. These authors further conclude that dispersive transport is due to multiple trapping in an exponential distribution of localised states.

The vitreous and evaporated specimen data presented in this report show clearly that the deviation from power law behaviour occurs mainly at times shorter than 10 μs. In the r.f. sputtered data this rapid decay is also observed and there is no evidence for power law behaviour over more than one decade. Thus since contact induced effects are negligible in this experimental arrangement, the initial rapid decay is genuine. Another feature seen in the sputtered data takes the form of a "bump" the position of which varies significantly with temperature. This "bump" could be due to either carrier interaction with a fairly well defined trapping level or recombination. Recombination can be neglected in the time interval considered due to the very long recombination lifetime of greater than 1s at room temperature (Mort et al[146]); any very fast initial geminate recombination has no effect on the subsequent current.

The "bump" position varies with temperature with a zero field activation energy of 0.42eV, in agreement with the activation

energy found in the photomobility experiment. Such agreement again supports evidence already obtained for the presence of fairly well defined trapping levels in arsenic triselenide. The density of states N(E) was calculated from the TP data, in order to determine the energy at which the maximum in the N(E) occurs, using various spectroscopic techniques and this analysis is presented in the next section.

At temperatures below 300K a power law was fitted to the TP data of the vitreous and evaporated specimens and the results are shown in figure 6.9. It is interesting to note that the value of α(TP) obtained from the vitreous specimen , at approximately 275K is similar in magnitude to α_1 obtained from the TOF measurement. However the value of α(TP) from the evaporated sample data is very much less than that measured in vitreous samples. This difference can be explained, in the absence of space charge if one considers that the difference in preparation method is likely to have an effect on the distribution of the localised states in the mobility gap. This could take the form of an increased broadening of trap levels in evaporated films (which will have a greater inherent disorder due to the fact that they were prepared at a substrate temperature very much less than the glass transition temperature). If a trap-limited band model were appropriate and the carriers did interact with a set of traps which have an energy distribution approximated by a gaussian function, Marshall[117] has shown that a broadening of the trap level would result in a greater degree of dispersion. A greater degree of dispersion would also occur for any other form of energy distribution.

7.4 Computer Simulations and Spectroscopic Analysis of The Transient Decay Results

Various spectroscopic interpretations have been discussed in detail in chapter 3, subsection 3.2.1. One such analysis was carried out on arsenic triselenide by Orenstein and Kastner [142] who simplified the complexity of the analysis by using the concept of a 'demarcation energy' introduced earlier by Arkhipov and Rudenko [147], and claimed that power law behaviour in the decay constituted evidence for an exponential distribution of states up to 0.62 eV above the valence band edge.

The results obtained from the present study suggest that structure exists at an energy 0.42 eV above the valence band edge. The photocurrent curve obtained for the sputtered material was analysed by the computer simulation techniques as described in section 4.2. These studies revealed that structure of width 0.05 eV with a density of six times the background density (taken as an exponential tail) incorporated at an energy 0.42 eV gave the best fit to the experimental data (see figure 7.1). The agreement between the general shape of the photodecay obtained from this model density of states and the actual experiment decay was excellent. It was difficult to obtain a characteristic tail temperature for the exponential distribution, because it is recognized that in this particular study as well as others that there is a large amount of experimental evidence for structure in the localised states at an energy of about 0.6eV above the valence band edge, the presence of which, would influence the rate of decay in the power law region.

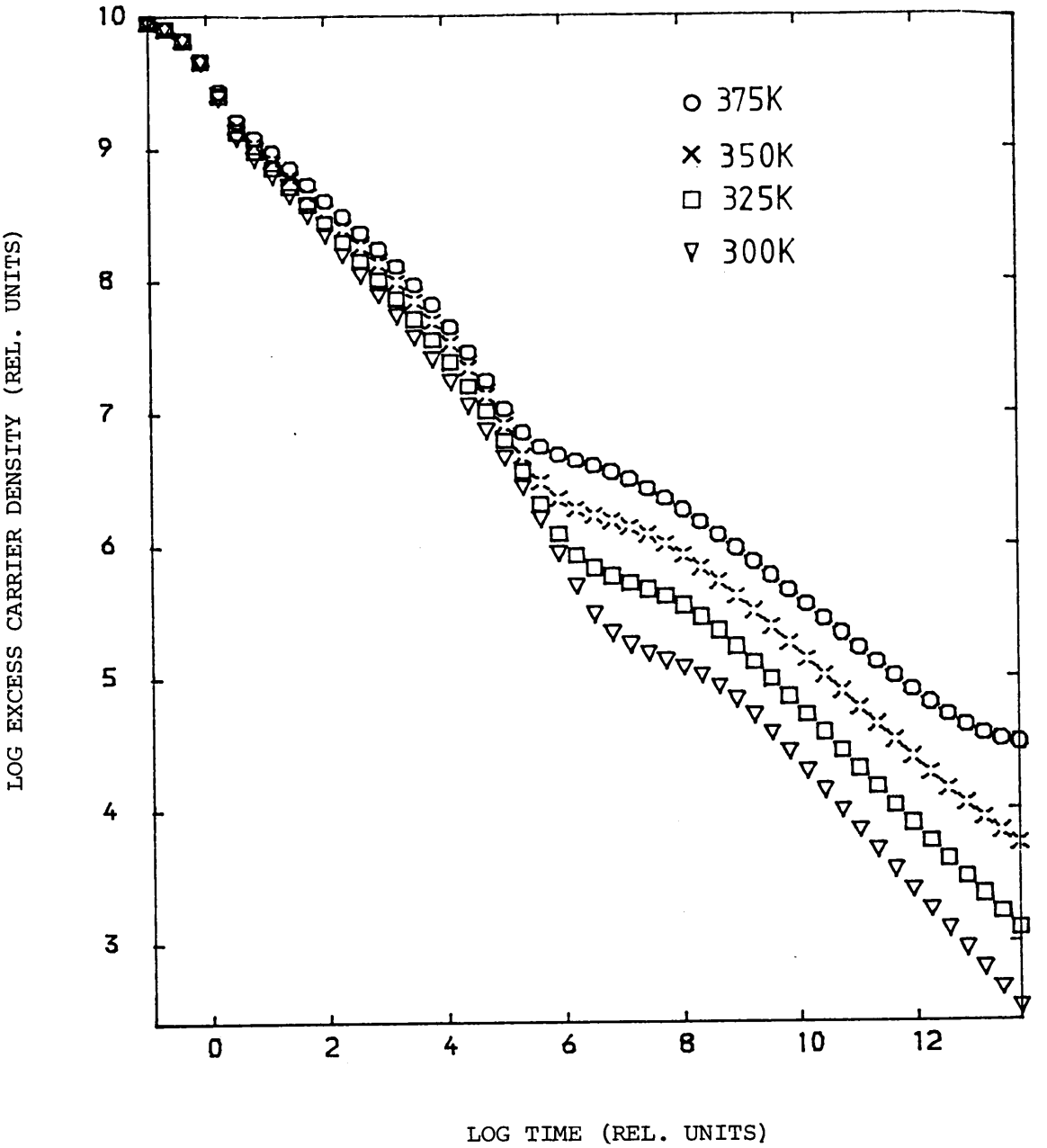

Figure 7.1

Computed transient decay (for the model shown in figure 4.11) which gave the best fit to the experimental data of figure 6.11.

T_c = 600K; E_t = 0.42 eV; ΔE = 0.05 eV; b = 6x background density.

Comparing the experimental data with the simulation data it can be seen from figures 6.11 and 7.1 that the initial rapid decay, representing carrier interaction with the structure incorporated at 0.42 eV, is followed by the intermediate regime, where the carriers have now reached some degree of quasi thermal equilibrium with the shallow centres in the exponential tail and with the feature. Finally the region where the power law behaviour occurs is reached where thermalisation is dominated by states deeper in the background tail than the structure.

If we assume an initial trapping time of 1pS, this gives a value of ν_0 equal to 1×10^{12} Hz. Further as in the simulation study, we take ν_0 to be constant with energy, in order to calculate the energy at which the onset of equilibrium occurs. This was calculated to be about 0.42 eV in agreement with both the computer model and the temperature dependence of the experimental data. This suggests that the basic assumptions are reasonable.

A possible check of these assumptions is to apply the spectroscopic analytical techniques described in section 3.2. The first spectroscopic interpretation of multiple trapping transport was offered by Tiedje and Rose[128] and later by Orenstein and Kastner[127]. They reduced the analytical complexity by applying the concept of a thermalisation energy, similar to one used in an earlier study by Arkhipov and Rudenko[147], to an exponential distribution of states. The energy E_D was defined such that the release time τ_r was equal to the experimental time interval since the creation of the excess carriers

(t). Thus at this energy $\nu.t=1$. Traps above the thermalisation energy would be in quasi thermal equilibrium with the extended states, whilst in the case of traps deeper than E_D it would be improbable that the trapped carriers would be released in time (t), giving $E_D=kT\ln\nu_o t$.

To evaluate this 'intuitive model', Marshall and Main[129] devised a simple procedure for obtaining the trap distribution. Assuming as Tiedje and Rose did that the trapped charge is located close to this energy E_D, than in quasi thermal equilibrium the following expression is obtained

$$n_t(E)/n_f = [N_t(E)/N_c]\exp(E/kT)$$
$$\simeq [N_t(E)/N_c].\nu t$$

where N_c is the effected density of extended states. Except at very short times, the great majority of charge is trapped rather than free, so that

$$n_t(E) \simeq N_o$$

$$N_t(E) \simeq (N_c N_o/\nu)(n_f t)^{-1}$$

$$\sim (N_c I_o/\nu)(I(t).t)^{-1}$$

(7.3)

Thus one can calculate $N_t(E)$ directly from the photocurrent decay data. Figure 7.2 shows the results of applying this procedure to the current data and the apparent features will be discussed later.

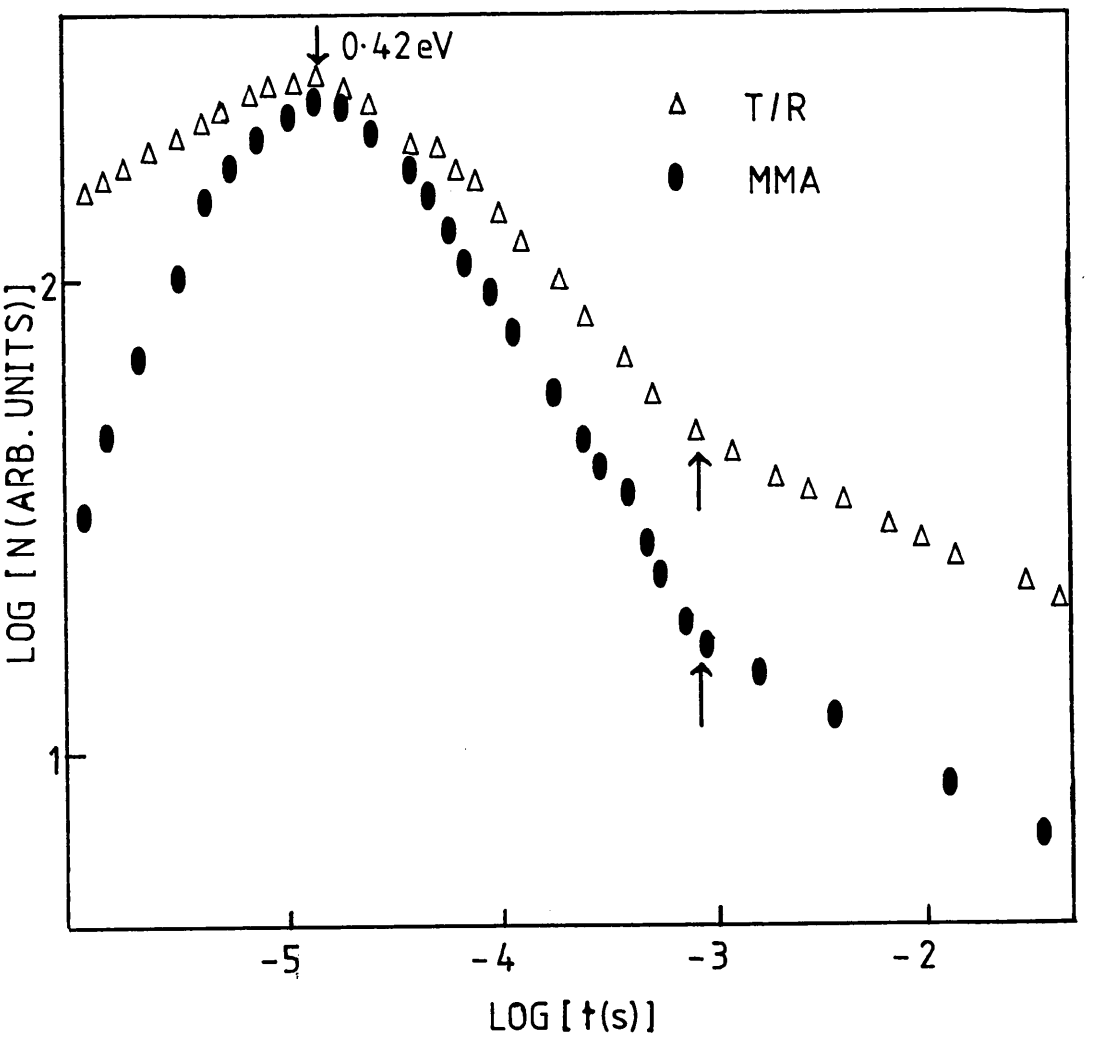

Figure 7.2

Comparison of both spectroscopic techniques used to analyse the photodecay data from figure 6.11. The main energy features are arrowed.

The above 'intuitive' concept has been subject to various objections, one of which (described in section 3.2) showed that the approximation used by Tiedje and Rose for the analysis of carrier thermalisation is unreliable for the case of three single discrete levels[129]. It is claimed that a more accurate (but also more complex) analysis is the spectroscopic technique used by Michiel et al[131, 132], who treated thermalisation in a more realistic (yet still approximate way) which allows spectroscopic analysis of the gap states too within a resolution of a few kT. This technique has been applied to measurements on bulk arsenic triselenide[132], where a maximum in the density of states at an energy of 0.45eV above the valence band has been deduced. This particular spectroscopic technique was applied to the sputtered photocurrent data obtained in this study.

Figure 7.2 shows the result of applying both of the above analyses to the transient decay data. The time scale may be converted to an energy scale assuming a value $\nu_0=10^{12}s^{-1}$ for the attempt to escape frequency. Two features are apparent from the result of this analysis.

(1). The positions of the maxima occur at about the same energy, i.e., 0.42eV$\pm$0.01eV

(2) The change over to power law behaviour occurs at an energy of approximately 0.5eV using both techniques.

From these characteristics it can be seen that both methods give excellent agreement for the positions of the main energy features. This suggests, for this type of distribution, that the use

of the thermalisation energy concept does not give rise to any serious inaccuracy in determining the main features in the density of states. This implies that both spectroscopic techniques are applicable where decays show a low degree of structure (as in the case of sputtered arsenic triselenide).

Applying the 'intuitive thermalisation' technique to the photocurrent data obtained for higher temperatures also gives good agreement in the position of the central maximum to within 0.01eV.* This agreement to a certain extent supports the assumption of $\nu_o=10^{12}s^{-1}$. From this value of ν_o one can calculate a capture coefficient if one assumes microscopic reversibility using the relation $\nu_o=N_vC$ with C equal to s.vth. Assuming a valence density of states $N_v=10^{19}cm^{-3}$, and a thermal velocity at room temperature of $1x10^7cm^2/s$, the capture coefficient C was calculated to be $1X10^{-7}cm^3/s$, which yields a capture cross section of $1x10^{-14}cm$. The values of C and s will be discussed further.

It is interesting to note that the good agreement in the position of the 0.42eV peak, at different temperatures provides a <u>new technique</u> for obtaining values of ν_o if applied over a wide enough temperature range. The presentation of the new technique is given below.

Firstly one has to realise that small changes in the peak energy E_D can be caused by significant changes in ν_o. For example if the wrong value of ν_o were assumed, then we use $E_D=kTln(\nu_o t)$ which can be split into the terms $kTln(\nu_o)$ + kTlnt. The first of these terms

* See figure 7.3

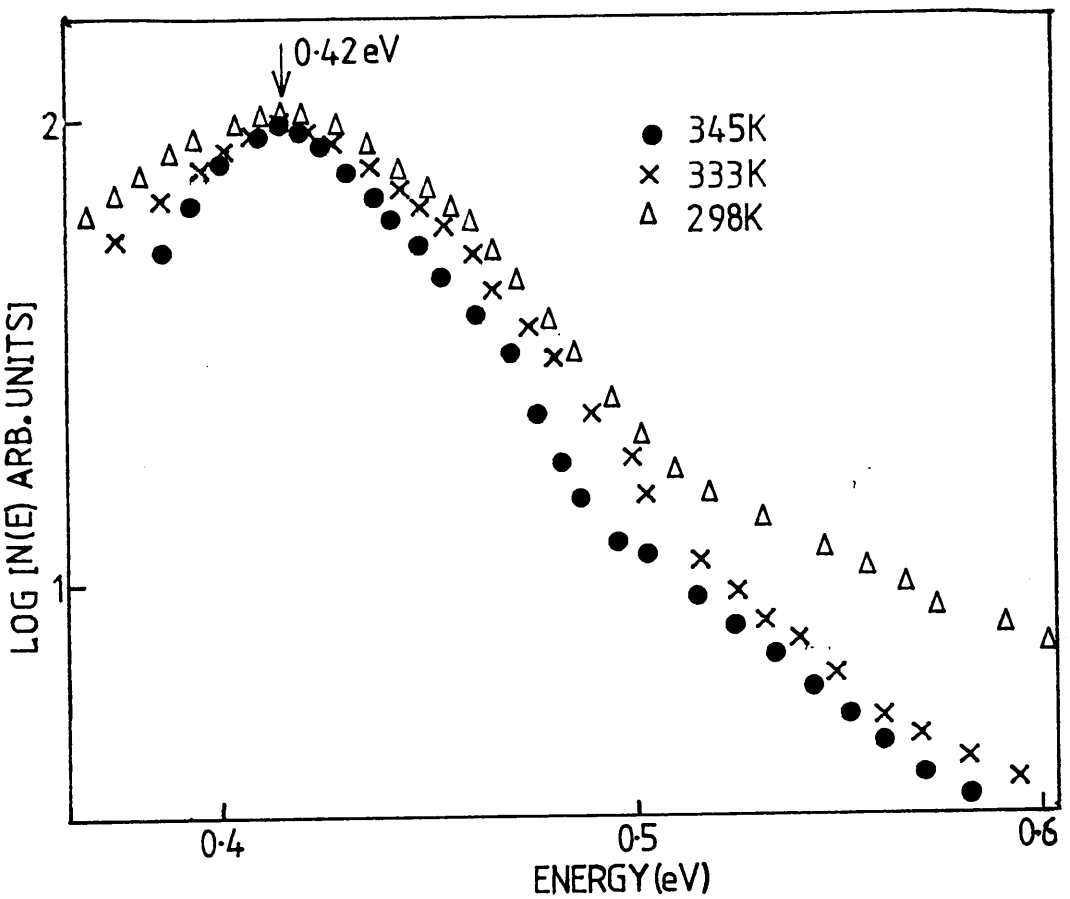

Figure 7.3

The density of states energy profile N(E) obtained by applying the 'intuitive thermalisation' concept to all the photodecay data from figure 6.11.

would represent the shift in the the position of the energy maximum since the second term is small and can be neglected. The shift $\Delta\nu_o/\nu_o$ has the following form,

$$\frac{\Delta\nu_o}{\nu_o} \simeq \exp[\Delta E / k(\Delta T)] \qquad (7.4)$$

With the present data, we can specify $\nu_o=10^{12}$Hz within two orders of magnitude. A greater accuracy would be achieved if the measurements were taken over a larger temperature range ΔT (say 100K). In this case it would be possible to decide whether the shift is a random shift about the maximum that would occur if it were due to experimental error, or whether it is a progressive shift due to selecting the wrong value of ν_o. If the latter were the case then equation (7.4) could be used to correct the value of ν_o.

It is also envisaged that if more prominent energy features were observed in the photodecay, such as in the case of arsenic triselenide crystals where three peaks are observed[133], that if necessary a corrected value of ν_o can be calculated from each peak giving an identification of the variation of ν_o with energy (if there is any variation at all). This technique could be very important, since the most serious objection which can be raised against any of the spectroscopic interpretations is the assumption of an energy independent ν_o. Since not much is known about the possible energy dependence of ν_o more information would be very desirable. However, one would expect little effect on the spectroscopic interpretation if

the variation of ν_0 with energy was slow.

Further to this point the value of capture coefficient calculated for the 0.42eV deep traps obtained in this study agrees well with a value of $1.1 \times 10^{-7} cm^3/s$, recently calculated by Sharp[148] for a trap level situated at an energy 0.6eV above the valence band edge, and is within order of magnitude agreement of the value calculated by Orenstein et al[142]. This agreement is remarkable for capture cross-section measurement, for which 'order of magnitude' agreement is often difficult to achieve. This agreement is encouraging and gives added confidence to the assumptions used in the above spectroscopic techniques.

It was stated above that it proved difficult to obtain a characteristic exponential tailing parameter, from the power law region in the photodecay data obtained from the sputtered sample. This was because it was suspected that structure deeper in the gap would increase the rate of decay in this power law region due to carrier interaction with a deeper level of states. On further examination of the density of states profile (figure 7.3) it could be argued that some structure can be detected at an energy of about 0.6eV (this trap level has been observed experimentally many times before in arsenic triselenide and is used in the interpretation of the steady state photoconductivity data discussed in section 7.5).

On analysing decay data from the vitreous sample, using the 'intuitive thermalisation', technique (the 336K decay curve where recombination does not effect the photocurrent), the profile of state

density shown in figure 7.4 was obtained. Looking at the profile there are two apparent features. Firstly the density rises to a plateau at an energy of 0.41eV. Secondly, there is a slow progressive increase in the density with energy until it decreases more rapidly at an energy of 0.61eV. These finding are consistent with the energy features in the density of states used in the analysis of the d.c. conductivity, drift mobility and steady-state photoconductivity. The feature at 0.61eV is more prominent in the density of states obtained for the vitreous material. These findings are consistent with the interpretation of the steady-state photoconductivity and photomobility results from the sputtered material where it is suggested that the states at the 0.42eV trap level 'mask' the 0.61eV level.

The intermediate region between the features could approximate to a power-law. The fact that no minimum in the density occurs in this region is a consequence of the smearing out effect introduced by the approximations in the Tiedje/Rose analysis.

7.5 Steady State Photoconductivity

The approximate activation energies at zero field measured from results presented in subsection 6.5.1 are listed below for sputtered and vitreous specimens.

		sputtered	vitreous
Steady State bimolecular	ΔE_b(eV)	-0.21	-0.31
Bimolecular decaytime	ΔE_γ(eV)	+0.13	+0.15
Trap limited mobility	ΔE_μ(eV)	-0.44	-0.61

The activation energy measured from the temperature dependence of the steady- state photoconductivity in the bimolecular regime was 0.24eV, but this value is sensitive to changes in the absorption constant with

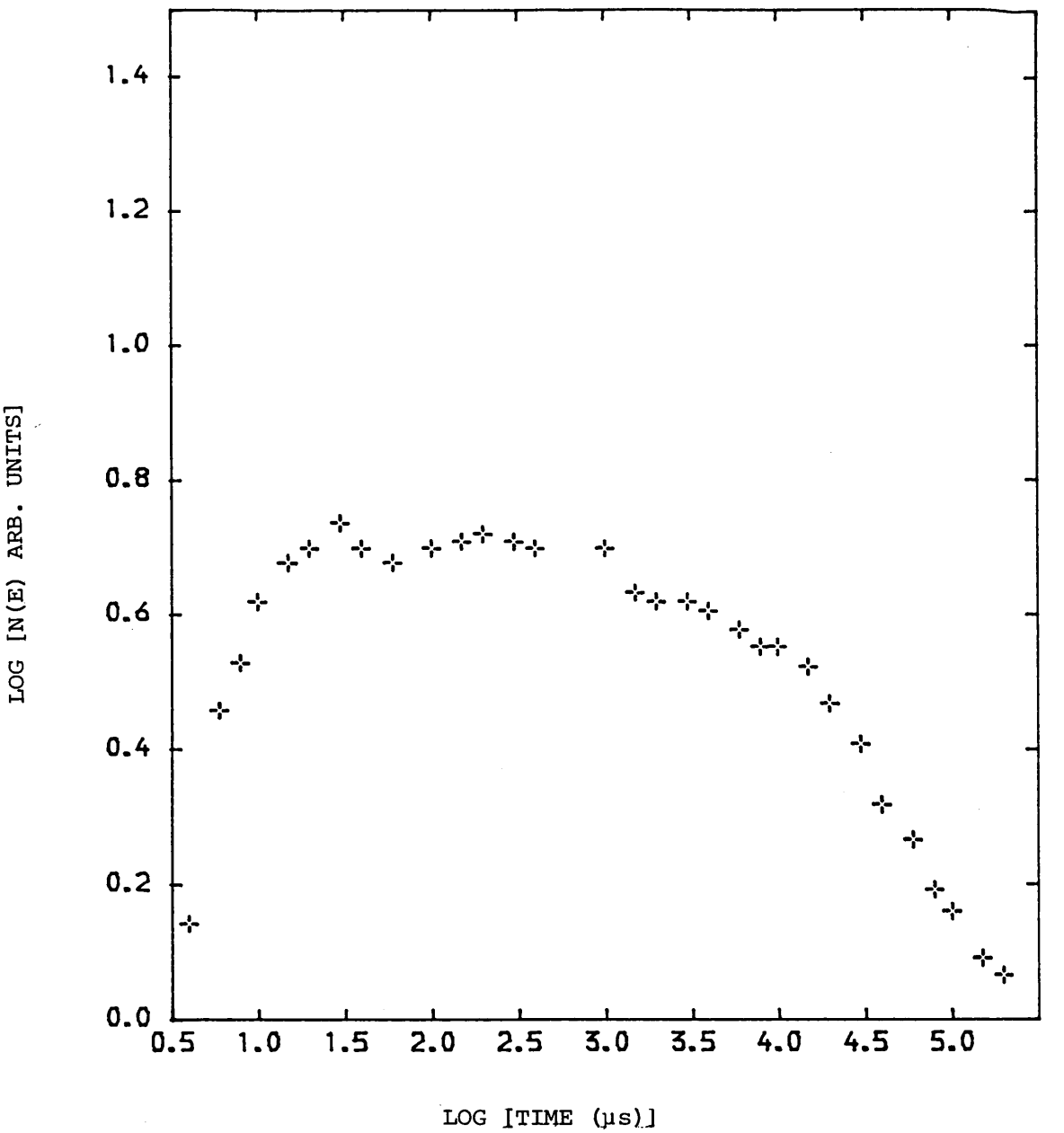

Figure 7.4

The 'intuitive thermalisation' technique applied to photodecay data obtained from the vitreous sample (the 336K decay curve shown in figure 6.8).

temperature at the photon energy used (2.1eV). Measurements of the spectral response of the photoconductivity[49], have shown that at the nominal optical gap energy, the relative quantum efficiency is well below its maximum, and does not saturate until the photon energy is approximately 0.5eV above the the optical gap energy (e.g at 295K E_o=1.85eV, the quantum efficiency η does not saturate until the incident photon energy equals 2.4eV). Therefore it is estimated that the corrected activation energy could be as low as 0.21eV.

The results obtained for the vitreous sample can be explained using the schematic band model shown in figure (7.5). This model contains three discrete trap levels at E_1, E_2 and E_3, corresponding to the energy levels 1.29eV, 0.61eV and 0.42eV respectively. The trap-limited mobility, measured in the vitreous specimen, has an activation energy 0.61eV and this represents the level E_2 in the schematic band model. The band localised B-L transport mechanism predicts a characteristic activation energy of $(E_2-E_v)/2$ for the steady state activation energy ΔE_b, which gives a calculated value of E_2 equal to 0.62eV, since ΔE_b=0.31eV in this specimen. Thus the values of E_2 obtained from both ΔE_b and ΔE_μ, are in agreement within experimental error. A localised to localised L-L transition can be ruled out since in the analysis [49] it predicts an activation energy of E_2-E_v , corresponding to 0.61 eV, for ΔE_b.

The analysis of subsection 3.1.12 for the decay of the excess hole density in the bimolecular regime assumed that the traps at E_2 remained in "contact" with the valence band throughout the

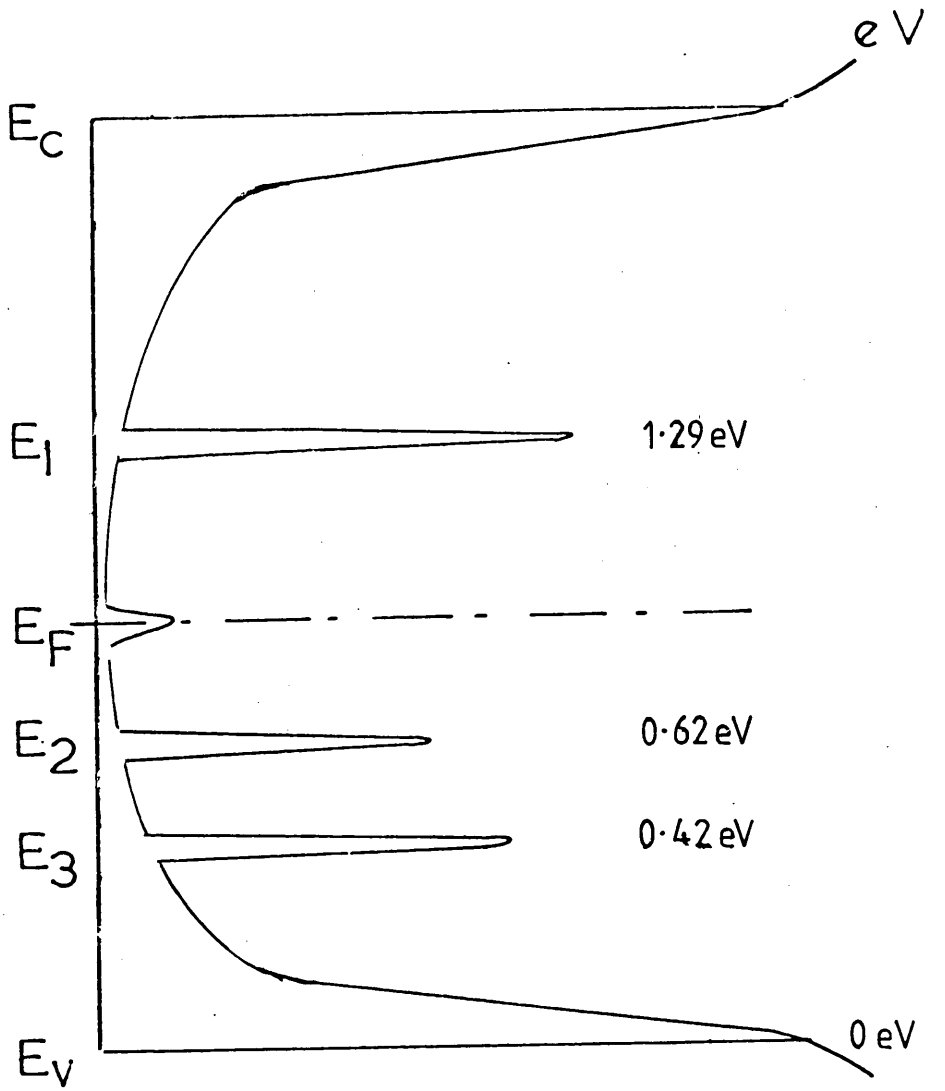

Figure 7.5

Schematic band diagram

decay, and predicted a hyperbolic decay i.e. equation (3.34). For B-L recombination τ_{cb} should increase with 1/T, with an activation energy $(E_2-E_v)/2$, 0.31eV (see equations (3.35) to (3.37)), while for L-L recombination, τ_{cb} should be temperature independent. The observed behaviour of $\Delta E\tau$ does not agree with either mechanism. Since L-L recombination has been discounted it is necessary to show that a B-L recombination mechanism can give rise to the "anomalous" temperature behaviour of τ_{cb}. Main[49], proposed the explanation shown in figure 7.6. He states that as emptying of traps at E_2 keeps pace with recombination, the trapping time τ_{t2} is shorter than the free hole lifetime τ_p. At low temperatures, τ_p <u>decreases</u> as is evident by the decrease in photocurrent ($\Delta I = \Delta G\tau_p$). This is due to the <u>increasing</u> occupation of recombination centres at E_1. On the other hand, unless the traps at E_2 become appreciably occupied, τ_{t2} remains roughly constant.

Thus, below some temperature Tx, the free recombination time τ_{pb}, becomes <u>shorter</u> than τ_{t2}, and much of the excess hole density can decay before the traps at E_2 begin to empty. Shallower traps, at E_3 or tail states, with trapping time (τ_{t3} say), may keep pace with the decay, so that the effective decaytime is still much longer than the true free lifetime. When $\tau_{t3}<<\tau_{pb}<<\tau_{t2}$, figure 7.6b shows the effective form of the decay. The initial fall is exponential, if the occupation of the recombination centres $N_1\Delta f1(\simeq N_2\Delta f2)$ is much greater than the excess density in the valence band and band-tail. The time constant τ_{cb} is given approximately by equation (7.5),

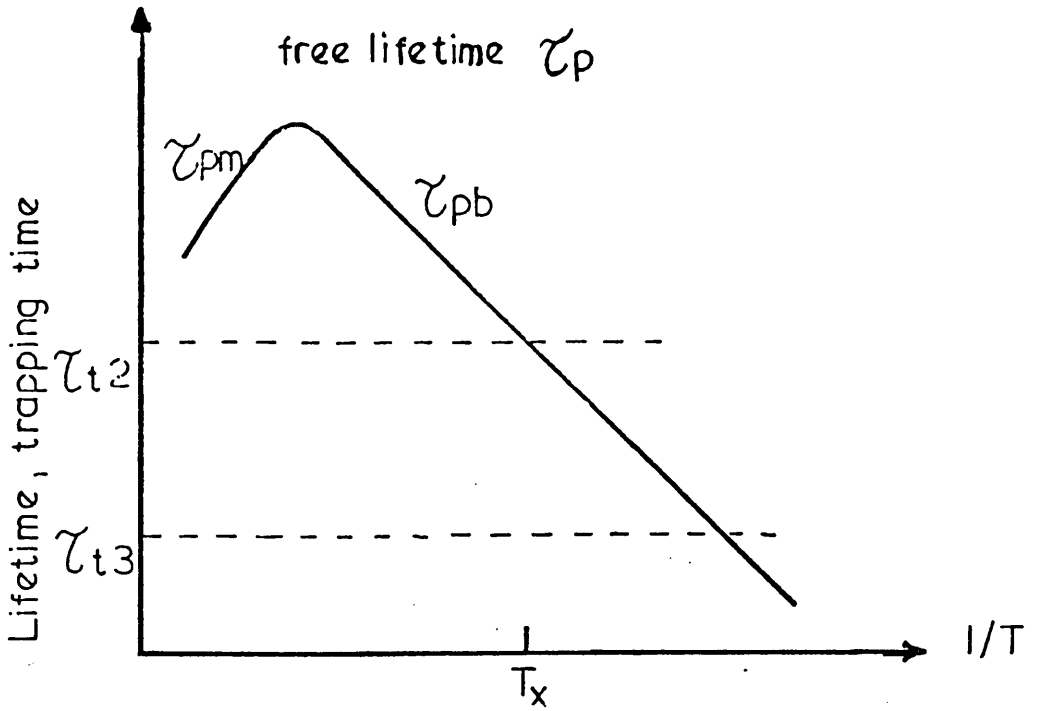

Figure 7.6(a)

Capture times vs 1/T

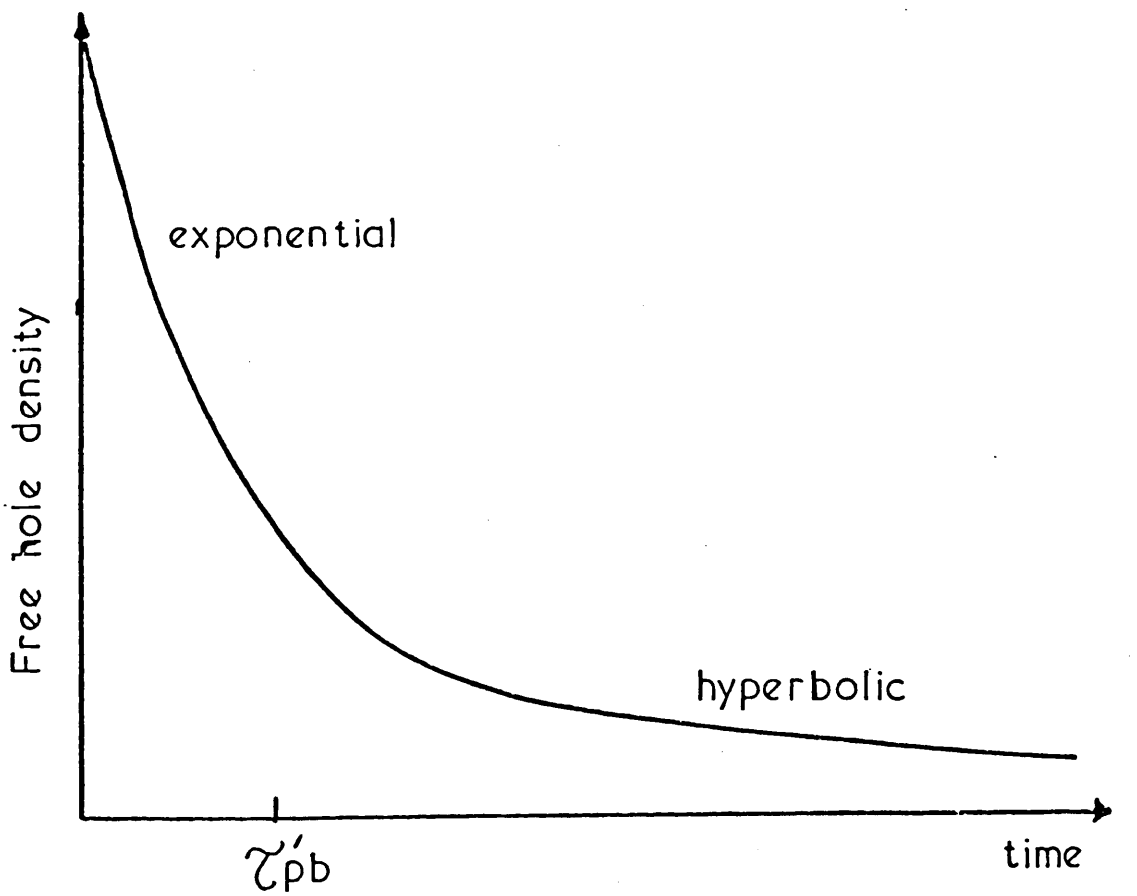

Figure 7.6(b)

The photodecay of the steady state photocurrent as predicted from Main's analysis (after ref.[49]).

$$\tau_{cb} \simeq N_3 (N_V N_2 C_p 2\Delta G)^{0.5} \exp\{[(E_3-E_V)-\tfrac{1}{2}(E_2-E_V)]/kT\} \quad (7.5)$$

In this rapid decay, the free hole density drops to the value $\Delta p'$, when the release rate from traps at E_2, not much altered from the steady state value, matches the recombination rate, the subsequent decay is a hyperbolic tail. Thus the activation energy predicted by equation(7.5) is $\Delta E_\tau(b)=[(E_3-E_V)-(E_2-E_V)/2]$ which predicts a value of ΔE_τ of 0.14eV in agreement with the measured value.

7.5.1 Sputtered Samples

If it is assumed that B-L recombination is dominant in these materials, as suggested by the pre-exponential factor of the photomobility and the fact that the decaytime is temperature dependent (L-L recombination predicts a temperature independent decaytime), then Main's analysis can again be applied. The value of ΔE_τ is 0.21eV which corresponds to a trap depth of E_3 in agreement with the photomobility activation energy. The results obtained from the transient photocurrent decay and the conductivity (see sections 3.2 and 6.2) also support the existence of this discrete energy level. Thus it appears that the E_3 trap level dominates over the E_2 level which undoubtedly also exists in sputtered arsenic triselenide.

If one designates the trapped hole concentration at E_3 as p_3 and that at E_2 as p_2, it can easily be shown that

$$P_3/P_2 = N_3/N_2 \exp[(E_3-E_2)/kT] \quad (7.6)$$

where N_3 and N_2 are the respective trap densities.

At room temperature, using equation (7.6) the trap occupancy p_3 is greater than p_2 when N_3 is approximately 1000 times greater than

N_2. Thus one would expect the E_3 level to dominate if $N_3 > N_2 \times 1000$. This implies a trap density of less than 1×10^{16} cm^{-3} for the E_2 level. Equation (7.6) also implies that a transition temperature should occur where the activation energy increases as the temperature is lowered to that representing the E_2 energy level. Unfortunately, due to the small size of photocurrent growth signal, the lower temperature limit for accurate measurement of the mobility was 270K, and a change over to steeper activated behaviour was not observed in this temperature range (for this particular specimen). It is anticipated that if more specimens were investigated a change over to steeper activated behaviour would undoubtedly be observed.

Although the initial rapid fall of the photocurrent decay is exponential, the activation energy obtained from the temperature dependence of the decaytime again does not agree with that predicted when it is assumed that the traps at E_2 remain in 'contact' with the valence band (see figure 6.15). Thus the theory used to explain the data from the vitreous sample was again applied. The activation energy predicted by equation (7.5) was 0.13eV, taking E_3 to be 0.44eV and E_2 to be 0.62eV, which is in rough agreement with the measured value of 0.11eV.

7.6 The Origin of the Fast Transit Pulse in Sputtered Material

The results of the transient photoconductivity experiment have shown that at room temperature, the carrier mobility and trap-limited carrier lifetime of sputtered arsenic triselenide are of order $8 \times 10^{-5} cm^2/Vs$ and $5 \times 10^{-3} s$, respectively. Using the deduced $\mu.\tau$ product of $4 \times 10^{-7} cm^2 V^{-1}$, and the experimentally applied field of

$1x10^5$, a hole $\mu.\tau.\mathcal{E}$ range of approximately 400 microns can be established. This is the distance that a free carrier travels before recombination. This implies, since this distance is many times greater than the electrode separation in the TOF configuration, that the carriers must traverse the specimen in times shorter than the recombination time. This appears to rule out the two suggested recombination mechanisms, that of surface and bulk recombination, proposed to explain the origin of the fast decaying transit pulse.

From the room temperature photomobility, a characteristic transit time can be obtained, since $t_t=d/\mathcal{E}\mu_\phi$ where d is the specimen thickness. Assuming an electric field of $1x10^5$V/cm and a specimen thickness of 5 microns, a value of t_t equal to 50 μs is obtained for carrier interaction with the E_3 level. Comparison of this value with the value of t_t=1.0ms obtained experimentally from the vitreous specimen informs us that the predicted carrier transit time is much faster in the sputtered material. Thus the proposed origin of the fast transit pulse is that of rapid trapping at the E_3 level. Nevertheless this value should have been within the detection limit of the oscilloscope amplifier (0.5μs). One can only therefore assume that the combination of small signal size with speed of transit pulse made measurement 'virtually' impossible (e.g. a photocurrent of 10^{-8}A represents a voltage of only 0.1mV, for a 10K sampling resistor).

Chapter 8

THE EFFECTS OF DOPING ARSENIC TRISELENIDE WITH NICKEL

Structural measurements were carried out on two representative doped specimens in the thickness range 100 to 200 angstroms using a transmission electron microscope. The specimens were prepared using 4% and 7% coverage by nickel of the active surface layer of the target. The films were sputtered onto carbon coated mica substrates. Microscope samples were obtained by floating the films off the mica onto the surface of distilled water. Pieces of the film were then collected on fine copper grids. Prior to mounting in the electron microscope, the samples were vacuum baked at 140C in order to reduce contamination effects. It is noted that as a result of this procedure some change in the film structure is a possibility since the films were deposited at a substrate temperature of room temperature. The author is grateful to Dr. A. Long and Mr. A. Mckenzie of Glasgow University who help with the structural and chemical analysis.

X-ray micro-analysis of the films revealed that to within an accuracy of 0.5 at. %, the atomic percentage in the films was in agreement with the figures deduced from target coverage calculations. This suggests that, to a first approximation, the sputtering rates of nickel and arsenic triselenide are the same. It will therefore be assumed that the atomic percentage of dopant incorporated in the films produced for transport studies is close to that expected from the target coverage.

The X-ray micro-analysis also revealed that the percentage

atomic ratio of arsenic to selenium was 1/1.46 or $As_2Se_{2.92}$ which is very close, to that of the bulk starting material, taken into account measurement error. This is very encouraging as it suggests that arsenic triselenide is sputtered stoichiometrically from the target.

Electron micrographs from the two samples showed low contrast structure of approximately 100 Å in scale, but the electron diffraction patterns obtained from the nickel doped films showed broad diffuse lines characteristic of an amorphous material. Comparing the sequence and the spacing of the rings with the diffraction pattern of pure amorphous triselenide [149] again suggested that the samples were indeed representative of the bulk material. There is no evidence to suggest that the 100 Å structure is caused by clusters of small crystalline nickel islands. If the structure were due to nickel crystallites one would expect additional sharper rings to occur in the diffraction pattern at the concentrations of nickel dopant used[150]. Hence, we infer that nickel is incorporated into the bulk in a well-distributed manner.

The effects of doping arsenic triselenide by co-sputtering the transition element nickel have been studied extensively. The experimental results obtained from this study are presented below.

8.1 d.c Conductivity

The conductivity curves for samples of r.f. sputtered arsenic triselenide doped with different amounts of nickel by co-sputtering are illustrated in figure 8.1. Details of the estimated nickel content for each film together with the corresponding room

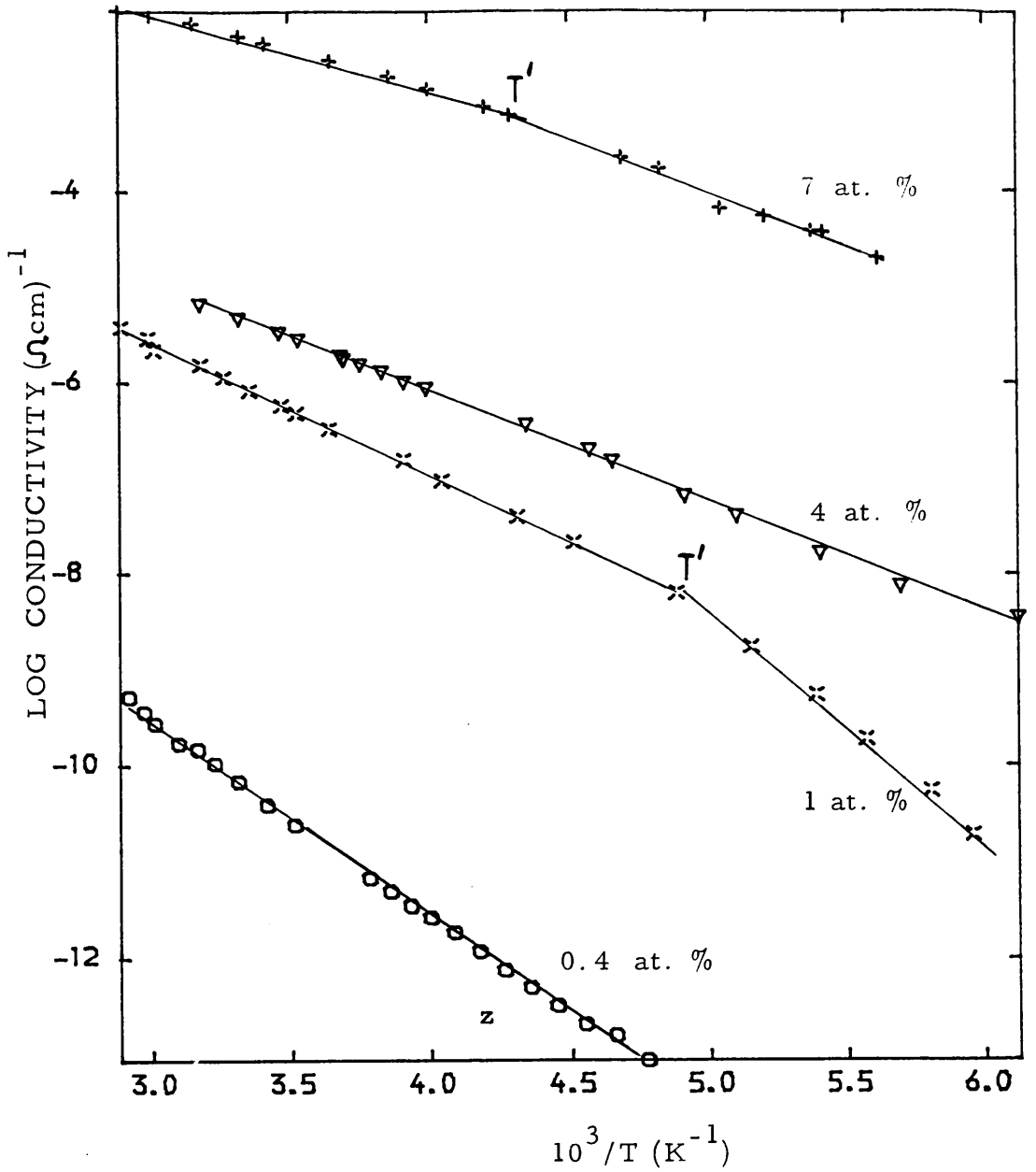

Figure 8.1

Arrhenius plot of the conductivity for four nickel doped films of arsenic triselenide. Specimen details are given in table 8.1.1.

temperature conductivity, conductivity pre-exponential and activation energy are shown in table 8.1.1. Details of the estimated optical gap and possible shift in the Fermi-level as discussed in the analysis (see section 8.4) are also included in table 8.1.1. One can observe from figure 8.1 and table 8.1.1 that the conductivity is dramatically increased as the dopant concentration increases, i.e., a 7% target coverage increases the room temperature conductivity by a factor of $1x10^{11}$, a 4% coverage by 10^8 and a 1% coverage by a factor of 10^7.

An interesting feature is the appearance of well defined activated regimes in the conductivity graphs with the activation energy decreasing with increasing temperature. Generally the addition of nickel causes a decrease in the activation energy as the dopant concentration is increased and a subsequent decrease in the pre-exponential factor by as much as four orders of magnitude (for the case of the 0.4 at. % sample). On examining the conductivity data for the 1 at. % and 7 at. % samples one observes a discontinuity, i.e. a shift to lower activation energies, at higher temperatures. For the 7 at. % sample, a decrease in activation energy from 0.24 eV to 0.15 eV occurs at a temperature (T') of 255K. For the 1 at. % sample one observes a decrease from 0.45 eV to 0.29 eV at a T' value of 205K. In the low temperature regime (the high activation energy regime) the value of pre-exponential suggests extended state conduction whereas in the high temperature regime the pre-exponential value is somewhat lower and may suggest a hopping conduction mechanism. This is anomalous, in that the opposite behaviour is expected when doping an amorphous semiconductor[151]. We will return to the discussion later.

%Ni	ΔE_σ (eV)		σ_o $(\Omega cm)^{-1}$		$\sigma_{R.T}$ $(\Omega cm)^{-1}$	E_{o2} (eV)	Δw (eV)
	High(T)	Low(T)	High(T)	Low(T)			
7 at. %	0.15	0.24	26		$4x10^{-3}$	1.55	0.62
4 at. %	0.26		0.1		$4x10^{-6}$	1.63	0.55
1 at. %	0.29	0.43	0.05	$5x10^{3}$	$7x10^{-7}$	1.71	0.57
0.2 at. %	0.42		$1x10^{-3}$		$8x10^{-11}$	1.74	0.46
0.2 at. %	0.92		90		$2x10^{-12}$		
0 at. %	0.93		50-100		$5x10^{-14}$	1.76	

Table 8.1.1

8.1.1 Thermoelectric Power Results

The variation in thermopower (S) with inverse temperature (figure 8.2) revealed that the 7 at. % sample was n-type in contrast to the p-type nature of the undoped material. A maximum occurs in the graph at approximately the same temperature at which the kink appears in the the conductivity curve from the same sample. The magnitude of the thermopower then decreases as the temperature is lowered, with an activation energy of 0.01eV. Eventually, the detection limit is reached at about 185K.

Detection of the thermopower proved difficult in specimens doped with less than 7at. % Ni, due to the large level of electrical noise pick-up. However, a small signal could be detected in the 4 at. % sample, and it's sign indicated the specimen to be p-type.

8.2 Optical Absorption

The variation of the optical absorption co-efficient with energy for three of the doped specimens is shown in figure 8.3 along with results taken from an undoped specimen. A marked increase in the optical absorption co-efficient with increasing nickel concentration can be seen, in the energy range 0.6eV to 1.7eV. This suggests that there is a dramatic increase in the tail state density with addition of nickel. There is also a change in slope in the graphs at about 1.4 eV$\pm$0.1eV. This feature is more apparent in data from the 0.4 at. % doped sample. The expression $\alpha h\nu=(h\nu-E_o)^2$ was fitted to the values of optical co-efficient not affected by the presence of the feature. This provides the possibility of estimating the optical gap E_o. The value of optical gap obtained using this method varied from 1.75eV in the

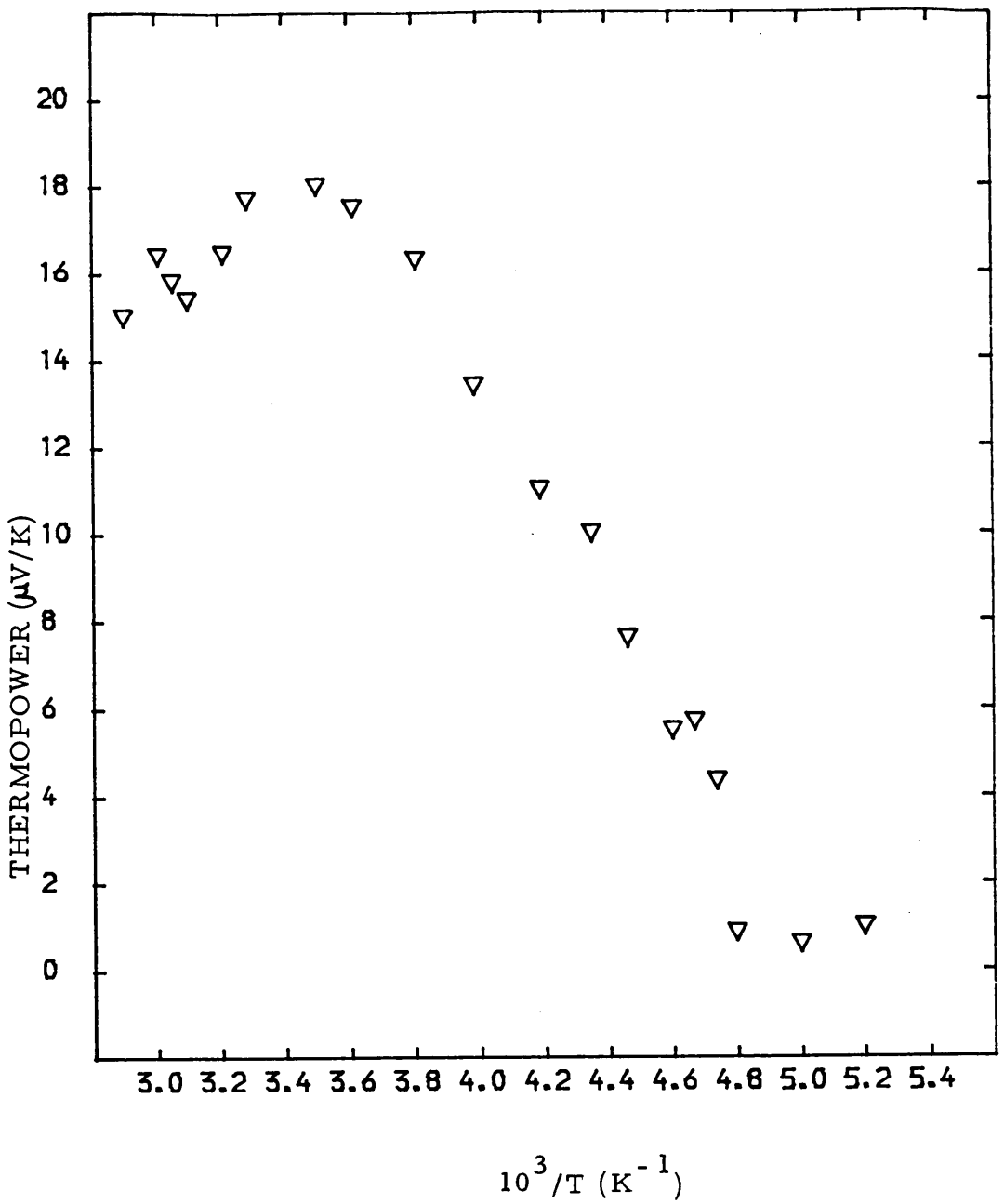

Figure 8.2

Thermopower versus inverse temperature for the 7 at. % doped sample.

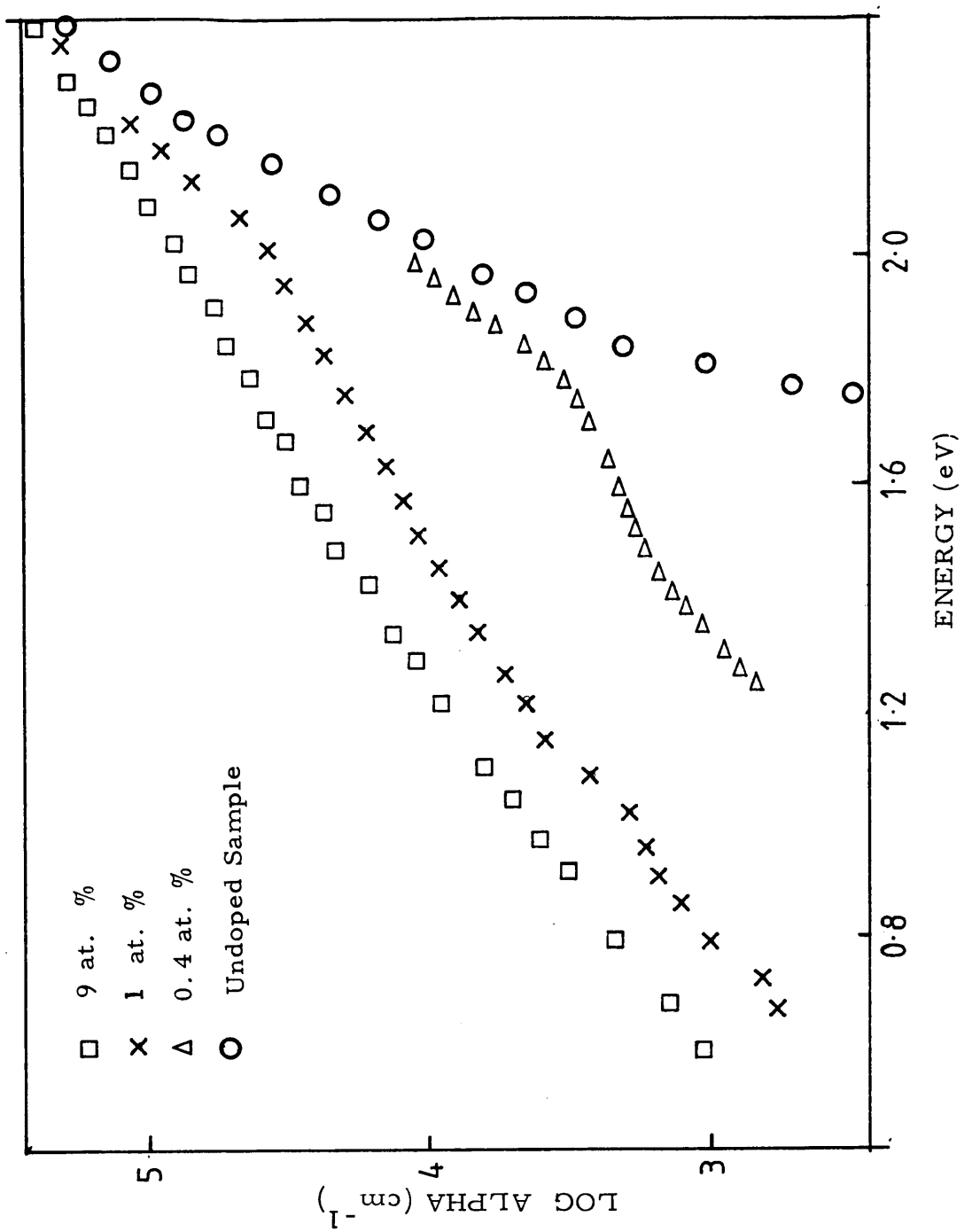

Figure 8.3

Optical absorption versus photon energy for nickel doped films of arsenic triselenide showing the development of the absorption tail.

undoped material to about 1.55eV in the 7 at. % doped sample, and these values are presented in table 8.1.1.

8.3 Photoconductivity Results

Figure 8.4 shows plots of the steady state photocurrent versus temperature for the 0.2 at. % nickel doped sample, at three different intensities, varying from 1.3×10^{15} $cm^{-2}s^{-1}$ to 5.4×10^{16} $cm^{-2}s^{-1}$. Due to the small signal levels over the whole temperature range investigated and the high background noise levels no results were obtained from the other more heavily doped samples. From figure 8.4 it could be argued that there are two regions in the curve. At high temperatures the photocurrent plots are singly activated with an energy of 0.21eV taking into account intensity and field dependence. At low temperature the photocurrent plots display continuous curvature moving towards lower effective activation energies with decreasing temperatures. The change over from one region to the other is dependent on intensity.

The relationship between the steady state photocurrent and the incident photon flux density is power law in nature and is shown in figure 8.5 for four different temperatures. These power laws are representative of the high intensity regime. From this regime a steady state photocurrent-intensity index γ was calculated for ten different temperatures and is shown in figure 8.6. With increasing temperature γ decreases from a value of 0.93 at 196K to a minimum value of 0.68 at 288K, then increases again to a value of 0.78 at 340K.

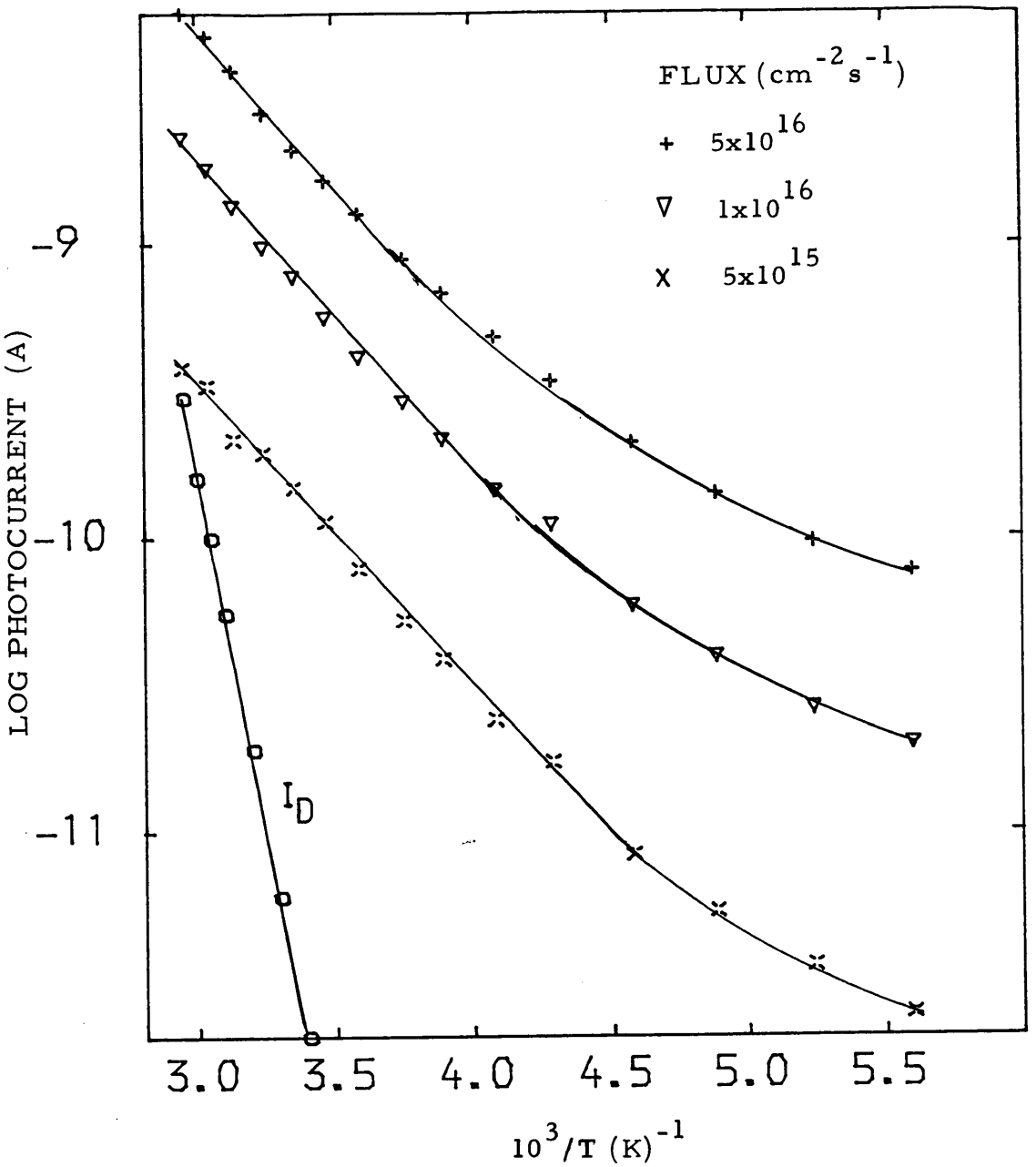

Figure 8.4

Photocurrent versus inverse temperature for the 0.2 at. % nickel doped specimen. The dark current I_D is also shown.

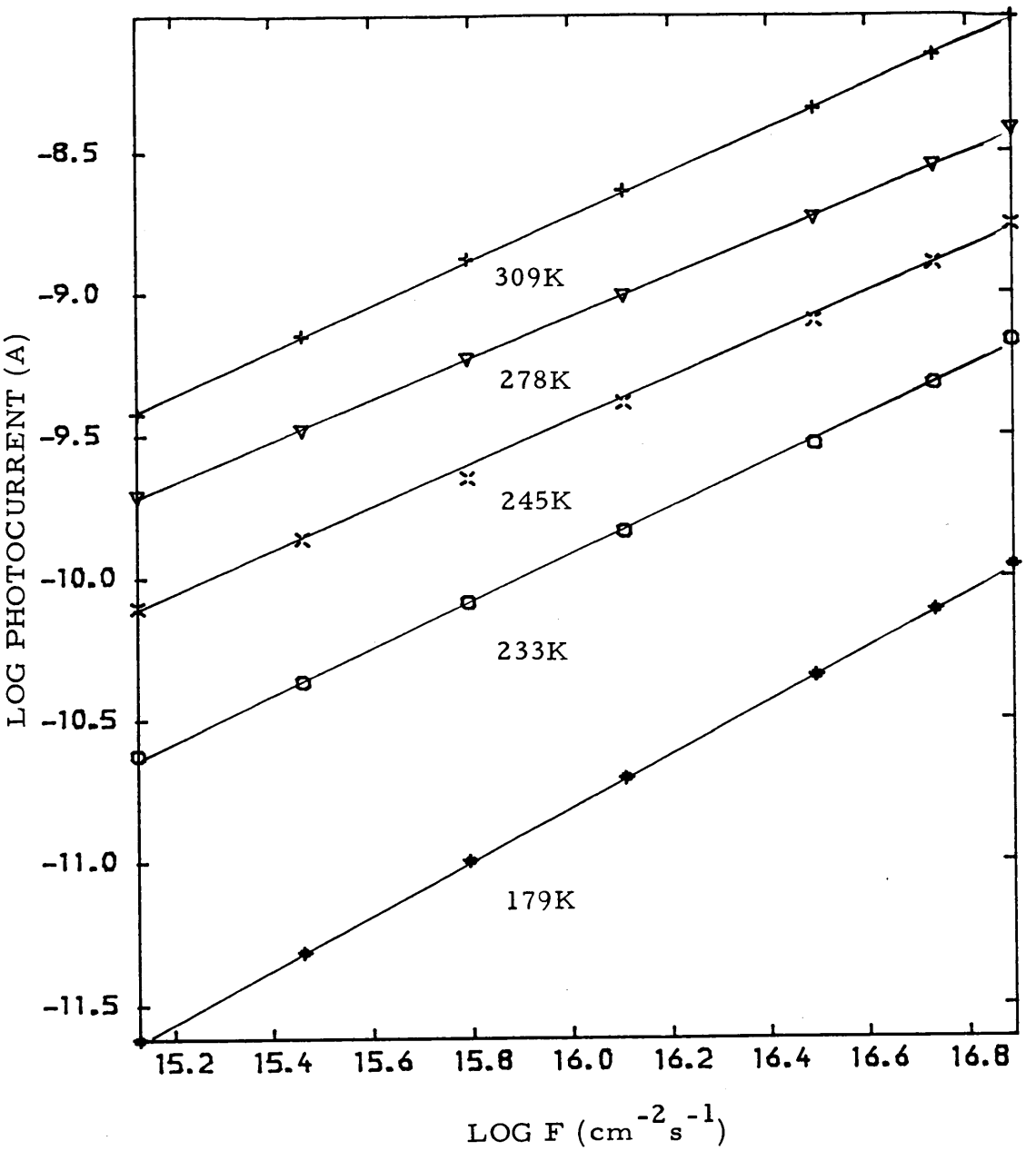

Figure 8.5

Log photocurrent versus log flux for five different temperatures. Data taken from the 0.2 at. % nickel doped sample.

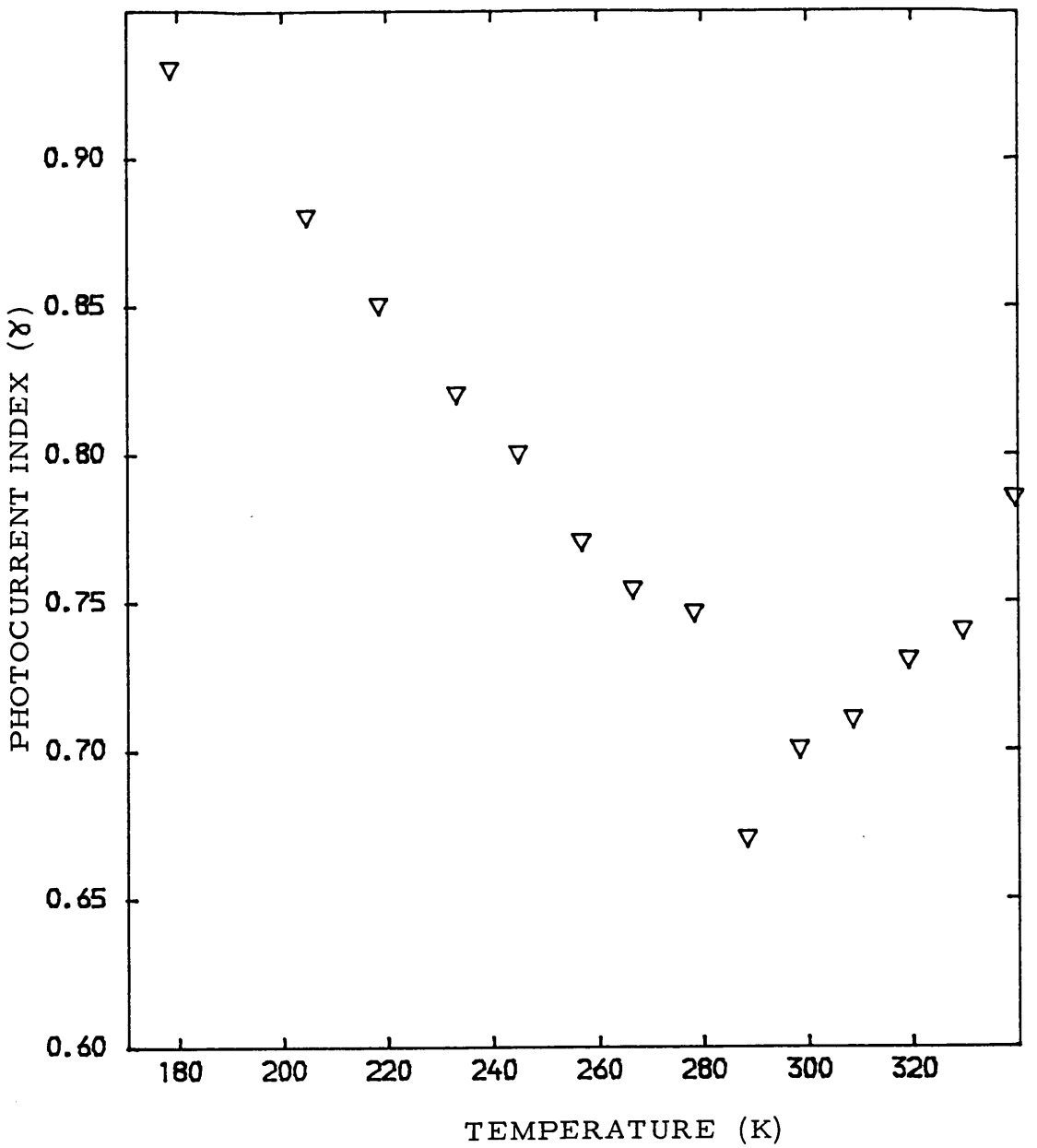

Figure 8.6

Variation of the photocurrent index γ with temperature for the 0.2 at. % nickel doped sample.

The variation of the photomobility and the decaytime with temperature are presented in figure 8.7 for this particular specimen. From the figure it is apparent that the mobility is singly activated (E_μ=0.22eV) with a room temperature value of $2x10^{-5}$ $cm^2V^{-1}s^{-1}$, this value is about half an order of magnitude lower than in the undoped sample. The decaytime, approximately equal to 1 ms at room temperature, is almost temperature independent with an activation energy of 0.02eV. The room temperature value of decaytime is about five times lower than in the undoped material.

8.4 Discussion and Analysis

The most relevant paper to that of the present study is by Kolomiets et al [152], on the modification of r.f. sputtered arsenic triselenide by co-sputtering nickel, and reference the work of Kolomiets et al will be made in the following discussion.

To elucidate the effect of the dopant nickel on the properties of sputtered arsenic triselenide let us consider the following. In unmodified films the optical gap is related to the conductivity activation energy by the relation $E_o=2(E_F-E_v)$, i.e., the Fermi-level is pinned in the middle of the mobility gap. When doping with nickel, E_F in the high temperature regime decreases more that the optical gap for the same sample. In these specimens the d.c. conductivity increases by up to 11 orders of magnitude and the conductivity activation energy decreases from about 0.92eV to about 0.15eV, whereas the optical gap shifts from 1.75eV (uncorrected for temperature dilation) to about 1.55 eV in the 7 at. % doped sample. This indicates that either the Fermi-level has shifted or a large

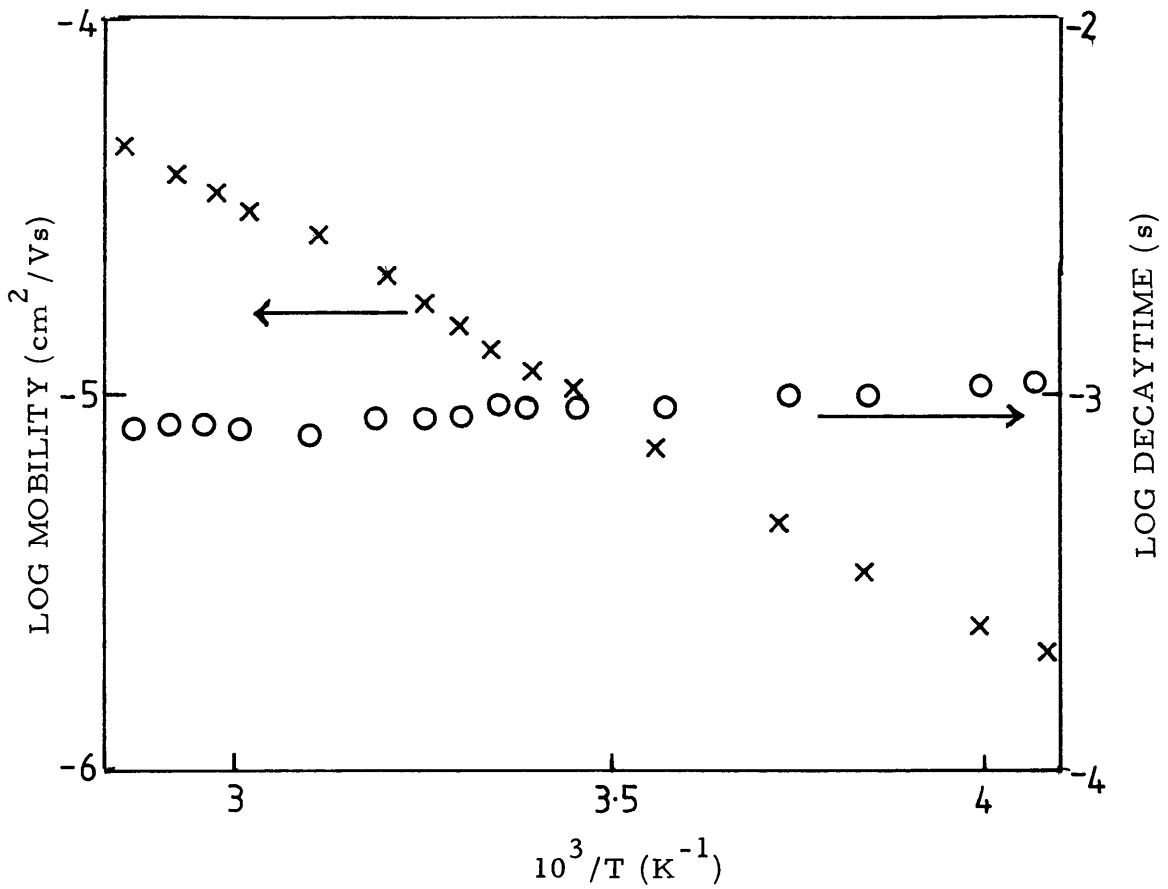

Figure 8.7

Photomobility and decay lifetime versus inverse temperature for the 0.2 at. % nickel doped sample.

increase in the number of gap states has occurred leading to a change in the conduction mechanism to hopping far from the mobility edge. Because the high temperature conductivity activation energy changes progressively with impurity concentration, it would appear that a change in the position of the Fermi-level is more likely. If the addition of nickel increased the density of a particular trap level, it is difficult to see why it would also change the energy position of the trap level for higher concentrations of additive.

Kolomiets et al's study of nickel doped arsenic triselenide also suggests this movement of the Fermi-level. They express their conductivity results in the form $\sigma = C\exp(-E/kT)$ and calculate from the appearance of an extrinsic slope the values of E and the pre-exponential factor C. They find that C decreases by up to four orders of magnitude when incorporating nickel. Despite this lowering of the conductivity pre-exponential factor to about $1 \times 10^{-2}\ \Omega^{-1}cm^{-1}$, which indicates that hopping conduction may be likely, they interpret their results in terms of a extended state conduction mechanism. They then analyse their results in terms of a shift in the Fermi-level towards the conduction band supposing that electrically active centres of donor type are formed. This is evidenced by a change in sign of the thermopower indicating n-type conduction at high dopant concentrations (greater than 4 at. %). In the composition range 0.5-4 at. % they found samples to be p-type suggesting that the Fermi-level is shifted more to the valence band than the conduction band.

The results obtained in the present study will be analysed

firstly in terms of extended state conduction and secondly in terms of a hopping transport mechanism. Evidence for and against each mechanism will be discussed referring to the other measurements made on these samples.

In the first case let us consider the main requirements which determine the suitability of an amorphous semiconductor for effective doping. For the density of states shown in figure 8.8 (representing a possible model for evaporated silicon [151]), if a band of N_D substitutional donors is introduced, most of the N_D electrons will condense at the Fermi-level, and E_F will move towards E_c by the amount ΔE_F. In thermal equilibrium the new Fermi-level position will be determined by the following neutrality conditions:

$$N_D = N_D^+ \simeq \int_{E_{FO}}^{E_c} \frac{g(E)\,dE}{1+\exp\left[\frac{E-E_F}{kT}\right]} + \Delta n(E_c) \tag{8.1}$$

As long as E_F remains below the donor band, $N_D^+ \simeq N_D$; but if E_F enters the band, some of the donors remain neutral and $N_D^+ < N_D$. In an amorphous semiconductor the term $\Delta n(E_c)$, representing the increase in the extended state conduction, is normally quite negligible as compared tp the first term. If E_{FO} lies in an energy range where g(E) is fairly constant, then small changes in the Fermi-level position and the fractional increase in the conductivity produced by doping are approximated by

$$\Delta E_F \simeq N_D / g(E_{FO}), \quad \frac{\Delta\sigma}{\sigma} \simeq \exp\left(\Delta E_F / kT\right)$$

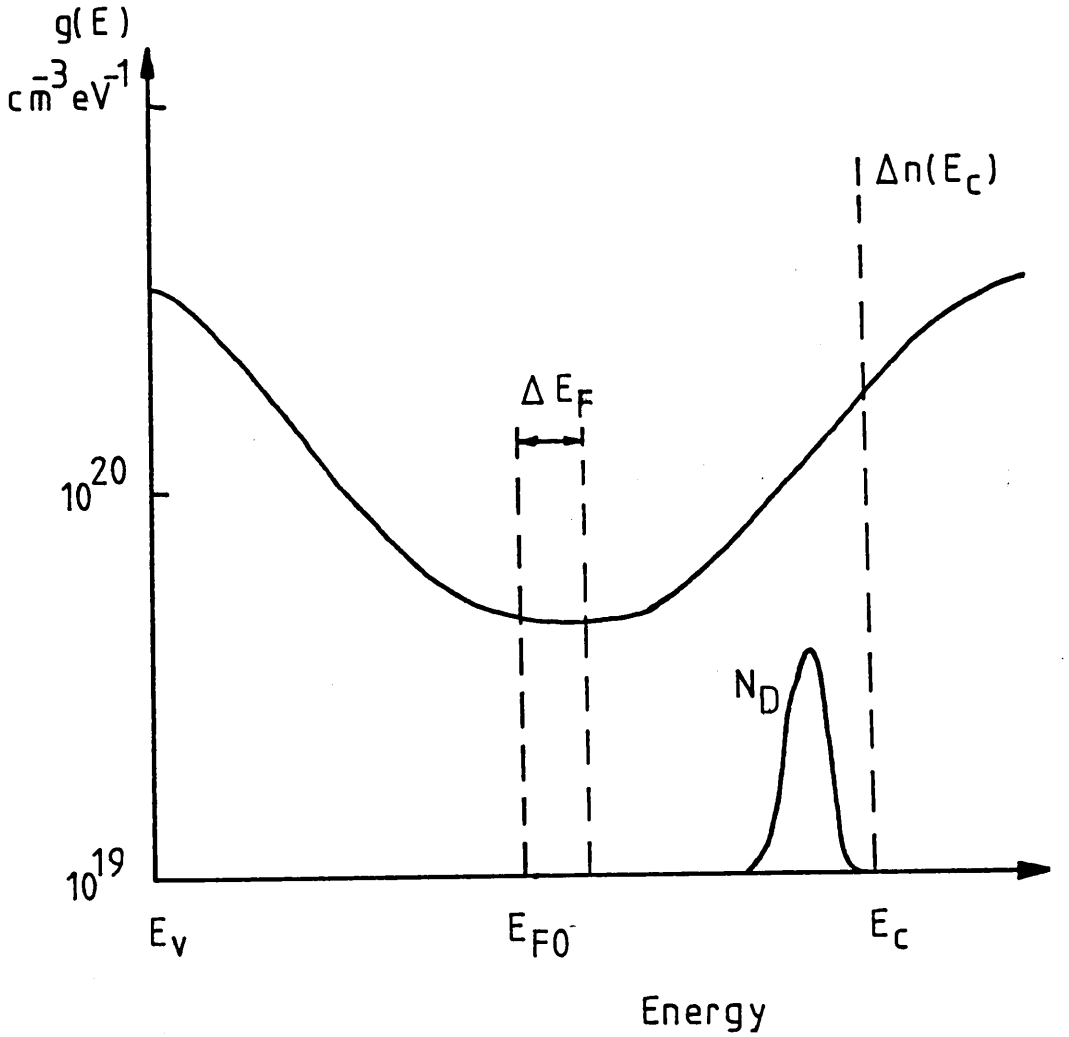

Figure 8.8

Schematic density of states in an amorphous semiconductor. E_{F0} is the position of the Fermi level in the undoped material and ΔE_F is the Fermi level shift when a band of N_D donors is introduced.

provided electron transport takes place well above E_{Fo}. It is clear from this argument that the most effective way of increasing the sensitivity to doping is by reducing $g(E_{Fo})$, which objective has successfully been achieved in amorphous silicon.

Before presenting a model density of states which may be used to explain the electronic and transport properties of nickel doped arsenic triselenide, one has to consider whether the material is p-type or n-type. The sign of the thermopower obtained for the 7 at. % sample implies that the material is n-type, but it is argued on page 181 that the small size of the signal obtained is indicative of hopping at the Fermi-level. If this were the case the sign of the thermopower is not representative of the conductivity type (see page 181). At concentrations lower than 4 at. %, thermopower measurements from this study and from the study of Kolomiets et al show the material to be p-type. It will therefore be assumed in the following analysis that the Fermi-level is shifted towards the valence band with the nickel impurities acting as acceptor states close to the valence band edge.

It is difficult to agree with Kolomiets et al's interpretation, in terms of a donor level, when one considers that they calculate shifts in the position of the Fermi-level of upto 0.6eV (in the 4 at. % sample) towards the conduction band edge, despite the fact that thermopower measurements indicate p-type conduction. One would expect the thermopower to indicate n-type conduction if this were the case.

In arsenic triselenide the model density of states is quite different from that used in the analysis above. The studies of the undoped material carried out in chapter 6 suggest that the model shown in figure 8.9 is more appropriate, i.e., an exponential tail extending above the valence band, with features at energy levels E_3 and E_2 superimposed upon it. It will be assumed in this model that the Fermi-level is pinned at 0.92 eV, the conductivity activation energy for the undoped material. The pinning of the Fermi-level could involve states with spin, since e.s.r. signals have been observed previously in unannealed sputtered material ('cold' deposition as in the present study [87]). It could also be explained in terms of the model suggested by Mott, Davis and Street who explain the pinning in terms of charged defects D^+ and D^- which may explain the absence of spin signal observed in the annealed material (i.e. no spin signal greater than 10^{15}-10^{16}, the limit of detection, has been observed). It will also be assumed that for the preparation conditions used, that concentration $[N_F]$ of the Fermi-level states does not change as larger numbers of impurities are added. The impurities lead to charged centres $[A^-]$ for the case of acceptors. When $[A^-]<[N_F]$ (where $[N_F] \simeq 10^{17}cm^{-3}$), the situation is not much different from that described previously and the Fermi-level remains pinned. This is the situation observed from the conductivity curve of the 0.2 at. % sample, where the high temperature regime gives an activation energy of 0.93eV. At lower temperatures the conduction channel moves to the E_3 trap level as in the undoped case and the conduction mechanism changes to hopping at this particular trap level with the Fermi-level remaining pinned in mid-gap. When the

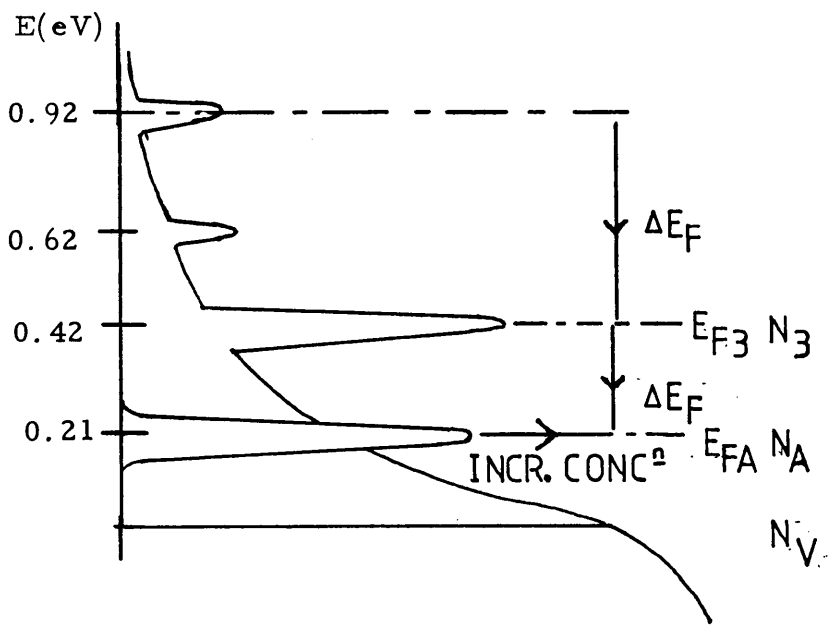

Figure 8.9

Schematic diagram of the proposed shift of the Fermi level for nickel doped arsenic triselenide towards each prominant energy feature. The feature at 0.42 eV being most prominant.

concentration of acceptors $[A^-]$ exceeds $[N_F]$, then the material behaves similarly to an ordinary partially compensated semiconductor as described in the model for silicon above, with $[A^-]$ shallow acceptors.

In the hydrogenic model the activation energy for an isolated acceptor A^o is related to the Rydberg constant R by

$$E_A = R m^* / m k^2$$

which yields $E_A \simeq 0.21$ eV for a material having a dielectric constant $k = 8.0$ and an effective mass $m^* = m$. Thus from expression (8.1) one would expect the Fermi-level to shift to the acceptor level E_A as in the case of silicon. This clearly does not occur in the conductivity curve from the 0.4 at. % doped sample which exhibits an activation energy of 0.42 eV and not that of 0.21 eV expected from the introduction of acceptors.

To understand the behaviour of the holes released from the acceptors it is necessary to take into account the distribution of localised states in the gap, and particularly the influence of the large density at the E_3 level on the position of the Fermi-level. It is proposed, assuming conduction to be via extended states, that the Fermi-level is shifted from the 0.92 eV energy position to the E_3, as shown in figure 8.9 with $[A^-] < N_3$, the trap density at E_3. This is a reasonable assumption since the density of states N_3 is much greater than the density of states at the Fermi-level $[N_F]$ (10^{18}-10^{19} compared

to 10^{16}-10^{17}). This may explain the value of activation energy (0.42 eV) obtained from the conductivity curve for the 0.4 at. % sample. This value of activation energy again appears in the 1.0 at. % samples, at low temperatures. Also observable from figure 8.1 is the appearance of a discontinuity at higher temperatures and this will be discussed in the next section.

For higher concentration of dopant $[A^-]>N_3$, it is anticipated that the Fermi-level will become unpinned again and move towards the predicted acceptor energy. The activation energies of 0.29eV, 0.26eV and 0.24eV calculated from the conductivity data for the 1 at. %, 4 at. % and 7 at. % samples show the progressive movement of the Fermi-level towards the impurity energy.

Figure 8.10 shows the Fermi-level shift predicted from the high temperature regime of the conductivity graphs, using the relation $\Delta W=E_o-2E_\sigma$ (the temperature dependence of the mobility gap being neglected) as a function of impurity concentration. Also shown in figure 8.10 are the results obtained by Kolomiets et. al. These results show good agreement suggesting a shift in the Fermi-level saturating at ΔE_F approximately equal to 0.65eV, thus one can estimate the depth of this level relative to the extended state conduction channel. The above interpretation assumes an unchanged transport mechanism of extended state conduction. In such a model, however, the prefactor σ_o should be the same for each film, but as shown in table 8.1.1 this certainly is not the case. A similar situation has been observed previously in doped r.f. glow discharge silicon and Jones et

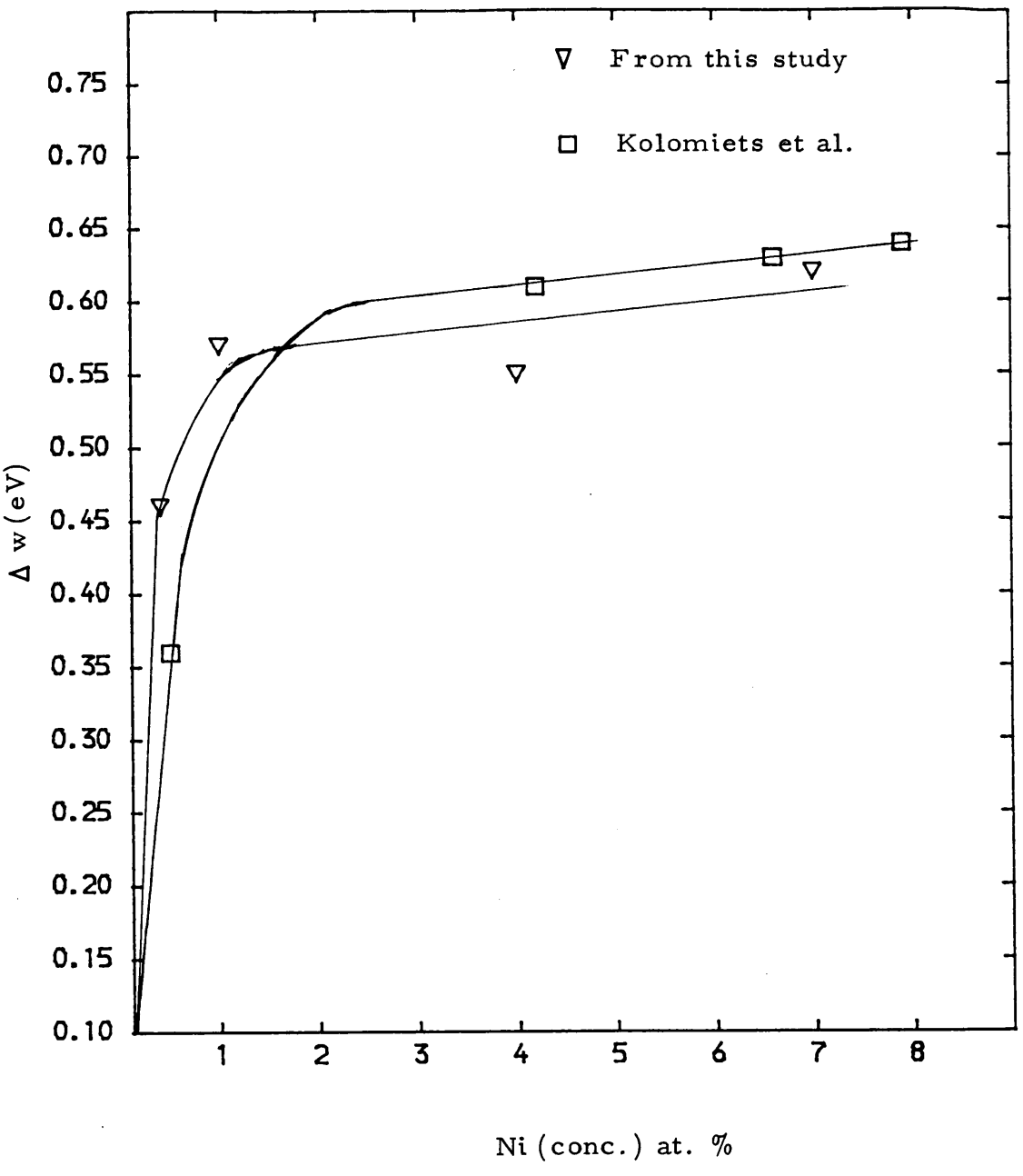

Figure 8.10

Plot of Δw (the shift of the Fermi-level towards the valence band edge) versus nickel dopant concentration. Results from the study of Kolomiets et al are also shown as discussed in the text.

al[153]. It is proposed that the above results can be explained in terms of shift in E_F with temperature, in such a manner as to reduce the apparent E_σ and σ_0.

At even higher concentrations of charge additives one would expect the impurity orbitals to overlap leading to thermally activated hopping conduction of the excess carriers amongst the charged centres and also the localised valence tail states.

The small value of the thermopower (maximum 16 μV/K) shown in figure 8.2 suggests that conduction in the 7 at. % sample takes place by the process of hopping at the Fermi-level. Analysis of the thermopower becomes difficult when such small values of S are obtained. However, if it is assumed that the current is carried by carriers within a few kT of the Fermi-level, then the sign of the thermopower depends on whether the density of states in the vicinity of E_F increases or decreases with energy and is in no way indicative of the conduction type[30].

If hopping were the dominant conduction mechanism the activation energies would indicate that hopping occurs in the 0.42eV trap level at low concentrations of impurity, with the Fermi-level shifting from mid-gap by up to 0.25eV to account for the activation energies encountered in the highly doped samples at low temperatures.

8.5 Discontinuities in the Conductivity Curves

Discontinuities in the activation energies of the conductivity curves have been observed before[154, 155] in amorphous silicon, the activation energy decreasing to a lower value at a set

temperature T'. Spear et. al.[154] attempt to explain this feature in terms of a shift of the mobility edge with temperature, showing that this effect can account for the observed activation energy at high temperature.

Spear et. al. explain the discontinuity using the following model. For the case of electron transport they define a unique reference energy, E_A the energy at which the onset of the tail states occurs to which the energies E_c and E_F, can be related. They suggest that where E_{Fo} lies within a density of states minimum, the temperature shift of the Fermi-level will be negligible. They then analyse the case in terms of a shift in the mobility edge.

It would prove futile to apply the above analysis to the conductivity data obtained from the nickel doped samples in this study, since firstly it has been predicted in the previous section that the Fermi-level does shift with temperature and secondly it has also been predicted that the Fermi-level lies close to a maximum in the density of states as opposed to the minimum that would be required in Spear et. al's analysis.

Mott[156] has analysed the effect of certain charged impurities on the conductivity in chalcogenide glasses. He suggests that elements such as copper or magnesium can have coordination number 4 and be negatively charged when incorporated into these glasses. He proposes that compensating charge is provided by D^+ centres when equilibrium with the charged impurities has been reached at the glass transition temperature. The law of mass action then ensures that the

concentration of D^- is small. Then under these conditions the Fermi-level is no longer pinned and the conductivity activation energy can decrease from that of the undoped specimen by as much as 1/3. Mott predicts that as T increases, there should be a transition from one regime to the other, the slope decreasing from $1/2E_\sigma$ to $1/3E_\sigma$. Thus for arsenic triselenide the slope should decrease from 0.92eV to 0.61eV in the high temperature regime. Fritzche and Kastner 39 on the other hand do not predict this change in slope except under special circumstances when large concentrations of charge centres are added. Even then the above situation is only permitted when equilibrium between the V.A.P.'s and the charge additives has occurred. Clearly this analysis is not valid for the present study in which the process of co-sputtering onto cold substrates (R.T) produces a non-equilibrium situation.

In conclusion we think that neither of the above interpretations can be used to explain our conductivity data. In order to explain the discontinuities, it is thought, that a rigorous theoretical analysis of the possible temperature shifts in E_c and E_F would be required. Such an analysis is outside the scope of the present study.

8.6 Photoconductivity Analysis

The steady-state photoconductivity results reveal some puzzling features, one of which is the variation of the photocurrent index with temperature. The photoconductivity index γ, which relates ΔP_{ss} to the photogeneration rate G, has values varying from 0.68 at 290K to 0.93 at 176K. An explanation of these results in terms of the

simultaneous occurrence of bimolecular and monomolecular recombination processes can be ruled out as this gives rise to $0.5<\gamma<1$ only for a variation of the steady state photoconductivity with flux intensity over a limited range [106], where as in the results shown in figure 8.5, γ is constant over several orders of magnitude. According to Rose [110] (see subsection, 3.1.9 page 69) it is possible to obtain values of γ between 0.5 and 1 when the quasi-Fermi-level passes through a continuum of trapping states whose density distribution is exponential. Thus the parameter

$$\gamma = \frac{T_c}{T+T_c} = \frac{\ell}{\ell+1} \qquad (8.2)$$

where (ℓ) equals T_c/T. A plot of $1/\gamma$ vs T is then expected to pass through T=0, at $\gamma=1$. The variation of γ and $1/\gamma$ with temperature clearly do not obey this relation, suggesting that the quasi-Fermi-level is not passing through an exponential distribution of states (see figure 8.11).

The photoconductivity analysis for the undoped material was carried out using the four level recombination model presented in subsection 3.1.8, page 66, and the most consistent mechanism was the relatively simple one of B-L recombination at all temperatures, with the Fermi-level pinned by a set of states 0.92 eV above the valence band edge. Such pinning has been discussed in detail in the analysis of the nickel doped conductivity data. It is assumed in the following analysis that the states, which are responsible play an insignificant role in recombination at all temperatures. Secondly the 'species' must be such that under high illumination, the charge density in these

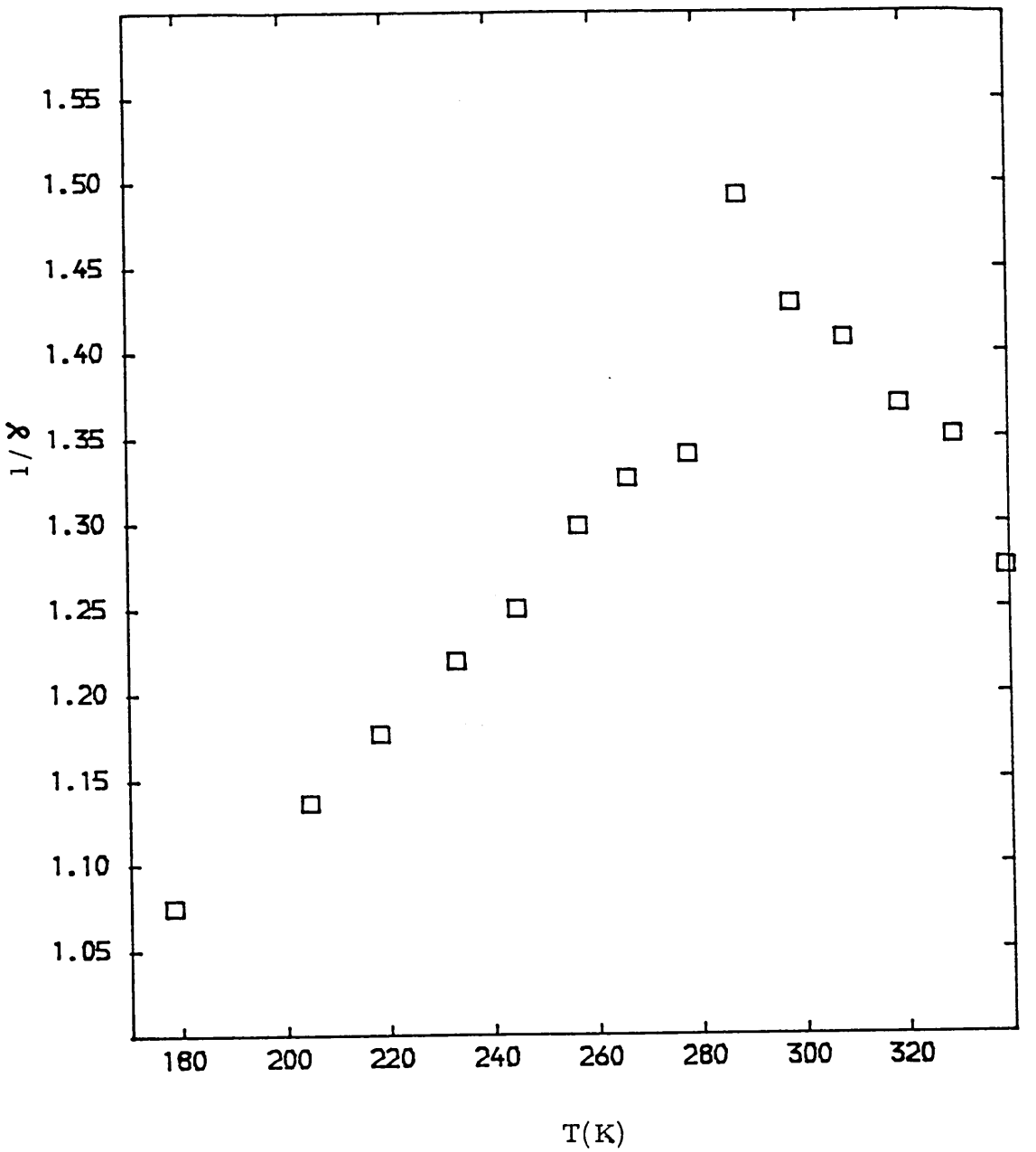

Figure 8.11

A plot of $1/\gamma$ versus temperature for the 0.2 at.% nickel doped sample.

states is less than in the recombination centres at E_1(1.29eV), and E_3 (0.42eV). The value of 0.42eV is chosen in this model, as it dominates the steady-state photoconductivity in the undoped sputtered material. It is assumed that the nickel dopant is incorporated at an energy E_4 (0.23eV) above the valence band edge, producing acceptor states. The photoconductivity results will now be explained in terms of this model. However it might be expected that the trap level at E_3 should be revealed in the photocurrent growth experiment, leading to an observed hole drift mobility activation energy of 0.42 eV, whereas the observed activation energy was only 0.21eV. One would expect at short times, from this particular density of states model that if the trapping time τ_{t4} is much less than τ_{t3}, that the E_4 level will dominate the initial rate of rise of the photocurrent and thus the mobility activation energy[49]. This could occur as a consequence of the nickel centres having a higher coulombic capture cross section. Thus assuming an extended state conduction mechanism, this activation energy represents the energy depth of the acceptor states, with respect to the valence band. In the steady-state, however, the 0.42 eV trapping level would dominate the 'transport' leading to a steady state bimolecular activation energy of 0.21 eV, as predicted by the recombination model. This model can also be used to account for the temperature independent decaytime. In this case the theory discussed in section 7.5, which involves the decay of the excess population of the valence band plus the traps at E_4 in time τ_{cb} before traps at E_3 are significantly affected, seems appropriate. Thus the predicted activation energy ΔE_τ (0.22eV)-0.21eV = 0.01 eV is in agreement with

the measured value of 0.02eV.

From the steady-state photoconductivity curves there is a 'break' from exponential behaviour at low temperatures. This could occur from one of three reasons; a change in the transport mechanism; a change in the recombination path; a change in the occupancy function for hole traps. The first two possibilities predict that the breakpoint would be intensity independent, which is clearly not the case as seen in figure 8.4 The last possibility is most plausible, i.e., the hole trap quasi Fermi-level approaches the trap level at E_3 as the temperature is reduced and the assumed quasi-thermal equilibrium no longer holds.

A transition to linear intensity behaviour below the break point might be expected, if the trap quasi Fermi-levels lie outwith the traps, but as can be seen in figure 8.6 there is no sudden increase to γ=1 at this temperature. In fact at the lowest temperature (176K), γ=0.93. The photoconductivity model discussed in subsection 3.1.8, assumes that the trap levels are discrete, while obviously in an amorphous material these levels are not discrete and spread in extent by a few kT. In this case the gradual change of γ to a linear value would occur at lower temperatures than 176K, where the trap occupancies f_1 of trap N_1 and f_3 of trap N_3 are controlled by recombination kinetics. In this limit photocurrent would become temperature independent.

8.6.1 Optical Absorption

At an energy of about 1.4eV, the absorption coefficient

deviates from the exponential shape and a shoulder develops, as indicated in figure 8.3. The magnitude of the shoulder depends on the preparation conditions, it increases with increased nickel concentration, suggesting that the shoulder is an extrinsic property related to defects. It is proposed, since there is general agreement that the optical transitions in this region (the absorption tail region) take place from defect states to empty states at the band edge, that the transitions are occurring from the defect level to the conduction band edge[157]. The defect states are therefore situated at about 1.4eV below the conduction band edge. If one then estimates a full width half maximum (FWHM) of approximately 0.3eV for the defect level[158], this places the defect level between 0.25eV and 0.55eV above the valence band edge, a position which agrees with the model density of states proposed for nickel doped arsenic triselenide.

Unfortunately to firmly establish the above proposal, and to obtain a possible density for the defect states, other experimental techniques, not available during the course of this study would have to be performed on the specimens. For example the strength $\Delta\alpha$ of the defect induced absorption band may be obtained by subtracting the estimated Urbach tail from the measured absorption spectra.

$$\Delta\alpha(h\nu) = \underset{\text{meas.}}{\alpha(h\nu)} - \alpha_0 \exp\left(\frac{h\nu}{E_0}\right) \qquad (8.3)$$

From studies of the absorption tail region in amorphous silicon, it has been shown that the integral absorption strength $\int \Delta\alpha(\nu)d\nu$ is proportional to the spin density N_s(e.s.r.) which may be determined from e.s.r. measurements[38], i.e.,

$$N_s = A \int \Delta \alpha(\nu) . d\nu$$

Jackson and Amer[38] found that A yields values for the defect density which are in perfect agreement with N_s. This leaves little doubt that the extra absorption directly involves dangling bonds and not just defects that occur under the same preparation conditions as the dangling bonds.

It is proposed that a future analysis, applying the above experimental techniques, would prove a fruitful and worthwhile exercise.

Chapter 9

INDIUM DOPED SAMPLE-RESULTS AND DISCUSSION

The structure of two indium doped specimens in the thickness range 200-300 angstroms was investigated. These specimens were prepared using 2% and 4% active area target coverage with indium. X-ray microanalysis of these films showed that the atomic percentage of indium in the films was in agreement to within 0.5% with the target coverage calculations. The X-ray microanalysis again revealed, as with the nickel doped samples, that the atomic percentage ratio of As/Se was in agreement with that of the bulk material.

Electron micrographs of the films showed them to be homogeneous down to a resolution of 50 angstroms, and the electron diffraction pattern was similar to that obtained in the nickel doped samples. These observations suggest that indium is entering the material in a homogeneous manner.

The influence of indium on the electronic and transport properties of r.f. sputtered arsenic triselenide is strikingly different from that found in the nickel doped samples, there being little variation in the major electronic characteristics with increased dopant concentration. Thus during the presentation and interpretation of the results, more attention will be paid to the results that are most contrasting, those from the least heavily doped sample, 0.2 at. %, and the most heavily doped sample, 4 at. %.

The d.c conductivity for the above mentioned samples is illustrated in figure 9.1 and in table 9.1.1. Estimations of the

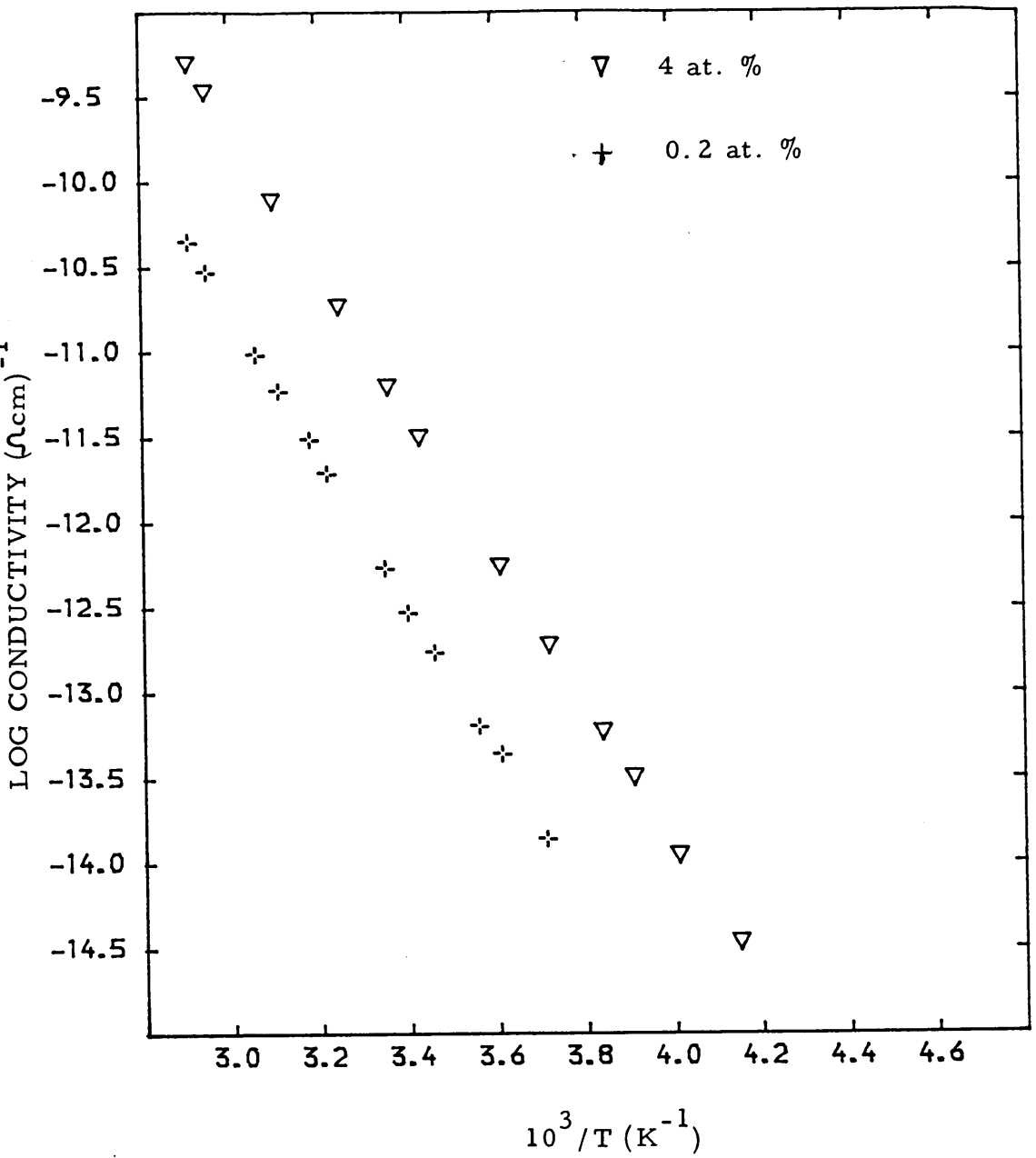

Figure 9.1

Variation of conductivity versus temperature for the two indium doped samples. Specimen details are given in table 9.1.1.

% In	ΔE_σ (eV)	σ(R.T) $(\Omega cm)^{-1}$	σ_o $(\Omega cm)^{-1}$	E_{o2} (eV)
4 at.%	0.89	8×10^{-12}	1550	1.72
0.2 at.%	0.91	6×10^{-13}	250	1.74
0 at.%	0.93	5×10^{-14}	50-100	1.76

Table 9.1.1

% In	$\Delta E_\mu \pm (0.01)$ (eV)	μ_p (cm^2/Vs)	σ_o $(\Omega cm)^{-1}$	N_t (cm^{-3})	N_{v_3} (cm^{-3})
4 at. %	0.41	1120	1550	1×10^{18}	1×10^{21}
0.2 at.%	0.43	105	250	3×10^{18}	3×10^{20}
0 at.%	0.44	10	50-100	8×10^{18} $\downarrow$ 2×10^{19}	8×10^{19} $\downarrow$ 2×10^{20}

Table 9.1.2

indium content together with the room temperature conductivity, zero field activation energy and pre-exponential are also provided in the table. From the table, it can be seen that a small decrease in the conductivity activation energy occurs from 0.93 eV in the undoped sample to about 0.89 eV in the 4 at. % sample. The introduction of indium also increases the conductivity pre-exponential by two orders of magnitude for this most heavily doped sample indicating that conduction remains via the extended states.

The optical absorption results are plotted in figure 9.2, for all of the indium doped samples prepared. In this figure $(\alpha h\nu)^{0.5}$ has been plotted as a function of photon energy. There is little shift (only about 0.03eV) in the absorption edge with increasing dopant concentration.

Thermopower measurements proved difficult and no measurements were obtained in the lightly doped samples. In the sample doped with 4 at. % indium, measurement of the thermopower, when it could be detected at high temperature, suggested p-type conduction. The magnitude of the thermopower was approximately 1mV/K at 80C.

9.1 Photoconductivity results

Figure 9.3 shows steady-state photoconductivity versus intensity measurement at three different temperatures, for the 4 at. % sample. The transition from low intensity (monomolecular) to high intensity (odd power law) behaviour is evident, with increasing flux density. Such a transition also occurs at still lower temperatures, but is experimentally less accessible, as shown in figure 9.4 for five

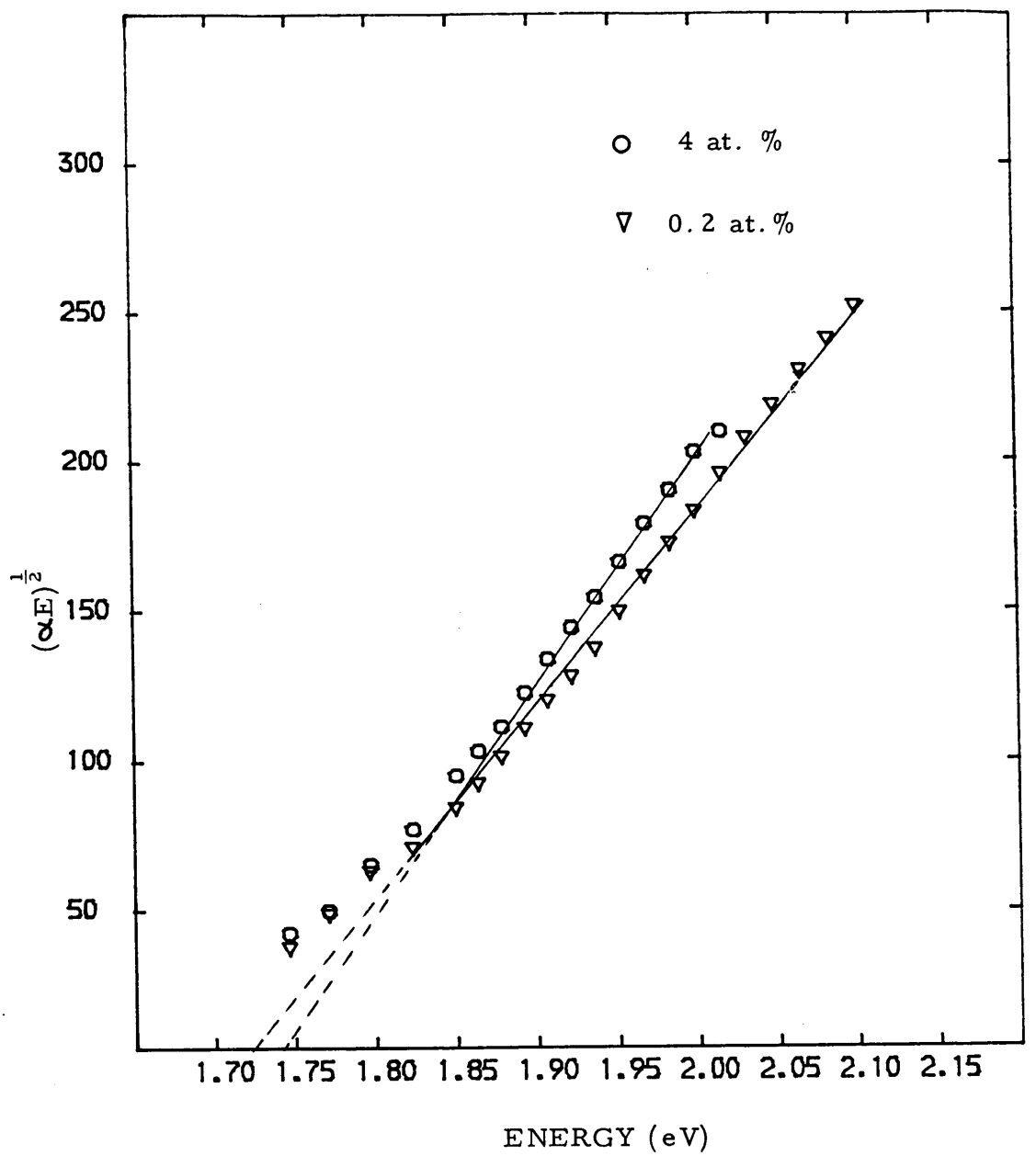

Figure 9.2

Plot of $(\alpha E)^{\frac{1}{2}}$ versus photon energy showing the variation in "optical gap" from specimen to specimen.

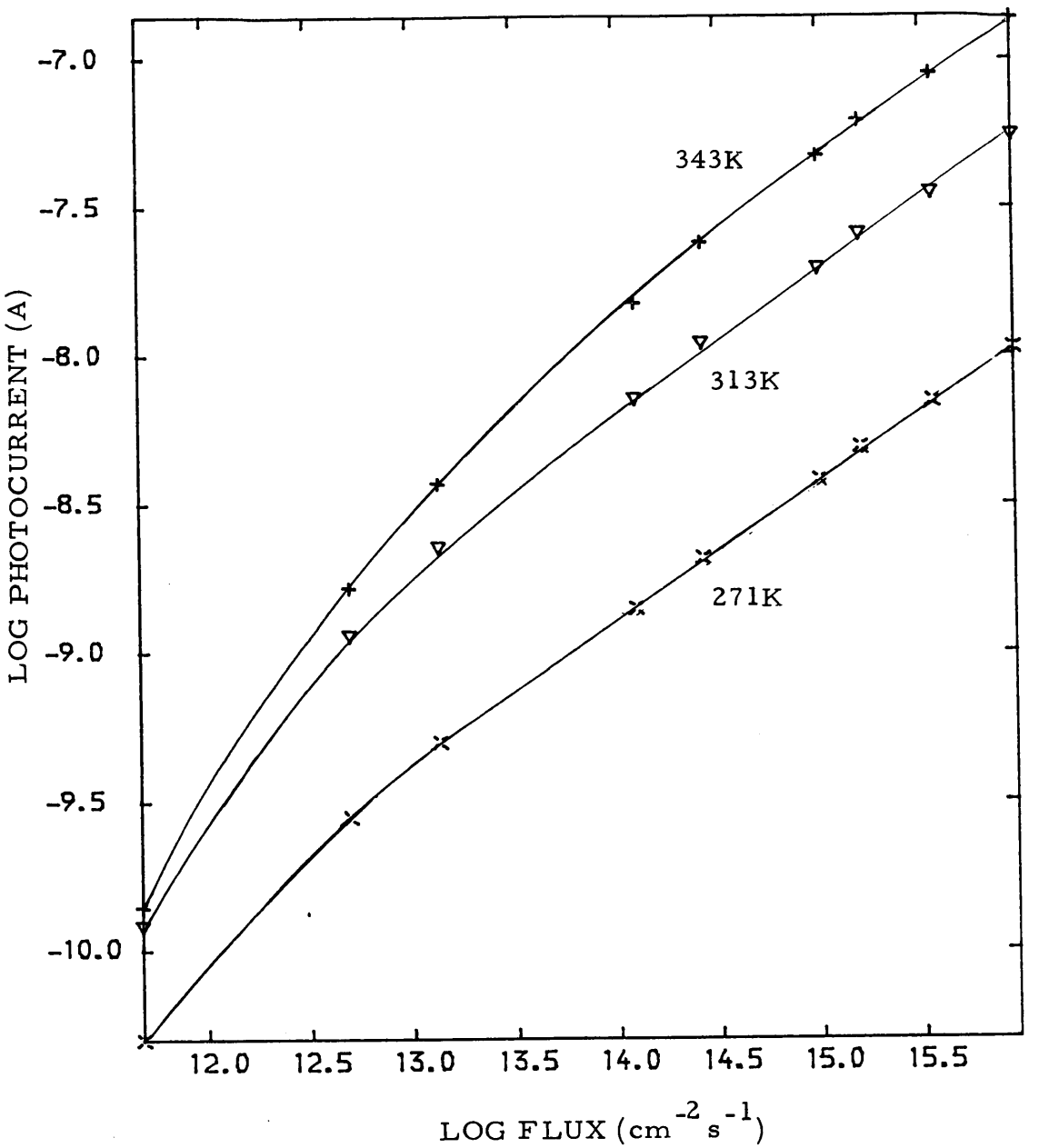

Figure 9.3

Steady State photocurrent versus photon flux for the 4 at. % indium doped sample. Data shown for three different temperatures.

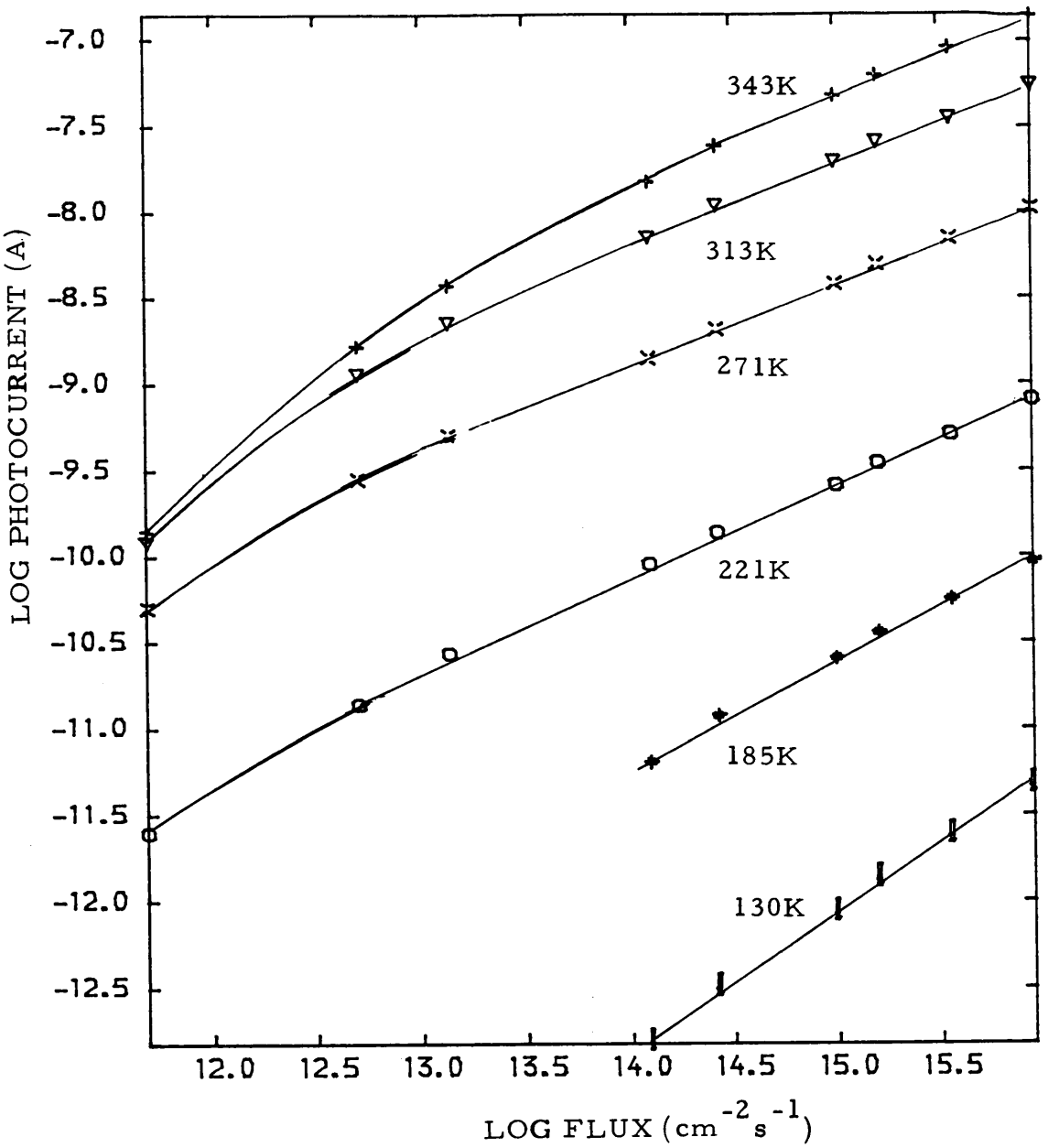

Figure 9.4

Same plot as figure 9.3 for six different temperatures.

different temperatures. The photocurrent index γ (high intensity regime) was calculated at each temperature and is shown in figure 9.5, with γ decreasing from a value of 0.76 at 130 K to a minimum of 0.5 at 270K until it increases again to a maximum value 0.55 at 340K. Also shown in figure 9.5 is the photocurrent index calculated for data from the 0.2 at. % sample, at twelve different temperatures. The index follows a similar trend to that of the 4 at. % sample, decreasing from a value of 0.78 at 152K to go through a minimum of 0.58 at 288K and then increase to a value of 0.63 at the highest temperature at which the measurement was performed (333K). Thus in the indium doped samples, as in the case of nickel, a sublinear relationship exists between the photocurrent and the photon flux density in the high-intensity regime.

The temperature dependence of the steady state photocurrent for both samples, measured at three photon flux levels is shown in figures 9.6 and 9.7 respectively. These figures give some indication of the change over from low-intensity to high-intensity behaviour. Also shown is the variation of dark current with temperature for both samples. Again, from these figures, two regions in the high-intensity regime can be observed. At high temperatures the photocurrent plots are singly activated. At low temperatures there is an intensity-dependent breakpoint (similar to that observed in the nickel doped samples), after which the photocurrent tends to flatten out at low temperatures. This behaviour will be discussed in the next section. An interesting observation from figures 9.6 and 9.7 is the increase in the photocurrent by about one order of magnitude from data

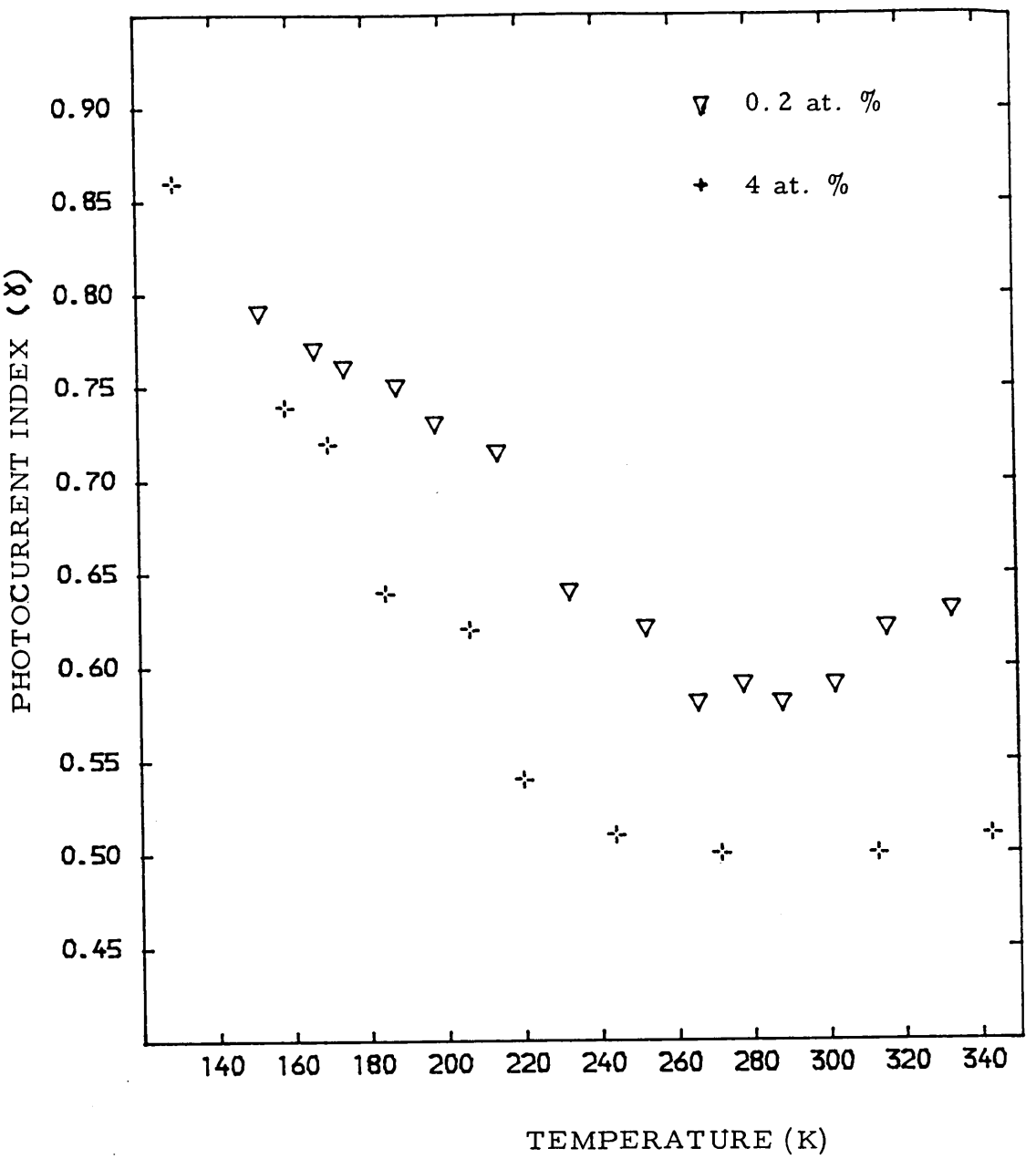

Figure 9.5

Variation of the photocurrent index γ versus temperature for for the 0.2 at. % and 4 at. % indium doped samples

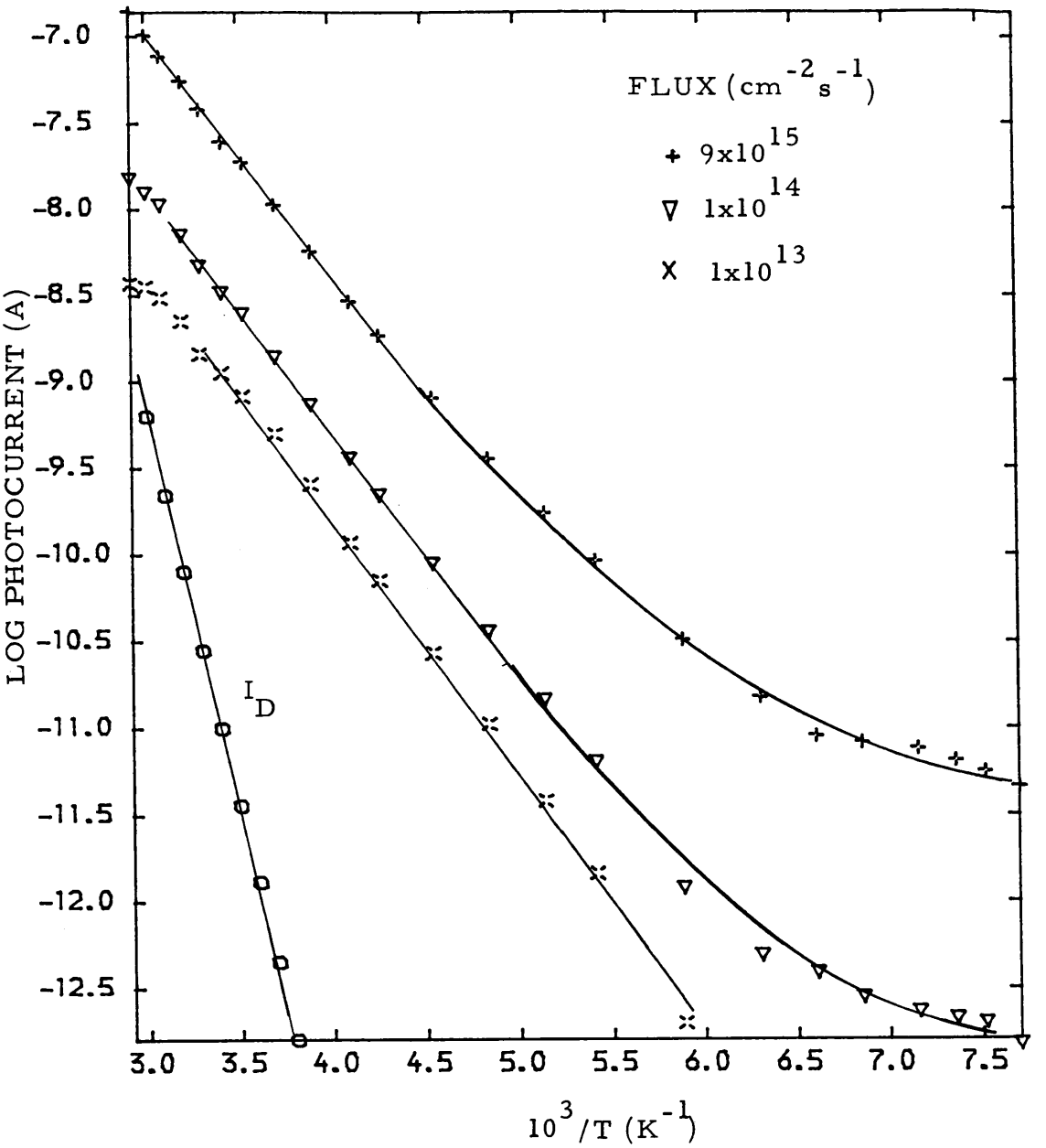

Figure 9.6

Photocurrent versus inverse temperature for the 4 at. % sample. The dark current I_D is also shown.

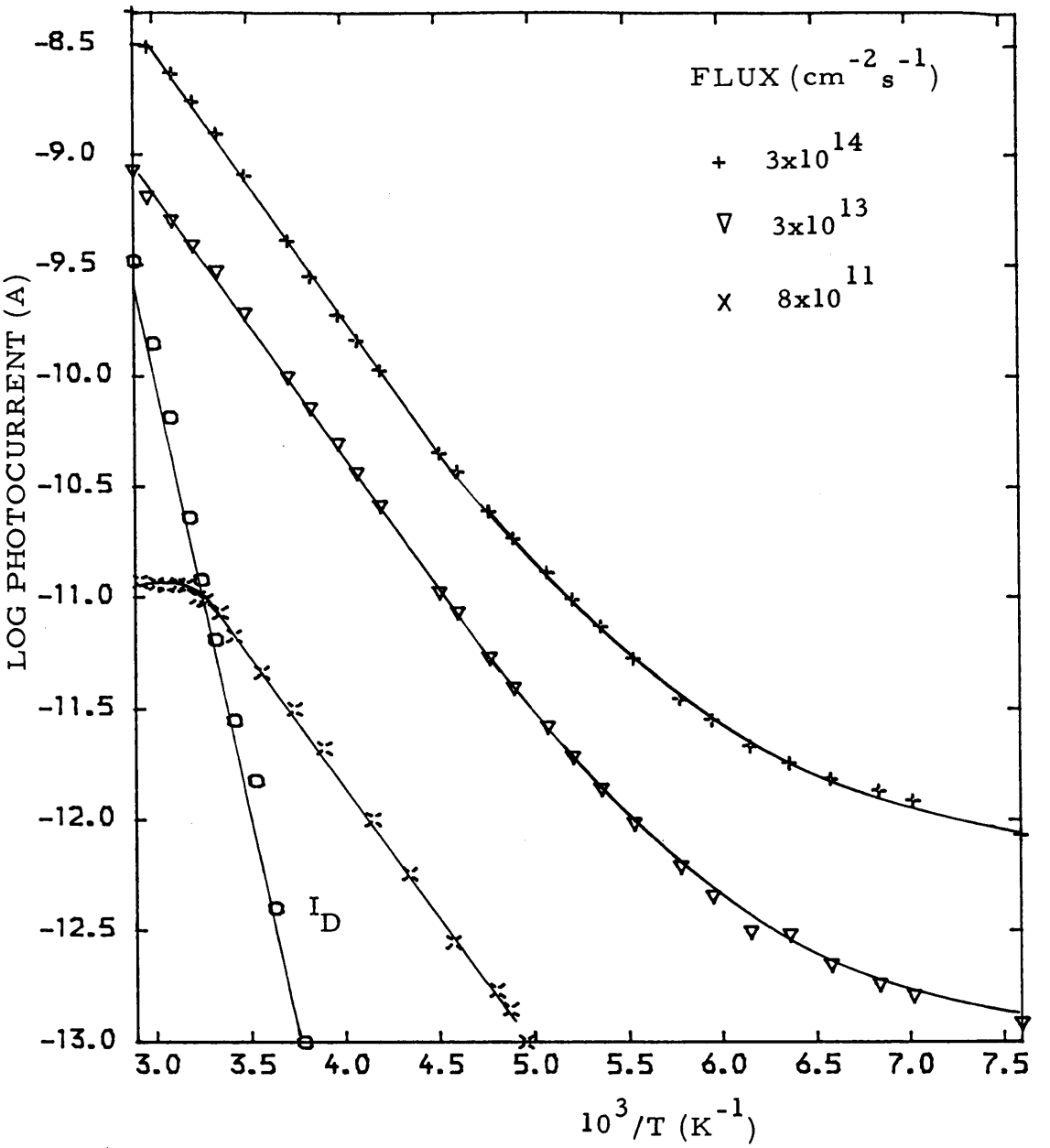

Figure 9.7

Same plot as figure 9.6 for the 0.2 at. % sample.

taken from the 0.2 at. % and 4 at. % doped samples. This implies that the photoconductivity increases with increased dopant concentration.

Plots of the variation of the photomobility and decaytime with temperature are shown in figures 9.8 and 9.9. An interesting feature is the slight decrease in the mobility activation energy from 0.43eV in the 0.2 at. % sample to about 0.41eV in the 4 at. % indium doped sample, while the mobility pre-exponential increases by over an order of magnitude (see table 9.1.2). The decaytime activation energy in both specimens is similar to that of the undoped material having values of 0.13 eV and 0.12 eV in the 0.2 and 4 at. % samples respectively compared to 0.11eV in the undoped case.

9.2 Transient Photoconductivity-Fast Charge

Measurement of the transient decay was restricted to the 0.2 at. % sample, as unfortunately structural deterioration of the 4 at. % indium doped sample occurred, the film flaking from the glass substrate. In figure 9.10 the photocurrent is plotted against time for three different intensities and in figure 9.11 for two different temperatures. It is interesting to note that features in the decay at specific times representing specific energies (see section 7.4, page 156) are not as pronounced as in the undoped specimen, and this will be discussed further.

9.3 Discussion and Analysis

Since the pre-exponentials of both carrier mobility and d.c conductivity, shown in table 9.1.2, suggest an extended state conduction mechanism the transport data will be analysed, as in the

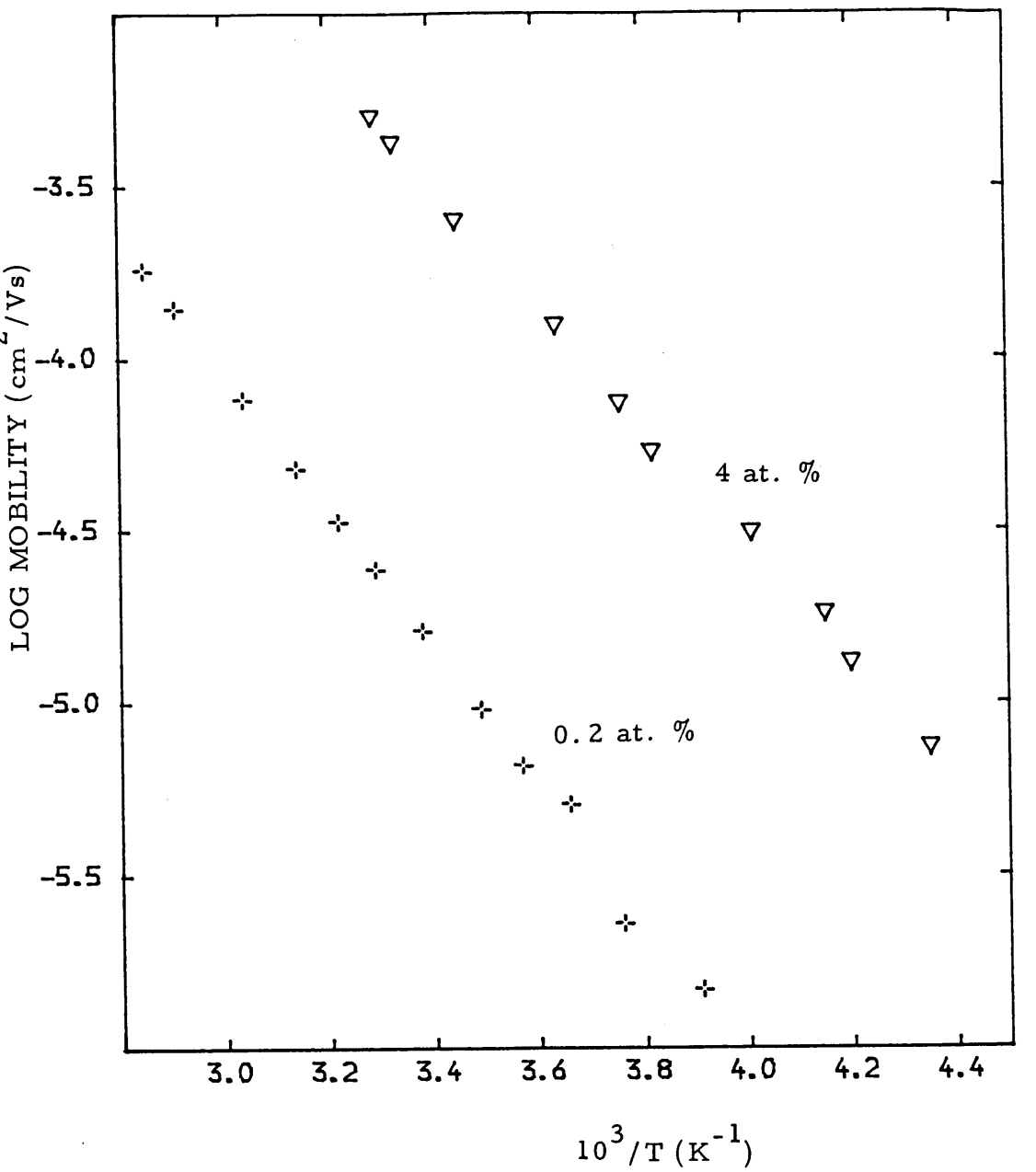

Figure 9.8

Plot of photomobility versus inverse temperature for the two indium doped samples.

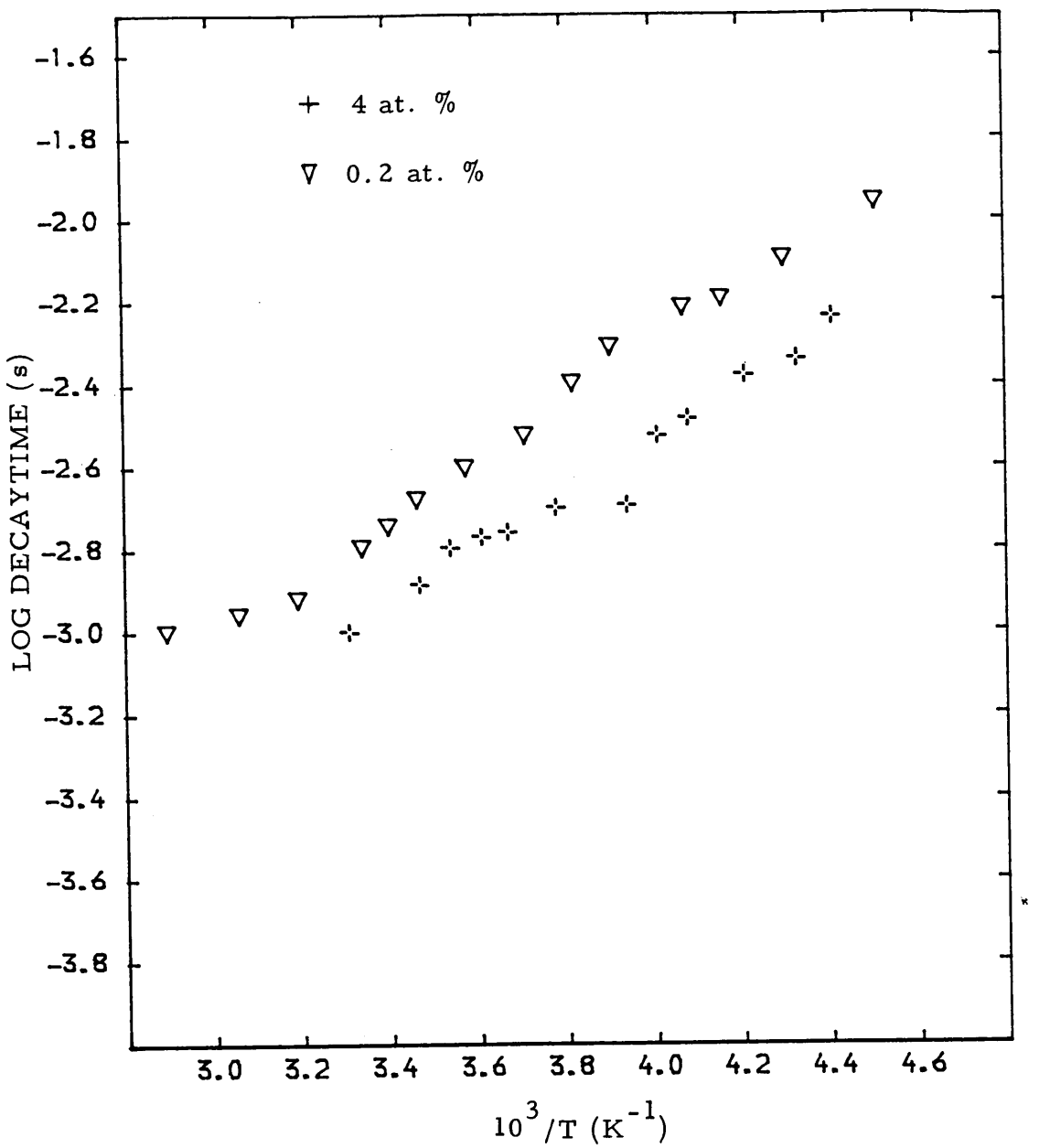

Figure 9.9

Plot of decay lifetime versus inverse temperature for the two indium doped samples.

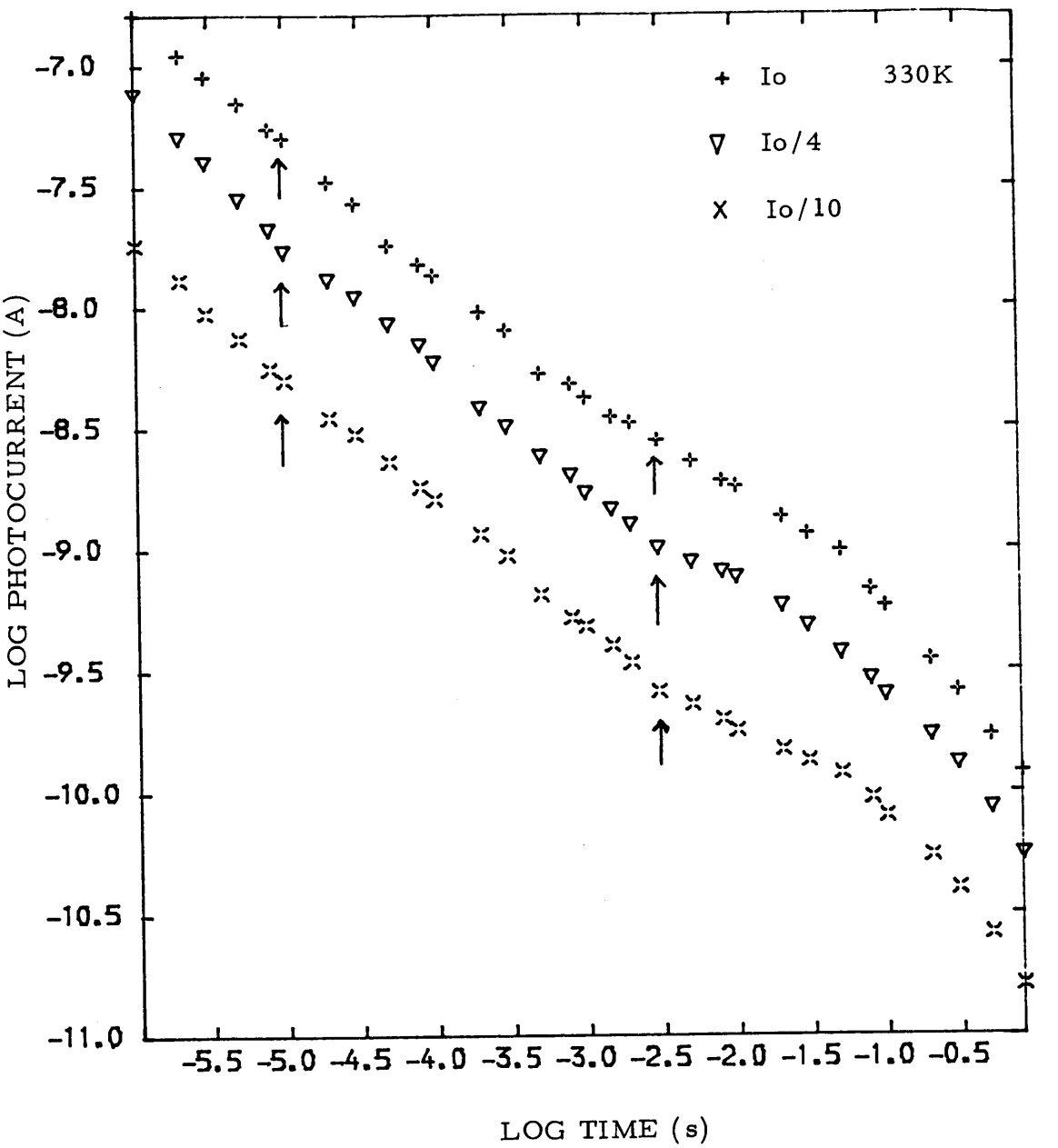

Figure 9.10

Fast charge transient decay data at three different laser intensities from the 0.2 at. % indium doped sample.

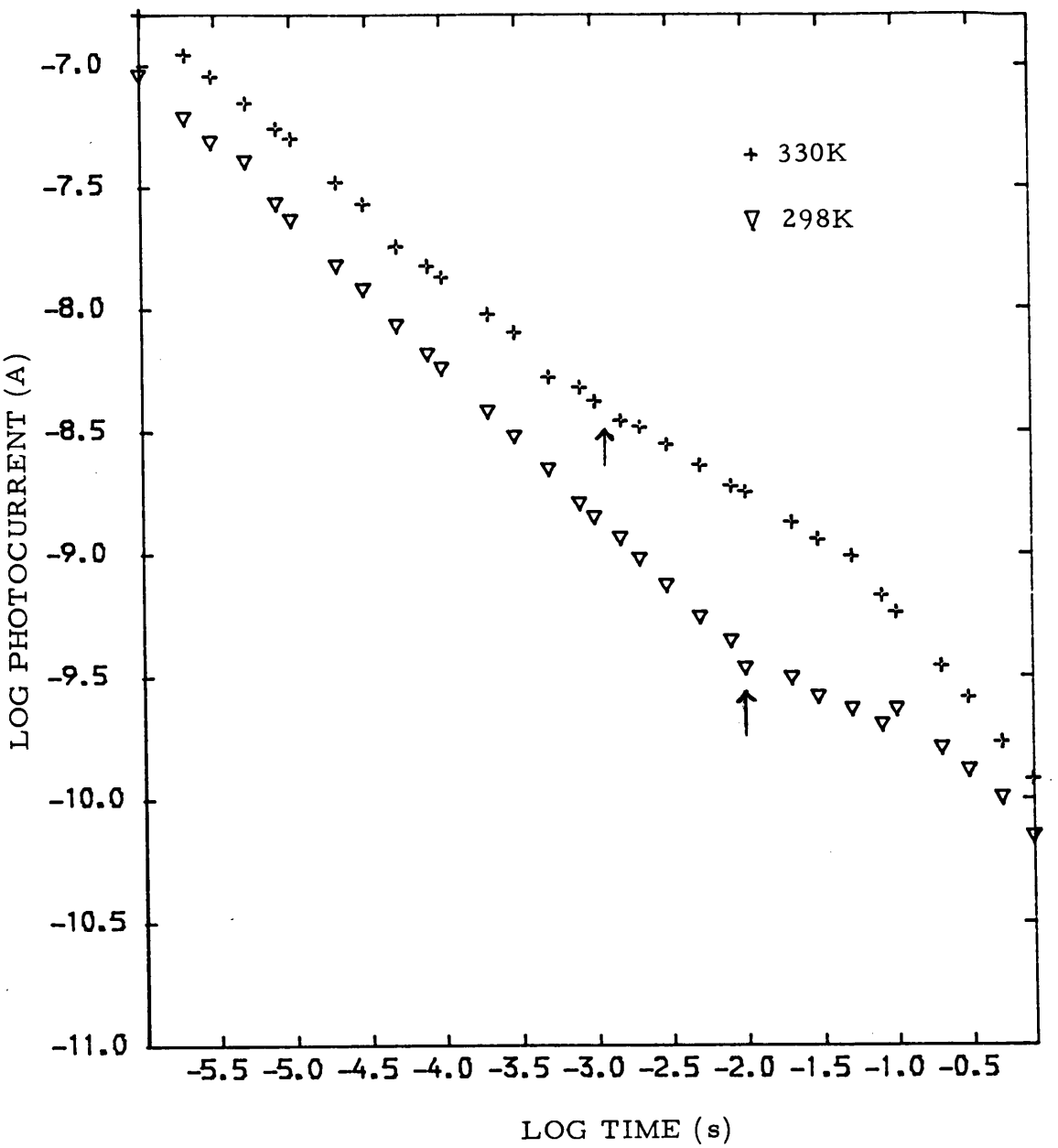

Figure 9.11

The decay of the photocurrent (fast charge) at two different temperatures and intensity Io for the 0.2 at. % indium doped sample. The position of the features arrowed vary with temperature.

undoped material using this mechanism. It is then possible to obtain a trap density (N_t) by combining the conductivity and mobility pre-exponential measurements via equation (7.2). This calculation yields a value for N_t of $3x10^{18}$ cm^{-3} for the 0.2 at. % doped sample and a value of $1x10^{18}$ cm^{-3} for the 4.0 at. % sample, after correction for temperature dilation of the mobility gap. Assuming a value of 1.0cm $^2V^{-1}s^{-1}$ for μ_o, values for N_v of $3.0x10^{20}$ cm^{-3} and $2.0x10^{21}$ cm^{-3} were obtained for both samples respectively, From table 9.1.2 it can be seen that the value of trap density in the doped samples is somewhat lower than that of the undoped material, and that the valence band density of states has increased in comparison. Also it can be seen from figures 9.8 and 9.1 that the increase in mobility tracks the increase in conductivity, from sample to sample in approximately a one to one relation. Additionally the activation energies for both the d.c. conductivity and the photomobility decrease by about the same amount for both doped samples. This correlation between the behaviour of the drift mobility and the d.c. conductivity for both processes suggests a modification of the transport channel by the dopants as opposed to a shift in the Fermi-level, and this is supported by the above valence band edge density calculations.

These results suggest the build up of new localised states at the valence band edge resulting in a maximum shift in the extended state conduction channel of approximately 0.03eV towards the Fermi-level for the most heavily doped sample. It is interesting to note that this shift is in agreement with the shift of the optical gap. Assuming p-type conduction, as observed in the thermopower

measurement, this shift implies that the build up of extra states occurs entirely at the valence band edge. Studies performed elsewhere, on more highly doped indium samples, also observe a red shift of the absorption edge (0.1 eV) of the same magnitude as the decrease in the transport conduction energies. Pfister and Morgan[159] interpret these results, in a similar manner to that suggested above, in terms of impurity related valence states which extend to approx. 0.1 eV above the hole transport states.

The density of states at the E_3 trap level decreases with increasing dopant concentration. This implies that the impurity states are incorporated in a manner which affects the trap density at this particular energy. Thus a fraction of the impurities alter the intrinsic trap density. This observation will be used in the interpretation of the transient photoconductivity and steady- state photoconductivity results in the following sections.

The transient decay data shown in figure 9.10, obtained from the 0.2 at. % doped sample are similar to those obtained from the vitreous sample, discussed in subsection 6.4.1. Deviations from power law behaviour occur at times shorter than 10 μs, and this represents carrier interaction with the E_3 level. It can be seen from figure 9.10 that the initial short-time decay region is not as rapid as that obtained from the undoped sputtered samples. This phenomenon, as revealed by the simulation studies of section 4.2, page 103, could occur due to either a decrease in the trapped density or a smearing out of the density of localised states at this particular energy

level. The calculation of the trap density at E_3 above suggest that the first proposed mechanism is responsible for the slowing down of trapping rate. Deviations from power law to shallower decay behaviour were observed beyond a time of 2ms for the 330K data. This time corresponds, using the thermalisation concept of section 7.4, to carrier equilibrium in the E_2 level, proving once again that this level does exist in sputtered arsenic triselenide. The fact that this level is more prominent in the indium doped material may be due to a combination of a decrease in the trap density at the E_3 level and an increase in the trap density at the E_2 level introduced by the indium impurities.

The decay data for three different nitrogen laser intensities are also shown in figure 9.10. From this figure it can be seen that the main features do not vary with intensity, the photocurrent increasing on a one to one ratio with increasing intensity. The very rapid decay region observed at times greater than 20mS is due to monomolecular recombination, and this mechanism has been discussed previously in section 7.3, page 154.

The steady state conductivity data will now be discussed in the light of the above findings. The activation energies of the temperature dependence of steady state photoconductivity in the bimolecular region for the two doped specimens are 0.30 eV for the 0.2 at.% sample and 0.29 eV for the 4 at. % sample. These values have been corrected for field and intensity dependence as well as for spectral response but are somewhat higher than the 0.22 eV value obtained for

undoped material. The band-to-localised recombination mechanism described in subsection 3.1.8, page 68, was applied to the data. It was found that the temperature dependence of the photoconductivity in this activated high-intensity region is controlled by traps at E_2 where E_2-E_v= 0.6eV in the 0.2 at.% sample and 0.58 eV in the 4 at. % sample. When the shift in the valence band edge is taken into account, this gives an energy value of about 0.61 ± 0.01 for this trap level. Therefore the E_2 level dominates the temperature dependence of the steady state photoconductivity in the doped specimens, whereas E_3 trap level dominates in the undoped specimens. This again implies that a decrease in the density of states at E_3 (and possible an increase in the density at E_2) occurs when incorporating indium.

The occurrence of a low temperature, intensity dependent, breakpoint in the steady state photocurrent (see figures 9.6 and 9.7) implies, as in the nickel doped specimens (see section 8.6, page 186), a change in the occupancy function for the hole traps. The position of the quasi Fermi-level was calculated from the estimated ratio $\Delta p/p_o$ for the break-point, and in each case, $E_{Fp} - E_F$ was approximately 0.3eV, which corresponds to a trap depth of 0.62ev in agreement with the steady state experiments. The fact that this value is roughly the same in both samples shows that the Fermi-level, for the dark equilibrium case, remains pinned and has not shifted. This again gives added support to the proposed model density of states, for indium doped arsenic triselenide.

The room temperature value of the decay lifetime varies

little between the doped specimens, implying that the increase in the steady state photocurrent value is due entirely to the calculated increase in mobility with higher concentration of dopant, as observed in figure 9.8. The activation energy of the decay lifetime varies by only about 0.02 eV, having a value of 0.13eV in the 0.2 at. % sample and a value of 0.11eV in the 4.0 at % sample. These activation energies are similar to that predicted from the assumed recombination mechanism discussed in section 7.5. The difference could again be accounted for by the variation in the valence band energy E_v.

The variation of the photocurrent index γ with temperature is similar to that observed in the nickel doped samples. Thus the argument based on the fact that the above applied recombination model uses idealised discrete levels instead of smeared 'amorphous' trap levels is again proposed.

Chapter 10

SUMMARY OF DISCUSSION

The electronic and transport properties of undoped and doped arsenic triselenide have been characterised experimentally in an extensive study. Measurement of optical absorption, time of flight (TOF), a recently developed technique related to time of flight which we term "transient photoconductivity" (TP), thermoelectric power and dark d.c. conductivity were made. The time of flight technique was improved in a manner which eliminated space charge distortion of the transit pulse. In addition, a photoconductivity experiment was developed in which the specimen is illuminated by a light emitting diode to a steady state conductivity level after which the intensity is modulated by a small percentage of the steady state value. From the rise and decay of this modulation, parameters such as photomobilities and carrier lifetimes can be measured.

10.1 Undoped Arsenic triselenide

The results obtained from vitreous, evaporated and sputtered samples were explained on the basis of a trap-limited band transport mechanism involving carrier interaction with two trap levels situated at energies E_2 (0.62eV) and E_3 (0.42eV) above the valence band edge. The density of states calculated for each trap level are summarised in Table 10.1.1.

The variation of the dispersion parameter α with temperature as measured from the TOF experiment in vitreous specimens supports the presence of structure in the distribution of localised states N(E) at the E_2 trap level. These results have recently been

Material	N_2 (0.62eV) (cm^{-3})	N_3 (0.42eV) (cm^{-3})
Vitreous	$1x10^{16}$	
Evaporated	$1x10^{16}$	$1x10^{18}$
Sputtered		$0.8\text{-}2x10^{19}$

Table 10.1.1

included in a review article written by Marshall [160].

Deviation from power law behaviour in the transient photodecay, again supports a structured N(E). A computer simulation of the thermalisation process was developed using model distributions of localised states in order to obtain N(E) from the data. Each distribution can be represented by a set of discrete levels. From this representation first order differential equations for each component of the model can be found and a fourth order Runge-Kutta or a matrix numerical integration technique was used to solve these. For sputtered material a continuous tail with a feature, width 0.05eV, of six times the background density incorporated at an energy E_3 gave the best fit to the experimental data.

Determination of N(E) using two other recently developed spectroscopic interpretations, the "intuitive thermalisation" analysis first applied in detail by Marshall and Main, and the more accurate analysis given by Michiel et al gave excellent agreement in the energy position of the main feature at E_3 in the density of states. This is the first time that different spectroscopic techniques have been applied to the same experimental data. Further application of the "intuitive thermalisation" technique to data obtained at higher temperatures also gave good agreement in the position of the energy feature E_3.

From the spectroscopic study it was realised that analysis of transient photocurrent data at different temperatures offered a <u>new technique</u> for obtaining values of the capture co-efficient if applied

over a wide enough temperature range. It was also realised that if there were a number of specific energy features prominent in the density of states that it may be possible to determine the energy dependence of the capture cross-section (if any).

Comparing sputtered material with that produced by other techniques, our analytical and experimental evidence implies that the process of r.f. sputtering introduces larger densities of trap states at the E_3 level.

10.2 Doped Arsenic Triselenide

Doping with nickel shifts the position of the Fermi-level by as much as 0.6eV towards the valence band edge. This results in conductivity increases of up to 11 orders of magnitude. Such massive increases in conductivity have never before been reported in arsenic triselenide. The shift is most pronounced in the dopant range 0.2 to 1.0 at. %. Further increase of the dopant concentration leads to only minor shifts in the Fermi-level, its position being stabilised.

Another novelty never before observed in doped arsenic triselenide is the discontinuity in the conductivity/temperature curves with the conductivity activation energy <u>decreasing</u> with increasing temperature.

The sign of the thermopower suggests n-type conduction in the most heavily doped specimen (7 at. %). This type of conduction has rarely been seen in doped chalcogenides where previous studies have shown the independence of conductivity on dopant concentration to be one of the distinctive features of the chalcogenide.

The shifts in the Fermi-level were explained using the intrinsic model density modified by the inclusion of an acceptor level representing the nickel impurities. The energy position of these states, estimated from the shift in the Fermi-level to be about 0.22eV below the valence band edge, was also evidenced from the photomobility and carrier lifetime activation energies. Further support for the presence of this dopant level was provided by optical absorption measurements in which a shoulder in the absorption tail, representing transitions from impurity states to extended states, became more apparent as the dopant concentration was increased.

The influence of indium on the electronic and transport properties is strikingly different from that of nickel; there being little variation of conductivity with increased dopant concentration. The small decrease in the optical gap is similar in magnitude to the decrease in conductivity and mobility activation energies, suggesting a modification of the extended state conduction channel by the impurity rather than a shift of the Fermi-level.

In support of this model, the valence band density of states was found to increase with increasing indium content whilst trap density N_3 was found to decrease. A decrease of N_3 was also inferred from the transient photoconductivity and steady state photoconductivity measurements.

10.3 Publications

As a result of the above findings the following papers have either been submitted or are to be submitted for publication.

1. "Evidence From Thermalisation of a Structured Distribution of States in Arsenic Triselenide", Authors; R.P.Barclay, J.M. Marshall, C.Main and M.Munro; Paper presented by the author at the 1984 Chelsea Meeting on Liquid and Amorphous Semiconductors.

2. "Validity of The 'Thermalisation Energy' Concept in the Determination of Localised State Distributions for Amorphous Semiconductors', Authors; J.M.Marshall and R.P.Barclay; Paper submitted for publication to the Mott Festschrift.

3. "The Transient Photodecay Process, and its Interpretation in the Case Disordered Single Crystals of Arsenic Triselenide", Authors; J.M.Marshall, R.P.Barclay and C.Dunn; "in preparation" to Phil. Mag. B.

4. "Transient Photoconductivity in Arsenic Triselenide: Computer Modeling and Circuit Analogues of the Thermalisation Process Involved", "in preparation".

5. "Measurements of D.C. Conductivity, Thermopower and Optical Absorption in Nickel Doped R.F. Sputtered Arsenic Triselenide", "in preparation".

6. "The Electrical, Electronic Transport and Optical Properties of Modified Films of Arsenic Triselenide Produced by Co-sputtering", "in preparation".

REFERENCES

1. Kolomiets, B T, Phys. Stat. Sol., Vol. 7, 359, 1964.

2. Kolomiets, B T, Phys. Stat. Sol., Vol. 7, 713, 1964.

3. Ovshinsky S R, Phys. Rev. Lett., Vol. 21, 1450, 1968.

4. Scharfe M E, Phys. Rev. B., Vol. 2, 5025, 1970.

5. Scher H and Montroll E W, Phys. Rev. B, Vol. 12, 2455, 1975.

6. Spear W E, LeComber P G and Snell A J, Phys. Rev. B, Vol. 38, 308, 1976.

7. Okano S and Suzuki M, J. Non Cryst. Sol., Vol. 59-60, 969, 1983.

8. Tohge N, Tsutomu M and Masami M, J. of Non-Cryst. Sol., Vol. 59-60, 999, 1983.

9. Bloch F, Z. Physik, Vol. 52, 555, 1928.

10. Frohlich H, Proc. R. Soc. A, Vol. 188, 521, 1947.

11. Mott N F, J. of Appl. Phys., Vol. 16, 49, 1967.

12. Anderson P W, Applied Physics, Vol. 109, 1492, 1958.

13. Thouless D J, Phys. Rep., Vol. 13C, 93, 1974.

14. Abou-Chacra R and Thouless D J, J. Phys. C, Vol. 7, 709, 1965.

15. N.F. Mott and E.A.Davis, Electronic Processes in Non-crystalline Materials, Claredon Press. Oxford, 1979.

16. Pepper M, Proc. R. Soc. A, Vol. 345, 169, 1975.

17. Ioffe A F, Bull Acad. Sci.(USSR), Vol. 15, 477, 1951.

18. Brodsky M H, Amorphous Semiconductors - Topics in Applied Physics, Springer Verlag, 1969.

19. Cohen M H, J. of Non-Cryst. Sol., Vol. 4, 391, 1970.

20. Hindley N K, J. of Non-Cryst. Sol., Vol. 5, 17, 1970.

21. Friedman L, J. of Non-Cryst. Sol., Vol. 6, 329, 1971.

22. Miller A and Abrahams S, Phys. Rev., Vol. 120, 745, 1960.

23. Twose W D, Ph.D Thesis, University of Cambridge, 1959.

24. Mott N F, Phil. Mag. B, Vol. 19, 835, 1969.

25. Mott, N F, J. Non-Cryst. Sol., Vol. 8-10, 7, 1972.

26. Efros B I and Shklovskii A L, J. of Phys. C, Vol. C8, L49, 1975.

27. Pollak M, Phil. Mag. B, Vol. 42, 781, 1980.

28. Emin D, Advances in Physics, Vol. 24, 305, 1975.

29. Holstein T, Ann. Phys., Vol. 8, 331, 1959.

30. Culter M and Mott N F, Phys. Rev. B, Vol. 181, 1336, 1979.

31. Fritzche H, Sol. State Comm., Vol. 9, 1813, 1971.

32. Overhof H, Phys. Status Solidi (b), Vol. 67, 709, 1975.

33. Davis, E A and Mott, N F, Phil. Mag. B, Vol. 22, 903, 1970.

34. J Tauc, Amorphous and Liquid Semiconductors, Plenum Press, London and New York, 1974.

35. Owen A E, Contemp. Phys., Vol. 11, 227, 1970.

36. Dow J D and Redfield D, Phys. Rev. B, Vol. 1, 3358, 1970.

37. Anderson D et al, J. of Non-Cryst. Sol., Vol. 35-36, 345, 1980.

38. Jackson W B and Amer M N, Phys. Rev. B, Vol. 25, 5559, 1982.

39. Alder D et al, Rev. Mod. Phys., Vol. 50, 203, 1978.

40. Weiser G, The Physics of Selenium and Tellurium, Springer Series in Solid-State Sciences, 1979.

41. Wright A C and Leadbetter A J, J. Phys. Chem., Vol. 17, 121, 1974.

42. Nemanisch R J, Street R A and Connell A N, Phys. Rev. B, Vol. 18, 6900, 1979.

43. Apling A J and Leadbetter A J, "Proc. 5th Int. Conf. on Amor. and Liq. Semicond.", J Stuke and W Brenig, ed., Garmisch-Partenkirchen, 1974, pp. 457.

44. Taylor P C, Bishop S G and Mitchell A, Phys. Rev. B, Vol. 12, 2455, 1975.

45. Phillips J C, J Non-cryst Sol., Vol. 35-36, 1159, 1979.

46. Szeftel J, Phys. Mag. B, Vol. 43, 549, 1981.

47. Rubinstein M and Taylor P C, Phys. Rev. B, Vol. 9, 4258, 1974.

48. Cohen M H, Fritzsche S R and Ovshinsky S R, Phys. Rev. Lett., Vol. 22, 1065, 1969.

49. Main C, Photoconductivity, Noise, and Related Phenomena in Some Amorphous Chalcogenide Semiconductors, PhD dissertation, University of Edinburgh, 1974.

50. Marshall J M and Owen A E, Phil. Mag., Vol. 24, 1281, 1971.

51. Mytilineou E and Roilos M, Phil. Mag. B, Vol. 37, 387, 1978.

52. Edmond J T, J. of Non-Cryst. Sol., Vol. 1, 39, 1968.

53. Marshall J M and Owen A E, Phil. Mag., Vol. 31, 1341, 1975.

54. Nagels P, Callaerts R and Denayer N, "Proc. 5th Int. Conf. on Amor. and Liq. Semicond.", J Stuke and W Brenig, ed., Garmisch-Partenkirchen, 1974, pp. 867.

55. Seager C H, Emin D and Quinn R K, Phys. Rev. B, Vol. 8, 4746, 1973.

56. Seager C H and Quinn R K, J. Non-Cryst. sol., Vol. 17, 386, 1975.

57. Klaffke and Wood, "Proc. 4th Int. Conf. on Non-Cryst. Sol.", Fritschat, ed., Trans. Tech., 1977, pp. .

58. Panasyuk L M et al, Sov. Phys. Semi., Vol. 14, 34, 1980.

59. Sharp A C, Marshall J M and Fortuna H F, "Proc. 9th Int. Conf. on Amor. and Liq. Semicond.", Deneuville, A, ed., Grenoble, 1981, pp. C4 159.

60. Provencher S W, J. Chem. Phys., Vol. 64, 2772, 1976.

61. De Wit and Crevecoeur J, J. Non Cryst. Sol., Vol. 8-10, 787, 1972.

62. Marshall J M and Miller G R, Phil. Mag., Vol. 27, 1151, 1973.

63. Marshall J M, Fisher F D nd Owen A E, "Proc. 5th Int. Conf. on Amor. and Liq. Semicond.", J Stuke and W Brenig, ed., Garmisch-Partenkirchen, 1974, pp. 1305.

64. Hurst C H and Davis E A, "Proc. 5th Int. Conf. on Amor. and Liq. Semicond.", J Stuke and W Brenig, ed., Garmisch-Partenkirchen, 1974, pp. 349.

65. Mott N F and Street R A, Phil. Mag., Vol. 36, 33, 1977.

66. Onsager L, Phil. Rev.B, Vol. 54, 554, 1938.

67. Pai D M and Enck R C, Phil. Rev. B, Vol. 11, 5163, 1975.

68. Pfister G, Phys. Rev. Lett., Vol. 33, 1474, 1974.

69. Fisher F D, Marshall J M and Owen A E, Phil. Mag., Vol. 33, 261, 1976.

70. Pfister G and Scher H, Phil. Mag. B, Vol. 15, 2062, 1977.

71. Pfister G and Scher H, Adv. Phys., Vol. 27, 747, 1978.

72. Kolomiets B T, Lebedev E A and Kazakova L P, Sov. Phys. Semicond., Vol. 12, 1049, 1978.

73. Sharp A C and Marshall J M, J. of Phys. C, Vol. 14, L761, 1981.

74. Marshall J M, J. of Phys. C, Vol. 10, 1283, 1977.

75. Pfister G, Phil. Mag. B, Vol. 36, 1147, 1977.

76. Pfister G et al, Phys. Rev. Lett., Vol. 41, 1318, 1978.

77. Anderson P W, Phys. Rev. Lett., Vol. 36, 953, 1975.

78. Mott N F, Davis E A and Street R A, Phil. Mag., Vol. 32, 961, 1975.

79. Ngai K L and Taylor P C, Phil. Mag. B, Vol. 37, 175, 1978.

80. Kastner M, Alder D and Fritsche H, Phys. Rev. Lett., Vol. 37, 1504, 1975.

81. Kastner M A and Fritsche H, Phil. Mag. B, Vol. 37,

1504, 1978.

82. Kolomiets B T, Manontova T N and Babaev A A, J. Non Cryst. Sol., Vol. 4, 289, 1970.

83. Kolomiets B T, J. Non Cryst. Sol., Vol. 8-10, 1004, 1972.

84. Street R A, Adv. Phys., Vol. 25, 347, 1976.

85. Cernogora et al, Sol. St. Commun., Vol. 19, 465, 1976.

86. Mollet et al, "Proc. 6th Int. Conf. on Amor. and Liq. Semicond.", Nauka, ed., Leningrad, 1975, pp. 237.

87. Bishop S G and Michell D L, Phys. Rev. B, Vol. 8, 5696, 1973.

88. Kastner M and Hudgens S J, Phil. Mag. B, Vol. 37, 665, 1978.

89. Mott N F, J. Phys. C, Vol. 30, 5433, 1980.

90. Street R A, Phys. Rev. B, Vol. 23, 861, 1981.

91. Bishop S G, Strom U and Taylor P C, Phys. Rev. Lett., Vol. 36, 534, 1976.

92. Bishop S G, Phys. Rev. B, Vol. 15, 2278, 1977.

93. Bishop S G and Taylor P C, J. of Non Cryst. Sol., Vol. 35-36, 909, 1980.

94. Muzuno K, Tanaka K and Kikuchi M, Sol. State Commun., Vol. 12, 999, 1973.

95. Ganin V M et al, Pisma v ZhTPh, Vol. 5, 7, 1979.

96. Ovshinsky S R, "Proc. 7th Int. Conf. on Amor. and Liq. Semicond.", W E Spear, ed., Edinburgh, 1977, pp. 519.

97. Kottwitz A et al, Structure, Physico-Chemical Properties and Application of Non-Cryst. Semiconductors, Kishinev, 1980.

98. Kolomiets B T, J. Non Cryst. Sol., Vol. 59-60, 973, 1983.

99. Tohge et al, Appl. Phys. Lett., Vol. 34, 640, 1979.

100. Nagels P et al, J. De Physique, Vol. 42, C4-907, 1981.

101. Bhatia K L, J. Non Cryst. Sol., Vol. 54, 173, 1983.

102. Saresbinov Sh Sh et al, J. De Physique, Vol. 42, C4-907, 1981.

103. Pfister G and Morgan M, Phil. Mag. B, Vol. 41, 209, 1980.

104. Van der Ziel A, Fluctuation Phenomena in Semiconductors, Butterworths, London, 1959.

105. Lax M, J. Phys. Chem. Sol., Vol. 8, 66, 1959.

106. Simmons J G and Taylor G W, J. Phys. C, Vol. 7, 3051, 1974.

107. Taylor G W and Simmons J G, J. Phys. C, Vol. 7, 3067, 1974.

108. Arnoldussen, T C, Phys. Rev. B., Vol. 9, 3377, 1974.

109. Weiser K. et al., "Proc. Tenth Int. Conf. Phys. Semicond.", Keller, Hensel and Stern, eds., US Atomic Commission, 1970, pp. 667.

110. Rose, A, Concepts in Photoconductivity and Allied Problems, Robert E. Krieger Publishing Co., 1978.

111. Vorokov, E et al, J. Non. Cryst. Sol., Vol. 15, 275, 1974.

112. Marshall J M and Street R A, Sol. Stat. Comm., Vol. 36, 959, 1977.

113. Pfister G and Griffiths C H, Phys. Rev. Lett., Vol. 40, 659, 1978.

114. Marshall J M and Sharp A C, J. Non-Cryst. Sol., Vol. 35, 99, 1980.

115. Tiedje T, Cebulka J M, Morel D and Abeles B, Phys. Rev. Lett., Vol. 46, 1425, 1983.

116. Marshall J M, Michiel H and Adriaenssens G J, Phil. Mag. B, Vol. 47, 211, 1983.

117. Marshall J M, Phil. Mag. B, Vol. 36, 959, 1977.

118. Silver M and Cohen L, Phil. Rev. B, Vol. 15, 3276, 1977.

119. Schmidlin F, Phys. Rev. B, Vol. 6, 2362, 1977.

120. Schmidlin F, Bull. Am. Phys. Soc., Vol. 22, 434, 1977.

121. Noolandi J, Phys. Rev. B, Vol. 16, 4466, 1977.

122. Noolandi J, Phys. Rev. B, Vol. 16, 4474, 1977.

123. Pollak M, J. Non-cryst. Sol., Vol. 35, 83, 1980.

124. Alder J and Silver M, Phil. Mag. B, Vol. 45, 307, 1982.

125. Schirmacker W, Sol. Stat Comm., Vol. 39, 39, 1981.

126. Orenstein J and Kastner M, Phy. Rev. Lett., Vol. 23, 161, 1979.

127. Orenstein J and Kastner M, Phy. Rev. Lett., Vol. 46, 1421, 1981.

128. Tiedje T and Rose A, Solid State Commun., Vol. 37, 48, 1983.

129. Marshall J M and Main C, Phil. Mag. B, Vol. 47, 471, 1983.

130. Kirby P B and Paul W, Phil. Rev. B, Vol. 45, 5373, 1982.

131. Michiel H, Marshall J M and Adriaenssens G J, Phil. Mag. B, Vol. 48, 181, 1983.

132. Michiel H, Adriaenssens G J and Marshall J M, J. Phys. C., Vol. 16, 1005, 1983.

133. Marshall J M and Dunn C, Private Comm., 1984.

134. Michiel H and Adriaenssens G J, Phil. Mag. B, Vol. 51, 27, 1985.

135. Zdenek A, Numerical Analysis, Wiley New York, 1955.

136. Main C, Private Comm., 1984.

137. Orenstein et al, J. of Non Cryst. Sol., Vol. 35-36, 951, 1980.

138. Jackson G N, Thin Film Solids, Vol. 5, 209, 1970.

139. Freeman L A, Thin Film Solids, Vol. 3, 367, 1969.

140. Spear W E, J. of Non Cryst. Solids, Vol. 1, 197, 1969.

141. Dolezalek F K and Spear W E, J. of Non Cryst. Solids, Vol. 4, 97, 1969.

142. Orenstein J et al, Phil. Mag. B, 23, 1982.

143. Petursson J, Optical Absorption and Photoconductivity in Simple Chalcogenide Glasses, PhD dissertation, University of Edinburgh, 1975.

144. Halpern V, "Proc. 7th Int. Conf. on Amor. and Liq. Semicond.", W E Spear, ed., Edinburgh, 1977, pp. 276.

145. Khan et al, Sol. State Comm., Vol. 45, 187, 1983.

146. Mort J et al, Sol. Stat. Comm., Vol. 39, 1329, 1981.

147. Arkhipov V I and Rudenko A I, J. of Non-Cryst Sol., Vol. 30, 163, 1978.

148. Sharp A C, Carrier Transport in Undoped and Doped Films of Amorphous Arsenic Triselenide, PhD dissertation, Dundee College of Technology, 1983.

149. Olley J A, A Study of Amorphous Solids Using Ion Bombardment, PhD dissertation, University of Cambridge, 1983.

150. Tanaka T et al, J. Vac. Soc. Japan, Vol. 23, 12, 1980.

151. Spear W E and LeComber P G, Phys. Rev. B, Vol. 33, 935, 1976.

152. Kolomiets B T et al, Solar Energy Materials, Vol. 8, 1, 1982.

153. Jones D I et al, Phil. Mag. B, Vol. 36, 541, 1977.

154. Spear W E et al, J. of Non-Cryst. Sol., Vol. 35/36, 357, 1980.

155. Beyer W and Fischer R, Appl. Phys. Lett., Vol. 31, 850, 1978.

156. Mott N F, Phil. Mag. B, Vol. 34, 1101, 1976.

157. Moddel et al, Phys. Rev. B, Vol. 22, 1918, 1980.

158. Collins et al, J. Non-Cryst. Sol., Vol. 35/36, 681, 1980.

159. Pfister G and Morgan M, Phil. Mag. B, Vol. 41, 191, 1980.

160. Marshall J M, Reports on Progress in Physics, Vol. 46, 1235, 1983.

ABSTRACT

COMPUTER PROGRAMMES USED IN THE SIMULATION OF THE TRANSIENT PHOTOCONDUCTIVITY

```
C       RUNGE-KUTTA PROGRAM USED IN THE SIMULATION OF THE
C       THE TRANSIENT PHOTOCONDUCTIVITY FOR THE CASE OF AN
C       EXPONENTIAL TAIL.
        REAL LL(50),L(50)
        DIMENSION H(200),G0(200),G1(200),G2(200),G3(200)
        DIMENSION C(200),R(200),PQ(200),QCS(100),Q(200),QF(200)
        INTEGER I,IMAX,IVAL,M
        DATA L(1),L(2),L(3),L(4),L(5),L(6)/1.0,2.0,3.0,4.0,6.0,8.0/
C
C       Value of capacitance
C
        CS=1.0
        Q0=1.0
        DO 660 I=1,200
        PQ(I)=0.0
660     Q(I)=0.0
C
C       Input of Data
C
        WRITE(5,500)
500     FORMAT(1H ,'  INPUT N,IMAX,H1')
        READ(5,501)N,IMAX,H1
501     FORMAT(I,I,F)
        DO 15 IVAL=1,44
15      L(IVAL+6)=10*L(IVAL)
        DO 17 IVAL=1,IMAX
        A=L(IVAL)
17      LL(IVAL)=ALOG10(A)
        DO 570 I=1,N
570     C(I)=CS*0.5*EXP(0.4*I)
        SUMMAT=0.0
        DO 590 I=1,N
        SUMMAT=SUMMAT+EXP(-0.1*I)
590     CONTINUE
        DO 580 I=1,N
        R(I)=SUMMAT/EXP(-0.1*I)
580     CONTINUE
C       Runge-Kutta algorithm
        INC=1
        X=0
6       I301=0
        DO 5 I=1,N
5       H(I)=Q(I)
        GOTO 301
70      DO 10 I=1,N
10      G0(I)=QF(I)
        Z=H1/2
100     DO 20 I=1,N
20      Q(I)=H(I)+Z*QF(I)
        GOTO 301
80      DO 30 I=1,N
30      G1(I)=2*QF(I)
        GOTO 100
90      DO 40 I=1,N
```

```
40      G2(I)=2*QF(I)
        Z=H1
        GOTO 100
110     DO 50 I=1,N
50      G3(I)=QF(I)
        DO 60 I=1,N
60      Q(I)=H(I)+((H1/6)*(G0(I)+G1(I)+G2(I)+G3(I)))
        X=X+H1
        IF(X.LT.1000.0)GOTO 55
        H1=5.0
55      IF(X.LT.100.0)GOTO 54
        H1=2.0
54      TOTALQ=0.0
        DO 65 I=1,N
65      TOTALQ=TOTALQ+(Q(I)-PQ(I))
        Q0=Q0-TOTALQ
        DO 66 I=1,N
66      PQ(I)=Q(I)
        TYPE *,X
C       Storage of receiving-end voltage
C
        IF(X.NE.L(INC))GOTO 75
        QCS(INC)=ALOG10(Q0)
        TYPE*, QCS(INC)
        INC=INC+1
75      IF(INC-(IMAX+1))6,215,215
C
C       Differential Equations
C
301     DO 303 I=1,N
303     QF(I)=(((Q0/CS)-(Q(I)/C(I)))/R(I))
        I301=I301+1
        IF(I301.EQ.1)GOTO 70
        IF(I301.EQ.2)GOTO 80
        IF(I301.EQ.3)GOTO 90
        IF(I301.EQ.4)GOTO 110
C
C       Graphical Output
        PSX=0.2
        PSY=0.2
215     CALL PAPER(1)
        CALL PSPACE(0.2,0.95,0.2,0.95)
        CALL MAP(LL(1),LL(IMAX),-7.0,1.0)
        CALL AXES
        CALL SCALES
        DO 999 M=1,IMAX
        CALL PLOTNC(LL(M),QCS(M),45)
        IF(M-IMAX)999,609,609
999     CALL JOIN(LL(M+1),QCS(M+1))
609     CONTINUE
        CALL PLACE(25,30)
        CALL TYPECS('N=',2)
        CALL TYPENI(N)
        CALL TYPECS('      H1=',9)
```

```
      CALL TYPENF(H1,3)
      CALL GREND
900   STOP
      END
```

```
C       TRANSIENT PHOTOCONDUCTIVITY SIMULATION OF A
C       GAUSSIAN DISTRIBUTION BY DR MAIN USING THE
C       TRANSITION MATRIX METHOD
        DOUBLE PRECISION A(100,100),B(100,100),C(100,100)
        DOUBLE PRECISION G(100),N1(100),N(100,60)
        DOUBLE PRECISION DT,DE,CN,S,BT,ED,CE,PB
        INTEGER TS,NL,H
        REAL X(100),Y(100)
        COMMON /C1/B,C
        WRITE(5,10)
10      FORMAT(1H ,'  INPUT TS,NL,DE,DT')
        READ(5,20)TS,NL,DE,DT
20      FORMAT(2I,2F)
        WRITE(5,15)
15      FORMAT(1H ,'  INPUT BT,ED,CE')
        READ(5,17)BT,ED,CE
17      FORMAT(3F)
C       SET UP DENSITY OF STATES
C       AND 'RELEASE DENSITY',N1(I)
        S=0.0
        DO 30 I=1,NL
        S=S+DE*DEXP(-((DFLOAT(NL/2-I)*DE/CE)**2))
        N1(I)=DEXP(-(ED+DFLOAT(I-NL/2)*DE))
30      CONTINUE
C       DENSITY PREFACTOR PB
        PB=BT/S
C       NORMALIZED DENSITY OF STATES
        DO 25 I=1,NL
        G(I)=DE*PB*DEXP(-((DFLOAT(NL/2-I)*DE/CE)**2))
        TYPE *,G(I)
25      CONTINUE
C       CAPTURE COEFFICIENT CN
        CN=1.0/BT
C       SET UP TRANSITION MATRIX,A(I,J)
        A(1,1)=1.0-DT
        DO 40 I=2,NL+1
        A(1,I)=N1(I-1)*CN*DT
        A(I,1)=G(I-1)*CN*DT
        A(I,I)=1.0-N1(I-1)*CN*DT
40      CONTINUE
C       SET UP DUMMY MATRIX,B(I,J)
        DO 50 I=1,NL+1
        DO 50 J=1,NL+1
        B(I,J)=A(I,J)
50      CONTINUE
C       COLLECT PARAMETER VALUES IN ARRAY N( )
C       INITIAL STEP
        DO 60 I=1,NL+1
        N(I,1)=B(I,1)
60      CONTINUE
C       MATRIX MULTIPLICATION
        DO 70 L=2,TS
        DO 80 I=1,NL+1
        DO 80 J=1,NL+1
```

```
      DO 80 K=1,NL+1
      C(I,J)=C(I,J)+B(I,K)*B(K,J)
80    CONTINUE
C     COLLECT PARAMETERS IN ARRAY N( )
      DO 90 I=1,NL+1
      N(I,L)=C(I,1)
90    CONTINUE
C     UPDATE MATRIX B;ZEROIZE C
      DO 85 M=1,NL+1
      DO 85 H=1,NL+1
      B(M,H)=C(M,H)
      C(M,H)=0.0
85    CONTINUE
70    CONTINUE
      DO 110 I=1,TS
      WRITE(5,100)N(1,I),I
100   FORMAT(F,I)
110   CONTINUE
C     SET UP TIME AXIS
      DO 120 I=1,TS
      X(I)=LOG10(DT)+FLOAT(I-1)*LOG10(2.0)
      Y(I)=LOG10(N(1,I))+10.0
      TYPE *,X(I)
120   CONTINUE
      CALL PAPER(1)
      CALL PSPACE(0.3,0.9,0.2,0.9)
      CALL MAP(X(1),X(TS)+0.5,Y(TS)-0.1,10.01)
      CALL SCALES
      CALL BORDER
      CALL CTRSET(4)
      CALL CTRMAG(18)
      DO 140 I=1,TS
      CALL PLOTNC(X(I),Y(I),50)
140   CONTINUE
      CALL GREND
      STOP
      END
```

```
C       TRANSIENT PHOTOCONDUCTIVITY SIMULATION OF A
C       MODEL EXPONENTIAL DISTRIBUTION WITH RECTANGULAR STRUCTURE
C       TRANSITION MATRIX METHOD
        DOUBLE PRECISION A(100,100),B(100,100),C(100,100)
        DOUBLE PRECISION G(100),N1(100),N(100,60,5)
        DOUBLE PRECISION DT,DE,CN,S,T,RD,KT,T1
        REAL ET,X(100),Y(100,10)
        INTEGER TS,NL,H,IET,JT
        WRITE(5,10)
10      FORMAT(1H ,'  INPUT TS,NL,TC,DT,T1')
        READ(5,20)TS,NL,TC,DT,T1
20      FORMAT(2I,3F)
C       SINGLE LEVEL DEPTH SELECTION
        WRITE(5,22)
22      FORMAT(1H '  INPUT DISCRETE LEVEL DEPTH, ET (EV)')
        READ(5,24)ET
24      FORMAT(F)
C       RELATIVE DENSITY OF STATES
        WRITE(5,26)
26      FORMAT(1H ,'  INPUT RELATIVE DENSITY OF DISCRETE LEVEL,RD')
        READ(5,28),RD
28      FORMAT(F)
C       TEMPERATURE STEPS
        DO 250 JT=1,4
        T=T1+(JT-1)*25
C       COMPUTE REDUCED ENERGY STEP,DE
        KT=8.625D-5*T
        DE=1.0/(DFLOAT(NL)*KT)
C       THIS TRUNCATES TAIL AT 1.0EV
C       LOCATE LEVEL NEAREST ET
        IET=IFIX(ET*FLOAT(NL)+0.5)
C       IET=DISCRETE LEVEL NUMBER
C       SET UP DENSITY OF STATES
C       AND 'RELEASE DENSITY',N1(I)
        S=0.0
        DO 30 I=1,NL
        G(I)=DE*DEXP(-DFLOAT(I)*DE*T/TC)
C       IS THIS CORRECT?
        S=S+G(I)
        N1(I)=DEXP(-DFLOAT(I)*DE)
30      CONTINUE
        S=S-G(IET)-G(IET-1)-G(IET+1)
        G(IET)=G(IET)*RD
        G(IET-1)=G(IET)
        G(IET+1)=G(IET)
        S=S+G(IET)+G(IET-1)+G(IET+1)
C       NORMALIZE CAPTURE COEFFICIENT,CN
        CN=1.0/S
C       SET UP TRANSITION MATRIX,A(I,J)
        A(1,1)=1.0-DT
        DO 40 I=2,NL+1
        A(1,I)=N1(I-1)*CN*DT
        A(I,1)=G(I-1)*CN*DT
        A(I,I)=1.0-N1(I-1)*CN*DT
```

```
40      CONTINUE
C       SET UP DUMMY MATRIX,B(I,J)
        DO 50 I=1,NL+1
        DO 50 J=1,NL+1
        B(I,J)=A(I,J)
50      CONTINUE
C       COLLECT PARAMETER VALUES IN ARRAY N( )
C       INITIAL STEP
        DO 60 I=1,NL+1
        N(I,1,JT)=B(I,1)
60      CONTINUE
C       MATRIX MULTIPLICATION
        DO 70 L=2,TS
        DO 80 I=1,NL+1
        DO 80 J=1,NL+1
        DO 80 K=1,NL+1
        C(I,J)=C(I,J)+B(I,K)*B(K,J)
80      CONTINUE
C       COLLECT PARAMETERS IN ARRAY N( )
        DO 90 I=1,NL+1
        N(I,L,JT)=C(I,1)
90      CONTINUE
C       UPDATE MATRIX B;ZEROIZE C
        DO 85 M=1,NL+1
        DO 85 H=1,NL+1
        B(M,H)=C(M,H)
        C(M,H)=0.0
85      CONTINUE
70      CONTINUE
        DO 110 I=1,TS
        WRITE(5,100)N(1,I,JT),I
100     FORMAT(F,I)
110     CONTINUE
C       SET UP X AND Y AXES
        DO 200 I=1,TS
        X(I)=LOG10(DT)+FLOAT(I-1)*LOG10(2.0)
        Y(I,JT)=LOG10(N(1,I,JT))+10.0
200     CONTINUE
250     CONTINUE
        CALL PAPER(1)
        CALL PSPACE(0.3,0.9,0.2,0.9)
        CALL MAP(X(1),X(TS),Y(TS,1)-0.1,10.01)
        CALL SCALES
        CALL BORDER
        CALL CTRSET(4)
        CALL CTRMAG(15)
        DO 220 I=1,TS
        CALL PLOTNC(X(I),Y(I,1),62)
220     CONTINUE
        DO 230 I=1,TS
        CALL PLOTNC(X(I),Y(I,2),51)
230     CONTINUE
        DO 240 I=1,TS
        CALL PLOTNC(X(I),Y(I,3),63)
```

```
240     CONTINUE
        DO 251 I=1,TS
        CALL PLOTNC(X(I),Y(I,4),54)
251     CONTINUE
        CALL GREND
        STOP
        END
```